INFORMATION TO USERS

CONJUGATE FREE CONVECTION HEAT TRANSFER IN VERTICAL ECCENTRIC ANNULI

BY

AHMAD JAMAL

A Thesis Presented to the

DEANSHIP OF GRADUATE STUDIES

KING FAHD UNIVERSITY OF PETROLEUM & MINERALS

DHAHRAN, SAUDI ARABIA

In Partial Fulfillment of the
Requirements for the Degree of

MASTER OF SCIENCE

In

MECHANICAL ENGINEERING

NOVEMBER 2002

UMI Number: 1412291

UMI®

KING FAHD UNIVERSITY OF PETROLEUM & MINERALS

DHAHRAN 31261, SAUDI ARABIA

DEANSHIP OF GRADUATE STUDIES
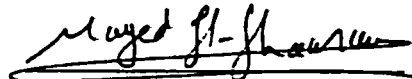
This thesis, written by

AHMAD JAMAL

Under the direction of his thesis advisor and approved by his thesis committee, has been presented to and accepted by the Dean of Graduate Studies, in partial fulfillment of the requirements for the degree of
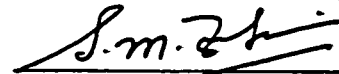
MASTER OF SCIENCE IN MECHANICAL ENGINEERING.

Thesis Committee
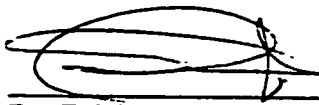
Dr. M. A. I. El-Shaarawi (Chairman)

Dr. Esmail M. A. Mokheimer (Co-Chairman)

Dr. Habib I. Abualhamayel (Member)

Dr. Syed M. Zubair (Member)

Dr. Mohammad Antar (Member)

Dr. Faleh A. Al-Sulaiman
Department Chairman

Prof. Osama Ahmed Jannadi
Dean of Graduate Studies

18/12/2002
Date

This work is dedicated to

My Father, Mother and

My Wife

ACKNOWLEDGEMENTS

iv

Razzaq Mohib for his useful suggestions during preparation of the presentation of my thesis. An expression of gratitude for all friends in KFUPM, particularly my house-mates Mr. Irfan-Ul-Haq, Mr. Tariq Saeed and Mr. Abid Maqsood for being cooperative.

Finally, I am grateful to my Parents, my wife, and all family members for their extreme moral support, encouragement and patience during the course of my studies here.

CONTENTS

LIST OF TABLES

LIST OF FIGURES

xviii

NOMENCLATURE

a   Location of the positive pole of the bipolar coordinate system on the x-axis of the Cartesian coordinate system, $r_{oi} \sinh \eta_i$

AVHF$_i$ Average heat flux on the inner solid-fluid interface

AVHF$_o$ Average heat flux on the outer solid-fluid interface

AVNU$_{i,fd}$ Average Nusselt number on inner solid-fluid interface in fully developed region

AVNU$_{o,fd}$ Average Nusselt number on outer solid-fluid interface in fully developed region

D$_h$ Hydraulic or equivalent diameter of annulus,

$$2(r_{io} - r_{oi}) = 2a(1 - NR_2)\cos ech\eta_o$$

$\dfrac{dp}{dz}$ Pressure gradient

e   Eccentricity (Distance between axes of the two cylinders)

E   Dimensionless eccentricity, $\dfrac{e}{(r_{io} - r_{oi})}$

f   Volumetric flow rate, $f = \pi (r_{io}^2 - r_{oi}^2)\overline{u}$

F   Dimensionless volumetric flow rate, $F = U_o(1 - NR_2^2)$

g   Gravitational body force per unit mass (acceleration)

Gr	Grashof number, $\dfrac{g\beta(T_w - T_o)D_h{}^3}{\gamma^2}$ (in case with isothermal walls)
Gr*	Modified Grashof number, $\dfrac{GrD_h}{l}$
h	Coordinate transformation scale factor
H	Dimensionless coordinate transformation scale factor, $\dfrac{h}{D_h}$
HF$_i$	Local heat flux on inner interface
HF$_o$	Local heat flux on outer interface
i	Index for bi-polar grid in the η-direction and the cylindrical grid in the radial direction
Iwall	Dimensionless thickness of inner cylinder wall, $NR_2 - NR_1$
j	Index for the bi-polar grid in the ξ-direction and the cylindrical grid in the tangential direction
K$_f$	Thermal conductivity of fluid
K$_s$	Thermal conductivity of solid
KR	Solid-fluid conductivity ratio, K_s/K_f
l	Height of channel
L	Dimensionless height of channel (value of Z at channel exit), $l/Gr*$
M	No. of intervals in each of the ξ & ϕ directions
N	Number of intervals in the η-direction

NR_1	Ratio between inner radius of inner cylinder and inner radius of outer cylinder, $\dfrac{r_{ii}}{r_{io}}$
NR_2	Ratio between outer radius of inner cylinder and inner radius of outer cylinder (Fluid annulus radius ratio), $\dfrac{r_{oi}}{r_{io}}$
NR_3	Dimensionless inner radius of outer cylinder, 1
NR_4	Ratio between outer radius of outer cylinder and inner radius of outer cylinder, $\dfrac{r_{oo}}{r_{io}}$
NSI	No. of radial intervals in the inner cylinder wall
NSO	No. of radial intervals in the outer cylinder wall
$NU_{i,ex}$	Local Nusselt number on inner solid-fluid interface at channel exit
$NU_{o,ex}$	Local Nusselt number on outer solid-fluid interface at channel exit
Owall	Dimensionless thickness of outer cylinder wall, $NR_4 - NR_3$
P	Dimensionless Pressure defect of fluid inside the channel at any cross section, $\dfrac{p' D_h^4}{\rho l^2 \gamma^2 Gr *^2}$
p_s	Hydrostatic pressure, $\rho\, g\, z$
p'	Pressure defect at any point, $p - p_s$
Q	Dimensionless heat absorbed from the entrance up to any particular elevation, $F\theta_m$

$\overline{Q}$ Dimensionless heat absorbed up to the annulus exit, i.e., values of Q at z = 1,

$F\theta_{m.ex}$

r_{ii} Inner radius of inner cylinder

r_{oi} Outer radius of inner cylinder

r_{io} Inner radius of outer cylinder

r_{oo} Outer radius of outer cylinder

R   Dimensionless radial coordinate, $\dfrac{r}{r_{io}}$

ΔR_i $\dfrac{NR_2 - NR_1}{NSI}$

ΔR_o $\dfrac{NR_4 - NR_3}{NSO}$

T   Temperature at any point

T_o Ambient or fluid entrance temperature

T_w Isothermal temperature of heated wall

U   Dimensionless axial velocity at any point, $\dfrac{ur_{io}^2}{l\gamma Gr*}$

$\overline{u}$ Average (mean) axial velocity

u_o Entrance axial velocity

U_o Dimensionless axial velocity at annulus entrance, $\dfrac{u_o r_{io}^2}{l\gamma Gr*}$

V   Velocity vector or dimensionless η-velocity component, $\dfrac{vD_h}{\gamma}$

W	Dimensionless ξ-velocity component, $\dfrac{wD_k}{\gamma}$
z	Axial coordinate (measured from the annulus entrance)
Z	Dimensionless axial coordinate in both the Cartesian and bipolar coordinate systems, $\dfrac{z}{lGr^{\bullet}}$
ΔZ	Dimensionless Axial step increment, $\dfrac{\Delta z}{lGr^{\bullet}}$

Greek Letters

η	First transverse bi-polar coordinate
η_i	Value of η on ther inner interface
η_o	Value of η on the outer intrfcace
$\Delta \eta$	Numerical grid mesh size in η-direction
θ	Dimensionless temperature, $\dfrac{(T - T_o)}{(T_w - T_o)}$ for isothermal walls case
θ_f	Value of θ in the fluid annulus
θ_m	Mean bulk temperature
$\theta_{m,ex}$	Mean bulk temperature at channel exit
$\theta_{m,fd}$	Fully developed value of θ_m
θ_{si}	Value of θ in the inner solid wall
θ_{so}	Value of θ in the outer solid wall.
γ	Kinematic viscosity of fluid, $\dfrac{\mu}{\rho}$

ρ	Density of Fluid
Ψ	Normalized value of ξ, $\dfrac{\xi}{\pi}$
α	Thermal diffusivity of fluid, $\dfrac{k}{\rho c_p}$
β	Volumetric coefficient of thermal expansion
ξ	Second transverse bi-polar point.
$\Delta\xi$	Numerical grid mesh size in ξ-direction
ϕ	Angle along the cylinder walls
$\Delta\phi$	$\dfrac{\pi}{M}$

THESIS ABSTRACT

Name: Ahmad Jamal

Title: Conjugate Free convection heat transfer in vertical eccentric annuli.

Degree: Master of Science

Major Field: Mechanical Engineering

Date of Degree: November 2002

Conjugate laminar free convection heat transfer in vertical eccentric annuli is numerically investigated. Heat transfer parameters such as temperature, heat flux and bulk mean temperature have been numerically obtained for a fluid of Prandtl number, Pr=0.7 in the eccentric annulus at different values of eccentricity, radius ratio, wall thickness and conductivity ratio. In addition to these parameters, the effect of conductivity ratio, eccentricity, wall thickness and radius ratio on channel height, required to induce specific flow rate, has also been investigated. The analysis has been carried out for two different pairs of thermal boundary conditions. One pair of boundary conditions comprises of one wall kept isothermal at inlet fluid temperature while the other wall heated isothermally whereas the other pair of boundary conditions consists of one wall kept adiabatic while the other wall heated isothermally. Furthermore, results of the present study are utilized for the first pair of boundary conditions to establish the limits, namely the critical values, for solid-fluid conductivity ratio, above which, and wall thickness, below which, the conjugate effect can be neglected for various eccentricity and radius ratio values. Also, for the second pair of boundary conditions, the optimum values of solid-fluid conductivity ratio and wall thickness, giving the maximum induced flow rate for a given channel height, have been obtained for various radius ratio and eccentricity values.

Master of Science Degree

King Fahd University of Petroleum and Minerals

Dhahran, Saudi Arabia

November 2002

" الملخـــص "

الأسم: أحمد جمـــــال

العنوان: إنتقال الحرارة المترافق بالحمل الحر في أنبوب حلقي لامركزي رأسي.

الدرجة: الماجستير.

المجال: الهندسة الميكانيكية.

تم دراسة إنتقال الحرارة الطبقي بالحمل الحر المترافق في أنبوب حلقي لامركزي رأسي باستخدام طرق عددية. وقد تم دراسة متغيرات إنتقال الحرارة في أنبوب حلقي لامركزي موضوع رأسياً في وسط مائع ذي رقم برانتل يساوي ٠٫٧ ولقد تم تغير نسبة القطر الداخلي الى الخارجي للانبوب الحلقي وكذلك تم تغير نسبة اللامركزية للانبوب كما تم تغير نسبة معامل انتقال الحرارة بالتوصيل للمادة الصلبة للانبوب والمائع بحيث يغطي المدى الموجود في الحالات العملية لسماكات الأنابيب الموجودة وذلك تحت تأثير زوجين من الظروف الحرارية على الجدارين الخارجي والداخلي للانبوب ويتميز أحد زوجي هذه الظروف الحرارية بالحفاظ على احد الجدارين عند درجة حرارة أعلى من درجة حرارة الوسط المائع المحيط بالانبوب والجدار الأخر يحفظ عند درجة حرارة المائع. ويتميز الزوج الأخر بالحفاظ على احد الجدارين عند درجة حرارة أعلى من درجة حرارة المائع ويبقى الجدار الأخر معزولاً حرارياً. ويجب ملاحظة أن تبادل الظروف الحرارية بين الجدار الداخلي والخارجي في كل من زوجي الظروف الحرارية السابقة ينتج عنه أربعة أنواع من الظروف الحرارية على جداري الأنبوب. ولقد تحت دراسة تأثير كل تلك المتغيرات على معدل سريان المائع بالحمل الحر داخل الأنبوب اللامركزي الرأسي وكمية الحرارة التي يمتصها هذا المائع. ولقد تم إستخدام نتائج الدراسة الحالية لحساب حدود فنسبة التوصيل الحراري التي يمكن فوقها إهمال تأثير الترافق كما تم تحديد سماكة الجدارن التى يمكن تحتها إهمال تأثير الترافق وذلك تحت تأثير الزوج الأول من الظروف الحرارية كما تم دراسة تأثير نسبة نصف القطر واللامركزية على هذه الحدود. كما تم حساب القيم المثلى لنسبة التوصيل الحراري وسماكة الجدران التي تعطي أعلى معدل لسريان المائع داخل الانبوب بالحمل الحر وكذلك أعلى معدل لامتصاص الحرارة من الأنبوب بواسطة المائع وكذلك تم دراسة تأثير نسبة نصف القطر واللامركزية على هذه القيم تحت تأثير الزوج الثانى من الظروف الحرارية.

Chapter 1

INTRODUCTION

The study of steady laminar induced flow in vertical eccentric annuli with conjugate heat transfer is of great importance because of its many engineering applications in electrical, nuclear, solar and thermal storage fields.

In the electrical field, in vertical electric motors and generators, the heat generated by irreversible electrical and mechanical processes is transferred through the air gap between the rotor and the stator by natural convection. The transfer of heat by free convection is always a factor in the cooling of such machines and may be the sole means of cooling small types of these devices. Another typical application is that of gas cooled nuclear reactor, in which cylindrical fissionable fuel elements are placed axially in vertical coolant chambers within the graphite moderator; the cooling gas is flowing along the channel parallel to the fuel element. In such a system, laminar free convection may provide the sole means of the necessary cooling during the shut down or accident periods. Natural convection also finds its critical application in nuclear waste storage field. Cooling of casks containing nuclear waste by natural convection can exceed thermal guidelines if positioning becomes overly eccentric [1]. A key problem in the storage of nuclear wastes is the determination of the insulating effect of the annular air space

fundamental thermal boundary conditions. One set of boundary conditions, namely boundary condition of first kind, comprises of one of the channel wall heated isothermally while the other wall maintained at inlet fluid temperature. The other set of boundary conditions, namely boundary condition of third kind, has one wall heated isothermally while the other wall kept adiabatic. Solution for this problem has not been reported in the literature. Results of this investigation determine limits for solid-fluid conductivity ratio above which, and wall thickness below which, the conjugate effect can be neglected for practical purposes. The effect of eccentricity (E), conductivity ratio (KR), wall thickness and radius ratio (NR_2) on the channel height required to induce a specific flow rate is also investigated. Furthermore, the present results can be used to refine the available conventional results to account for the coupling of conduction and convection for systems with low values of conductivity ratio and/or thick walls particularly at high eccentricities.

The literature survey made during the present work is summarized in chapter 2. The objectives of the present work along with the general problem formulation are outlined in chapter 3. Method of solution is outlined in chapter 4. Different possibilities to represent continuity of temperature and continuity of heat flux on the solid-fluid interfaces of the geometry and axial step increment techniques, tried, are described in chapter 5. Validation of the present work by comparisons with the available solutions is presented in chapter 6. Chapter 7 and 8 describe the influence of conductivity ratio (KR), eccentricity (E), wall thickness and radius ratio (NR_2) on channel height, required to induce specific flow rate of a Newtonian fluid along with the results for critical conductivity ratio (KR) and critical wall thickness employing boundary conditions of first and third kind, respectively. Finally, conclusions and recommendations are presented in chapter 9.

Chapter 2

LITERATURE REVIEW

Considerable work has been done to study the problem of flow and heat transfer in annuli, both concentric and eccentric. However, this literature review will focus on free and forced convection in annuli and on conjugate heat transfer in ducts of various geometries.

2.1. Conjugate Solutions in Various Geometries

Literature until 1976, pertinent to conjugate heat transfer in ducts of various geometrical shapes, has been reviewed by Shah and London [2]. Using the finite-difference method, Faghri and Sparrow [3] solved numerically the steady conjugate heat transfer with hydrodynamically fully developed laminar flow in a thick walled circular tube. Pagliarini [4] considered the same problem with the exception that the flow is hydrodynamically developing. Wen and Jang [5] performed experiments to determine the heat transfer coefficients for forced convection airflow over a cylindrical obstacle, inclined and yawed relative to the oncoming flow.

Using Laplace-transform technique, Krishan [6] analytically solved the transient conjugate problem for hydrodynamically and thermally fully developed laminar pipe flow with viscous dissipation. Olek et al. [7] considered the same problem by means of a

method of separation of variables and concluded that the degree of conjugation and viscous dissipation may have a great impact on the temperature distribution in the fluid. Higuera and Ryazantsev [8] presented, analytically, an analysis of the laminar natural convection flow due to localized heat source on the centerline of a long vertical pipe the walls of which were kept at constant temperature. Bilir [9] used finite difference method to analyze unsteady conjugate heat transfer in thermally developing laminar pipe flow, involving two-dimensional wall and fluid axial conduction. Floryan and Novak [10] numerically investigated free convection heat transfer in multiple parallel vertical channels with isothermal walls. Systems consisting of two, three and infinite number of channels located side by side and with aspect ratios ranging from 5 to 20 and for Grashof numbers based on the channel width up to 105 were analyzed by them.

Al-Nimr and El-Shaarawi [11] obtained an exact analytical solution for the unsteady conjugated forced convection heat transfer in a steady slug flow inside circular and parallel plate ducts. Using numerical techniques, Sucec [12] solved the transient heat transfer problem found for a fluid within a parallel plate duct having sinusoidal generation with axial position in the duct wall. He determined wall temperature, surface heat flux and fluid bulk mean temperature as a function of position and time.

Madina et al. [13] numerically analyzed the steady state conjugate heat transfer process between two counter flowing forced streams separated by a wall with finite thermal conductivity. They obtained numerically the distribution of the temperature of the plates as well as the overall heat transfer rates. Mosaad [14] presented analytical solution for coupled heat transfer between laminar forced convection along and conduction inside a flat plate wall. He combined the energy equations for the fluid and the plate wall under

fluid temperature. Combinations of solutions corresponding to these fundamental boundary conditions may be used to obtain solutions for more complicated boundary conditions found in practice.

Using an approximate integral method, Heaton et al. [20] solved the governing equations for the heat transfer in annular passages for simultaneously developing velocity and temperature profiles in laminar flow. Coney and El-Shaarawi [21] investigated laminar forced convection heat transfer in concentric annuli with simultaneously developing hydrodynamic and thermal boundary layers. The hydrodynamic entry length problem was solved first to obtain the velocity profiles using an extension of the linearized finite difference technique; then the energy equation was solved for the temperature profiles by means of implicit finite difference technique. Further analysis was done numerically by El-Shaarawi and Alkam [22] to obtain the transient solution for the laminar forced convection in the entrance region of a concentric annulus using the finite difference scheme.

El-Shaarawi and Al-Nimr [23] presented analytical solutions for fully developed free convection in open-ended vertical concentric annuli. They investigated four fundamental boundary conditions and obtained the corresponding solutions. El-Shaarawi and Al-Attas [24] developed a finite difference scheme for solving the boundary layer equations governing the unsteady laminar free convection flow in open-ended vertical concentric annuli. They presented the numerical results for a fluid of $Pr=0.7$ in an annulus of radius ratio 0.5. Cadiou et al. [25] investigated numerically the free convective flow in narrow horizontal air filled concentric annuli without considering the conjugate effect. Hadjadj et al. [26] used the control volume finite difference method to solve for laminar

free convection heat transfer in two concentric vertical cylinders. Leppinen [27] examined, analytically, free convection problem in the shallow annular gap between two concentric circular cylinders to obtain asymptotic solution.

El-Shaarawi and Sarhan [28] solved the problem of developing laminar free convection in open-ended vertical concentric annuli with a rotating inner cylinder for which the energy and momentum equations are coupled through the buoyancy term. In their analysis, El-Shaarawi and Sarhan assumed that the pressure defect at the entrance of the annulus should equal to a negative value to be obtained by applying Bernoulli's equation at the entrance. Results were presented for boundary conditions of the third kind (i.e. one wall is kept isothermal while the other is kept adiabatic). As a special case of previous one, El-Shaarawi and Sarhan [29] presented the results for the developing laminar free convection in heated vertical open-ended concentric annuli with stationary walls for the boundary condition of the third kind. Lor and Chu [30] investigated forced and mixed convection in finite vertical concentric cylindrical annuli. They analyzed the heat transfer rates and flow patterns in concentric vertical cylinders using control volume finite difference technique. They considered the inner cylinder rotated and heated while the outer cylinder fixed and cooled.

2.3. Conjugate Solutions in Concentric Annuli

Sakikabara et al. [31] analytically investigated the steady conjugate heat transfer problem in an annulus with a heated core and an insulated outside tube when the laminar flow is hydrodynamically fully developed. McGrath et al. [32] worked on combined

convection and radiation heat transfer for absorbing-emitting gas in the entrance region of a finite length concentric annular duct. They incorporated method of lines and IMSL (FORTRAN Maths/Stats Library) fifth order Runge-kutta verner method, available as a subroutine in IMSL Library, to discritize the non-linear PDE & radiation transport equation into a set of ODE & solve ODE respectively.

El-Sharaawi et al. [33] presented a finite difference scheme to solve the transient conjugate heat transfer problem in a concentric annulus with simultaneously developing hydrodynamic and thermal boundary layers. The annular forced flow was taken as laminar with constant physical properties and the thermally transient problem was initiated by a step change in the prescribed isothermal temperature of the inner surface of the inside tube while the outer surface of the external tube was kept adiabatic.

Using finite difference technique, El-Shaarawi and Negm [34] solved the laminar conjugate natural convection problem in a vertical open-ended concentric annuli. They provided the solution for a Newtonian fluid of Prandtl number 0.7 in a fluid annulus of radius ratio 0.5. El-Shaarawi and Negm [35] also worked on the transient conjugate free convection heat transfer in open-ended vertical concentric annuli. The range for Grashof number they have considered in their paper is $500 \leq Gr^* \leq 10^5$ for transient case, where Gr^* is defined as modified Grashof no. $(D_h Gr/l)$, where D is the equivalent hydraulic diameter of annulus and l is the height of annulus.

complete the model. Fully developed forced convection in eccentric annuli has been treated numerically by Suzuki [42]. The finite difference equivalents of the governing equations of velocity and temperature fields written in bi-polar coordinates were solved using an iterative procedure.

Manglik and Fang [43] obtained numerical solution for laminar, fully developed, forced convective heat transfer in eccentric annuli. With an insulated outer surface, they used two types of boundary conditions: constant wall temperature and uniform axial heat flux with constant peripheral temperature on the inner surface of the annulus. El-Shaarawi et al. [44] proposed a model capable of describing the forced flow in the entry region of an eccentric annuli without need of assumptions dependent on prior knowledge of the mechanism of transverse flow. They also developed a numerical algorithm to solve the obtained model. El-Shaarawi et al. [45] developed a finite difference numerical algorithm to solve a boundary-layer model describing the laminar forced convection heat transfer in the entry region of eccentric annuli.

Yao [46] studied the natural convection in slightly eccentric annuli for small Rayleigh number. He first considered two cylinders with inner circular cylinder and an outer cylinder of arbitrary shapes. He formulated the perturbation equations for the outer cylinder with contour having a small deviation from a circular cylinder, which caused the slight eccentricity to the inner circular cylinder. Ho and Lin [47] studied specifically, natural convection of cold water, encompassing a density inversion, within an eccentric cylindrical annulus. They solved it numerically via a finite difference method.

Utilizing the boundary-layer model in bipolar coordinates, El-Shaarawi and Mokheimer [48,49] investigated developing free convection in open-ended vertical

eccentric annuli having different boundary conditions with one surface isothermally heated while the opposite wall isothermally cooled and maintained at the inlet fluid temperature. They solved the above mentioned problem using finite-difference technique for a fluid of Prandtl number 0.7 in an annulus of radius ratio 0.5 for three values of the dimensionless eccentricity, namely, 0.1, 0.5 and 0.7. The conjugate effect was not considered in their research.

Singh and Rajvanshi [50] utilized bipolar coordinate system to determine the heat transfer between eccentric rotating cylinders. They imposed no restriction on eccentricity. They did not consider the thickness of the cylinder. Sathyamurthy et al. [51] presented a numerical study for fully developed laminar mixed convection in a vertical eccentric annular duct. They solved the equations governing the velocity and temperature using a body conforming grid and finite volume technique. Moukalled and Darwish [52] used the bounded skew central difference scheme to study numerically the combined effect of vertical and horizontal eccentricities on natural convection in an annulus between a heated horizontal cylinder and its square enclosure. They used four Rayleigh Nos. (Ra=10^3, 10^4, 10^5 and 10^6), three aspect ratios (0.1, 0.2, 0.3) and eccentricity values ranging from -0.3 to 0.3.

2.5. Conjugate Solutions for Forced Convection in Eccentric Annuli

El-Shaarawi and Haider [53] studied the conjugate forced convection heat transfer in eccentric annuli. They presented results for a fluid of Prandtl number 0.7 flowing in an

annulus of radius ratio 0.5. They considered heated isothermal inner surface of core tube while the outer surface of external tube maintained at inlet fluid temperature.

To the best of writer's knowledge and as is evident from this literature review, solution for the problem of conjugate free convection heat transfer in vertical eccentric annuli has not been reported in the literature which motivated the author to carry out the present work.

Chapter 3

OBJECTIVES AND PROBLEM FORMULATION

3.1. Objectives

Lack of information about conjugate free convection in vertical eccentric annuli was the motivation behind the present work, which is aimed at obtaining a solution for the conjugate heat transfer problem with laminar free convection in vertical eccentric annuli. The objectives of this present study are to:

1. Investigate the influence of conductivity ratio (KR), inner and outer wall thickness, eccentricity (E) and radius ratio (NR_2) on the incoming flow rate for fundamental thermal boundary conditions of first and third kind.

2. Compute the limit for solid-fluid conductivity ratio above which, the conjugate effect can be neglected for practical purposes.

3. Compute the limit for wall thickness, below which the conjugate effect can be neglected.

3.2. Free Convection Phenomenon

The geometry, cross-section of which is shown in Fig. (3.1), comprises an eccentric annulus between two vertical cylinders of finite height and thickness, open at both ends

14
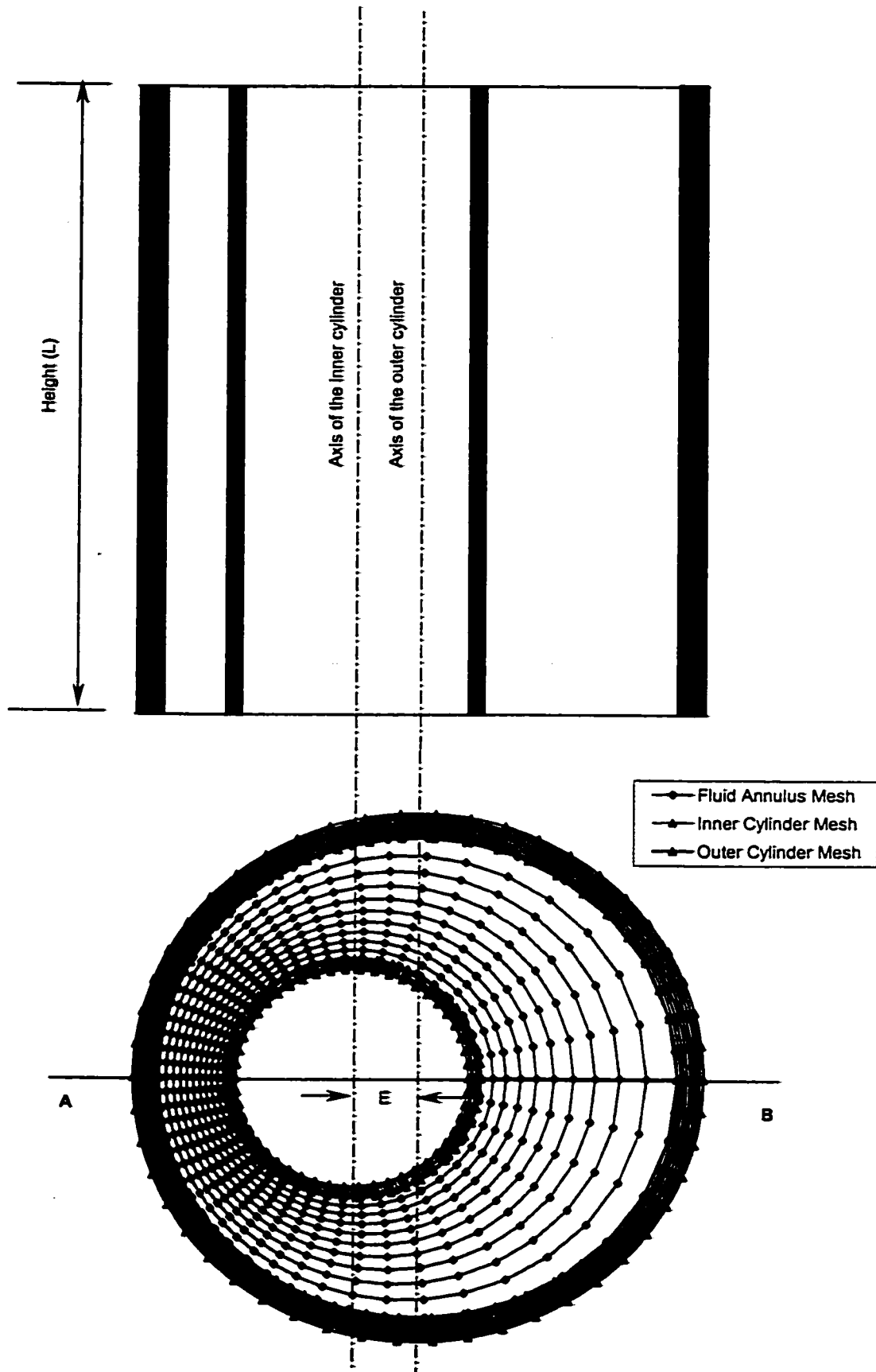
Fig.3.1. Complete Mesh of Eccentric Annuli

NSO=8, NSI=5, N=10, M=50, E=0.5, NR$_2$=0.5, Inner wall thickness=0.05, Outer wall thickness=0.1

and immersed in a stagnant Newtonian fluid of infinite extent maintained at constant temperature T_o. Free convection flow is induced inside this annular channel as a result of either heating one of the channel walls isothermally while keeping the other wall at ambient temperature (Boundary condition of first kind) or isothermally heating one of the channel walls while keeping the other wall adiabatic (Boundary conditions of third kind). The fluid enters the channel at the ambient temperature T_o and is assumed to have constant physical properties but obeys the Boussinesq approximation according to which its density is allowed to vary with temperature in only the gravitational body force term of the vertical (axial) momentum equation. Thus Boussinesq approximation neglects the compressibility effect everywhere except for the buoyancy force term. Body forces in other than the vertical direction, viscous dissipation, internal heat generation and radiation heat transfer are absent. If the channel is sufficiently high, fully developed flow conditions can be achieved.

It is evident from Fig.3.1 that the eccentric annular geometry is symmetric about line AB, therefore, only the half symmetric section is taken for the analysis. Figure 3.2 shows the 2-D cross-section of the half symmetric geometry of the eccentric annular region. The axes of the two eccentric cylinders are perpendicular to the plane of the paper.
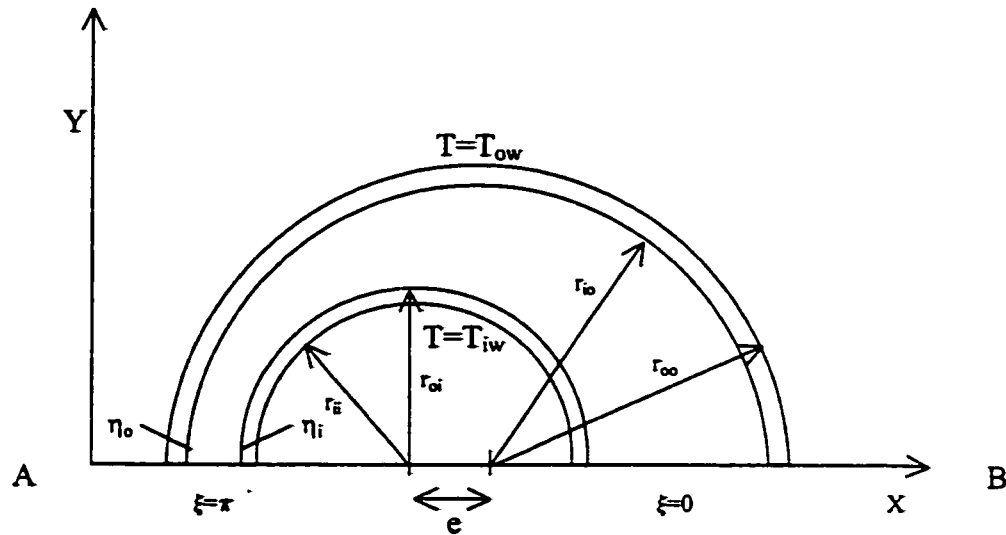
Fig. 3.2. Two Dimensional Cross section of the geometry under consideration

Because of the asymmetry involved in the geometry under consideration the cylindrical coordinate will be difficult to use in expressing the governing equations in the fluid annulus. The most powerful orthogonal curvilinear coordinate system which could be used to express the partial differential equations describing the flow and heat transfer through eccentric annuli is the bipolar coordinate system. The bipolar coordinate system is nothing but a set of orthogonal eccentric cylinders. So, the boundary surfaces of an eccentric annulus may be taken as one of the coordinates and the other coordinate will be the set of the eccentric cylinders, which orthogonally intersect the boundaries of the annulus [54]. Since the cylinder walls have uniform thickness, the cylindrical coordinate system is more appropriate for the solid walls, therefore, the energy equation for the solid

cylinder walls will be expressed in cylindrical coordinates whereas the governing equations for fluid in the annulus will be written in bi-polar coordinates.

3.3. Problem Formulation

3.3.1. Governing Equations

The governing equations, i.e. the momentum equations, the continuity equation and the energy equation, transformed into bipolar coordinates for the free convection in the eccentric fluid annulus [54] are as follows:

Continuity Equation

$$\frac{\partial(hw)}{\partial \xi} + \frac{\partial(hv)}{\partial \eta} + \frac{\partial(h^2 u)}{\partial z} = 0$$

Momentum Equation In Z-Direction

$$\rho\left(\frac{\partial u}{\partial t} + \frac{w}{h}\frac{\partial u}{\partial \xi} + \frac{v}{h}\frac{\partial u}{\partial \eta} + u\frac{\partial u}{\partial z}\right) = F_z - \frac{\partial p}{\partial z} + \frac{\mu}{h^2}\left(h^2\frac{\partial^2 u}{\partial z^2} + \frac{\partial^2 u}{\partial \eta^2} + \frac{\partial^2 u}{\partial \xi^2}\right)$$

Momentum Equation In ξ-Direction

$$\rho\left(\frac{\partial w}{\partial t} + \frac{w}{h}\frac{\partial w}{\partial \xi} + u\frac{\partial w}{\partial z} - \frac{v^2}{h^2}\frac{\partial h}{\partial \xi} + \frac{v}{h^2}\frac{\partial(hw)}{\partial \eta}\right) = F_\xi - \frac{1}{h}\frac{\partial p}{\partial \xi} + \frac{\mu}{h}\left\{ \begin{array}{l} \dfrac{\partial^2(hw)}{\partial z^2} + \dfrac{1}{h^2}\dfrac{\partial^2(hw)}{\partial \eta^2} + \dfrac{1}{h^2}\dfrac{\partial^2(hw)}{\partial \xi^2} + \\[2mm] \dfrac{2}{h^2}\dfrac{\partial h}{\partial \xi}\dfrac{\partial(hu)}{\partial z} + \dfrac{2}{h^3}\dfrac{\partial h}{\partial \eta}\left[\dfrac{\partial(hv)}{\partial \xi} - \dfrac{\partial(hw)}{\partial \eta}\right] \end{array} \right\}$$

Momentum Equation In η-Direction

$$\rho\left(\frac{\partial v}{\partial t}+\frac{v}{h}\frac{\partial v}{\partial \eta}+u\frac{\partial v}{\partial z}-\frac{w^2}{h^2}\frac{\partial h}{\partial \eta}+\frac{w}{h^2}\frac{\partial(hv)}{\partial \xi}\right)=F_\eta-\frac{1}{h}\frac{\partial p}{\partial \eta}+\frac{\mu}{h}\left\{\begin{array}{l}\dfrac{\partial^2(hv)}{\partial z^2}+\dfrac{1}{h^2}\dfrac{\partial^2(hv)}{\partial \xi^2}+\dfrac{1}{h^2}\dfrac{\partial^2(hv)}{\partial \eta^2}+\\[2mm]\dfrac{2}{h^2}\dfrac{\partial h}{\partial \eta}\dfrac{\partial(hu)}{\partial z}-\dfrac{2}{h^3}\dfrac{\partial h}{\partial \xi}\left[\dfrac{\partial(hv)}{\partial \xi}-\dfrac{\partial(hw)}{\partial \eta}\right]\end{array}\right\}$$

Energy Equation For Fluid

$$\rho C_p\left(\frac{\partial T}{\partial t}+\frac{w}{h}\frac{\partial T}{\partial \xi}+\frac{v}{h}\frac{\partial T}{\partial \eta}+u\frac{\partial T}{\partial z}\right)=\frac{k}{h^2}\left(\frac{\partial^2 T}{\partial \xi^2}+\frac{\partial^2 T}{\partial \eta^2}+h^2\frac{\partial^2 T}{\partial z^2}\right)+\mu\phi+Q'''$$

Energy Equation for Solid in Cylindrical Coordinates [55]

$$\frac{\partial^2 T}{\partial r^2}+\frac{1}{r}\frac{\partial T}{\partial r}+\frac{1}{r^2}\frac{\partial^2 T}{\partial \phi^2}+\frac{\partial^2 T}{\partial z^2}=0$$

3.3.2. Dimensionless Form of the Governing Equations

Using dimensionless parameters indicated in nomenclature, the governing equations can be written in dimensionless form in order to make them applicable for any value of the parameters and for any similar problem.

Continuity Equation

$$\frac{\partial(HW)}{\partial \xi}+\frac{\partial(HV)}{\partial \eta}+4(1-NR_2)^2\frac{\partial(UH^2)}{\partial Z}=0$$

Momentum Equation In Z-Direction

$$\frac{W}{H}\frac{\partial U}{\partial \xi}+\frac{V}{H}\frac{\partial U}{\partial \eta}+4(1-NR_2)^2 U\frac{\partial U}{\partial Z}=\frac{\theta}{4(1-NR_2)^2}-\frac{1}{4(1-NR_2)^2}\frac{\partial P}{\partial Z}+\frac{1}{H^2}\left(\frac{\partial^2 U}{\partial \xi^2}+\frac{\partial^2 U}{\partial \eta^2}+\frac{H^2}{Gr^2}\frac{\partial U}{\partial Z^2}\right)$$

Momentum Equation In ξ-Direction

$$\frac{W}{H}\frac{\partial W}{\partial \xi}+\frac{V}{H^2}\frac{\partial(HW)}{\partial \eta}+4(1-NR_2)^2 U\frac{\partial W}{\partial Z}-\frac{V^2}{H^2}\frac{\partial H}{\partial \xi}=-\frac{Gr^2}{H}\frac{\partial P}{\partial \xi}+\frac{1}{H^3}\left[\frac{\partial^2(HW)}{\partial \eta^2}+\frac{\partial^2(HW)}{\partial \xi^2}\right]+$$

$$\frac{1}{HGr^2}\frac{\partial^2(HW)}{\partial Z^2}-\frac{2}{H^4}\left[\frac{\partial(HW)}{\partial \eta}-\frac{\partial(HV)}{\partial \xi}\right]\frac{\partial H}{\partial \eta}+\frac{8(1-NR_2)^2}{H^2}\frac{\partial H}{\partial \xi}\frac{\partial U}{\partial Z}$$

Momentum equation in η-Direction

$$\frac{V}{H}\frac{\partial V}{\partial \eta}+\frac{W}{H^2}\frac{\partial(HV)}{\partial \xi}+4(1-NR_2)^2 U\frac{\partial V}{\partial Z}-\frac{W^2}{H^2}\frac{\partial H}{\partial \eta}=-\frac{Gr^2}{H}\frac{\partial P}{\partial \eta}+\frac{1}{H^3}\left[\frac{\partial^2(HV)}{\partial \eta^2}+\frac{\partial^2(HV)}{\partial \xi^2}\right]+$$

$$\frac{1}{HGr^2}\frac{\partial^2(HV)}{\partial Z^2}+\frac{2}{H^4}\left[\frac{\partial(HW)}{\partial \eta}-\frac{\partial(HV)}{\partial \xi}\right]\frac{\partial H}{\partial \xi}+\frac{8(1-NR_2)^2}{H^2}\frac{\partial H}{\partial \eta}\frac{\partial U}{\partial Z}\qquad .$$

Energy Equation For Fluid

$$\frac{W}{H}\frac{\partial \theta}{\partial \xi}+\frac{V}{H}\frac{\partial \theta}{\partial \eta}+4(1-NR_2)^2 U\frac{\partial \theta}{\partial Z}=\frac{1}{Pr H^2}\left(\frac{\partial^2 \theta}{\partial \eta^2}+\frac{\partial^2 \theta}{\partial \xi^2}+\frac{H^2}{Gr^2}\frac{\partial^2 \theta}{\partial Z^2}\right)\qquad .$$

Energy Equation For Solid

$$\frac{\partial^2 \theta_s}{\partial R^2}+\frac{1}{R}\frac{\partial \theta_s}{\partial R}+\frac{1}{R^2}\frac{\partial^2 \theta_s}{\partial \phi^2}=0$$

For outer cylinder, $\theta_s = \theta_{so}$ & R vary from $NR_3{=}1$ to NR_4

For inner cylinder, $\theta_s = \theta_{si}$ & R vary from NR_1 to NR_2

3.3.3. Problem Simplification & Order of Magnitude Analysis

In developing the above equations for the above problem, the following simplifying assumptions were used.

1. The flow is steady.

2. The fluid is Newtonian with constant properties.

3. Body forces along ξ and η direction are absent.

4. There is no magnetic effect.

5. Internal heat generation and viscous dissipation are absent.

6. The cylinder walls have thermal boundary conditions uniformly distributed along the whole lengths, so there is no temperature gradient in cylinder walls in axial (Z) direction.

Order of magnitude analysis is a very powerful technique to simplify the problem by eliminating those terms in the governing equations, which have negligible contribution in the solution. The details of the order of magnitude analysis are given in Mokheimer's work [54].

After performing the order of magnitude analysis keeping under consideration all the assumptions, the resulting final equations are as follows:

Continuity Equation

$$\frac{\partial(HW)}{\partial \xi} + \frac{\partial(HV)}{\partial \eta} + 4(1-NR_2)^2 \frac{\partial(UH^2)}{\partial Z} = 0 \qquad (3.1)$$

Momentum Equation In Z-Direction

$$\frac{W}{H}\frac{\partial U}{\partial \xi} + \frac{V}{H}\frac{\partial U}{\partial \eta} + 4(1-NR_2)^2 U\frac{\partial U}{\partial Z} = \frac{\theta}{4(1-NR_2)^2} - \frac{1}{4(1-NR_2)^2}\frac{\partial P}{\partial Z} + \frac{1}{H^2}\left(\frac{\partial^2 U}{\partial \xi^2} + \frac{\partial^2 U}{\partial \eta^2}\right)$$

$$(3.2)$$

Momentum Equation In ξ-Direction

$$\frac{W}{H}\frac{\partial W}{\partial \xi}+\frac{V}{H^2}\frac{\partial(HW)}{\partial \eta}+4(1-NR_2)^2U\frac{\partial W}{\partial Z}-\frac{V^2}{H^2}\frac{\partial H}{\partial \xi}=\frac{1}{H^3}\left[\frac{\partial^2(HW)}{\partial \eta^2}+\frac{\partial^2(HW)}{\partial \xi^2}\right]$$

$$-\frac{2}{H^4}\left[\frac{\partial(HW)}{\partial \eta}-\frac{\partial(HV)}{\partial \xi}\right]\frac{\partial H}{\partial \eta}+\frac{8(1-NR_2)^2}{H^2}\frac{\partial H}{\partial \xi}\frac{\partial U}{\partial Z}$$

(3.3)

Energy Equation For Fluid

$$\frac{W}{H}\frac{\partial \theta}{\partial \xi}+\frac{V}{H}\frac{\partial \theta}{\partial \eta}+4(1-NR_2)^2U\frac{\partial \theta}{\partial Z}=\frac{1}{\Pr H^2}\left(\frac{\partial^2 \theta}{\partial \eta^2}+\frac{\partial^2 \theta}{\partial \xi^2}\right)$$

(3.4)

Integral Form of The Continuity Equation

$$\overline{U}=\frac{8(1-NR_2)}{\pi(1+NR_2)}\int_0^\pi \int_{\eta_o}^{\eta_i}UH^2d\eta d\xi$$

(3.5)

Energy Equation For Solid

$$\frac{\partial^2 \theta_s}{\partial R^2}+\frac{1}{R}\frac{\partial \theta_s}{\partial R}+\frac{1}{R^2}\frac{\partial^2 \theta_s}{\partial \phi^2}=0$$

(3.6)

For outer cylinder, $\theta_s=\theta_{so}$ and R varies from $NR_3=1$ to NR_4

For inner cylinder, $\theta_s=\theta_{si}$ and R varies from NR_1 to NR_2

Momentum equation in η-direction (i.e. Radial like direction) is dropped since, the η-velocity component (V) is much smaller than that in both ξ & Z directions. Axial diffusion of momentum in the fluid and that of energy in both fluid and solid (i.e. $\frac{\partial^2}{\partial Z^2}$ terms) are omitted. The pressure is taken to be a function of the axial coordinate only $\left(i.e.\frac{\partial P}{\partial \eta}=\frac{\partial P}{\partial \xi}=0\right)$.

3.3.4. Boundary Conditions

Equations (1) through (6) are subjected to the following boundary conditions:

For $Z = 0$ and $\eta_o < \eta < \eta_i$, $V = W = 0$, and $U = U_o$, $P = -U_o^2/2$

For $Z = L$ and $\eta_o < \eta < \eta_i$, $P = 0$

For $Z \geq 0$ and $\eta = \eta_i$, $U = V = W = 0$

For $Z \geq 0$ and $\eta = \eta_o$, $U = V = W = 0$

Case	Inner Boundary, r_{ii}	Outer Boundary, r_{oo}
1.I	$\theta_{si} = 1.0$	$\theta_{so} = 0$
1.O	$\theta_{si} = 0$	$\theta_{so} = 1.0$
3.I	$\theta_{si} = 1.0$	$\dfrac{\partial \theta_{so}}{\partial R} = 0$
3.O	$\dfrac{\partial \theta_{si}}{\partial R} = 0$	$\theta_{so} = 1.0$

For $Z > 0$ and $\xi = 0$ and π (the line of symmetry):

$$\frac{\partial V}{\partial \xi} = \frac{\partial W}{\partial \xi} = \frac{\partial U}{\partial \xi} = \frac{\partial \theta}{\partial \xi} = \frac{\partial \theta_s}{\partial \phi} = 0$$

For $Z > 0$ and $R = NR_2$ and $R = NR_3 = 1$ (i.e. the interfaces)

$\theta_f = \theta_s$, continuity of temperature

$$k_f \left(\frac{1}{H} \frac{\partial \theta}{\partial \eta} i + \frac{1}{H} \frac{\partial \theta}{\partial \xi} j \right) = k_s \left(\frac{\partial \theta_s}{\partial R} i + \frac{1}{R} \frac{\partial \theta_s}{\partial \phi} j \right)$$, Continuity of heat flux

i, unit vector in the η and R directions

Chapter 4

NUMERICAL ANALYSIS AND METHOD OF

SOLUTION

As stated in chapter 3, there is no possible means to solve the set of dimensionless equations (3.1) through (3.6) analytically. Therefore, these governing equations will be numerically treated using finite difference technique to solve for the three velocity components, pressure and temperature in the fluid and the two solid cylinders.

The existing computer program, developed by Mokheimer [54] was used to obtain the results reported in [44, 45, 48 and 49]. The program was modified by Haider [55] for the forced convection case to incorporate the inner and outer cylinder wall thickness and the solid fluid conductivity ratio. In the present work, the program has been modified for the free convection case to take the conjugate effect into consideration. Since the governing equations for the fluid are in bipolar coordinate system whereas the energy equations for the solids are in cylindrical coordinate system, the two grids are linked by applying the principals of continuity of temperature and heat flux at the two interfaces. The finite difference equations and the method to solve for the velocity, pressure and temperature values are described in the following sections.

25

4.1. Finite Difference Equations

Figure (4.1) shows the numerical grid of the geometry. The total number of equations is seven (7) and equals the number of unknowns, namely, P, U, V, W, θ_f, θ_{si} & θ_{so}. For outer solid wall, energy equation will be applied on each grid point of outer wall. Similarly, for the inner solid wall, energy equation will be applied at each grid point of inner wall. For the annular fluid, there are five equations, which will be applied at each of its grid points. Using backward differences to express all first derivatives with respect to Z and the first derivative of (HV) with respect to η in the continuity equation and replacing the second and other first order derivatives in η and ξ directions by central finite differences, equations (3.1) through (3.6) can be written in the following forms, respectively:

Continuity Equation

$$\frac{H(i,j+1)\,W(i,j+1)-H(i,j-1)\,W(i,j-1)}{2\Delta\xi}+\frac{H(i,j)\,V(i,j)-H(i-1,j)\,V(i-1,j)}{\Delta\eta}$$

$$+\,4(1-NR_2)^2 H^2(i,j)\frac{U(i,j)-U^*(i,j)}{\Delta Z}=0 \tag{4.1}$$

Z-Momentum Equation

$$\left(\frac{1}{(\Delta\eta)^2}+\frac{V(i,j)H(i,j)}{2\Delta\eta}\right)U(i-1,j)-\left(\frac{2}{(\Delta\eta)^2}+\frac{2}{(\Delta\xi)^2}+4(1-NR_2)^2\frac{(H(i,j))^2 U^*(i,j)}{\Delta Z}\right)U(i,j)$$

$$+\left(\frac{1}{(\Delta\eta)^2}-\frac{V(i,j)H(i,j)}{2\Delta\eta}\right)U(i+1,j)+\left(\frac{1}{(\Delta\xi)^2}+\frac{W(i,j)H(i,j)}{2\Delta\xi}\right)U(i,j-1)$$

$$+\left(\frac{1}{(\Delta\xi)^2}-\frac{W(i,j)H(i,j)}{2\Delta\xi}\right)U(i,j+1)-\frac{1}{4(1-NR_2)^2}\frac{(H(i,j))^2 P}{\Delta Z}$$

$$=-\frac{1}{4(1-NR_2)^2}\frac{(H(i,j))^2 P^*}{\Delta Z}-\frac{1}{4(1-NR_2)^2}(H(i,j))^2\theta(i,j)-4(1-NR_2)^2\frac{(H(i,j)U^*(i,j))^2}{\Delta Z}$$

$$\tag{4.2}$$

Fluid Annulus Mesh
Inner wall mesh
Outer wall mesh

θ_{so} (NSO+1,jj+1)

θ_f (1,j)

θ_{so} (NSO+1,jj)

θ_{si} (1,jj+1)

θ_f (N+1,j)

θ_{si} (1,jj)

A

E

N+1

1

B

1

NSO+1

NSI+1

1

Fig.4.1. Two-Dimensional Half Symmetric Mesh of Eccentric Annuli

NSO=10, NSI=5, N=15, M=25, E=0.5, NR_2=0.5, Inner wall thickness=0.05, Outer wall thickness=0.1

ξ-Momentum Equation

$$\frac{W^*(i,j)}{H(i,j)}\frac{W(i,j+1)-W(i,j-1)}{2\Delta\xi}+\frac{V^*(i,j)}{(H(i,j))^2}\frac{H(i+1,j)W(i+1,j)-H(i-1,j)W(i-1,j)}{2\Delta\eta}$$

$$+4(1-NR_2)^2U^*(i,j)\frac{W(i,j)-W^*(i,j)}{\Delta Z}-\frac{(V^*(i,j))^2}{(H(i,j))^2}\frac{H(i,j+1)-H(i,j-1)}{2\Delta\xi}$$

$$=\frac{1}{(H(i,j))^3}\left\{\begin{array}{l}\dfrac{H(i-1,j)W(i-1,j)-2H(i,j)W(i,j)+H(i+1,j)W(i+1,j)}{(\Delta\eta)^2}\\[4pt]+\dfrac{H(i,j-1)W(i,j-1)-2H(i,j)W(i,j)+H(i,j+1)W(i,j+1)}{(\Delta\xi)^2}\end{array}\right\}$$

$$-\frac{2}{(H(i,j))^4}\left(\frac{H(i+1,j)-H(i-1,j)}{2\Delta\eta}\right)\left\{\begin{array}{l}\dfrac{H(i+1,j)W(i+1,j)-H(i-1.,j)W(i-1,j)}{2\Delta\eta}\\[4pt]-\dfrac{H(i,j+1)V(i,j+1)-H(i,j-1)V(i,j-1)}{2\Delta\xi}\end{array}\right\}$$

$$+\frac{8(1-NR_2)^2}{(H(i,j))^2}\frac{H(i,j+1)-H(i,j-1)}{2\Delta\xi}\frac{U(i,j)-U^*(i,j)}{\Delta Z}$$

(4.3)

Energy Equation for Fluid

$$\frac{W^*(i,j)}{H(i,j)}\frac{\theta_f(i,j+1)-\theta_f(i,j-1)}{2\Delta\xi}+\frac{V^*(i,j)}{H(i,j)}\frac{\theta_f(i+1,j)-\theta_f(i-1,j)}{2\Delta\eta}+4(1-NR_2)^2U^*(i,j)$$

$$\frac{\theta_f(i,j)-\theta_f^*(i,j)}{\Delta Z}=\frac{1}{\Pr(H(i,j))^2}\left(\begin{array}{l}\dfrac{\theta_f(i-1,j)-2\theta_f(i,j)+\theta_f(i+1,j)}{(\Delta\eta)^2}+\\[4pt]\dfrac{\theta_f(i,j-1)-2\theta_f(i,j)+\theta_f(i,j+1)}{(\Delta\xi)^2}\end{array}\right)$$

(4.4)

Integral Form Of The Continuity Equation

$$\overline{U}=\frac{8(1-NR_2)}{\pi(1+NR_2)}\left(\begin{array}{l}\displaystyle\sum_{j=2}^{M}\sum_{i=2}^{N}U(i,j)(H(i,j))^2+0.5\sum_{i=2}^{N}U(i,1)(H(i,1))^2+\\U(i,M+1)(H(i,M+1))^2\end{array}\right)\Delta\eta\Delta\xi$$

(4.5)

$\theta_f(i,2) = \theta_f(i,0)$, $\theta_s(i,2) = \theta_s(i,0)$

For $Z > 0$ and $\xi = \pi$ → Line of symmetry at the Narrowest gap

$U(i, M) = U(i, M+2)$, $V(i, M+2) = V(i, M+2)$, $W(i, M) = W(i, M+2)$

$\theta_f(i, M) = \theta_f(i, M+2)$, $\theta_s(i, M) = \theta_s(i, M+2)$

Since the temperature field comprises three separate grids, for the outer tube 'i' varies from $i = 1$ at the outer boundary to $i = $ NSO+1 at the outer interface; for the fluid annulus, from $i = 1$ at the outer interface to $i = $ N+1 at the inner interface; and for the inner tube from $i = 1$ at the inner interface to $i = $ NSI+1 at the inner boundary. Thus, $i = $ NSO+1 of the cylindrical grid in the outer wall is coincident with $i = 1$ of the bi-polar grid in the eccentric fluid annulus. Similarly, $i = $ N+1 of the bipolar grid coincides with $i = $ 1 of the cylindrical grid in the inner wall. The boundary conditions are imposed at $i = 1$ of the outer cylindrical grid and $i = $ NSI+1 of the inner cylindrical grid.

4.3. Interface Conditions

With the boundary conditions imposed at the inner surface of the inner cylinder and the outer surface of the outer cylinder, the interface conditions are unknown. Also, the eccentric annulus is fitted with a bi-polar mesh resulting in M+1 mesh points at each interface whereas the walls have cylindrical mesh, therefore, the three grids are linked by applying the principles of continuity of temperature and continuity of heat flux at all points on both interfaces.

At the interface points, continuity of temperature and continuity of heat flux can be expressed in finite difference form as:

$$\theta_f(N+1,j) = \theta_{si}(1,j)$$

$$\theta_f(N+1,j+1) = \theta_{si}(1,j+1)$$

$$\theta_f(N+1,j-1) = \theta_{si}(1,j-1) \tag{4.10}$$

$$KR*H(N+1,j)\left[\frac{\theta_{si}(2,j)-\theta_{si}(1,j)}{\Delta R_i} + \frac{1}{NR_2}\frac{\theta_{si}(1,j+1)-\theta_{si}(1,j-1)}{2\Delta\phi}\right] =$$

$$\frac{\theta_f(N+1,j)-\theta_f(N,j)}{\Delta\eta} + \frac{\theta_f(N+1,j+1)-\theta_f(N+1,j-1)}{2\Delta\xi}$$

where, $2 \le j \le M$

4.3.2. Continuity of Temperature and Heat Flux at the Outer Interface

4.3.2.1. Temperature and Heat Flux Relations at Corner Points

The two corner points at the outer interface ($R = NR_3 = 1$) are shown as bold points 1 and 4 in Fig. (4.1).

The temperature and heat flux conditions at $R = NR3 = 1$ (Outer Interface) are:

At $\xi = 0$ (Widest Gap)

$$\theta_f(1,1) = \theta_{so}(NSO+1,1)$$

$$KR*H(1,1)\left[\frac{\theta_{so}(NSO+1,1)-\theta_{so}(NSO,1)}{\Delta R_o}\right] = \frac{\theta_f(2,1)-\theta_f(1,1)}{\Delta\eta} \tag{4.11}$$

At $\xi = \pi$ (Narrowest Gap)

$$\theta_f(1,M+1) = \theta_{so}(NSO+1,M+1)$$

$$KR*H(1,M+1)\left[\frac{\theta_{so}(NSO+1,M+1)-\theta_{so}(NSO,M+1)}{\Delta R_o}\right] = \frac{\theta_f(2,M+1)-\theta_f(1,M+1)}{\Delta\eta}$$

$$\tag{4.12}$$

4.3.2.2. Temperature and Heat Flux Relation at Rest of the Outer Interface

The rest of the mesh points on ($2 \leq j \leq M$) the outer interface can be seen in Fig. (4.1).

$$\theta_f(1,j) = \theta_{so}(NSO+1,j)$$
$$\theta_f(1,j+1) = \theta_{so}(NSO+1,j+1)$$
$$\theta_f(1,j-1) = \theta_{so}(NSO+1,j-1)$$

$$KR * H(1,j) \left[\frac{\theta_{so}(NSO+1,j) - \theta_{so}(NSO,j)}{\Delta R_o} + \frac{1}{NR_3} \frac{\theta_{so}(NSO+1,j+1) - \theta_{so}(NSO+1,j-1)}{2\Delta\phi} \right] =$$
$$\frac{\theta_f(2,j) - \theta_f(1,j)}{\Delta\eta} + \frac{\theta_f(1,j+1) - \theta_f(1,j-1)}{2\Delta\xi}$$

$$(4.13)$$

where, $2 \leq j \leq M$

The temperature values at the cylindrical mesh points of the inner and outer interfaces are calculated using the principles of continuity of temperature and heat flux as described before. The temperature values at bipolar mesh points of inner and outer interfaces are calculated using linear interpolation. At both interfaces, temperature at every mesh point of the bipolar grid is evaluated using the temperatures at the two neighboring mesh points of the cylindrical grid. The X-coordinate of the grid points is used for this purpose. This interpolation can be expressed as follows (See Fig.4.1):

Fluid temperature at the outer interface:

$$\theta_f(1,j) = \theta_{so}(NSO+1,jj) + \left[\theta_{so}(NSO+1,jj+1) - \theta_{so}(NSO+1,jj) \right] \left[\frac{X_f(1,j) - X_{so}(1,jj)}{X_{so}(1,jj+1) - X_{so}(1,jj)} \right]$$

$$(4.14)$$

Fluid temperature at the inner interface:

$$\theta_f(N+1,j) = \theta_{si}(1,jj) + [\theta_{si}(1,jj+) - \theta_{si}(1,jj)]\left[\frac{X_f(N+1,j) - X_{si}(1,jj)}{X_{si}(1,jj+1) - X_{si}(1,jj)}\right] \qquad (4.15)$$

Where,

$X_f(1,j)$ is the X-coordinate of bipolar grid points on the outer interface.

$X_f(N+1,j)$ is the X-coordinate of bipolar grid points on the inner interface.

$X_{so}(1,jj)$ is the X-coordinate of cylindrical grid points on the outer interface.

$X_{si}(1,jj)$ is the X-coordinate of cylindrical grid points on the inner interface.

The relations presented in this section calculate all the unknown temperature values at the interfaces. The solution goes from the outer wall towards the inner wall smoothly with all the boundary conditions at the two solid-fluid interfaces are unknown.

4.4. Method of Solution

1. The finite difference equations (4.1) through (4.7) are linearized by assuming that where the product of two unknowns occur, one of them is given approximately by its value at the previous axial step, the variable superscripted with an asterisk (*). Thus the finite difference equations (4.1) to (4.7) represent a complete mathematical model of seven equations in seven unknowns (U,V,W,P,θ, θ_{si} and θ_{so}) and are numerically solved in the manner described hereinafter. Due to symmetry, these equations need to be solved in only half the domain, i.e. for $0 \leq \xi \leq \pi$ The variables $U,V,W,$ $\theta,$ θ_{si} and θ_{so} are computed, for a given axial location (Z), at the intersections of the grid lines, i.e. the mesh points. The problem under investigation is governed by six dimensionless parameters,

namely, the radius ratio (NR$_2$), the eccentricity (E), the Prandtl number (Pr), conductivity

ratio (KR) and thicknesses of the two walls (Owall and Iwall). For a fluid of a given *Pr* in

an annulus of given *NR$_2$* and *E*, the solution starts by calculating the corresponding values

of η_i and η_o by means of the following equations, respectively.

$$\eta_i = \log_e \left[\frac{NR_2\left(1 + E^2\right) + \left(1 - E^2\right)}{2NR_2 E} + \sqrt{\left(\frac{NR_2\left(1 + E^2\right) + \left(1 - E^2\right)}{2NR_2 E}\right)^2 - 1} \right] \tag{4.16}$$

$$\eta_o = \log_e \left[\frac{NR_2\left(1 - E^2\right) + \left(1 + E^2\right)}{2E} + \sqrt{\left(\frac{NR_2\left(1 - E^2\right) + \left(1 + E^2\right)}{2E}\right)^2 - 1} \right] \tag{4.17}$$

Where,

NR_2 = Fluid Annulus Radius Ratio, r_{oi}/r_{io}

Selecting the numbers of increments in η and ξ directions (*N* and *M* respectively)

the values of $\Delta\eta$ & $\Delta\xi$ can be computed by using the following equations, respectively.

$$\Delta\eta = \frac{\left(\eta_i - \eta_o\right)}{N} \tag{4.18}$$

$$\Delta\xi = \frac{\pi}{M} \tag{4.19}$$

where,

N = Total number of mesh points along η- direction in fluid annulus.

M = Total number of mesh points along ξ-direction in fluid annulus.

Similarly, for the solid walls, by selecting the values of *NR$_1$* and *NR$_4$* and the number

of radial (*R*) increments in the outer and inner walls and the number of increments in the

tangential (ϕ) direction (*NSO, NSI* and *M,* respectively) the values of ΔR_o, ΔR_i and $\Delta \phi$ can be determined by means of the following equations.

$$\Delta R_o = \frac{(NR_4 - NR_3)}{NSO} \tag{4.20}$$

$$\Delta R_i = \frac{(NR_2 - NR_1)}{NSI} \tag{4.21}$$

$$\Delta \phi = \frac{\pi}{M} \tag{4.22}$$

where,

NSO = Total number of mesh points along radial direction in outer wall.

NSI = Total number of mesh points along radial direction in inner wall.

M = Total number of mesh points along circumferential direction in outer and inner walls.

2. For free convection, assume a value for the uniform axial velocity profile at the entrance U_o. Since $W = V = 0$, the inlet pressure will be $P_o = -\frac{U_o^2}{2}$ for this free convection case.

3. The energy equations for the fluid (4.4) and solid (4.6 and 4.7) are simultaneously solved for the temperatures using Gauss-Seidel iteration at a particular cross-section. The simultaneous solution of equations (4.4, 4.6 & 4.7) results in obtaining the unknown values of θ_f, θ_{si} and θ_{so} at the next cross-section.

4. Within the Gauss-Seidel iteration, the temperature values of cylindrical grid points at the two interfaces are calculated using principles of continuity of temperature and continuity of heat flux. The temperature values of bipolar grid points at both the

interfaces are computed by interpolating between the temperature values of the two neighboring cylindrical grid points at both sides of each bipolar grid point. It must be remembered that bipolar coordinate system is used in eccentric fluid annulus while cylindrical coordinate system is used in the two solid walls.

5. Now to solve for the two unknowns P and U at the aforesaid plane, the integral form of the continuity equation (4.5) and the finite difference form of the axial momentum equation (4.2) can be used. The set of algebraic equations result from the application of the axial momentum equation at each interior node of the solution grid along with that equation resulted from expressing the integral continuity equation using the trapezoidal rule is put in a matrix form. The general format for this matrix corresponds to N segments in η-direction and M segments in ξ-direction. The method of solving this matrix is an extension to the special form of the modified Gauss-Jordan elimination scheme [54, 55].

6. ξ-Momentum equation (4.3) is solved for W-velocity component using Gauss-Seidel iteration method.

7. Continuity equation (4.1) is used to evaluate V-velocity component at all the interior grid points.

Steps 2-7 are repeated to advance axially until the pressure defect (P) becomes zero for the free convection.

Chapter 5

ON THE NUMERICAL MODEL

5.1. Introduction

Conjugate free convection heat transfer in vertical eccentric annuli will be numerically solved using the finite-difference scheme developed in chapter 4. A numerical model is developed to perform the thermal and flow analysis of free convection in vertical eccentric annuli along the whole height of the annular channel. This chapter is devoted to describe in detail the capabilities of the computer code. Different features and possible options of expressing the governing equations in finite difference forms are emphasized in this chapter.

5.2. Interpolation at the Interfaces

The inner surface temperature of the outer cylinder, which is actually the outer solid-fluid interface and the outer surface temperature of the inner cylinder, which is the inner solid-fluid interface, are unknown. The temperatures at the two interfaces have to be calculated in order to solve for the whole domain. For this purpose, the principles of continuity of temperature and continuity of heat flux are applied to solve for the boundary conditions on both inner and outer interfaces.

The geometry of the problem, shown in Fig. (5.1), consists of two eccentric cylinders. That makes an eccentric fluid annulus between the two cylinders. The most suitable orthogonal curvilinear coordinate system which can be used to express the partial differential equations describing the flow and heat transfer through eccentric annuli is the bipolar coordinate system. However, since the cylinder walls have uniform thickness, the cylindrical coordinate system is more appropriate for the solid walls. The use of bipolar coordinate system in the eccentric fluid annulus and cylindrical coordinate system in the cylinder walls has resulted in un-matched mesh points for both systems at the two interfaces, as shown in Fig. (5.1). This un-matching of mesh points at the two interfaces lead us to use, in terms of polar mesh points, interpolation to calculate the bipolar mesh point values at the two interfaces. The interpolation technique uses the variable values and coordinates of the two neighboring cylindrical coordinate mesh points at the interface to calculate the value of each bipolar mesh point at that interface. Two types of interpolations can be considered. One is the linear interpolation and the other is the logarithmic interpolation. A constraint lies in logarithmic interpolation. As the initialization of mesh points is taken as zero (0), therefore, logarithmic interpolation fails to execute (Log of zero (0) is infinity (∞)). This can only be used if non-zero initialization is used but one cannot be sure as some zero value may come during the calculations. Hence logarithmic interpolation cannot be used in the present situation. Hence, the only option left is the linear interpolation that will be used in the computer code.

Equations (4.8-4.13) represent the continuity of temperature and continuity of heat flux relations for four points at the inner and outer interfaces on the line of symmetry and
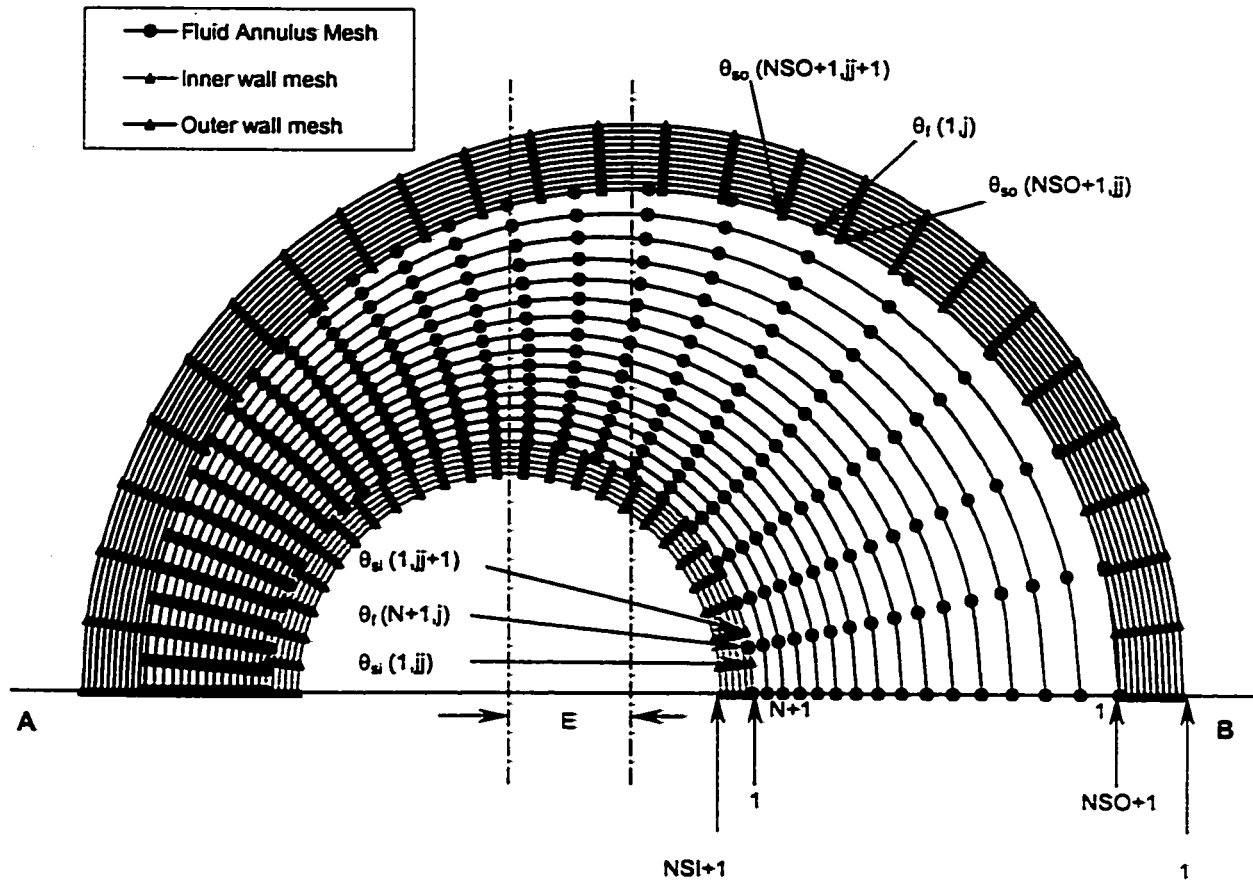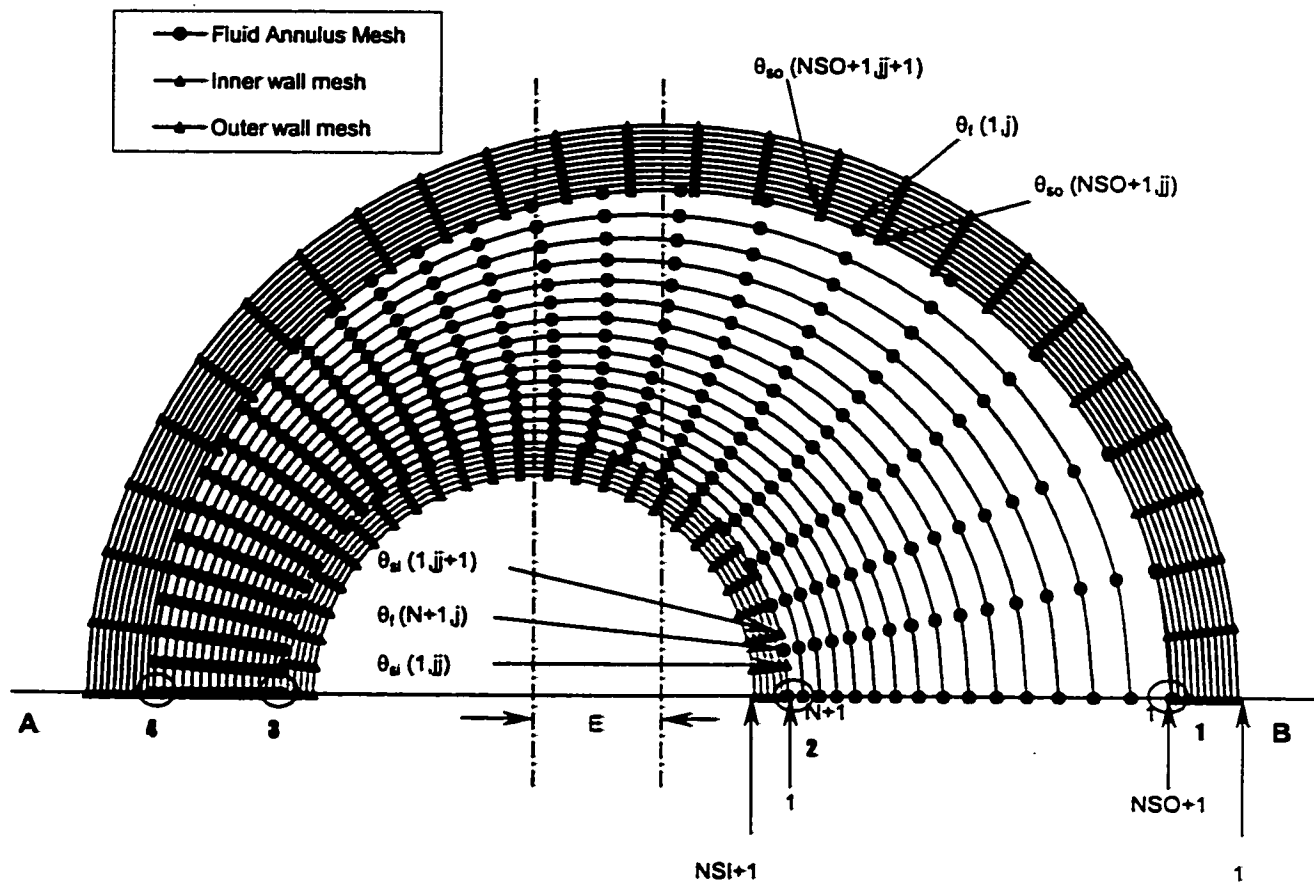
Fig.5.1. Two-Dimensional Half Symmetric Mesh of Eccentric Annuli

NSO=10, NSI=5, N=15, M=25, E=0.5, NR$_2$=0.5, Inner wall thickness=0.05, Outer wall thickness=0.1

for all the cylindrical coordinate mesh points on inner and outer interfaces. It is observed in the heat flux relations of the four symmetry points at the two interfaces (Eqs.4.8, 4.9, 4.11 and 4.12) that there is no temperature gradient along ϕ and ξ directions. The reason is that due to symmetry, equal amount of heat is flowing in clockwise and counter-clockwise directions at these four points so the net effect of heat flow is zero. For the rest of the cylindrical coordinate mesh points, heat is flowing in ϕ and ξ directions as well, as can be seen in eqs. (4.10) and (4.13). Here, continuity of temperature and continuity of heat flux can either be applied on only 4 corner points at the two interfaces on the line of symmetry, for simplicity as done by Haider [55], or on all the cylindrical coordinate mesh points on both outer and inner interfaces. In this way, all the boundary conditions in the domain are calculated and now the equations to calculate the temperatures on all internal mesh points in eccentric annulus and cylindrical walls can be used.

5.3. Axial Increment

Axial increment along the channel height is a very important factor in the computation. Since very large gradients occur near the entrance, the axial step is kept very small so that change in behavior of the values can be analyzed precisely. As the flow moves along the channel, the gradient decreases and need of very small axial step size ceases. A constant, relatively large axial step can be kept when the values of gradients are very small. Three different axial formulations are tested. One is the linear axial increment, which is used by Mokheimer [54] and Haider [55] in their work. The second increment

earlier in section 5.2. Only radial heat flux is to be formulated at these four points, i.e. bold 1, 2, 3 and 4, as shown in Fig. (5.1). The limitation in using the continuity of temperature and continuity of heat flux on only four corner points is that the temperature values on the all mesh points sense the temperature change after many iterations.

5.4.2. Continuity of Heat Flux on All Points of Cylindrical Mesh Points at Both Solid-Fluid Interfaces Using Central Finite Difference Scheme in Circumferential Direction

The second case involves heat flux formulation on all the mesh points on both solid walls at the interfaces for cylindrical coordinate system. As there is no symmetry along the circumference due to eccentricity, heat will flow circumferentially as well as radially. Thus heat flux cannot be ignored on these points. Writing the equation in finite difference form needs some consideration. Central finite difference scheme is applied to express the terms of circumferential heat flux, while forward and backward schemes are implemented on radial heat flux terms for both solid and fluid. The advantage in applying the continuity of temperature and continuity of heat flux on all the interface mesh points is that the actual heat transfer phenomenon is depicted on the interface walls and also, the temperature change is sensed sooner in the iteration procedure than the case in which heat flux is applied only on the four corner points at the interfaces. This fact has been verified by performing special runs having one code using continuity of heat flux principle at only 4 corner points while the other code applying the continuity of heat flux principle on all interface mesh points.

5.4.3. Continuity of Heat Flux on All Points of Cylindrical Mesh Points at Both Solid-Fluid Interfaces Using Forward Finite Difference Scheme in Circumferential Direction

The third possibility is similar to the second one, i.e., the values at all mesh points of the interface are coupled using heat flux relation. The only difference is that circumferential terms are using forward difference scheme instead of central differential scheme.

5.5. Axial Increment Size

5.5.1. Significance

The axial step size determines how much accuracy is achieved. If the step size is small, the flow and thermal behaviors can be more accurately computed. The values of the variables near the entrance of the channel change considerably, that's why small incremental steps are needed in order to monitor the rapid change in such values. After some distance, the smaller axial step becomes insignificant as the change in values becomes small.

5.5.2. Axial Steps

The existing computer program, developed by Mokheimer [54], was using linear axial increment with the initial step size $\Delta Z = 1 \times 10^{-10}$. This step size gradually increased to values of $\Delta Z = 5 \times 10^{-10}$, 1×10^{-9}, 5×10^{-9}, 1×10^{-8}, 1×10^{-7}, 1×10^{-6}, 1×10^{-5}, 1×10^{-4} and 1×10^{-3}

after 5, 10, 20, 30, 40, 50, 60, 80 & 100 steps respectively. The final step size was $\Delta Z = 1\times10^{-3}$ which remained constant after 100 axial steps. In the present work, a gradual and smooth increase of the axial step was considered. This includes step change in the axial step. Initially, same constant final value of $\Delta Z = 1\times10^{-3}$ was used for exponential and hyperbolic increments but, later on, it was further reduced to 1×10^{-4} due to the reason that latter ΔZ, i.e. 1×10^{-4} is 10 times less than the previous one and it can compute more values for a particular channel height thus giving better representation of the gradient variations.

5.5.3. Linear increase of the Axial Increment

This was the existing model for axial increment which is presently modified to make axial increment ΔZ starting from 1×10^{-10} and reaching a constant value of 1×10^{-4} after 100 steps. Figures (5.2) and (5.3) show the graph of total axial distance and axial increment against the number of axial steps respectively. It can be seen from Fig. (5.2), the total axial distance moved by the fluid from the inlet in case of linear axial formulation seems to change its behavior suddenly after some number of steps. This behavior is better understood from Fig. (5.3). There is step change in the axial-step size after certain number of steps, in case of linear formulation. As ΔZ is involved in the calculations of the fluid annulus energy equation, calculation of axial momentum equation, determination of V-velocity component and also in the Nusselt number calculations, any sudden jump in axial step size ΔZ may lead to discontinuity in the above calculations. To avoid any such doubt, smooth continuous axial step size increment needs to be implemented. For this purpose,
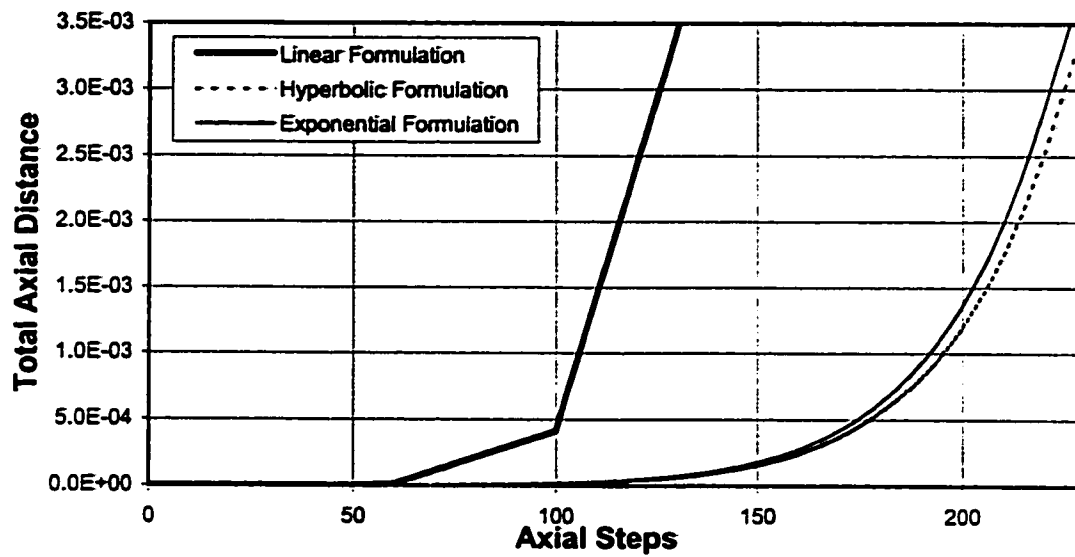
Fig.5.2. Graph of Axial Steps versus Total Axial Distance
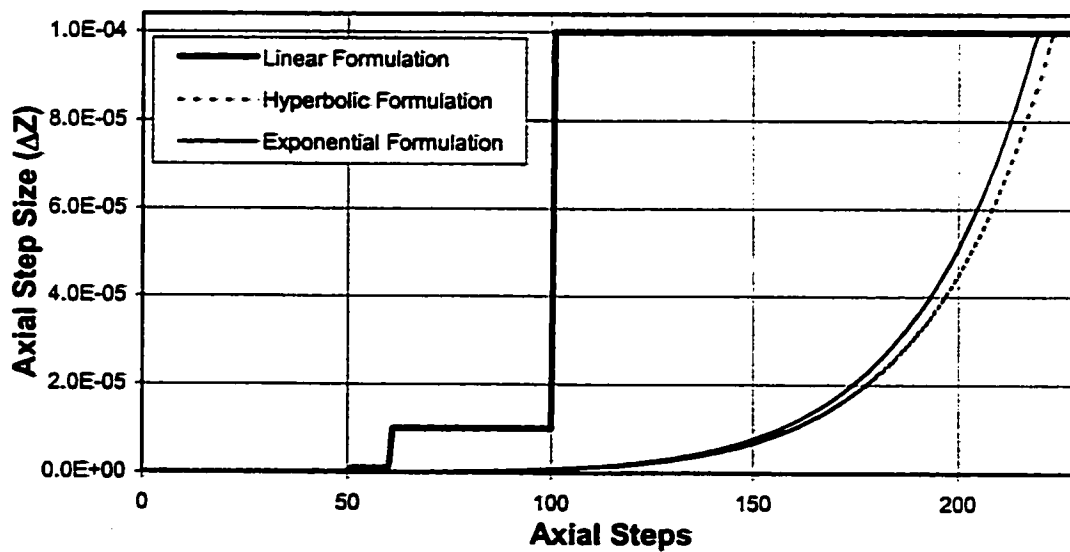
Fig.5.3. Graph of Axial Steps versus Axial Step Size

ΔZ = Axial step size

Z_1 = Number of axial steps

In order to find the value of constant, one can equate the above equation to 1×10^{-10}, which is ΔZ for the first axial step (Z_1=1). The value of the constant comes out to be 6.49.

Hence nine versions of computer code might be obtained using the same finite difference equations of the same governing equations when one uses different combinations of the ways to express the axial step increase, expressing the continuity of axial heat flux principle at only 4 corner points or at all interface mesh points. All 9 versions of the computer code are shown in the tabular form in Table 5.1.

The present study is for free convection. Factors such as heat flux on both interfaces, mixed mean temperature and heat absorbed in the fluid describe the thermal behavior in the geometry circumferentially and along the height. Other factors such as program running time and number of axial steps describe the behavior of computer code execution. Table 5.2. gives different values for the above-mentioned 9 models, related to free convection, for an incoming dimensionless axial velocity (U_o = 0.005). It is quite obvious that model 2 is taking more time than model 1. The same behavior can also be observed between models 4 & 5 and 7 & 8. The increase in time is due to the increase in axial steps as all the computations have to be done in each axial step. This increase in time is not so significant but if the program runs at high incoming flow rate, this will be a prominent factor.

Exponential or hyperbolic axial formulation has also a noticeable impact on the channel height. The channel height has decreased from 5.11×10^{-4} to 4.69×10^{-4} (about 8.2

Table 5.2. Some Results for the versions of Computer Code Tested

Ktype	Parameters	Model								
		1	2	3	4	5	6	7	8	9
Free (Ktype = 1)	$HF_{i,ex}$	3.17105	3.22166	3.22083	3.12735	3.14917	3.14822	3.12805	3.15023	3.1493
	$HF_{o,ex}$	-1.3453	-1.3206	-1.3212	-1.3494	-1.3346	-1.3353	-1.3495	-1.3346	-1.3353
	$NU_{i,ex}$	5.46746	5.4756	5.47675	5.36187	5.36449	5.36536	5.36162	5.36488	5.3658
	$NU_{o,ex}$	3.20297	3.20828	3.20762	3.23805	3.23187	3.23128	3.23933	3.23309	3.23247
	$\theta_{m,ex}$	4.20E-01	4.12E-01	4.12E-01	4.17E-01	4.13E-01	4.13E-01	4.17E-01	4.13E-01	4.13E-01
	$Z_{,ex}$	5.11E-04	4.69E-04	4.71E-04	5.11E-04	4.89E-04	4.90E-04	5.11E-04	4.89E-04	4.90E-04
	Time(min.)	3.17096	5.09883	5.04401	3.23047	5.30768	5.30664	3.225	5.3388	5.31226
	No. of steps	101	176	173	101	177	174	101	177	174

Configuration Used in the model

$NR_1 = 0.3$ $N = 20$

$NR_2 = 0.5$ $NSO = 15$

$NR_3 = 1.0$ $NSI = 15$

$NR_4 = 1.2$ $KR = 10$

$E = 0.5$ $PR = 0.7$

$M = 20$ $U_0 = 0.005$

                $CASE = 1.1$

%) when we shift from linear to hyperbolic axial step formulation. Also the number of axial steps has increased. Comparing hyperbolic & exponential axial increments in Table.5.2, the model having hyperbolic axial increment (models 2, 5 and 8) use more axial steps as compared to exponential step formulation (models 3, 6 and 9) and hence, take more time. Although the difference seems small but other cases may increase the time difference, therefore, exponential step increment formulation will be used for the final computer code for further analysis. Coming to the heat flux formulation, only four-point heat flux model is not able to describe the actual phenomenon. Due to eccentricity, heat will definitely flow circumferentially as well as radially in the present problem, so this consideration along the circumferential interfaces will take us closer to actual process. It is better to take the heat flux considered throughout the interface wall. It should be remembered that heat flux relation is used to get the mesh point temperature values for the solid walls at inner and outer interfaces. On the basis of above discussion, temperature and heat flux continuity principle will be used on all cylindrical mesh points along the circumference of both interfaces. The selection between central and forward difference schemes in heat flux relation will be made on the basis of the following discussion. The central difference has a truncation error of second order, i.e., $O(h^2)$ while a forward and backward difference has truncation error of the first order, i.e., $O(h)$. This makes the central difference scheme having less error than forward difference. A scheme having less error should be the choice for selection, therefore, the central finite difference scheme, having less error, will be used in the heat flux relation in the present model. Other parameters are also compared for general values trend. From the above analysis, model 6

looks most suitable for further analysis. It takes less time than the exponential axial increment with forward finite difference scheme.

5.6. Grid Independence

It is an established fact that the solution of finite difference scheme has errors but the error can be minimized by increasing the number of grid points or in other words, decreasing the mesh size. As the mesh points increases, the solution approaches the exact solution. A stage comes when increasing the number of mesh points doesn't affect the solution much. This is called Grid independence. Different mesh sizes are tested to verify this fact. Twelve different mesh sizes each for fluid annulus and inner & outer solid walls are tested, as shown in Table 5.3.

Table. 5.3. Investigated Combinations of mesh sizes for Grid Independence Test

Mesh config-urtion	Fluid (NxM)	10 x 10	10 x 15	15 x 10	15 x 15	15 x 20	20 x 15	20 x 20	20 x 25	25 x 25	25 x 30	30 x 25	30 x 30
	Solid (NSI& NSO)	10 & 10	10 & 15	15 & 10	15 & 15	15 & 20	20 & 15	20 & 20	20 & 25	25 & 25	25 & 30	30 & 25	30 & 30

Increasing the number of mesh points N in the η-direction reduces the percentage difference from the reference mesh (30x30) in fluid annulus. Different trend with some exceptions is observed in case of increasing M alone in the ξ-direction. The same behavior is observed in the solid walls in which the 30 x 25 mesh size in both the inner and outer walls is taken as reference.

The selection of a suitable mesh size is done by first taking 15 segments in the radial direction of each of the solid walls and varying the mesh size in the fluid annulus. Grid

size of 30 x 30 is taken as reference mesh. Table 5.4 shows clearly that mesh size of 25 x 25.i.e. 25 segments along η direction and 25 segments along ξ direction has percent difference of values, shown in the Table, less than 1 % from the reference mesh size values and, therefore, has been selected. The execution time reported in Table 5.4 is on a Pentium III processor having 600 MHz of CPU speed and 64 MB RAM. The mesh size in solid walls is selected by taking the chosen 25 x 25 mesh size in fluid annulus and varying the number of segments in outer and inner walls as shown in Table 5.5. The number of segments along the ϕ-direction in the solid walls are taken to be the same as in the ξ-direction in the fluid annulus, i.e. 25 segments.

The selected mesh size in both walls is on the basis of a specified % difference from reference values, which is less than 1% in local heat flux at inner & outer interfaces (HF_i & HF_o), local Nusselt number at inner & outer interfaces ($AVNU_i$ & $AVNU_o$) and mean Bulk temperature (θ_m). Also the reference mesh is taken to be 30 & 30 radial increments in inner & outer walls respectively. The standard dimensions of inner and outer tube, shown in Table 7.1 indicate that the outer wall thickness is almost double that of the inner tube. Therefore, the number of mesh points in the radial direction in the outer and inner walls is selected to have the same proportion as the thickness of the two walls. Table 5.6 shows three such possible combinations. The combination of 10 segments and 20 segments along radial direction for inner and outer cylinders, respectively, are selected to be used. This is because this mesh-size combination matches the wall thickness proportion and gives accurate enough results, as shown in Table 5.6.

Table. 5.4. Grid Independence Test for Fluid Annulus

Fixed Config.	Value	Fixed Config.	Value	Fixed Config.	Value	Fixed Config.	Value	Fixed Config.	Value	Ref.	30 x 30
NSI	15	NR$_2$	0.5	Owall	0.2	F	0.01	KR	10	ex	Exit
NSO	15	Pr	0.7	Iwall	0.2	Case	1,1	E	0.5		

Parameters		10x10	10x15	15x10	15x15	15x20	20x15	20x20	20x25	25x25	25x30	30x25	30x30
								Fluid-Annulus Mesh (N x M)					
HF$_{i,ex}$	Value	2.942066	2.941774	2.942860	2.942589	2.942500	2.944112	2.944036	2.943998	2.946222	2.946270	2.949074	2.949082
	% Diff.	0.238	0.248	0.211	0.220	0.223	0.169	0.171	0.172	0.097	0.095	0.000	
HF$_{o,ex}$	Value	-1.469305	-1.469314	-1.469067	-1.469030	-1.468983	-1.468309	-1.468238	-1.468204	-1.467074	-1.467037	-1.465612	-1.465601
	% Diff.	0.253	0.253	0.236	0.234	0.231	0.185	0.180	0.178	0.101	0.098	0.001	
NU$_{i,ex}$	Value	5.086655	5.085592	5.065389	5.064119	5.063586	5.055509	5.054928	5.054663	5.050683	5.050607	5.048941	5.048845
	% Diff.	0.749	0.728	0.328	0.303	0.292	0.132	0.120	0.115	0.036	0.035	0.002	
NU$_{o,ex}$	Value	3.484977	3.485527	3.505911	3.506594	3.506847	3.515705	3.515973	3.516085	3.520960	3.521028	3.523932	3.524012
	% Diff.	1.108	1.092	0.514	0.494	0.487	0.236	0.228	0.225	0.087	0.085	0.002	
θ$_{m,ex}$	Value	0.421611	0.421547	0.419026	0.418934	0.418890	0.417643	0.417591	0.417568	0.416669	0.416650	0.415902	0.415890
	% Diff.	1.376	1.360	0.754	0.732	0.721	0.422	0.409	0.403	0.187	0.183	0.003	
Z$_{ex}$	Value	0.003796	0.003796	0.005096	0.005096	0.005096	0.006096	0.006096	0.006096	0.006796	0.006796	0.007496	0.007496
	% Diff.	49.360	49.360	32.017	32.017	32.017	18.677	18.677	18.677	9.338	9.338	0.000	
No. of Steps	Value	156.0	156.0	169.0	169.0	169.0	179.0	179.0	179.0	186.0	186.0	193.0	193.0
	% Diff.	19.171	19.171	12.435	12.435	12.435	7.254	7.254	7.254	3.627	3.627	0.000	
Time (min.)	Value	0.903516	1.459180	1.262305	2.088021	3.263542	2.961328	4.902995	7.642838	13.014520	21.750520	22.525000	35.345510
	% ratio	2.556	4.128	3.571	5.907	9.233	8.378	13.872	21.623	36.821	61.537	63.728	

Table. 5.5. Grid Independence Test for Solid Walls

Fixed Config.	Value	Fixed Config.	Value	Fixed Config.	Value	Fixed Config.	Value	Fixed Config.	Value	Fixed Config.	Value
N	25	NR_2	0,5	Owall	0,2	F	0,01	KR	10	Ref.	30 x 30
M	25	Pr	0,7	Iwall	0,2	Case	1,1	E	0,5	ex	Exit

Parameters		Number of Radial Increments In Solid-Wall Mesh (NSI & NSO)											
		10 & 10	10 & 15	10 & 20	15 & 15	15 & 20	20 & 15	20 & 20	20 & 25	25 & 25	25 & 30	30 & 25	30 & 30
$HF_{i,ex}$	Value	2,94567	2,94627	2,947493	2,94622	2,94699	2,94590	2,94671	2,94795	2,94731	2,94910	2,94616	2,94793
	% Diff.	0,07666	0,05631	0,014824	0,05801	0,03189	0,06886	0,04138	0,00068	0,02103	0,03969	0,06004	
$HF_{o,ex}$	Value	-1,46706	-1,46725	-1,46776	-1,46707	-1,46731	-1,46681	-1,46701	-1,46740	-1,46689	-1,46753	-1,46610	-1,46672
	% Diff.	0,02318	0,03614	0,070634	0,02386	0,04023	0,00614	0,01977	0,04636	0,01159	0,05523	0,04227	
$NU_{i,ex}$	Value	5,05142	5,05145	5,051694	5,05068	5,05045	5,04909	5,04889	5,04856	5,04570	5,04543	5,04101	5,04076
	% Diff.	0,21148	0,21207	0,216912	0,19680	0,19223	0,16525	0,16129	0,15474	0,09800	0,09264	0,00496	
$NU_{o,ex}$	Value	3,51930	3,52071	3,523738	3,52096	3,52304	3,52134	3,52339	3,52670	3,52723	3,53203	3,52800	3,53273
	% Diff.	0,38016	0,34025	0,254534	0,33317	0,27429	0,32241	0,26438	0,17069	0,15569	0,01981	0,13389	
$\theta_{m,ex}$	Value	0,41686	0,41675	4,17E-01	0,41667	0,41649	0,41655	0,41636	0,41608	0,41588	0,41549	0,41556	0,41518
	% Diff.	0,40464	0,37815	0,438364	0,35888	0,31553	0,32998	0,28421	0,21677	0,16860	0,07467	0,09153	
$Z_{,ex}$	Value	0,00680	0,00680	6,81E-03	0,00680	0,00690	0,00690	0,00690	0,00700	0,00700	0,00710	0,00710	0,00710
	% Diff.	4,22535	4,22535	4,084507	4,22535	2,81690	2,81690	2,81690	1,40845	1,40845	0,00000	0,00000	
No. of Steps	Value	186,0	186,0	186	186,0	187,0	187,0	187,0	188,0	188,0	189,0	189,0	189,0
	% Diff.	1,58730	1,58730	1,587302	1,58730	1,05820	1,05820	1,05820	0,52910	0,52910	0,00000	0,00000	
Time (min.)	Value	11,64518	11,81165	12,148	13,11986	13,41081	14,52148	14,86751	15,14935	16,57467	17,11302	18,23717	18,67467
	% Diff.	62,35816	63,24958	65,05068	70,25484	71,81284	77,76030	79,61324	81,12245	88,75482	91,63760	97,65725	

Table.5.6. Comparison of values Between 3 Mesh Combinations in Inner and Outer Cylinder Walls

Parameters/ Wall+mesh specs.	Iwall*=0.11, Owall**=0.18					Iwall=0.1, Owall=0.2				
	25 & 25	12 & 25		10 & 20		25 & 25	12 & 25		10 & 20	
	Value	Value	% Difference compared with 25 & 25	Value	% Difference compared with 25 & 25	Value	Value	% Difference compared with 25 & 25	Value	% Difference compared with 25 & 25
HF_i	2,01342	2,01479	0,068	2,01418	0,037	2,03656	2,03753	0,048	2,03697	0,020
HF_o	-7,71E-01	-7,74E-01	0,406	-7,73E-01	0,298	-7,56E-01	-7,60E-01	0,462	-7,58E-01	0,316
θ_m	3,82E-01	3,83E-01	0,133	3,83E-01	0,242	3,95E-01	3,96E-01	0,148	3,96E-01	0,250
NU_i	3,26036	3,26526	0,150	3,26647	0,187	3,36884	3,37371	0,145	3,37503	0,184
NU_o	2,01581	2,02131	0,273	2,01694	0,056	1,91182	1,9178	0,313	1,91307	0,065
Z	6,01E-04	6,01E-04	0,000	6,01E-04	0,000	5,77E-04	5,77E-04	0,000	5,77E-04	0,000
Number of steps	179	179	0,000	179	0,000	178	178	0,000	178	0,000
Time	18,3	14	23,497	12,8	30,055	18,3	14	23,497	12,9	29,508

* Iwall = Inner Wall Thickness

** Owall = Outer Wall Thickness

5.7. Selected Numerical Model

From the above discussion, computer code using central finite-difference scheme in the continuity of heat flux relation on boundary points, linear interpolation and exponential increase in axial increment size is the final choice to do further analysis. Furthermore, mesh sizes of NxM=25x25, NSOxM=20x25 and NSIxM=10x25 are selected in the fluid annulus, outer cylinder wall and inner cylinder wall, respectively.

Chapter 6

VALIDATION OF PRESENT COMPUTER CODE

6.1. Introduction

A physical phenomenon can be analyzed using set of equations. These equations are valid only if they describe almost the same behavior as that of the system under consideration. The solution of these equations can be achieved either by analytical or numerical methods. But in both cases, the validation of these equations can be done by comparing the results with the results obtained experimentally. A numerical model of these equations can also be validated by the results obtained previously by other investigators, after adopting the same conditions as that of the previous work. If the results of the numerical model show good agreement with the previous results, then it is considered as a valid model and can be used for further analysis.

To check the adequacy of the present computer code, special runs are carried out. In order to validate for the conventional forced case, reported by Trombetta [39], Feldman [40], Mokheimer [54] and Haider [55], very large values of thermal conductivity ratio (KR) and very thin walls are used. These values correspond to KR=1000, inner wall thickness=0.001, NR_2=0.5, NR_3=1.0 and outer wall thickness=0.002. For comparison with Haider [55], mesh sizes of NxM=20x20, NSOxM=16x20 and NSIxM=8x20 are used in

fluid annulus, outer cylinder and inner cylinder, respectively. These values are kept constant for the validation purpose.

6.2. Comparison With Forced-Convection Results

6.2.1. Conventional Forced Convection Heat Transfer Case

The results of the present computer code, with E=0.5 and 0.6, for the fully developed heat transfer parameters are in excellent agreement with the conventional case results [39,40,55]. Table 6.1 gives comparisons between the present numerical solutions and other corresponding conventional solutions available in the literature. The configurations, shown in Table 6.1a, are selected to simulate forced convection heat transfer having negligible thickness of channel walls, i.e. $NR_1=0.499$, $NR_2=0.5$, $NR_3=1.0$, $NR_4=1.002$ and very high conductivity ratio, i.e. KR=1000. The purpose of selecting these values is to minimize the conjugation effect so that results can be compared and verified with conventional case. Thermal boundary conditions of the first kind is used, which has isothermally heated inner wall (T_w) while the outer wall is at the inlet fluid temperature (T_o), while 0.7 and 0.6 are the values of Prandtl number and eccentricity, respectively.

The values of parameters are compared with that of Haider [55] and Trombetta [39]. Fully developed pressure gradient $(dp/dz)_{fd}$ is verified by Haider [55] and Shah and London [2]. A mutual comparison is also presented to show the adequacy of the present work. The percentage error between the present work and Shah and London [2] for heat flux at the inner wall $(HF_{I,FD})$ and fully developed pressure gradient $(dp/dz)_{fd}$ is almost the

Table.6.1. Comparison With Available Results For Eccentric Annuli Having Linear Axial Increment

CONFIGURATION

NR_1=0.499	N = 20
NR_2=0.5	M = 20
NR_4=1.002	NSI = 8
KR=1000	NSO = 16
E=0.6	Case = 1.I
Pr=0.7	Forced Convection

Table.6.1a. Fully developed forced flow

Parameters/ Models	Present	Haider [55]	% error	Present	Shah and London [2]	% error	Haider [55]	Shah and London [2]	% error
$(dp/dz)_{fd}$	32.2466	32.2070	0.1229	32.2466	31.8180	1.3470	32.2070	31.8180	1.2226
	Present	Haider [55]	% error	Present	Trombetta [39]	% error	Haider [55]	Trombetta [39]	% error
$HF_{i,fd}$	3.5948	3.5930	0.0500	3.5948	3.5820	0.3573	3.5930	3.5820	0.3071
$AVNU_{i,fd}$	5.7407	5.7380	0.0468	5.7407	5.7460	0.0925	5.7380	5.7460	0.1392
$AVNU_{o,fd}$	4.7616	4.7620	0.0077	4.7616	4.7540	0.1606	4.7620	4.7540	0.1683

Table.6.1b. Fully developed forced flow

CONFIGURATION

NR₁=0.499	N = 20
NR₂=0.5	M = 20
NR₄=1.002	NSI = 8
KR=1000	NSO = 16
E=0.5	Case = 1.I
Pr=1.0	Forced Convection

PARAMETERS/MODEL	Present	Haider [55]	% error	Present	Feldman [40]	% error	Haider [55]	Feldman [40]	% error
$(dp/dz)_{fd}$	35.7237	35.7300	0.0177	35.7237	35.3400	1.0857	35.7300	35.3400	1.1036
$\theta_{m,fd}$	0.3793	0.3793	0.0021	0.3793	0.3848	1.4314	0.3793	0.3848	1.4293
$AVNU_{i,fd}$	5.3842	5.3830	0.0221	5.3842	5.3900	0.1078	5.3830	5.3900	0.1299
$AVNU_{o,fd}$	4.3172	4.3180	0.0178	4.3172	4.3080	0.2143	4.3180	4.3080	0.2321

Table.6.1c. Developing forced flow

Z/MODEL	θ_m			$AVNU_i$			$AVNU_o$		
	Present	Haider [55]	% error	Present	Haider [55]	% error	Present	Haider [55]	% error
0.001	0.0417	0.0416	0.2810	15.1060	15.1190	0.0857	0.0001	0.0001	6.6847
0.01	0.1527	0.1526	0.0977	7.6672	7.6680	0.0101	1.5364	1.5370	0.0363
0.1	0.3517	0.3517	0.0052	5.3489	5.3500	0.0198	4.3336	4.3340	0.0094

Z/MODEL	θ_m			$AVNU_i$			$AVNU_o$		
	Present	Feldman [40]	% error	Present	Feldman [40]	% error	Present	Feldman [40]	% error
0.001	0.0417	0.0362	15.2400	15.1060	13.0800	15.4896	0.0001	0.0004	82.2257
0.01	0.1527	0.1319	15.8067	7.6672	6.8580	11.7998	1.5364	3.4600	55.5942
0.1	0.3517	0.3209	9.6037	5.3489	5.1840	3.1817	4.3336	4.6010	5.8120

Z/MODEL	θ_m			$AVNU_i$			$AVNU_o$		
	Feldman [40]	Haider [55]	% error	Feldman [40]	Haider [55]	% error	Feldman [40]	Haider [55]	% error
0.001	0.0362	0.0416	14.9171	13.0800	15.1190	15.5887	0.0004	0.0001	80.9524
0.01	0.1319	0.1526	15.6937	6.8580	7.6680	11.8110	3.4600	1.5370	55.5780
0.1	0.3209	0.3517	9.5980	5.1840	5.3500	3.2022	4.6010	4.3340	5.8031

(dp/dz) PRESSURE GRADIENT

HF_i HEAT FLUX ON THE INNER INTERFACE

$AVNU_i$ NUSSELT NO. ON THE INNER INTERFACE

$AVNU_o$ NUSSELT NO. ON THE OUTER INTERFACE

θ_m MIXED MEAN TEMP.

Z AXIAL DISTANCE MEASURED FROM THE INLET

same as that between Shah and London [2] and Haider [55]. The present model gives better results for fully developed average Nusselt number at inner and outer interfaces than that of Haider [55] by taking the results obtained by Shah and London [2] as reference . Table 6.1b has the same configuration except for eccentricity, E=0.5, and Prandtl number, Pr =1.0. This Table compares the results of four parameters calculated in the present computer code with that of Feldman [40] and Haider [55]. This Table is helpful for the observer to have the complete comparative analysis of the selected parameters. Table 6.1c shows the axial development of the selected parameters. Linear axial increment is used as was used by Haider [55]. Since very large gradients exist near the entrance, computations are made with very small axial steps near the entrance (ΔZ=1 x 10^{-10}); the axial step size being gradually increased several times as the flow moves downstream to reach a maximum value of ΔZ=1 x 10^{-3} near fully developed region. It can be observed that as we move further in the axial direction, the percentage error decreases until fully developed conditions are achieved where percentage error lies around 1%. Haider [55] compared his results for these three parameters with Feldman [40]. The present computer code also gives satisfactory results and even better for some cases.

Another tabular comparison is made for three different parameters at different eccentricities between the present work and that reported by Mokheimer [54]. Table 6.2 gives a good picture of the percentage error between the values, which is obviously less than 1%. It should be kept in mind that the same linear axial increment, which was used by Mokheimer [54] for this validation. As there are no solid walls in the work of Mokheimer [54], the mesh size of 20 and 10 segments along the radial (R) direction and

Table.6.2. Comparison With Available Results By Mokheimer [45] For Conventional Forced Convection

CONFIGURATION

NR$_1$=0.499	N = 20
NR$_2$=0.5	M = 20
NR$_4$=1.002	NSI = 25
KR=1000	NSO = 25
E=0.6	Case = 1.l
Pr=0.7	

E	$\theta_{m,fd}$			$Nu_{i,fd}$			$Nu_{o,fd}$		
	Present	Mokheimer	% error	Present	Mokheimer	% error	Present	Mokheimer	% error
0.1	0.4084	0.4084	0.0183	4.9228	4.9223	0.0092	3.5296	3.5299	0.0085
0.2	0.4059	0.4057	0.0572	4.9597	4.9593	0.0087	3.6183	3.6184	0.0040
0.3	0.4006	0.4005	0.0244	5.0412	5.0412	0.0004	3.7643	3.7643	0.0004
0.4	0.3934	0.3935	0.0169	5.1787	5.1794	0.0131	3.9822	3.9819	0.0083
0.5	0.3845	0.3847	0.0318	5.3991	5.3980	0.0212	4.2973	4.2962	0.0253
0.6	0.3738	0.3740	0.0574	5.7404	5.7432	0.0489	4.7617	4.7607	0.0207
0.7	0.3600	0.3604	0.1165	6.3043	6.2885	0.2518	5.4937	5.4992	0.1000
0.8	0.3413	0.3417	0.1180	7.2795	7.2773	0.0302	6.8477	6.8441	0.0522

25 segments each in the circumferential (φ) direction in outer and inner cylinder walls, respectively, were taken for each cylinder wall. This fine mesh size will definitely improve the result even though very slightly.

The graphical comparison shown in Fig. (6.1) is for the axial development of mixed mean temperature at different eccentricities for forced convection. At the start of the channel, the values of mixed mean temperature for different eccentricities are very close to each other and thus approach the fully developed values for different eccentricities. These values gradually part from each other as the flow moves down the channel. The curves, obtained by El-Shaarawi et al.[45] and the present computer code, for each eccentricity show good agreement with each other, as shown in Fig. (6.1).

6.2.2. Conjugate Forced Convection Heat Transfer Case

The present computer code is also validated for conjugate forced convection. The comparison is presented graphically rather than in tabular form. Figures (6.2) and (6.3) show the graphical comparison solely with the work done by Haider [55]. All these figures are for forced convection heat transfer. Figure (6.2) is showing the developing temperature profiles across the widest gap for an eccentricity, E=0.5 and conductivity ratio, KR=1. Rest of the configurations is shown below the graph. Outer wall thickness is taken twice the inner wall thickness and so is the number of mesh grids, just like Haider [55] did, for comparison. You can see the gradual development of the temperature profile across the widest gap towards the fully developed profile. The overlapping of curves 7 & 8 is an indication that flow has become fully developed, so as the temperature profile.
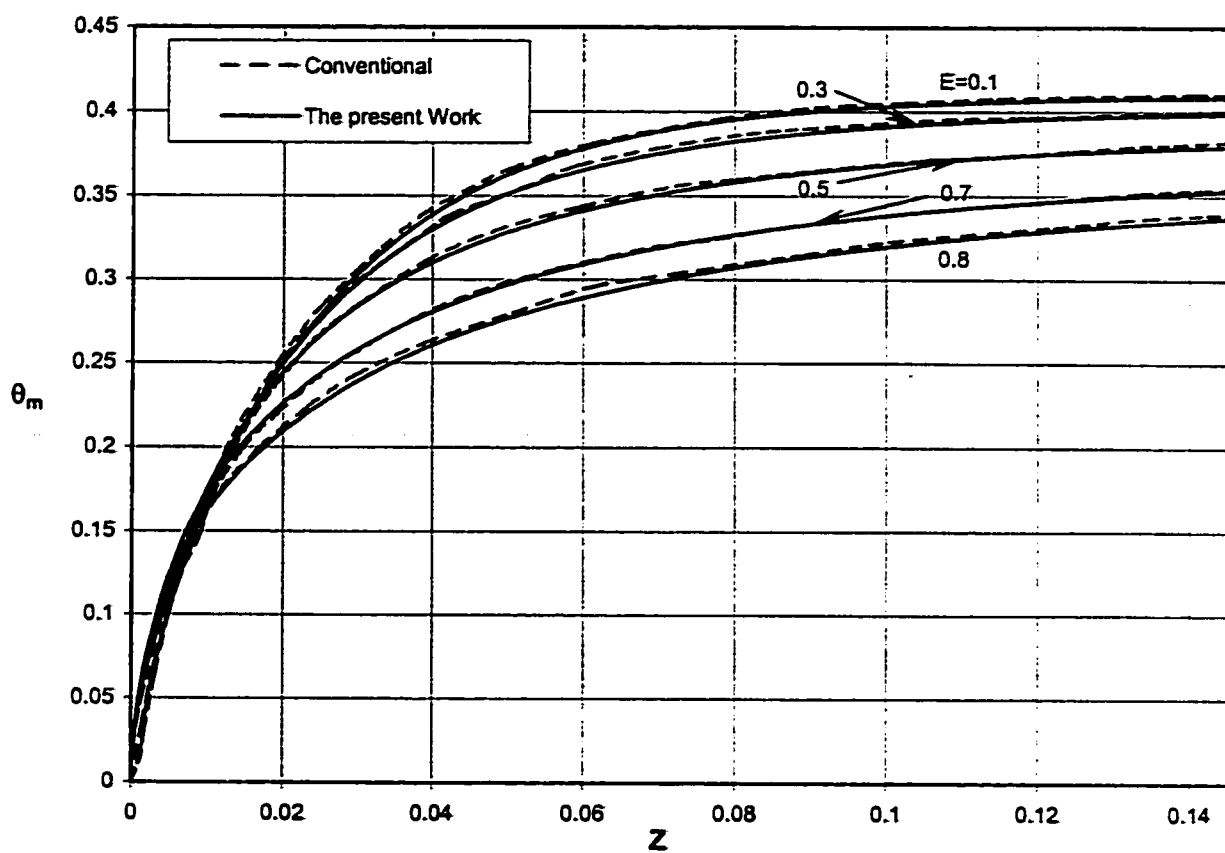
Fig.6.1. Comparison between the present results and those of conventional Forced Convection [47] for mixed mean temperature against Z for various values of Eccentricity in an annulus of NR_2=0.5

NR_2=0.5, N=20, M=20, NSI=25, NSO=25, NR1=0.499, NR4=1.002, KR=1000, Pr=0.7, Case=1.I
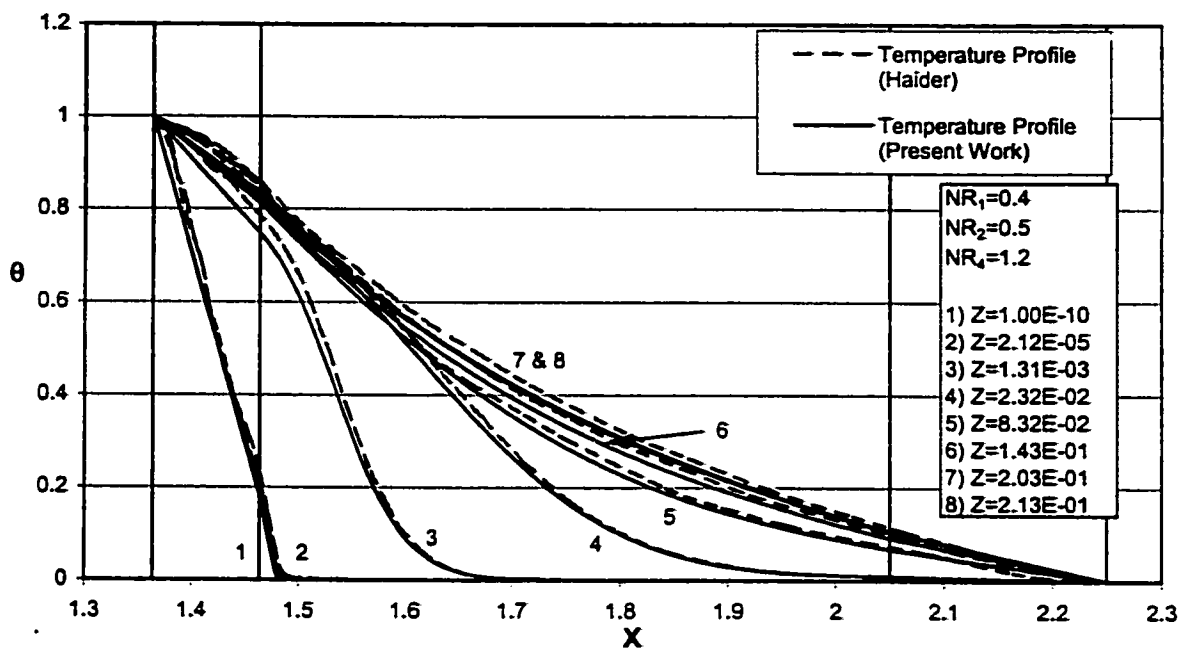
Fig.6.2. Comparison between the present results and those of Conjugate Forced Convection [55] for the Developing Temperature profiles across the widest Gap. E=0.5, KR=1
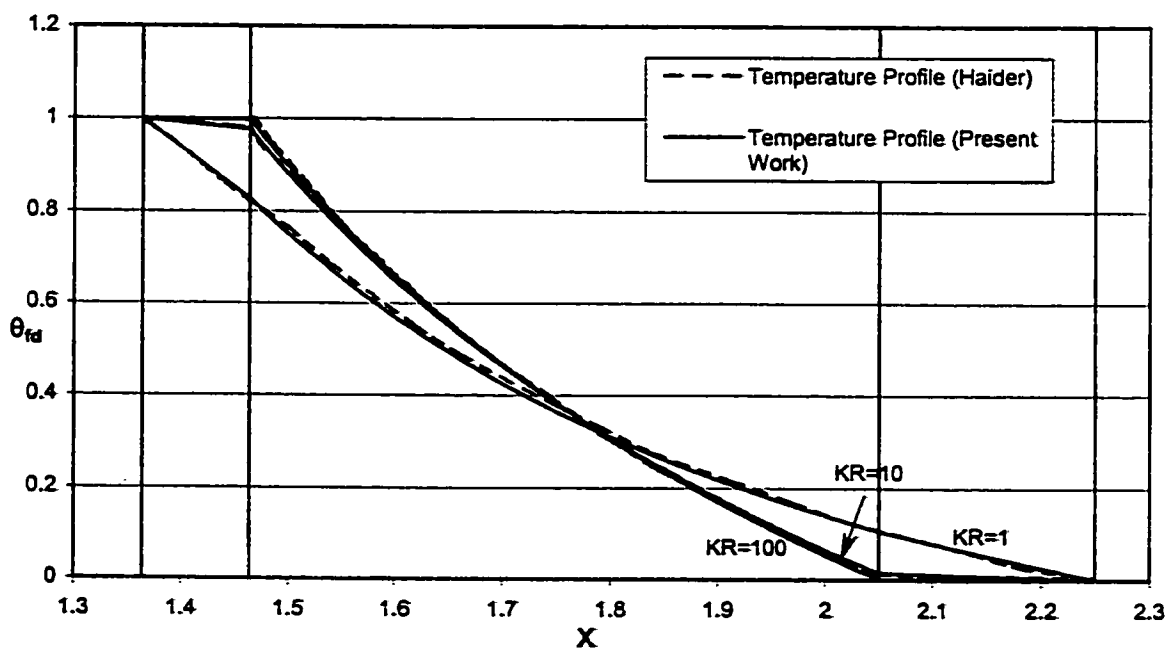
Fig.6.3. Comparison between the present results and those of Conjugate Forced Convection [55] for the fully Developed Temperatuer profile Across the widest Gap for E = 0.5

Now this curve will not change for other cross sections at lengths beyond $Z = 2.03 \times 10^{-1}$. Axial station (8) is the additional station to show that the profile has actually reached fully developed conditions. The same temperature profile is observed at the same axial distance in the graph obtained by Haider [55]. The closeness of the two curves shows that the results obtained from the present computer program are consistent with the results obtained by Haider [55].

Figure (6.3) shows a comparison between the present and Haider's work [55] for the fully developed temperature profiles at the widest gap for three different values of KR, namely, 1,10,100. An additional value of KR=500 was also used to show that there is no change in the temperature profile after a certain value of KR or in other words, the conjugation effect is suppressed.

6.3. Comparison With the Results For Conventional Free Convection

First comparison is made in Table 6.3 for the channel height, required to suck specific flow rate under thermal boundary conditions of first kind,. In free convection, the fully developed conditions are reached by the fluid flow when the channel height is large enough. Conventional conditions are achieved by using very thin walls and high conductivity ratio. The value of Prandtl number is taken as 0.7. Mesh size is the same as reported by Mokheimer [54], i.e. 20 segments each along η and ξ directions. Finer mesh is used in the solid walls. 20 segments along radial direction each for inner and outer walls are used and 25 segments along ϕ direction are used. Different values of induced flow rate is compared with the conventional case and as it is obvious from Table 6.3 that

Table.6.3. Free Convection, Case 1.I , E=0.5

U$_o$ x 10^3	Channel Height (L x 10^5)		
	Reported by Mokheimer [54]	Present Work	% error
4.0	28.50	28.23848	0.92
5.0	43.60	42.75080	1.95
6.0	67.50	65.56201	2.87
7.0	102.00	100.61290	1.36
8.0	158.00	156.74190	0.80
9.0	265.00	257.50800	2.83
10.0	501.00	490.08870	2.18
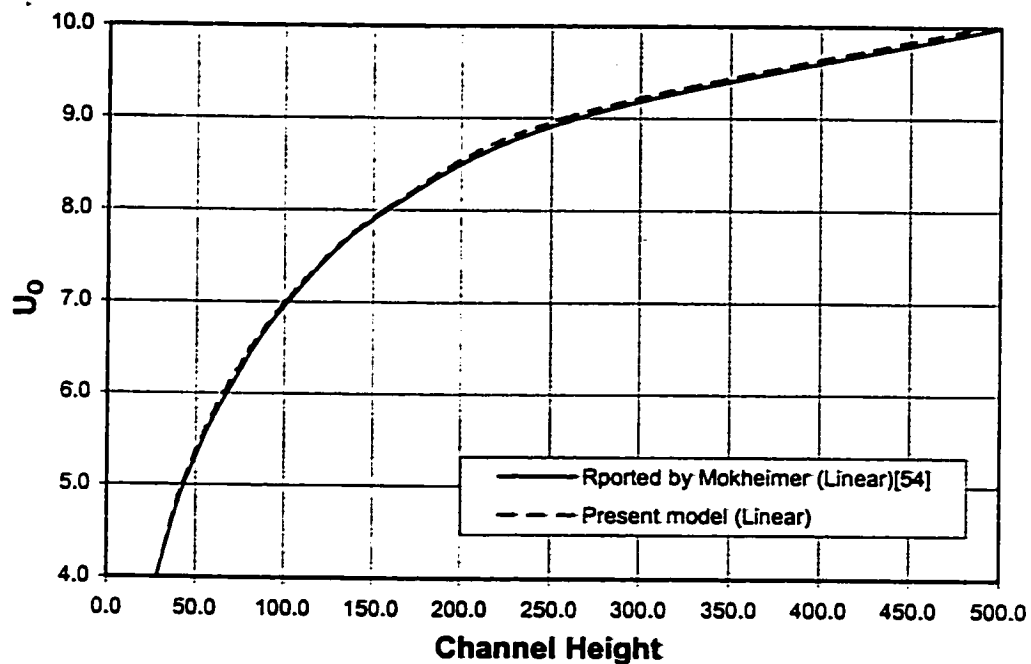
Fig.6.4. Graphical comparison of Flow Velocity versus Channel Height between Mokheimer [54] and Present work for Conventional Free Convection

Configuration

N = 20	NR$_3$ = 1.0
M = 20	NR$_4$ = 1.002
Pr = 0.7	KR = 1000
NR$_1$ = 0.499	NSI = 25
NR$_2$ = 0.5	NSO = 25

Table.6.4. Nusselt Number Averaged for the Cases 1.I & 1.O at Inner and Outer Interface

E	Case 1.I						Case 1.O					
	AVNU$_I$			AVNU$_O$			AVNU$_I$			AVNU$_O$		
	Mokheimer [54]	Present	% error	Mokheimer [54]	Present	% error	Mokheimer [54]	Present	% error	Mokheimer [54]	Present	% error
0.1	5.2368	5.2454	0.1640	3.2478	3.2411	0.2072	4.7061	4.7019	0.0907	3.7760	3.7815	0.1454
0.2	5.2847	5.3056	0.3952	3.3199	3.3033	0.4993	4.7497	4.7362	0.2826	3.8673	3.8849	0.4556
0.3	5.3755	5.4178	0.7883	3.4447	3.4103	0.9978	4.8326	4.8054	0.5641	4.0240	4.0617	0.9377
0.4	5.5268	5.6015	1.3517	3.6316	3.5690	1.7237	4.9716	4.9333	0.7711	4.2562	4.3122	1.3151
0.5	5.7679	5.7891	0.3681	3.8996	3.8803	0.4948	5.1930	5.1884	0.0880	4.5860	4.5931	0.1542
0.6	6.1510	6.2142	1.0264	4.2872	4.2279	1.3839	5.5440	5.5142	0.5369	5.0594	5.1090	0.9803
0.7	6.7840	6.8117	0.4087	4.8794	4.8507	0.5866	6.1218	6.0857	0.5897	5.7785	5.8430	1.1155
0.8	7.9466	8.0325	1.0818	5.9010	5.8089	1.5597	7.1796	7.1265	0.7397	7.0137	7.1151	1.4461
0.9	10.7610	10.9518	1.7730	8.2538	8.0388	2.6043	9.7342	9.7318	0.0249	9.8472	9.8540	0.0700
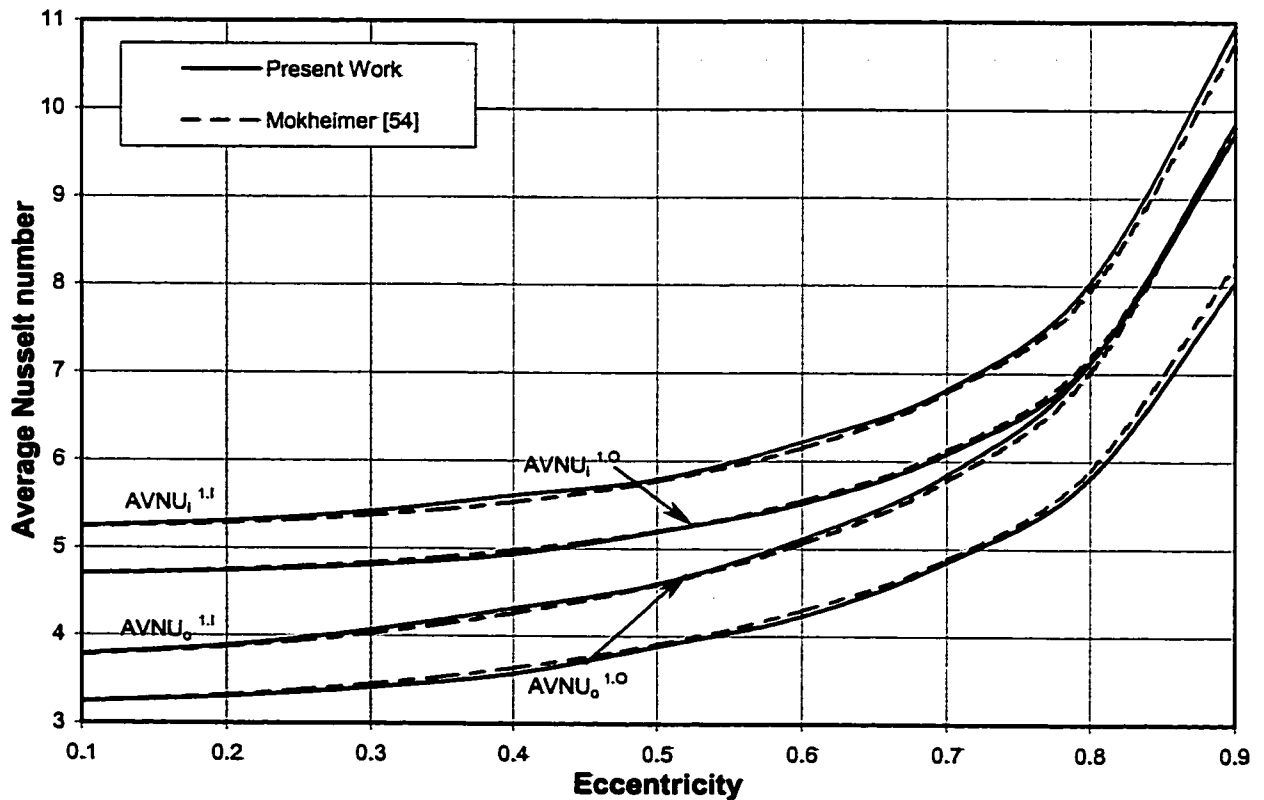
Fig.6.5. Comparison between the present results and those of Mokheimer [54] for the Nusselt number Averaged around the circular arc of the inner and outer walls for Cases 1.O and 1.I for Conventional Free Convection

Ktype=1, NR$_2$=0.5, N=20, M=20, NSI=25, NSO=25, NR$_1$=0.499, NR$_2$=0.5, NR$_4$=1.002, Pr=0.7, KR=1000

Chapter 7

RESULTS AND DISCUSSION FOR BOUNDARY CONDITION OF FIRST KIND

7.1. Introduction

This chapter discusses the effect of solid-fluid conductivity ratio (KR), eccentricity (E), radius ratio (NR$_2$) and walls thickness on incoming flow rate and other heat transfer parameters as function of the channel height employing fundamental boundary condition of first kind. It is to remind the reader that the boundary condition of first kind comprises of inner cylinder wall kept at a prescribed isothermal temperature while outer cylinder wall kept isothermal at ambient temperature for case (1.I). These boundary conditions switch their places for case (1.O). The selected values of inner and outer walls thickness are taken from the standard practical values shown in Table 7.1. The values of solid-fluid conductivity ratio (KR) are selected in such a way to represent all of its practical values shown in Table 7.2. The four controlling factors; KR, E, NR$_2$ and wall thickness are explicitly required to solve the problem under consideration for a fluid of a specific Prandtl number. The values of these parameters, used for computation, are shown in Table 7.3.

Table.7.1. Radius Ratios for Standard Steel Pipes

Nominal Size (Inch)		Radius Ratio				Dimensionless Tube Thickness	
Inner	Outer	ASTM Schedule #	NR$_1$	NR$_2$	NR$_4$	Inner	Outer
1/4	1	Sch. 40	0.35	0.51	1.25	0.17	0.25
1/4	1	Sch. 80	0.32	0.56	1.37	0.25	0.37
3/8	1 1/4	Sch. 40	0.36	0.49	1.2	0.13	0.2
3/8	1 1/4	Sch. 80	0.33	0.53	1.3	0.2	0.3
1/2	1 1/2	Sch. 40	0.39	0.52	1.18	0.14	0.18
1/2	1 1/2	Sch. 80	0.36	0.56	1.27	0.2	0.27
3/4	2	Sch. 40	0.4	0.51	1.15	0.11	0.15
3/4	2	Sch. 80	0.38	0.54	1.22	0.16	0.22
1	2 1/2	Sch. 40	0.42	0.53	1.16	0.11	0.16
1	2 1/2	Sch. 80	0.41	0.57	1.24	0.15	0.24
1 1/2	4	Sch. 40	0.4	0.47	1.12	0.07	0.12
1 1/2	4	Sch. 80	0.39	0.5	1.18	0.1	0.18

Table.7.2. Common Values of KR

Material	Thermal Conductivity (W/m-^{0}C)
Air @ 300 K	0.02624
Carbon Steel (1 % C)	43
Water - Saturated @ 300 K	0.613
Cast Iron (4 % C) @ 293 K	52
Engine Oil (SAE 50) @ 293 K	0.145
Aluminum Metal @ 293 K	236
Asbestos @ 273 K	0.154
Plastic	0.48

Solid Fluid Conductivity Ratio (KR)			
Materail / Fluid	Air	Water	Oil
Aluminum	8993.9	384.99	1627.59
Cast Iron	1981.71	84.83	358.62
Steel	1638.72	70.15	296.55
Plastic	18.29	0.78	3.31
Asbestos	5.87	0.25	1.06

Table.7.3. Variable Parameters Used in the Analysis

KR	E	NR$_2$	IWALL	OWALL
1	0.1	0.1	0.01	0.02
5	0.3	0.3	0.05	0.1
10	0.5	0.5	0.1	0.2
50	0.7	0.7	0.2	0.4
100				
1000				

Iwall   Dimensioless inner cylinder wall thickness

Owall   Dimensionless outer cylinder wall thickness

Fig.7.1. Variation of Flow Rate with Channel Height for Different Values of Conductivity Ratio (KR) (Case 1.I)

$NR_2 = 0.5$, Inner Wall Thickness = 0.1, Outer Wall Thickness = 0.2, $E = 0.5$
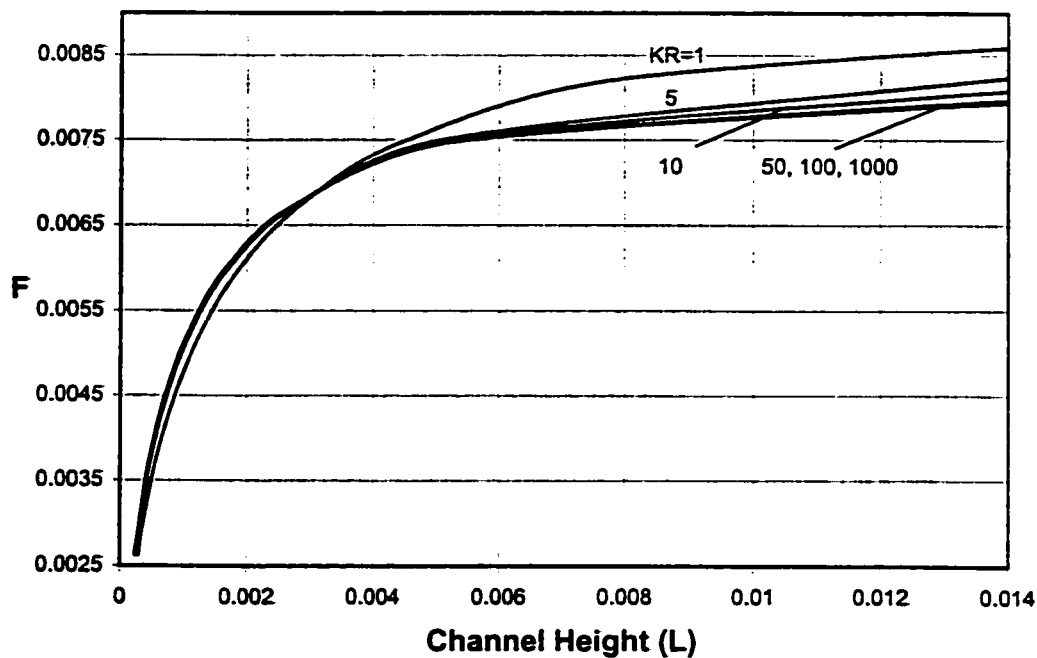

Fig.7.2. Variation of Flow Rate with Channel Height for Different Values of Conductivity Ratio (KR) (Case 1.O)

$NR_2 = 0.5$, Inner Wall Thickness = 0.1, Outer Wall Thickness = 0.2, $E = 0.5$
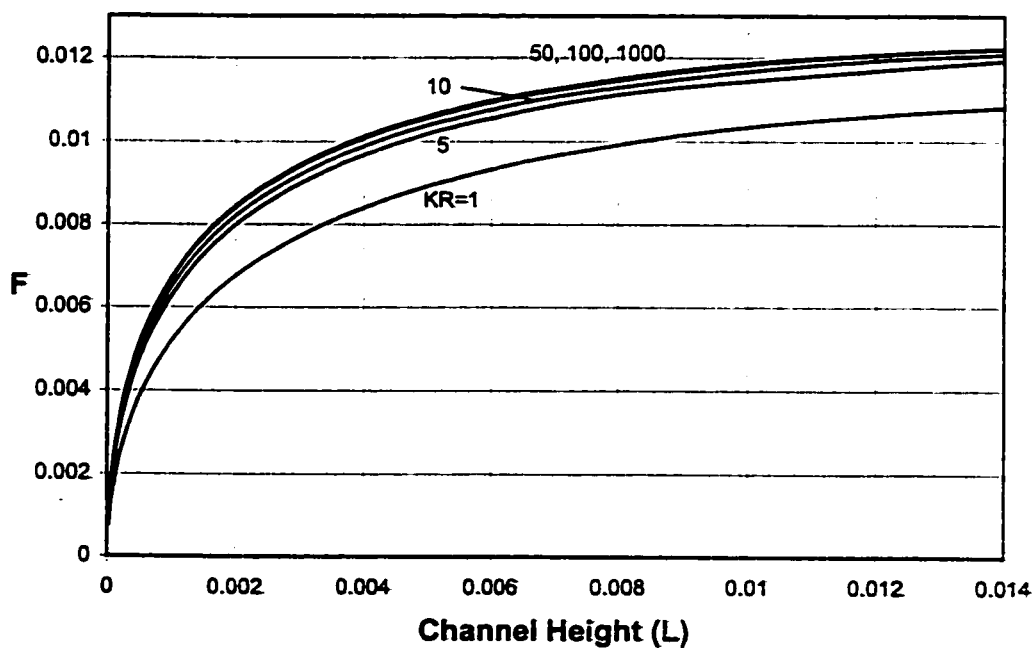
For case (1.I), when the channel height is small and solid-fluid conductivity ratio increases, the temperature on the inner solid-fluid interface increases. The outer wall effect is not prominent in this case because the heat signal is not fully sensed by the outer interface due to short channel height. This results in the increased flow rate into the channel. For high channels, the situation reverses because the outer wall cooling effect dominates due to its larger surface area at high solid-fluid conductivity ratio enabling more heat to flow through the outer wall. The result is the decrease of temperature on outer solid-fluid interface. This reduces the induced flow rate into the channel. For case (1.O), the effect of increasing solid-fluid conductivity ratio on induced flow rate remains consistent for all the channel height range, i.e. having increased flow rate with increasing values of conductivity ratio. In this case the outer wall heating effect is dominant on the cooling effect of the inner wall throughout the channel height. The effect of increased flow rate enables the fluid to absorb more heat, thus raising the mean temperature within the annulus, which increases the buoyancy force driving more flow to be induced in the channel.

Figures (7.3-7.20) explain this phenomenon. These figures have been obtained for a specific flow rate of 0.0075 for case (1.I) and 0.0105 for case (1.O). All the circumferential analysis is carried out at an axial (vertical) location of 4.36×10^{-3} for case (1.I) and 4.86×10^{-3} for case (1.O).

7.2.1.2. Local Heat Flux (HF)

Figures (7.3) and (7.4) show the circumferential variation of local heat flux with solid-fluid conductivity ratio on inner and outer interfaces respectively for case (1.I). Here it is necessary to define the sign convention of heat flux. The value of heat flux is taken positive if it causes heat to flow into the fluid annulus whereas it is taken negative if heat flows out of fluid annulus and can also be interpreted as the heat removal from the fluid. Both of the Figs. (7.3) and (7.4) show increase in the value of heat flux with increasing solid-fluid conductivity ratio but the difference is that the inner solid-fluid interface is increasing the heating effect while the outer interface is contributing to the increasing cooling effect of the channel. This is also true for case (1.O) and similar behavior is observed on outer and inner solid fluid interfaces as shown in Figs. (7.5) and (7.6). The only difference is that the heat is flowing from outer cylinder wall to the inner cylinder wall for case (1.O). In this case, the heat flow through the inner interface is not enough to cool the whole domain; this makes the heating effect of outer wall dominant due to its larger surface area, therefore, increasing the flow rate. The values of the heat flux come closer to each other at high values of solid-fluid conductivity ratio as can be seen in Figs. (7.3-7.6). This is an indication of the reduced conjugate effect.

7.2.1.3. Circumferential Temperature (θ)

The increased heat flux on both solid-fluid interfaces, at higher values of solid-fluid conductivity ratio increases the temperature on the inner active (Heat Transfer) interface while decreases it on the outer interface as can be seen in Figs. (7.7) and (7.8) for case

Fig.7.5. Circumferential Variation of Local Heat Flux on Outer Interface at an Axial (vertical) Location of 4.86×10^{-3} for Different Values of Conductivity Ratio (Case 1.O)

$NR_2 = 0.5$, Inner Wall Thickness = 0.1, Outer Wall Thickness = 0.2, E = 0.5

Fig.7.6. Circumferential Variation of Local Heat Flux on Inner Interface at an Axial (vertical) Location of 4.86×10^{-3} for Different Values of Conductivity Ratio (Case 1.O)

$NR_2 = 0.5$, Inner Wall Thickness = 0.1, Outer Wall Thickness = 0.2, E = 0.5

Fig.7.7. Circumferential Variation of Temperature on Inner Interface at an Axial (vertical) Location of 4.36 x 10^{-3} for Different Values of Conductivity Ratio (Case 1.I)

NR_2 = 0.5, Inner Wall Thickness = 0.1, Outer Wall Thickness = 0.2, E = 0.5
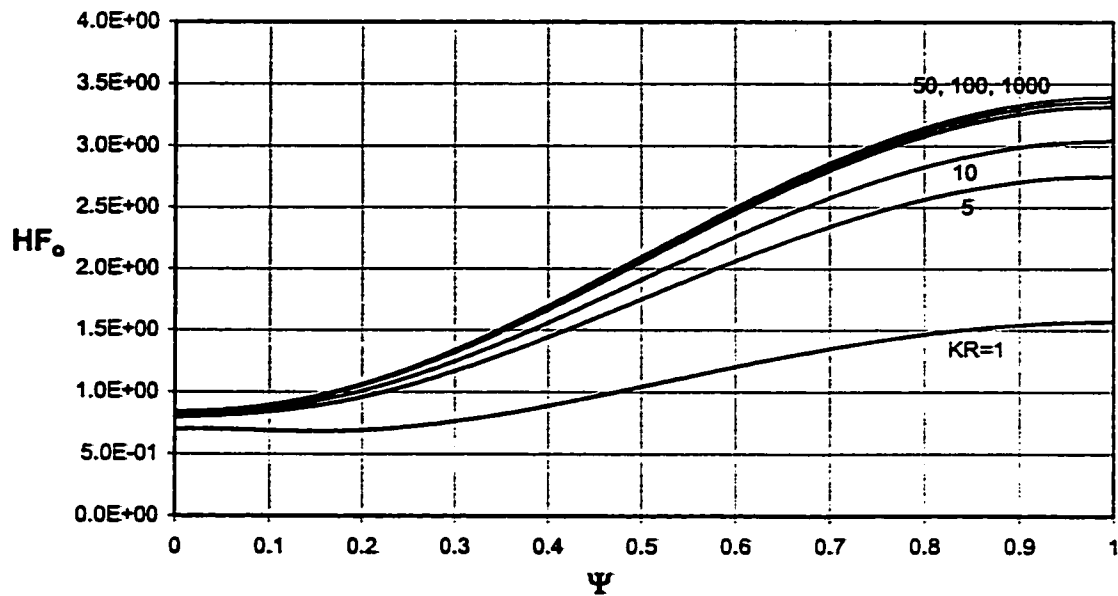

Fig.7.8. Circumferential Variation of Temperature on Outer Interface at an Axial (vertical) Location of 4.36 x 10^{-3} for Different Values of Conductivity Ratio (Case 1.I)

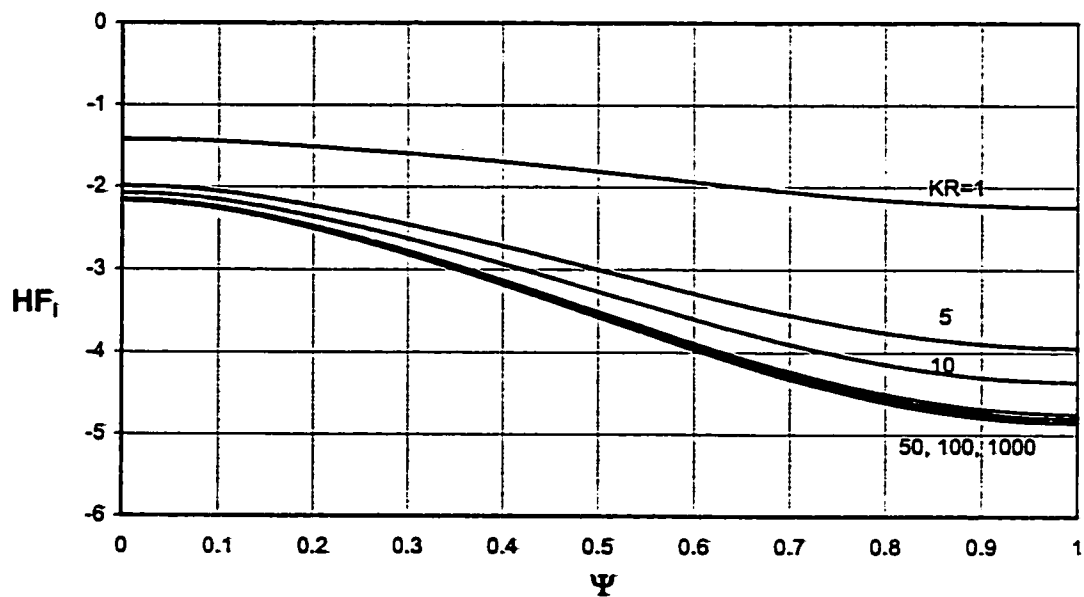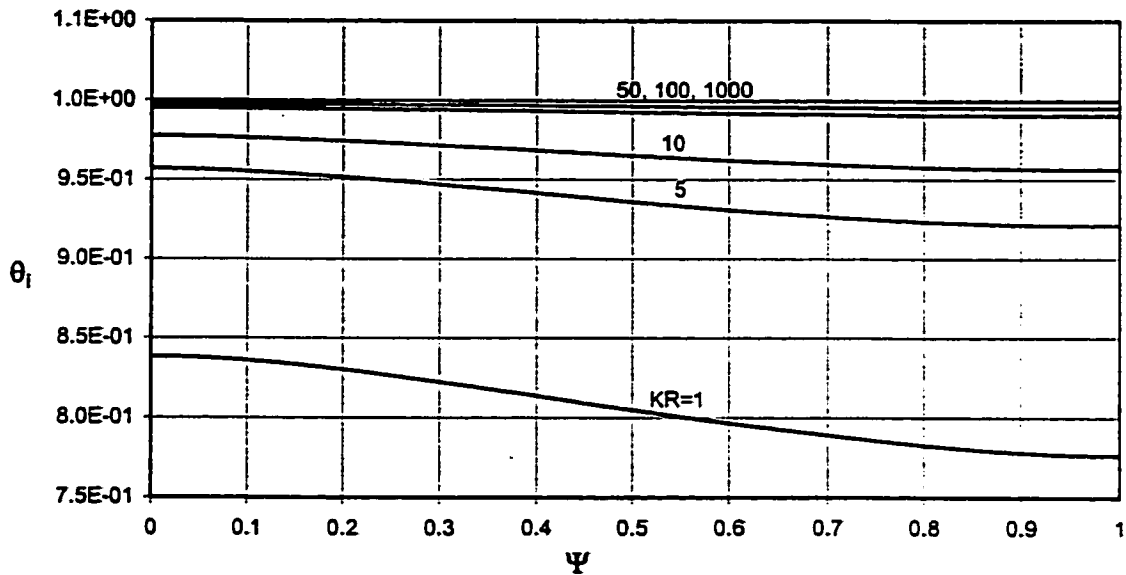NR_2 = 0.5, Inner Wall Thickness = 0.1, Outer Wall Thickness = 0.2, E = 0.5

(1.I). Opposite behavior of circumferential temperature values is observed for case (1.O) as shown in Figs. (7.9) and (7.10).

7.2.1.4. Temperature Profile

The temperature variation with conductivity ratio along the line of symmetry can be shown with the help of the temperature profiles across the fluid annulus at the widest and the narrowest gaps as shown in Figs. (7.11) and (7.12), respectively, for case (1.I). The temperature values on both the solid-fluid interfaces for case (1.O) behave in a similar reversed manner as can be seen in Figs. (7.13) and (7.14).

7.2.1.5. Average Heat Flux (AVHF)

Figures (7.15-7.18) show the variation of the average heat flux for different values of KR along the axial distance of the channel for cases (1.I) and (1.O). The average heat flux increases with the conductivity ratio on both the interfaces. This means that the amount of heat entering and leaving the fluid annulus has increased. For case (1.I), heat enters the fluid annulus through inner interface while leaves through outer interface. For case (1.O), the places of heat entering and exiting the fluid annulus are interchanged. It is observed, from the figures for both cases (1.I and 1.O), that the curves of average heat flux become almost horizontal at large values of Z (away from the channel entrance) indicating that fully developed conditions are approached.

Fig.7.9. Circumferential Variation of Temperature on Outer Interface at an Axial (vertical) Location of 4.86 x 10^{-3} for Different values of Conductivity Ratio (Case 1.O)

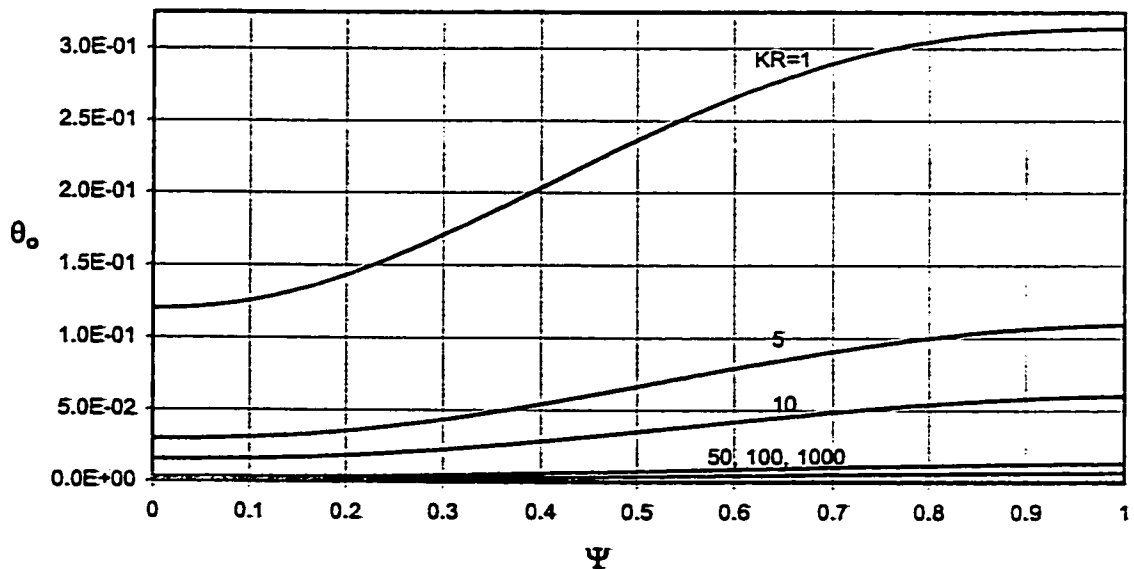$NR_2 = 0.5$, Inner Wall Thickness = 0.1, Outer Wall Thickness = 0.2, E = 0.5

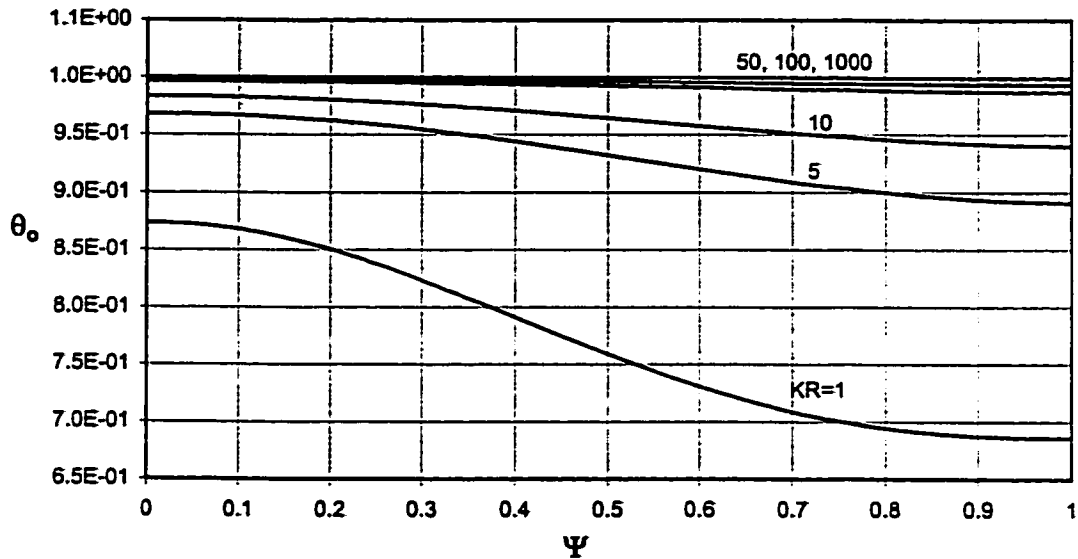**Fig.7.10.** Circumferential Variation of Temperature on Inner Interface at an Axial (vertical) Location of 4.86 x 10^{-3} for Different values of Conductivity Ratio (Case 1.O)

$NR_2 = 0.5$, Inner Wall Thickness = 0.1, Outer Wall Thickness = 0.2, E = 0.5

Fig.7.11. Temperature Variation across the Widest Gap (Ψ=0) at Axial (Vertical) Location of 4.36×10^{-3} for Different Values of Conductivity Ratio (Case 1.I)

NR_2 = 0.5, Inner Wall Thickness = 0.1, Outer Wall Thickness = 0.2, E = 0.5

Fig.7.12. Temperature Variation across the Narrowest Gap (Ψ=1) at Axial (Vertical) Location of 4.36×10^{-3} for Different Values of Conductivity Ratio (Case 1.I)

NR_2 = 0.5, Inner Wall Thickness = 0.1, Outer Wall Thickness = 0.2, E = 0.5

Fig.7.13. Temperature Variation across the Widest Gap ($\Psi=0$) at Axial (Vertical) Location of 4.86×10^{-3} for Different Values of Conductivity ratio (Case 1.O)

$NR_2 = 0.5$, Inner Wall Thickness = 0.1, Outer Wall Thickness = 0.2, E = 0.5
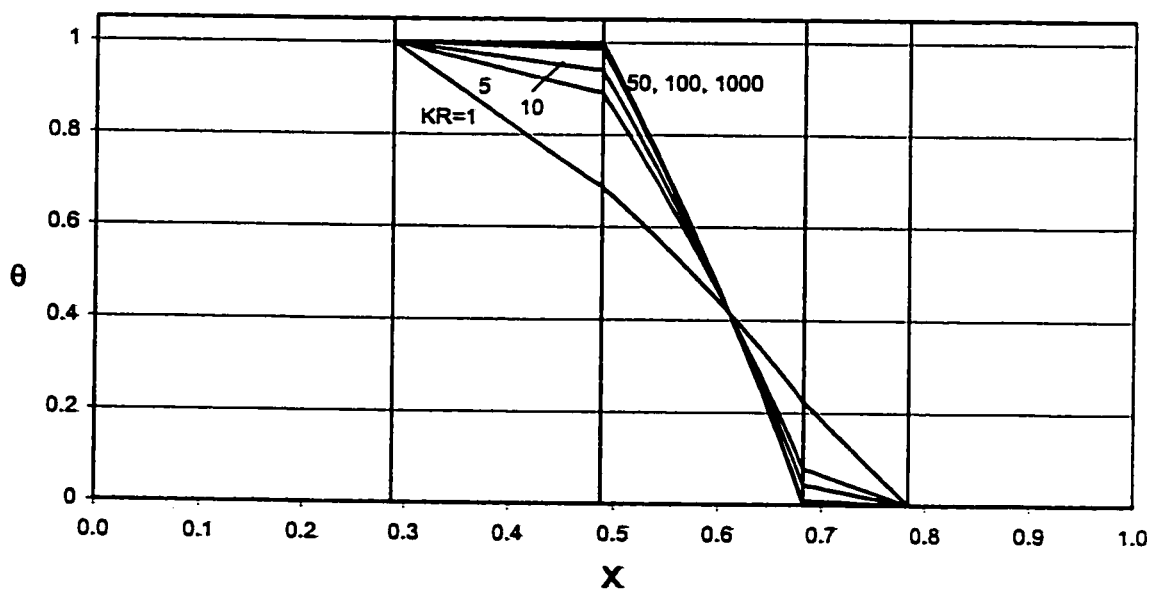
Fig.7.14. Temperature Variation across the Narrowest Gap ($\Psi=1$)at Axial (Vertical) Location of 4.86×10^{-3} for Different Values of Conductivity ratio (Case 1.O)

$NR_2 = 0.5$, Inner Wall Thickness = 0.1, Outer Wall Thickness = 0.2, E = 0.5
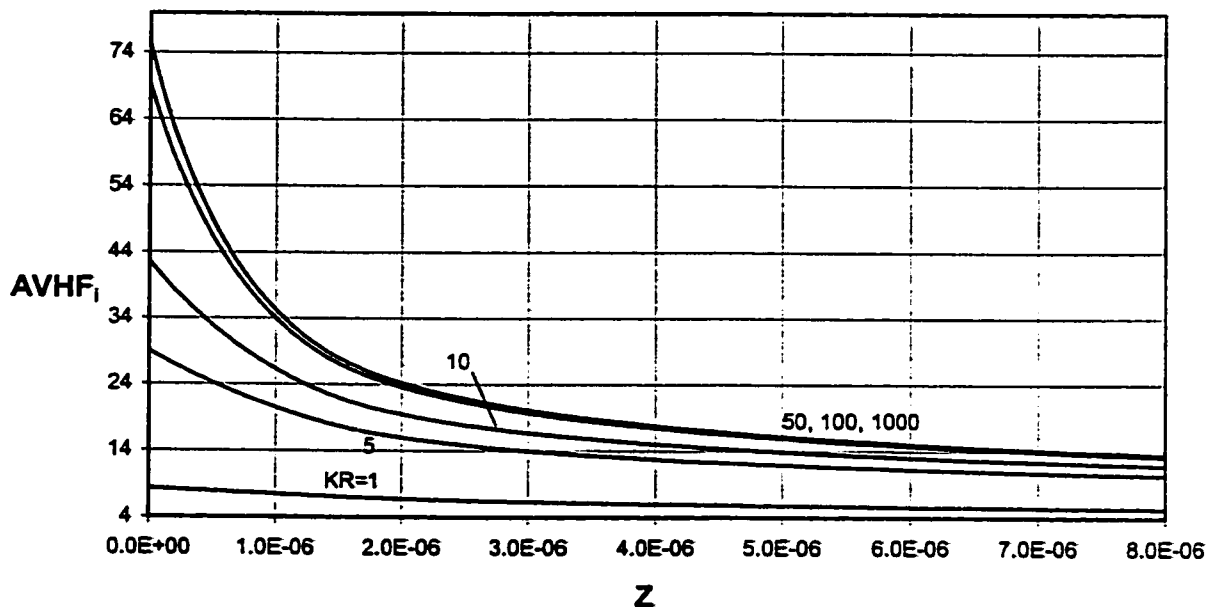
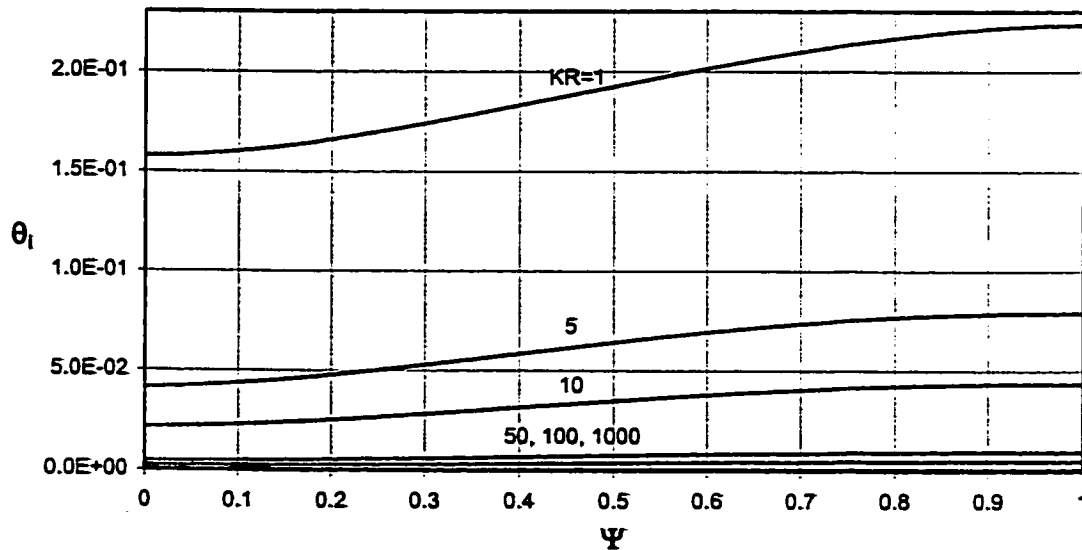**Fig.7.15.** Axial Variation of Average Heat Flux at Inner Interface for
Different Values of Conductivity Ratio (Case 1.I)

$NR_2 = 0.5$, Inner Wall Thickness $= 0.1$, Outer Wall Thickness $= 0.2$, $E = 0.5$
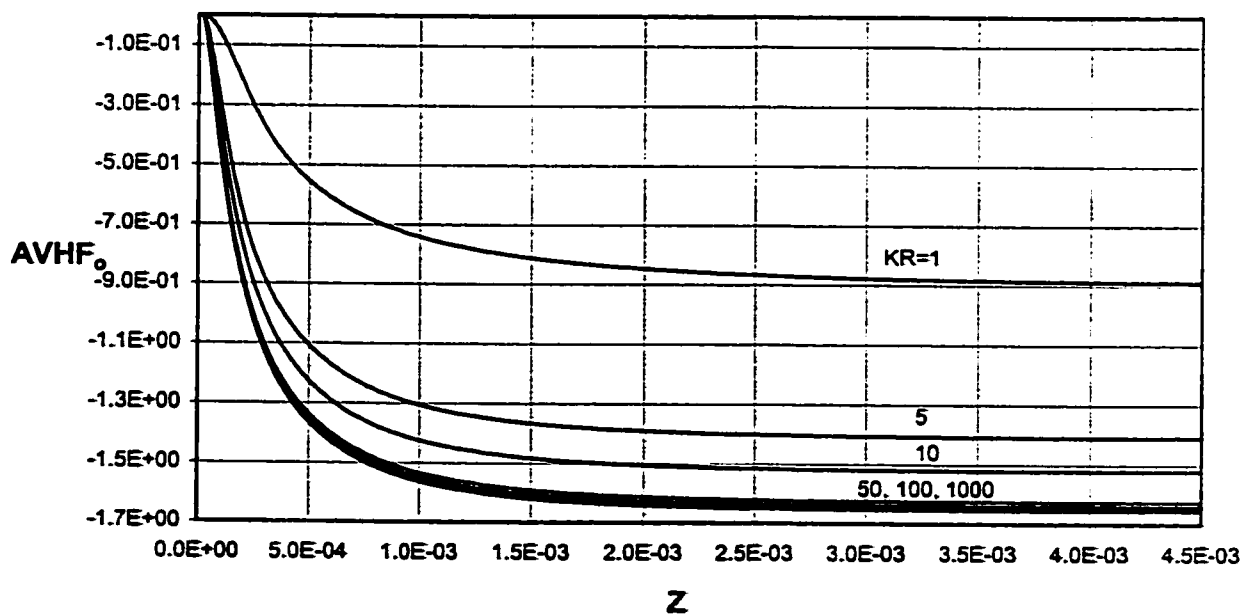
Fig.7.16. Axial Variation of Average Heat Flux at Outer Interface for
Different Values of Conductivity Ratio (Case 1.I)

$NR_2 = 0.5$, Inner Wall Thickness $= 0.1$, Outer Wall Thickness $= 0.2$, $E = 0.5$

Fig.7.17. Axial Variation of Average Heat Flux at Outer Interface for Different Values of Conductivity Ratio (Case 1.O)

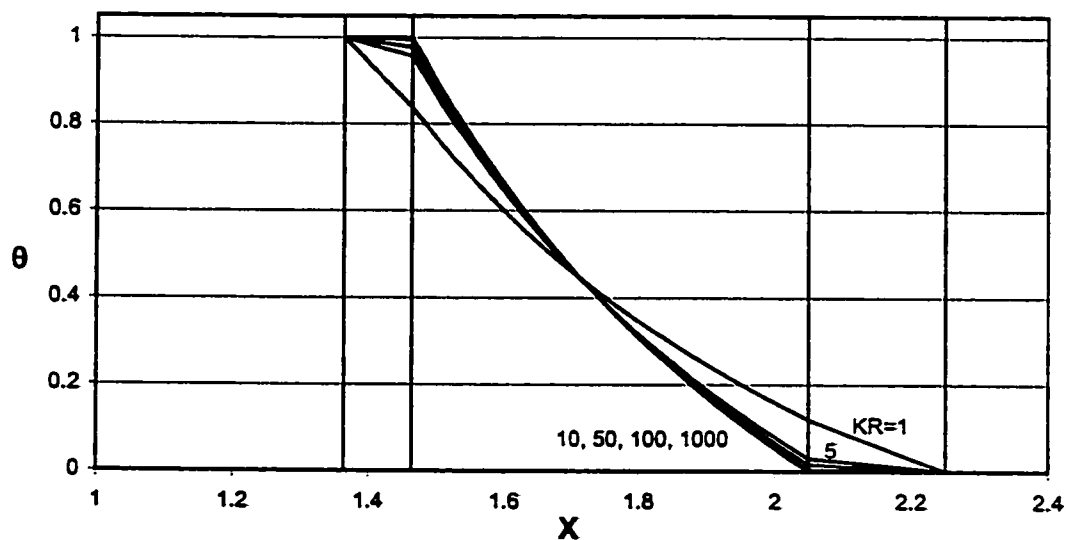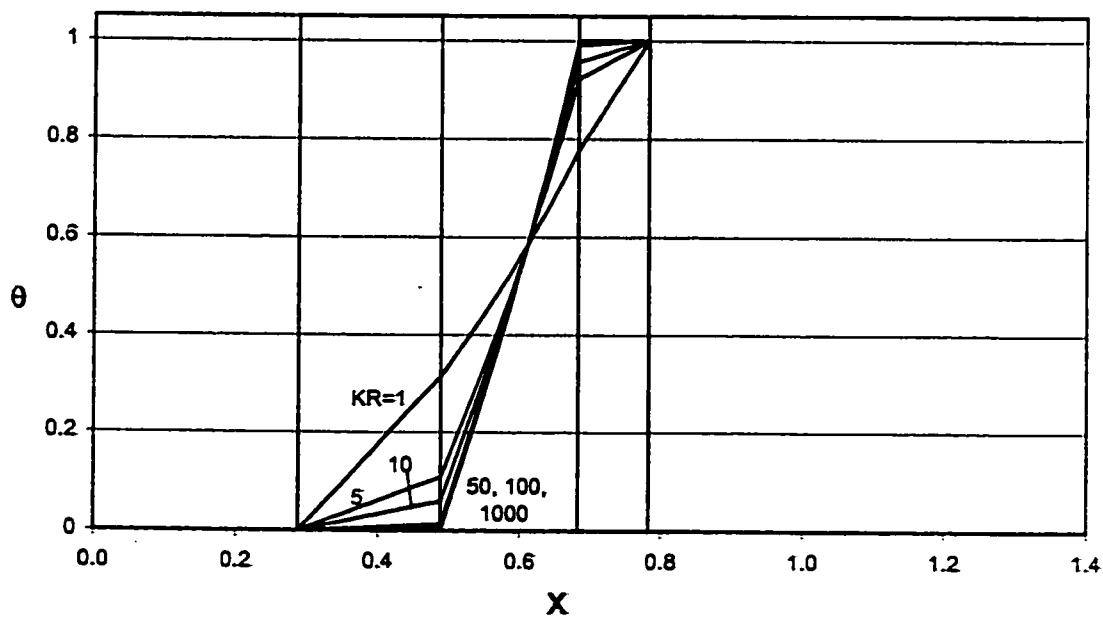$NR_2 = 0.5$, Inner Wall Thickness = 0.1, Outer Wall Thickness = 0.2, $E = 0.5$

Fig.7.18. Axial Variation of Average Heat Flux at Inner Interface for Different Values of Conductivity Ratio (Case 1.O)

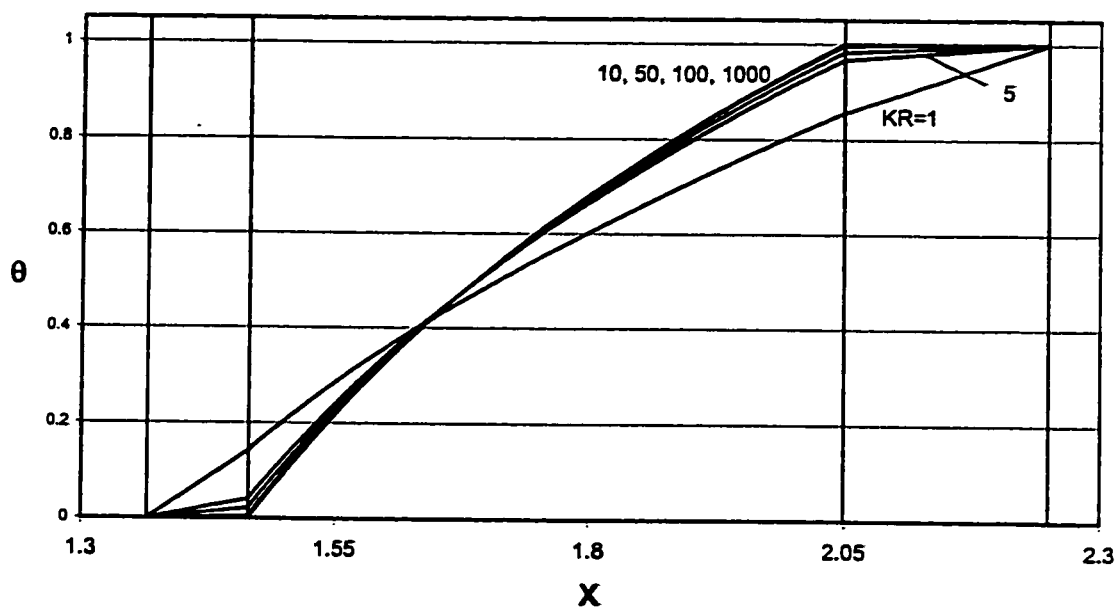$NR_2 = 0.5$, Inner Wall Thickness = 0.1, Outer Wall Thickness = 0.2, $E = 0.5$

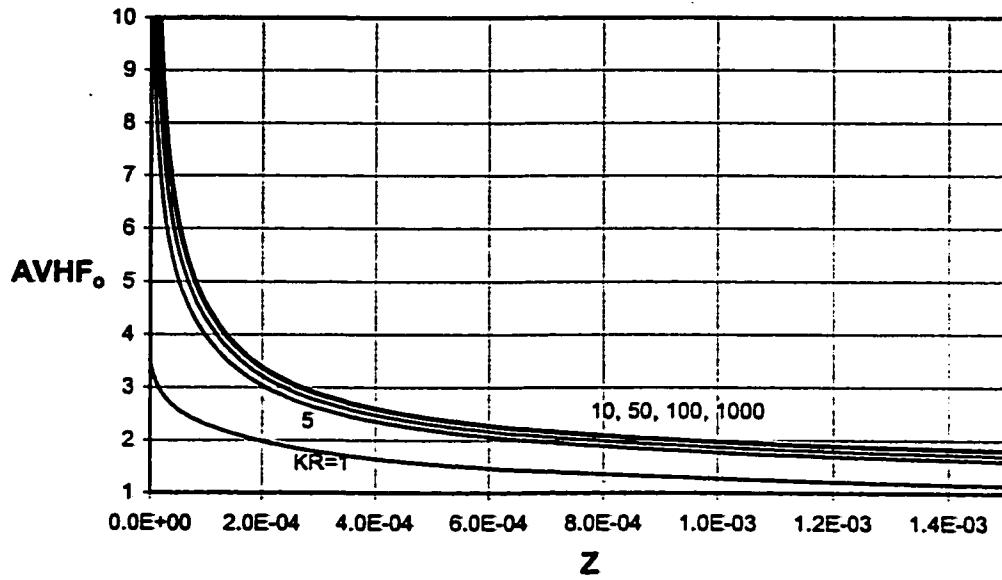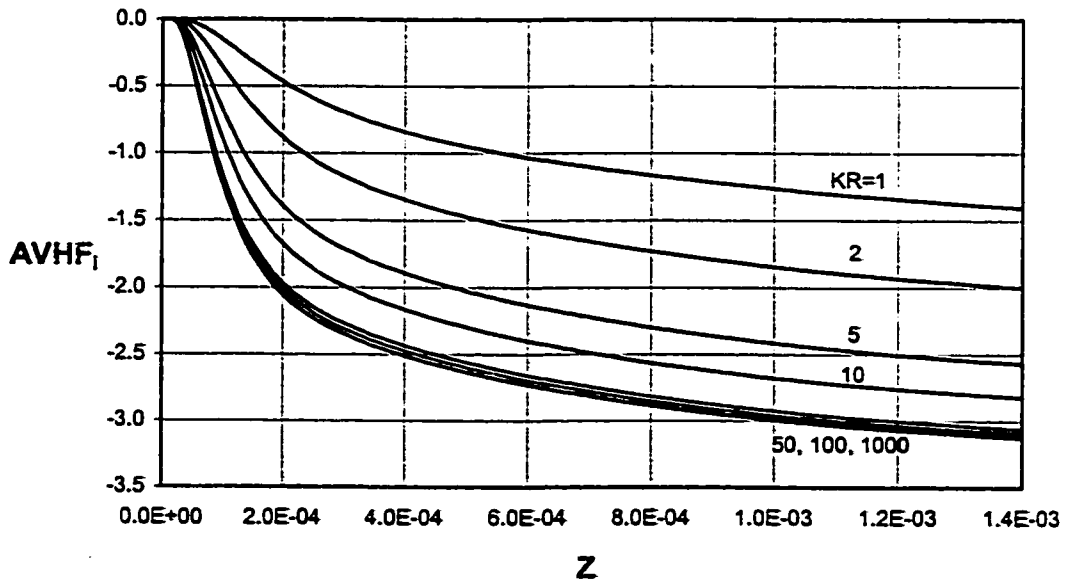### 7.2.1.6. Total Heat Absorbed ($\overline{Q}$)

Figure (7.19) shows the variation of the total heat absorbed ($\overline{Q}$) by the fluid versus channel height (L) for different values of solid-fluid conductivity ratio for case (1.I). Two trends can be seen in the figure. For short channels, higher values of solid-fluid conductivity ratio shows greater heat absorbed in the fluid whereas this trend reverses for high channels. Increasing the conductivity ratio increases the amount of heat added through the inner wall but the heat signal is not fully sensed by the outer wall in such short channels. Therefore, more heat is gained by the fluid through the isothermally heated inner wall than that lost by the fluid through the outer wall maintained at the ambient temperature. This results in the rise of mean fluid temperature and hence the flow rate. For high channels, the amount of heat lost by the fluid though the outer wall increases at high values of conductivity ratio, thus, decreasing the amount of heat absorbed by the fluid. This reduces the mean fluid temperature, which in turn reduces the buoyancy driving force that induces the flow into the channel resulting in a reduced flow rate. Only one trend of having an increased heat absorbed by the fluid at higher values of the conductivity ratio is observed for case (1.O), as shown in Fig. (7.20). The heating effect of outer wall remains dominant throughout the channel height because the heat flowing from the outer wall is much more than that lost through the inner wall due to its less surface area. This accumulation of heat in the fluid assists the increased heating effect on outer interface, with increasing conductivity ratio, in inducing more flow rate in the channel.

Fig.7.19. Total Heat Absorption versus Channel Height for Different Values of Conductivity Ratio (Case 1.I)

$NR_2 = 0.5$, Inner Wall Thickness $= 0.1$, Outer Wall Thickness $= 0.2$, $E = 0.5$
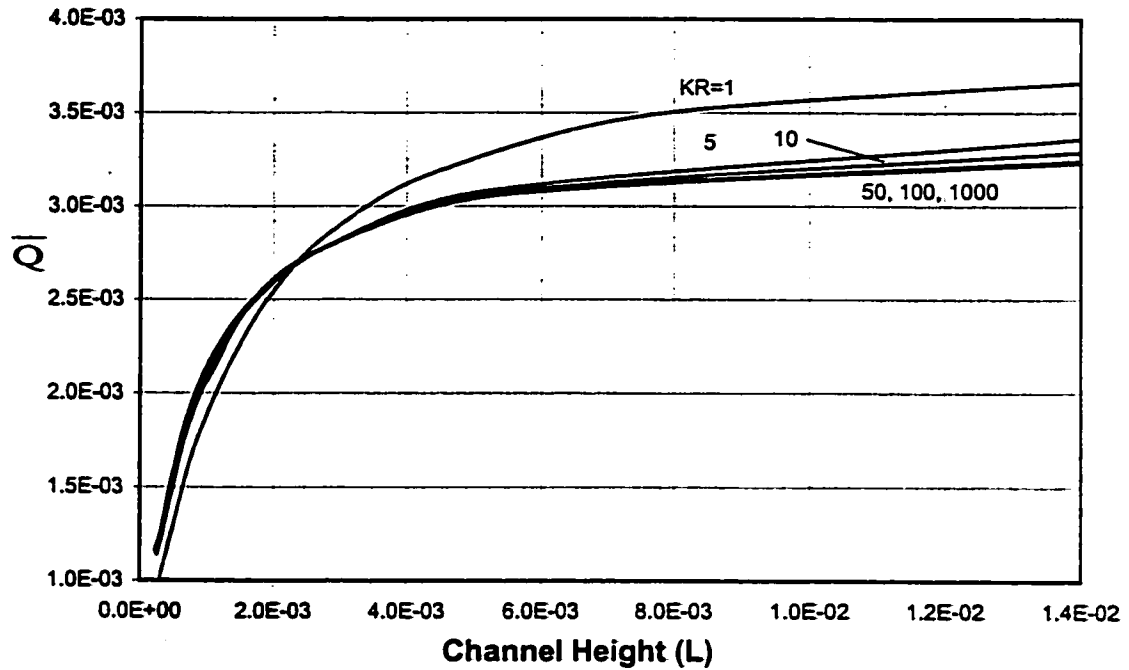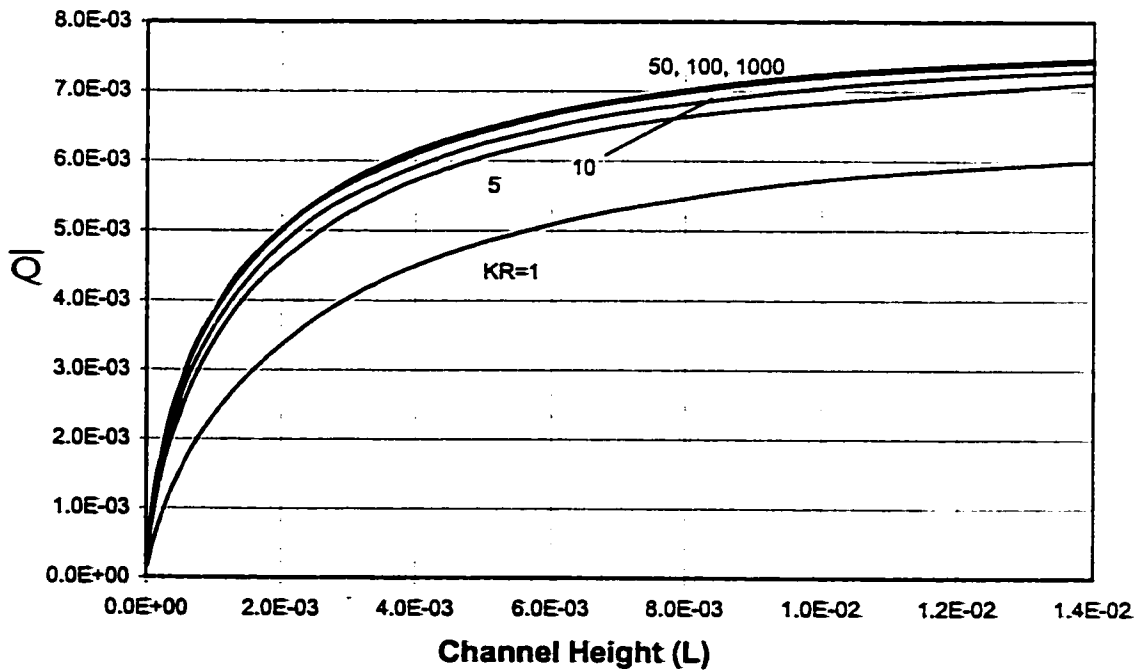

Fig.7.20. Total Heat Absorption versus Channel Height for Different Values of Conductivity Ratio (Case 1.O)

$NR_2 = 0.5$, Inner Wall Thickness $= 0.1$, Outer Wall Thickness $= 0.2$, $E = 0.5$

7.2.2. Effect of Eccentricity (E)

This analysis is carried out using geometry of annulus radius ratio 0.5, inner and outer walls thickness of 0.1 and 0.2, respectively and conductivity ratio 10.

7.2.2.1. Induced Flow Rate (F)

Figures (7.21) and (7.22) present the variation of induced flow rate with the channel height for different values of the eccentricity for cases (1.I) and (1.O) respectively. It is observed that at a given channel height, the flow rate induced is greater for case (1.O) than for case (1.I), as can be seen in Fig. (7.23). This is attributed to the larger heating surface in case (1.O) than in case (1.I). For both cases (1.I and 1.O) and given radius ratio, conductivity ratio and channel height, increasing the eccentricity increases the induced flow rate. The reason is that eccentricity increases/decreases the resistance to flow on the narrowest ($\psi = 1$)/widest ($\psi = 0$) gap side of the annulus. The axial velocity profile develops with increasing/decreasing values on the widest ($\psi = 0$)/narrowest ($\psi = 1$) gap side of the annulus resulting in net increase of higher heat transfer coefficient. This is due to the increase in the heat transfer to the fluid by convection at the widest gap ($\psi = 0$). This increases the mean fluid temperature leading to increased flow rate. Considering very short channels, both cases (1.I and 1.O) show reverse trend, i.e. increasing the eccentricity decreases the induced flow rate. The reason is that for small eccentricity, the heat flows almost uniformly from the heated wall in all directions but does not find enough channel height for the fluid to take the heat by convection thus resulting in decreased mean fluid temperature and leads to the decrease in induced flow rate.

Fig.7.21. Variation of Flow Rate with Channel Height for
Different Values of Eccentricity (Case 1.I)

$NR_2 = 0.5$, Inner Wall Thickness = 0.1, Outer Wall Thickness = 0.2, KR = 10
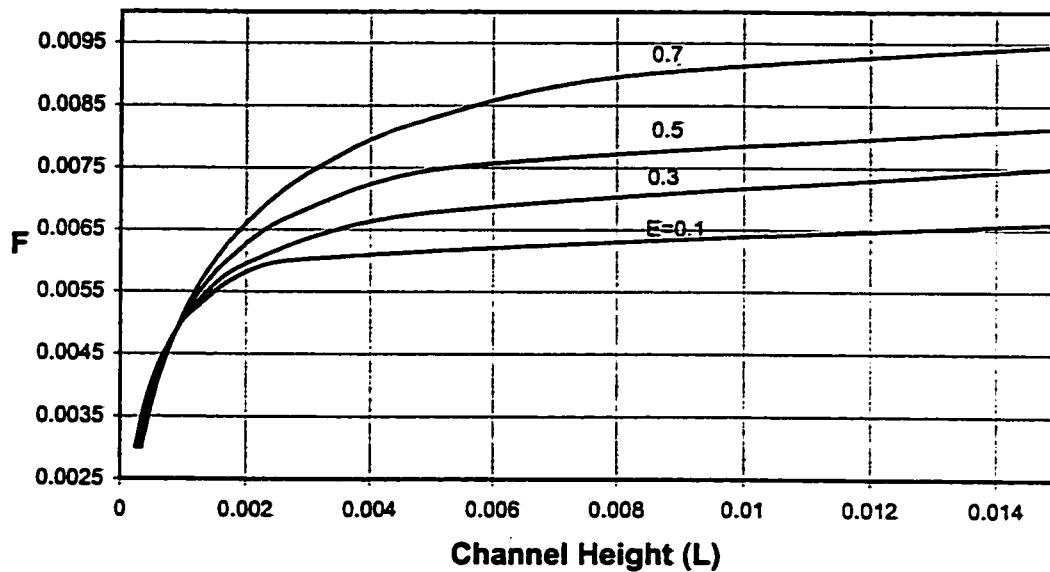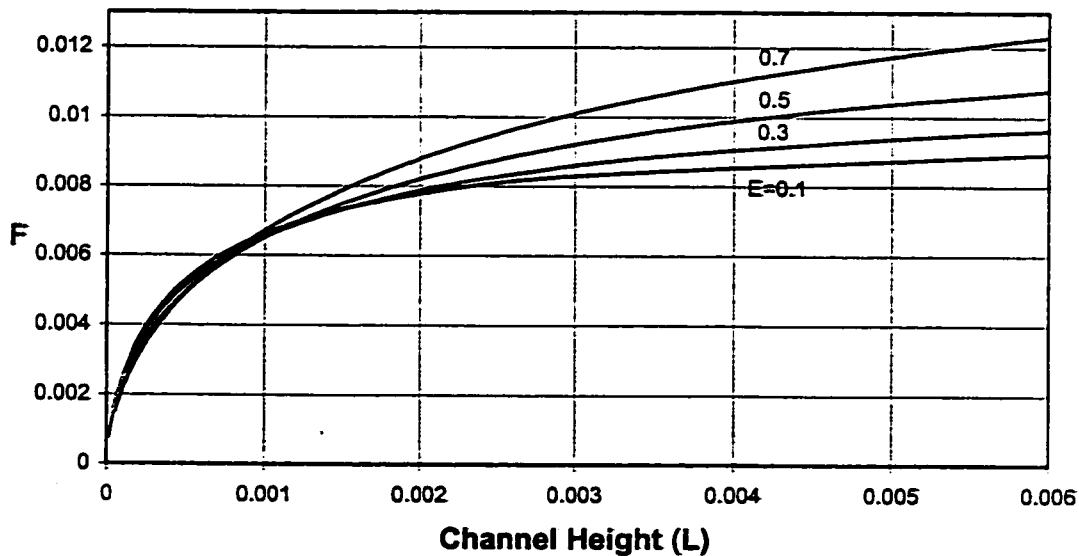

Fig.7.22. Varaition of Flow Rate With Channel Height for
Different Values of Eccentricities (Case 1.O)

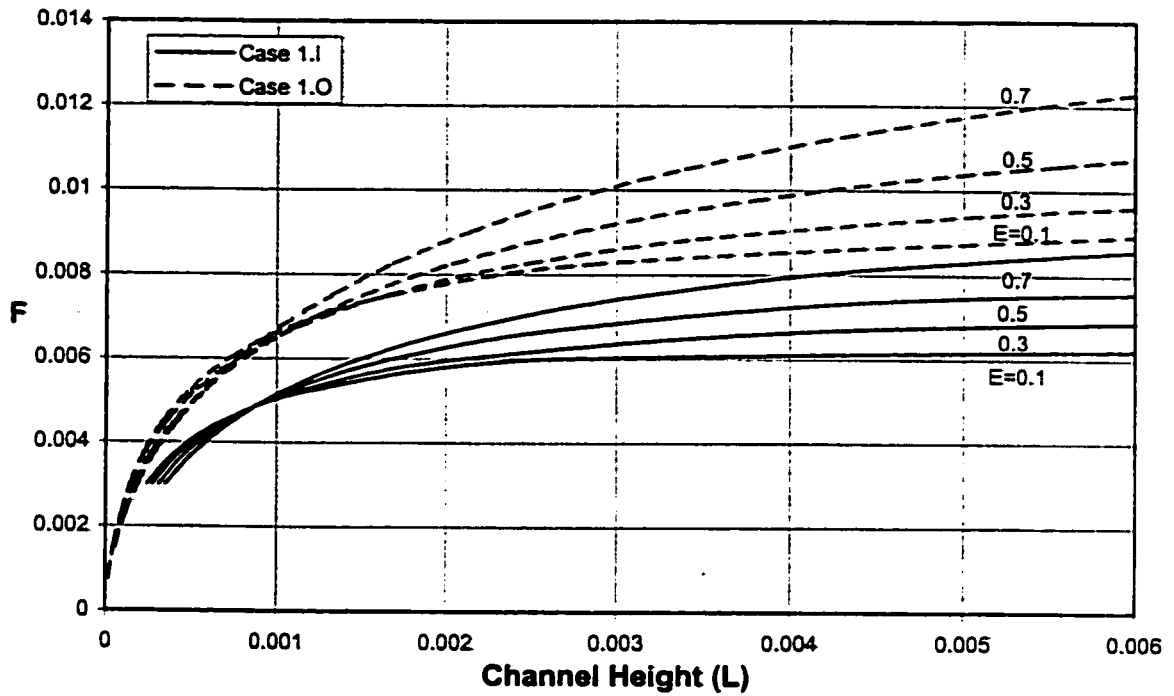$NR_2 = 0.5$, Inner Wall Thickness = 0.1, Outer Wall Thickness = 0.2, KR = 10

Fig.7.23. Comparison of Flow Rate with Channel Height for Different Eccentricities among Cases (1.I) and (1.O)

$NR_2 = 0.5$, Inner Wall Thickness = 0.1, Outer Wall Thickness = 0.2, KR = 10

7.2.2.2. Local Heat Flux (HF)

Figures (7.24-7.27) show the effect of eccentricity on the circumferential variations of local heat flux on inner and outer interfaces for cases (1.I) and (1.O) at a specific flow rate of 0.006 for case (1.I) and 0.009 for case (1.O). All the circumferential analysis is carried out at an axial (vertical) location of 1.37×10^{-3} for case (1.I) and 1.99×10^{-3} for case (1.O). Figures (7.24) and (7.25) show very small variation in local heat flux along the circumference of the cylinder walls at low eccentricity for case (1.I). The variation increases on both solid-fluid interfaces with eccentricity. The reason is that with the increase of eccentricity, the thermal resistance to heat flow at the narrowest gap ($\psi = 1$) decreases due to reduced distance whereas the resistance to heat flow increases at the widest gap ($\psi = 0$) due to increased distance. Figures (7.26) and (7.27) show the same trend for case (1.O) as seen for case (1.I). The only difference is that the heating and cooling walls have switched their places. The reason for negative values of heat flux on outer interface (case 1.I) and inner interface (case 1.O) is already explained in section 7.2.1.

7.2.2.3. Circumferential Temperature (θ)

The rise in narrowest gap ($\psi = 1$) interface temperature of the cooling wall (outer wall for case 1.I and inner wall for case 1.O) due to increased heat flux can be seen in Figs. (7.28-7.31) for cases (1.I) and (1.O). From Figs. (7.28) and (7.29), small eccentricity shows almost uniform interface temperatures along the circumference (of high value at inner wall and low value at outer wall) for case (1.I). The increase of eccentricity causes
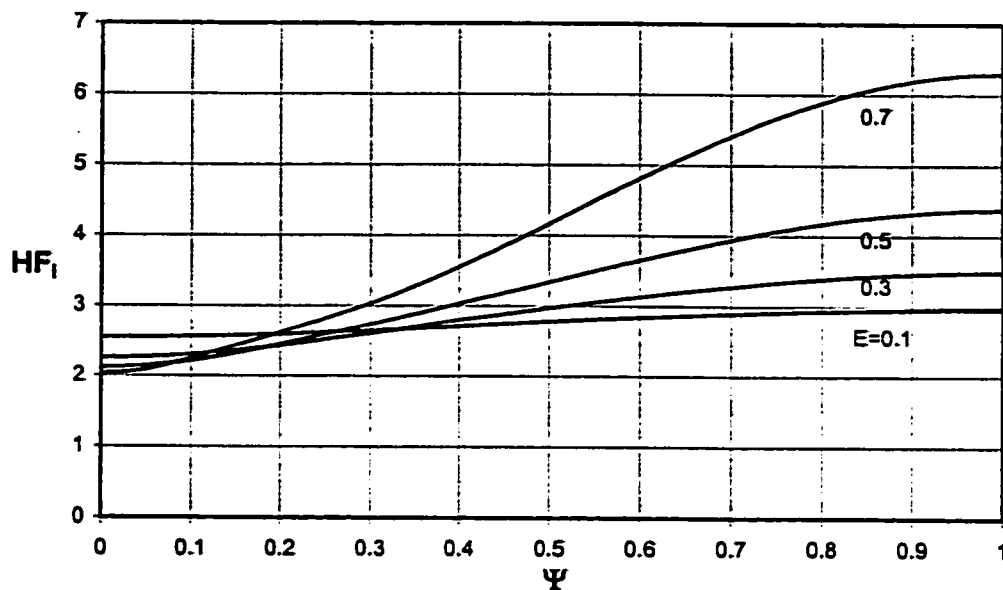
Fig.7.24. Circumferential Variation of Local Heat Flux on Inner Interface at an Axial (vertical) Location of 1.37×10^{-3} for Different Values of Eccentricity (Case 1.I)

$NR_2 = 0.5$, Inner Wall Thickness = 0.1, Outer Wall Thickness = 0.2, KR = 10

Fig.7.25. Circumferential Variation of Local Heat Flux on Outer Interface at an Axial (vertical) Location of 1.37×10^{-3} for Different Values of Eccentricity (Case 1.I)

$NR_2 = 0.5$, Inner Wall Thickness = 0.1, Outer Wall Thickness = 0.2, KR = 10

Fig.7.28. Circumferenctial Variation of Temperature on Inner Interface at an Axial (vertical) Location of 1.37×10^{-3} for Different Values of Eccentricities (Case 1.I)

$NR_2 = 0.5$, Inner Wall Thickness $= 0.1$, Outer Wall Thickness $= 0.2$, $KR = 10$

Fig.7.29. Circumferenctial Variation of Temperature on Outer Interface at an Axial (vertical) Location of 1.37×10^{-3} for Different Values of Eccentricities (Case 1.I)

$NR_2 = 0.5$, Inner Wall Thickness $= 0.1$, Outer Wall Thickness $= 0.2$, $KR = 10$
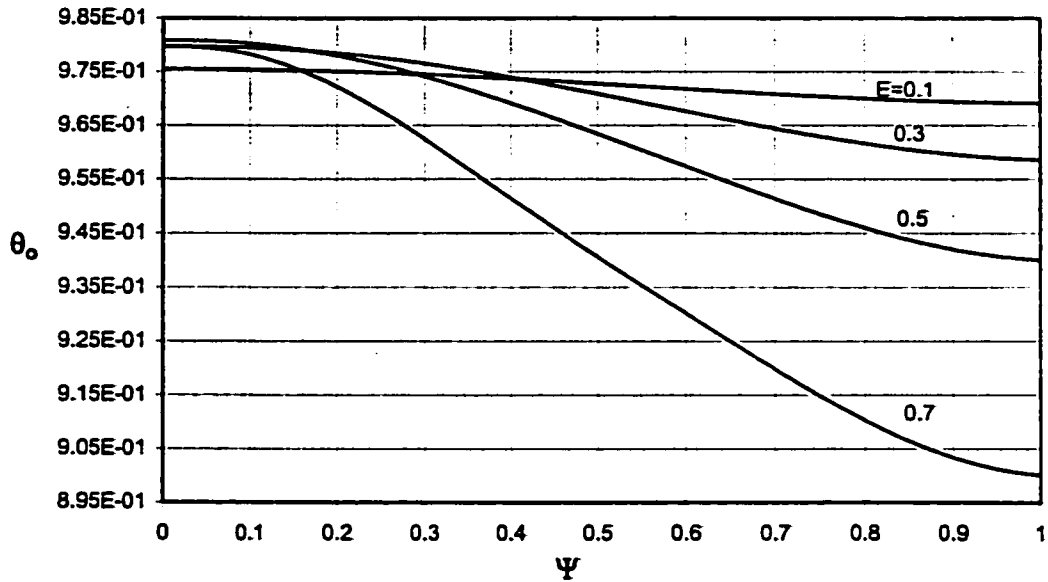
Fig.7.30. Circumferential Variation of Temperature on Outer Interface at a Channel Height of 1.99 x 10^{-3} for Different Values of Wall Thickness (Case 1.O)

$NR_2 = 0.5$, Inner Wall Thickness = 0.1, Outer Wall Thickness = 0.2, KR = 10
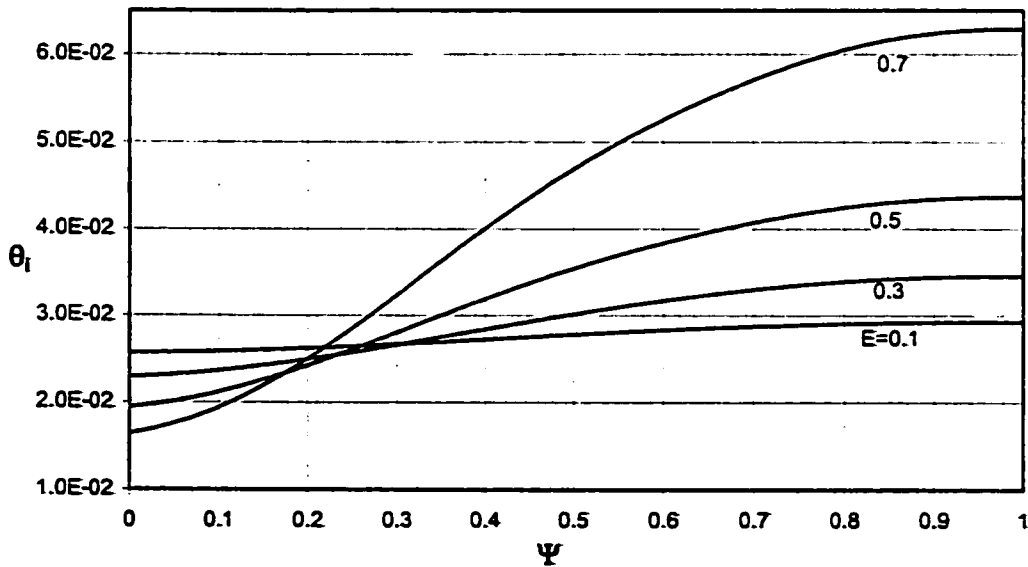
Fig.7.31. Circumferential Variation of Temperature on inner Interface at a Channel Height of 1.99x10^{-3} for Different Values of Wall Thickness (Case 1.O)

$NR_2 = 0.5$, Inner Wall Thickness = 0.1, Outer Wall Thickness = 0.2, KR = 10
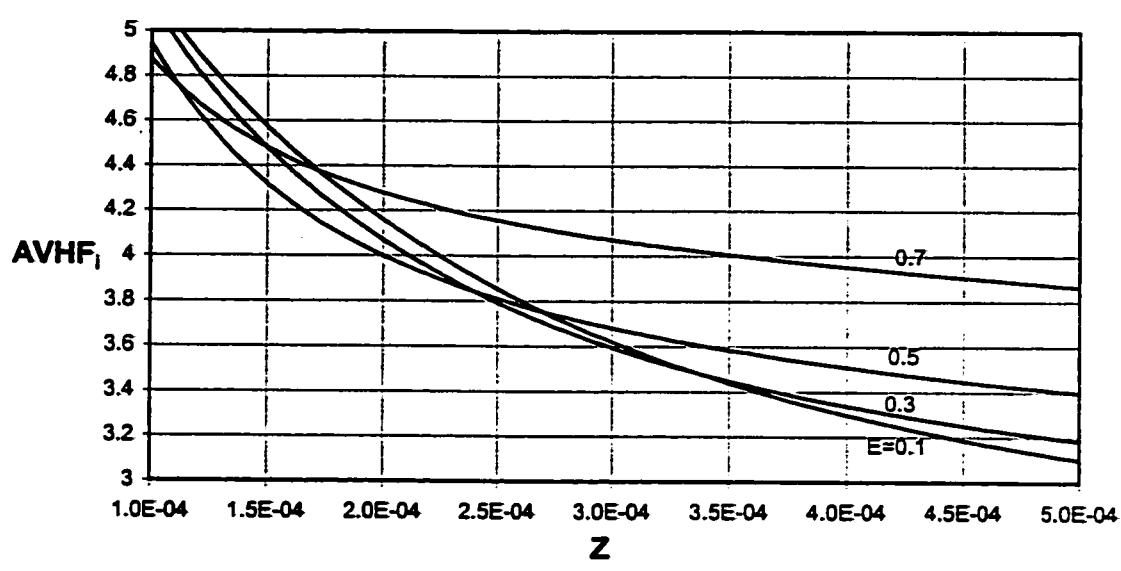
Fig.7.32. Axial Variation of Heat Flux at Inner Interface for Different Values of Eccentricity (Case 1.I)

$NR_2 = 0.5$, Inner Wall Thickness = 0.1, Outer Wall Thickness = 0.2, KR = 10
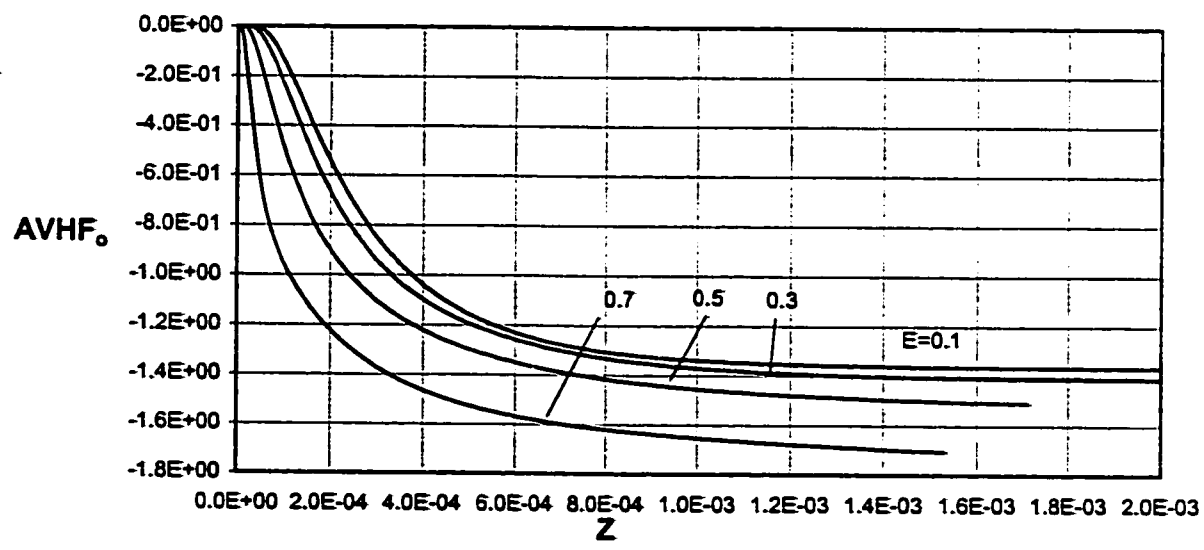
Fig.7.33. Axial Variation of Heat Flux at Outer Interface for Different Values of Eccentricity (Case 1.I)

$NR_2 = 0.5$, Inner Wall Thickness = 0.1, Outer Wall Thickness = 0.2, KR = 10
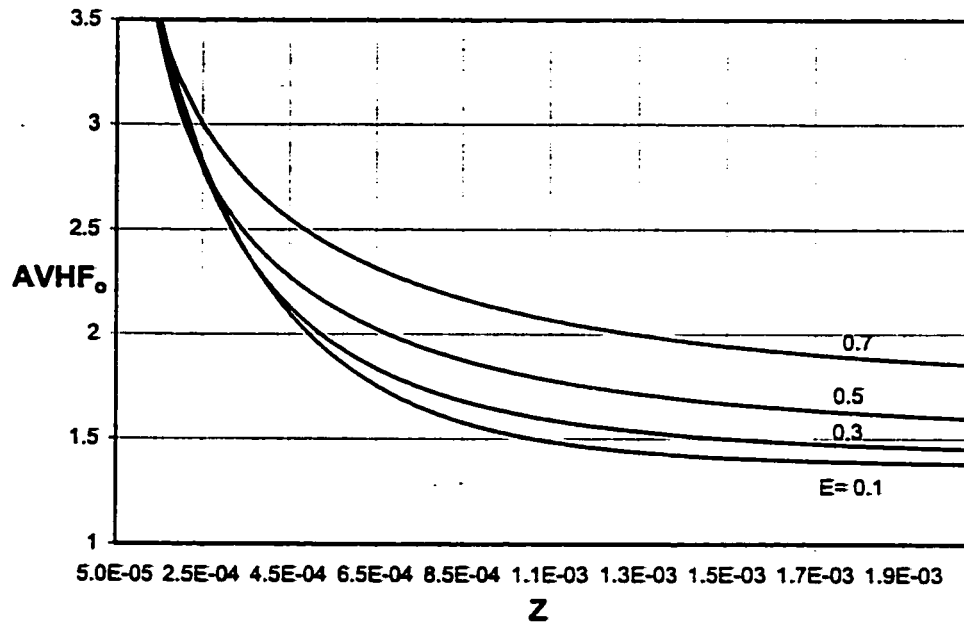
Fig.7.34. Axial Variation of Average Heat Flux at Outer Interface for Different Values of Eccentricities (Case 1.O)

$NR_2 = 0.5$, Inner Wall Thickness = 0.1, Outer Wall Thickness = 0.2, KR = 10
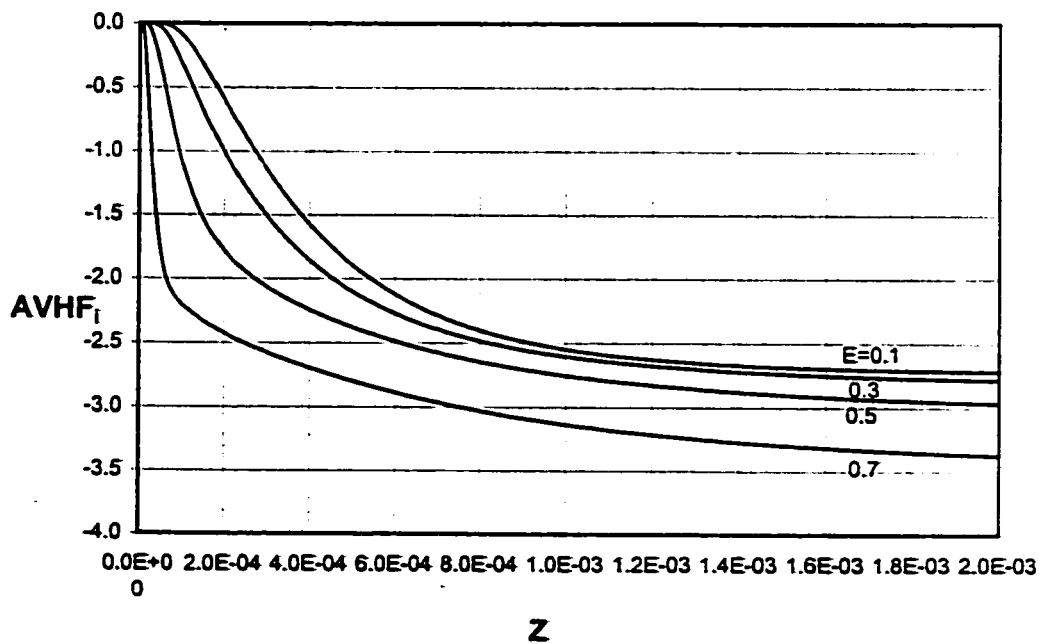
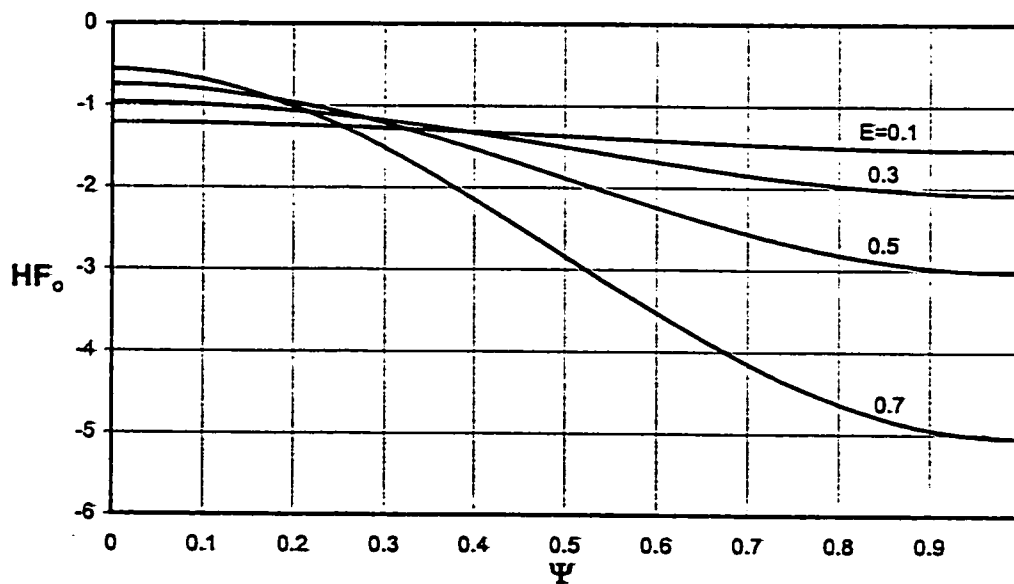**Fig.7.35.** Axial Variation of Average Heat Flux at Inner Interface for Different Values of Eccentricities (Case I.O)

$NR_2 = 0.5$, Inner Wall Thickness = 0.1, Outer Wall Thickness = 0.2, KR = 10
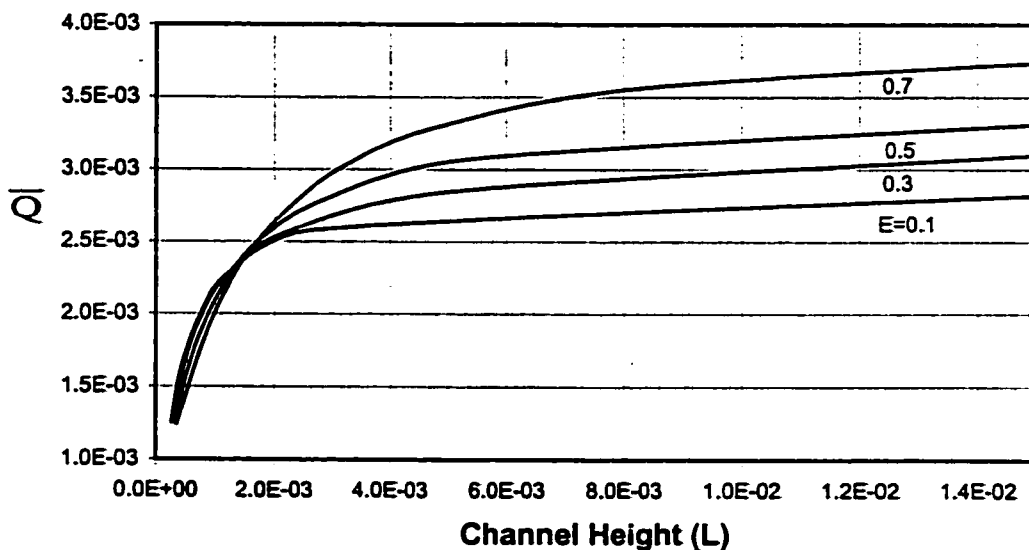
Fig.7.36. Total Heat Absorption versus Channel Height for Different Values of Eccentricity (Cas 1.I)

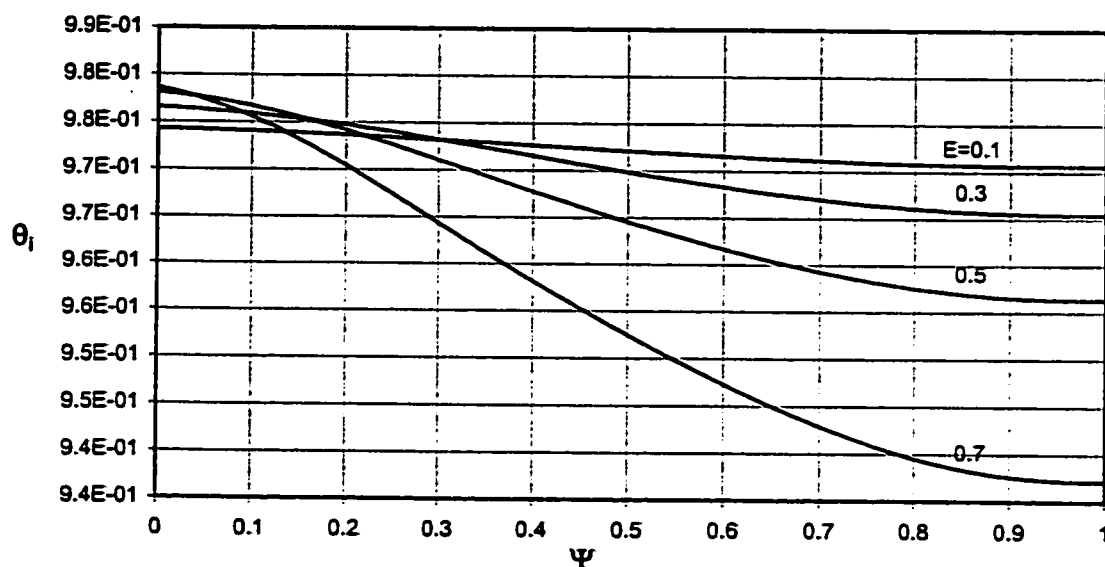$NR_2 = 0.5$, Inner Wall Thickness = 0.1, Outer Wall Thickness = 0.2, KR = 10
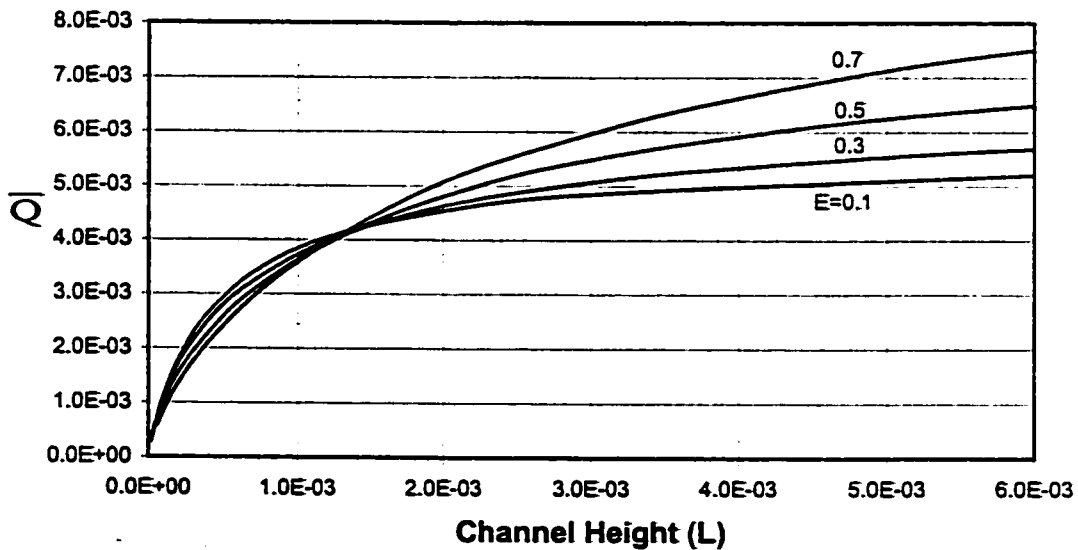
Fig.7.37. Total Heat Absorption versus Channel Height for Different Values of Eccentricity (Cas 1.O)

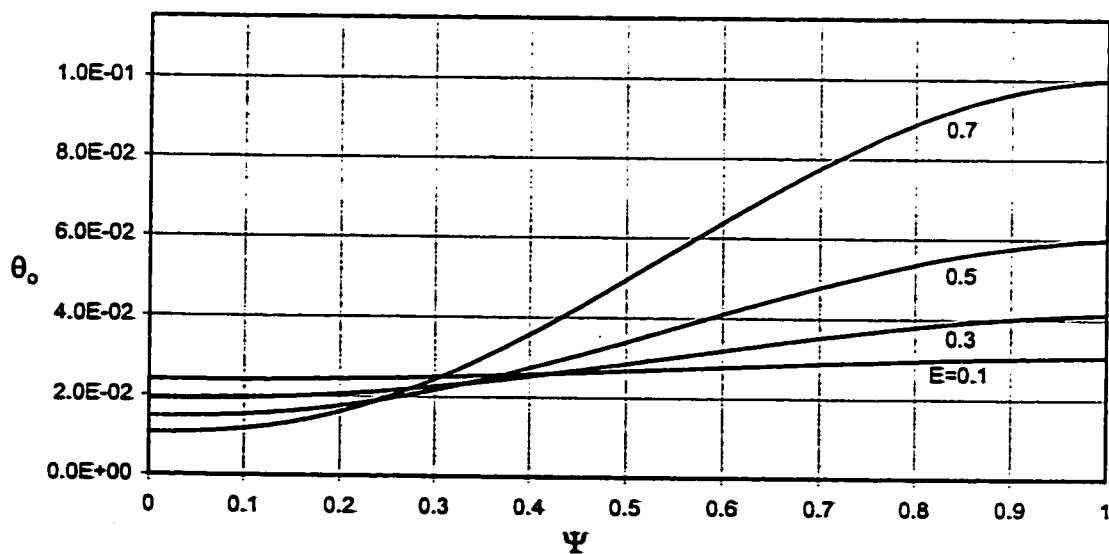$NR_2 = 0.5$, Inner Wall Thickness = 0.1, Outer Wall Thickness = 0.2, KR = 10

amount of heat gained by the fluid is less at high eccentricity. This trend reverses for high channels. This is also true for case (1.O) as shown in Fig. (7.37). The reason is that for high channels (Large values of L), when eccentricity increases, the fluid flow at the widest gap develops with higher values of velocity as compared to the narrowest gap, because the widest gap offers less resistance to fluid flow. This increases the coefficient of heat transfer at the widest gap and enhances the ability of fluid to absorb more heat, thus causing more flow rate to be induced in the channel. The opposite happens for short channels as the flow doesn't find enough channel height to develop sufficient buoyancy effect to gain more velocity in the widest gap ($\psi = 0$) as eccentricity increases; this results in a decrease in the heat absorbed by the fluid and directly affects the induced flow rate.

7.2.3. Effect of Radius Ratio (NR₂)

This analysis is carried out using geometry of, inner and outer walls thickness of 0.1 and 0.2 respectively, eccentricity 0.5 and conductivity ratio 10.

7.2.3.1. Induced Flow Rate (F)

Figures (7.38) and (7.39) show the effect of the annulus radius ratio (NR₂) on the dimensionless flow rate for case (1.I). For given eccentricity, wall thicknesses and conductivity ratio, increasing the annulus radius ratio increases the dimensionless flow rate. This is also true for case (1.O) as can be seen in Fig. (7.40). This increase in the
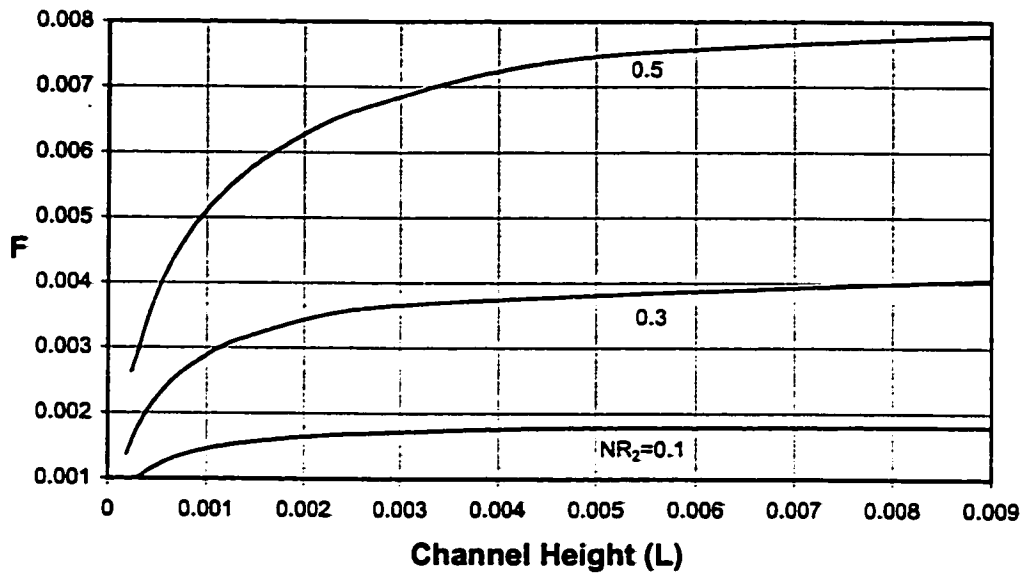
Fig.7.38. Variation of Flow Rate with Channel Height for Different Values of Radius Ratio (Case 1.I)

KR = 10, Inner Wall Thickness = 0.1, Outer Wall Thickness = 0.2, E = 0.5
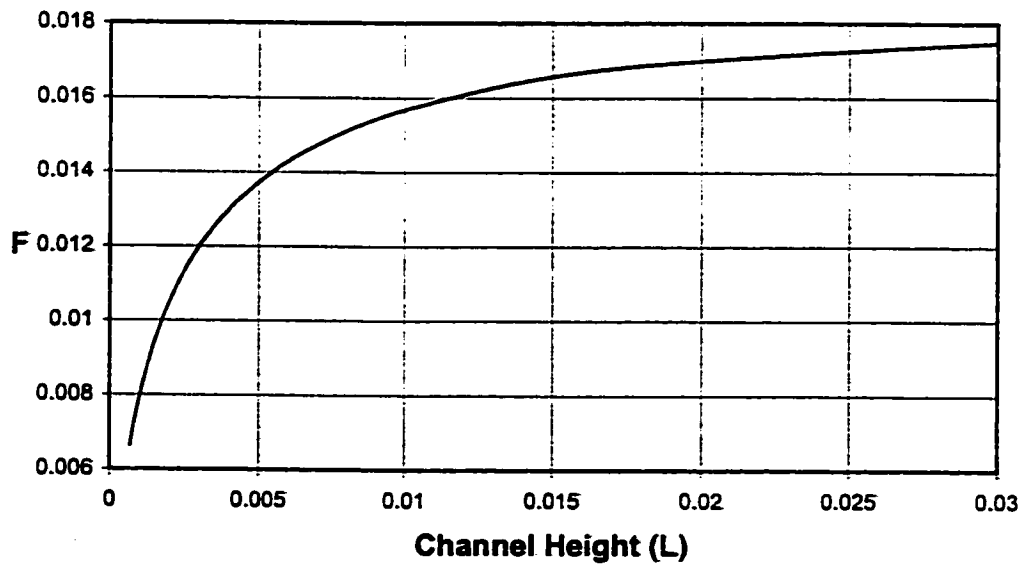
Fig.7.39. Variation of Flow Rate with Channel Height for Radius Ratio = 0.7 (Case 1.I)

KR = 10, Inner Wall Thickness = 0.1, Outer Wall Thickness = 0.2, E = 0.5

dimensionless flow rate becomes helpful in the cooling of channels having the same conductivity ratio and walls thickness for both cases (1.I and 1.O).

Figures (7.41) and (7.42) are obtained by plotting the values of dimensionless flow rate at a channel height (L) of 0.002 and fully developed (maximum) values of the same parameter against the corresponding annulus radius ratios (NR_2), respectively or case (1.I). Both figures, obtained from Figs. (7.38) and (7.39), show increasing trend of the dimensionless flow rate with increasing radius ratio. Similarly, Figs. (7.43) and (7.44) are obtained by taking the dimensionless flow rate at a channel height (L) of 0.002 and the fully developed values of the same parameter against the corresponding radius ratios respectively for case (1.O) and shows the same increasing trend with radius ratio as for case (1.I).

As fluid annulus radius ratio (NR_2) is the ratio of the outer radius of the inner cylinder to the inner radius of the outer cylinder ($\frac{r_{oi}}{r_{io}}$), therefore an increase in the radius ratio might mean the annulus cross sectional area has decreased. Physical understanding says that smaller annulus area should have small flow rate. This is checked for case (1.I) by converting the dimensionless flow rate into its dimensional form ($f = \pi \gamma Gr(r_{io} - r_{oi})F$) and plotting it against the radius ratio in Fig. (7.45). Still the flow behavior is not explained. Increasing the radii, i.e. r_{oi} and r_{io}, in such a way that the radius ratio remains the same, increases the annulus cross sectional area and hence the dimensional flow rate, which does not explain the trend shown in Fig. (7.45). Therefore, the dimensional flow rate per unit area is determined and plotted against the corresponding radius ratios as shown in Fig. (7.46). Now this explains the behavior that
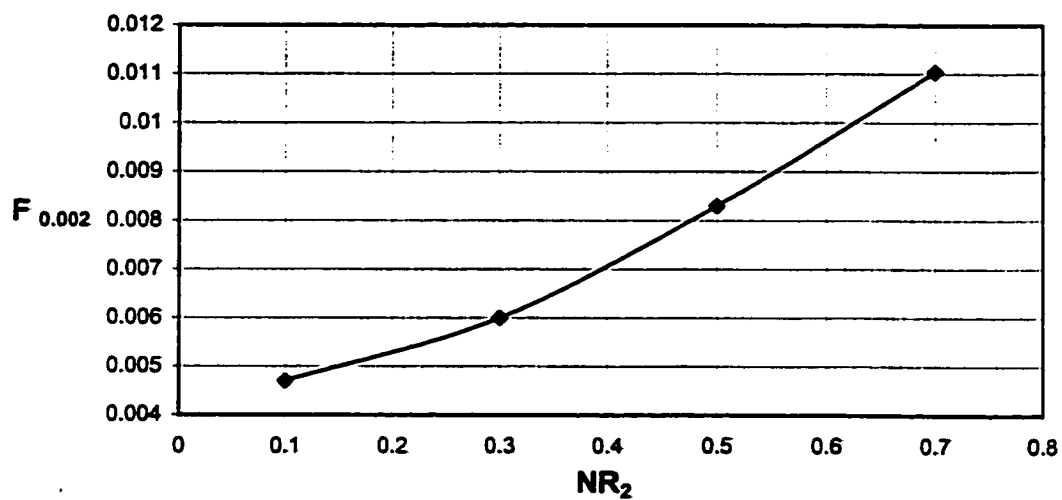
Fig.7.43. Flow Rate Variation with Radius Ratio at a
Channel Height of 0.002 (Case 1.O)

KR = 10, Inner Wall Thickness = 0.1, Outer Wall Thickness = 0.2, E = 0.5

Fig.7.44. Maximum Flow Rate Variation with Radius
Ratio (Case 1.O)

KR = 10, Inner Wall Thickness = 0.1, Outer Wall Thickness = 0.2, E = 0.5
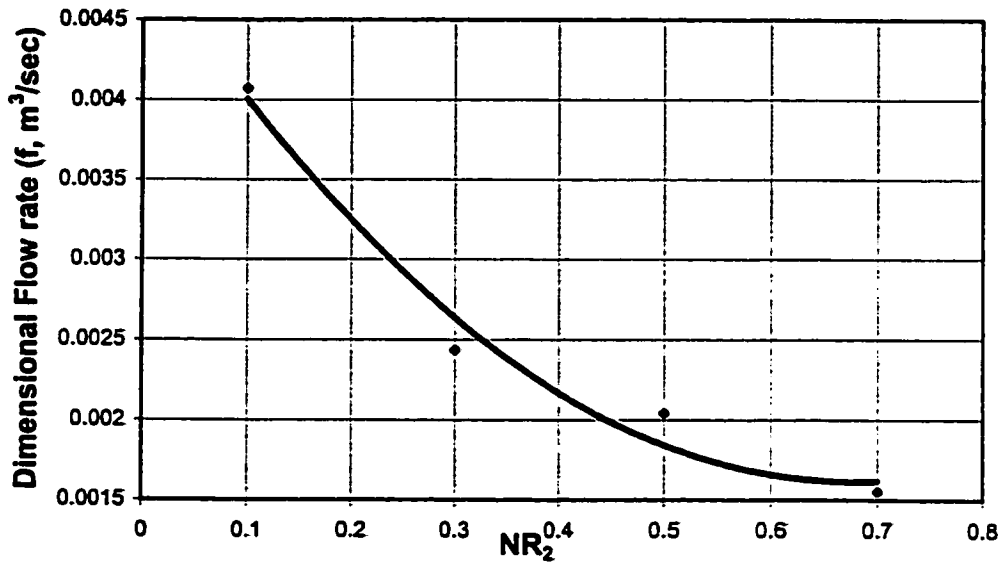
Fig.7.45. Dimensional Flow Rate Variation with Radius Ratio
(NR$_2$) (Case 1.I)

KR = 10, Inner Wall Thickness = 0.1, Outer Wall Thickness = 0.2, E = 0.5
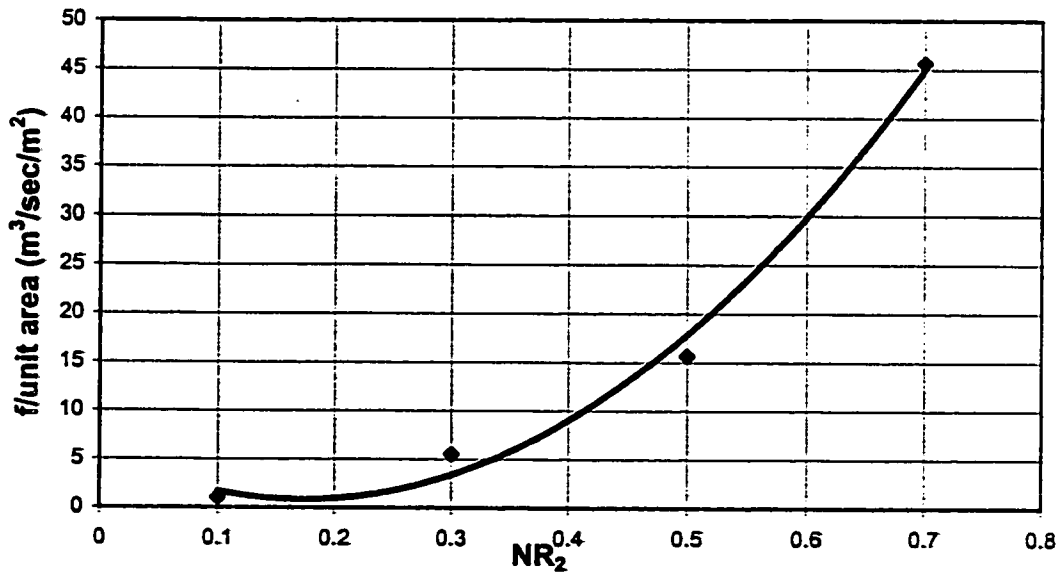
Fig.7.46. Dimensional Flow Rate per unit Area varying with
Radius Ratio (NR$_2$) (Case 1.I)

KR = 10, Inner Wall Thickness = 0.1, Outer Wall Thickness = 0.2, E = 0.5

whatever the radii may be, the flow rate per unit area increases when the annulus radius ratio is increased. Figures (7.47) and (7.48) show the dimensional flow rate behavior in the fluid annulus for case (1.O) and can be explained in a similar way as for case (1.I).

7.2.3.2. Total Heat Absorbed ($\overline{Q}$)

Increasing the radius ratio (NR_2) has a direct impact on the total heat absorbed by the fluid as can be seen in Figs. (7.49) and (7.50) for case (1.I). The same behavior is observed for case (1.O) as shown in Fig. (7.51). This is attributed to the decreased distance in the annulus for heat to flow and increased fluid flow rate per unit area enabling more heat to be absorbed by it.

7.2.4. Effect of Wall Thickness

This analysis is carried out using conductivity ratio 2, annulus radius ratio 0.5 and eccentricity 0.5.

7.2.4.1. Induced Flow Rate (F)

Figure (7.52) shows the variation of flow rate with channel height at selected values of walls thickness for case (1.I). Two different trends of flow rate variation with increasing walls thickness are observed. For short channels, the flow rate is more for thin walls whereas this behavior reverses for high channels. Thick walls have the same opposing effect as that for walls with small conductivity ratio. i.e. inner wall resisting the heat to flow into the fluid while outer wall preventing the heat to flow out of the fluid. For

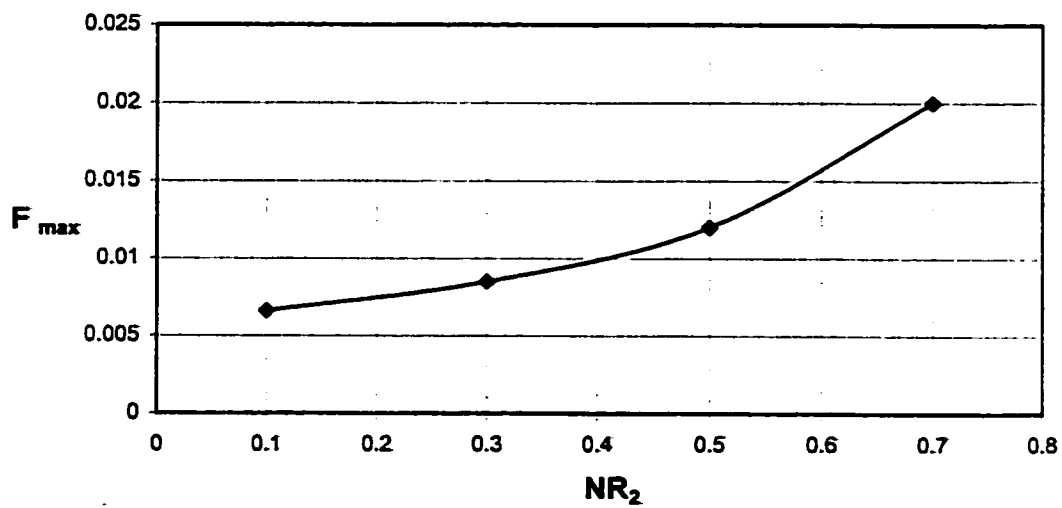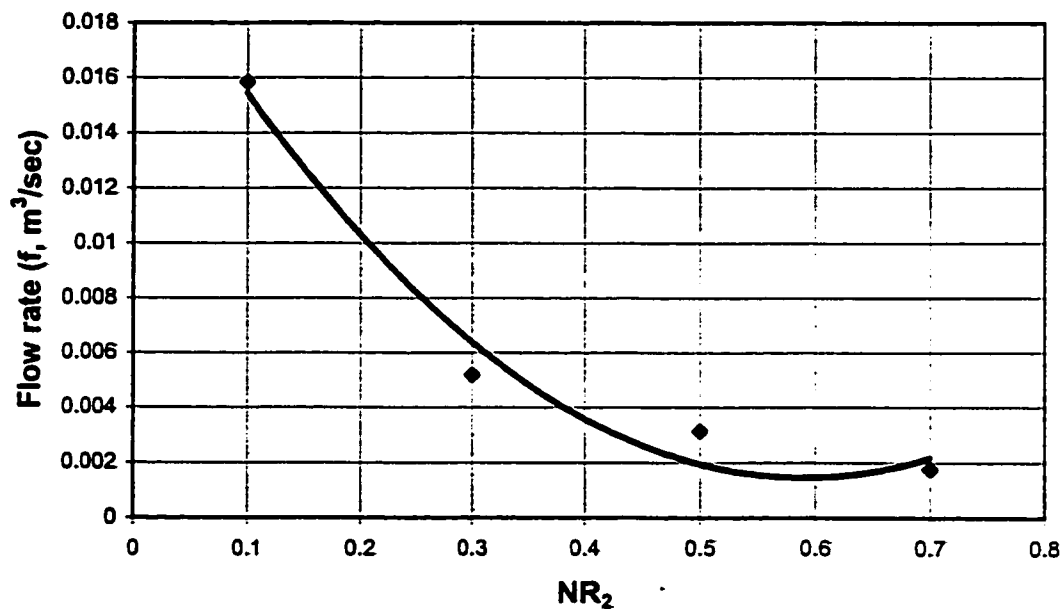**Fig.7.47.** Dimensional Flow Rate Variation with Radius Ratio
(NR$_2$) (Case 1.O)

KR = 10, Inner Wall Thickness = 0.1, Outer Wall Thickness = 0.2, E = 0.5
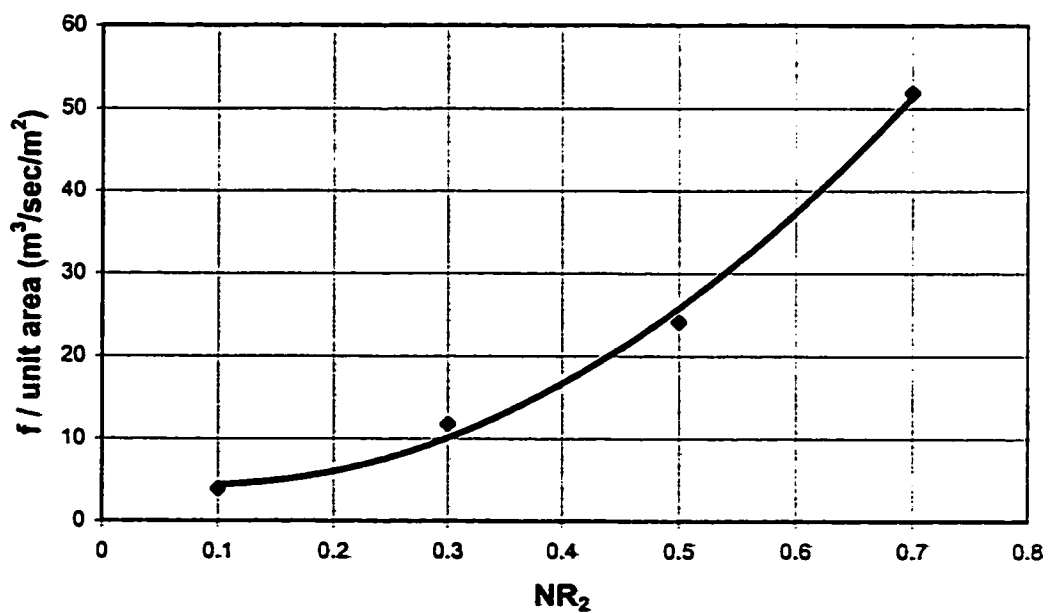
Fig.7.48. Dimensional Flow Rate per unit Area varying with
Radius Ratio (NR$_2$) (Case 1.O)

KR = 10, Inner Wall Thickness = 0.1, Outer Wall Thickness = 0.2, E = 0.5
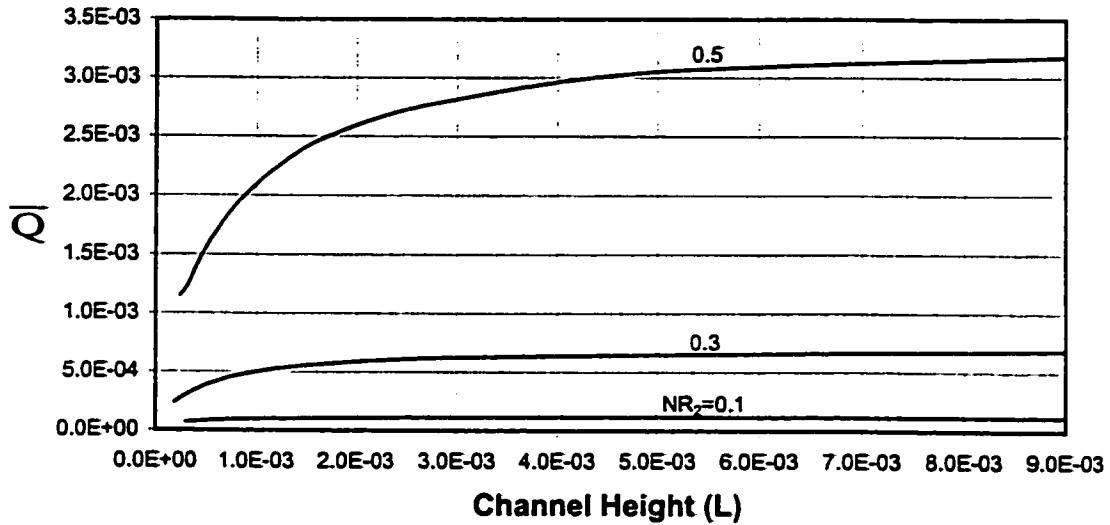
Fig.7.49. Total Heat Absorption versus Channel Height for Different Values of Radius ratio (Case 1.I)

KR = 10, Inner Wall Thickness = 0.1, Outer Wall Thickness = 0.2, E = 0.5
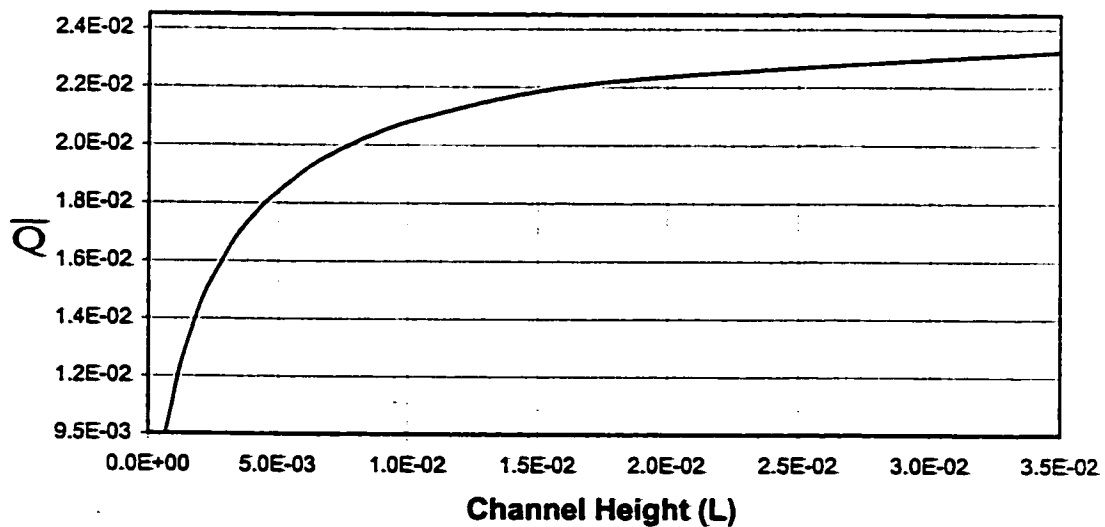
Fig.7.50. Total Heat Absorption versus Channel Height for Radius ratio 0.7 (Case 1.I)

KR = 10, Inner Wall Thickness = 0.1, Outer Wall Thickness = 0.2, E = 0.5
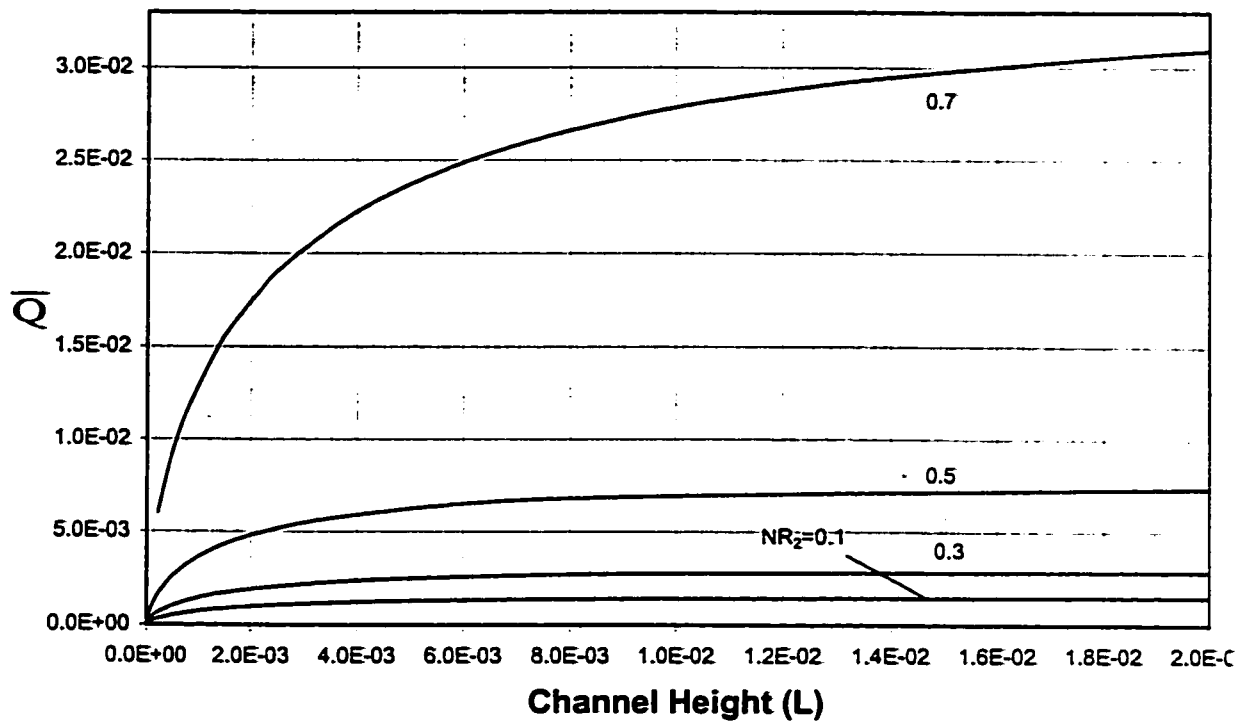
Fig.7.51. Total Heat Absorption Vs Channel Height for Different
Values of Radius Ratio (Case 1.O)

KR = 10, Inner Wall Thickness = 0.1, Outer Wall Thickness = 0.2, E = 0.5
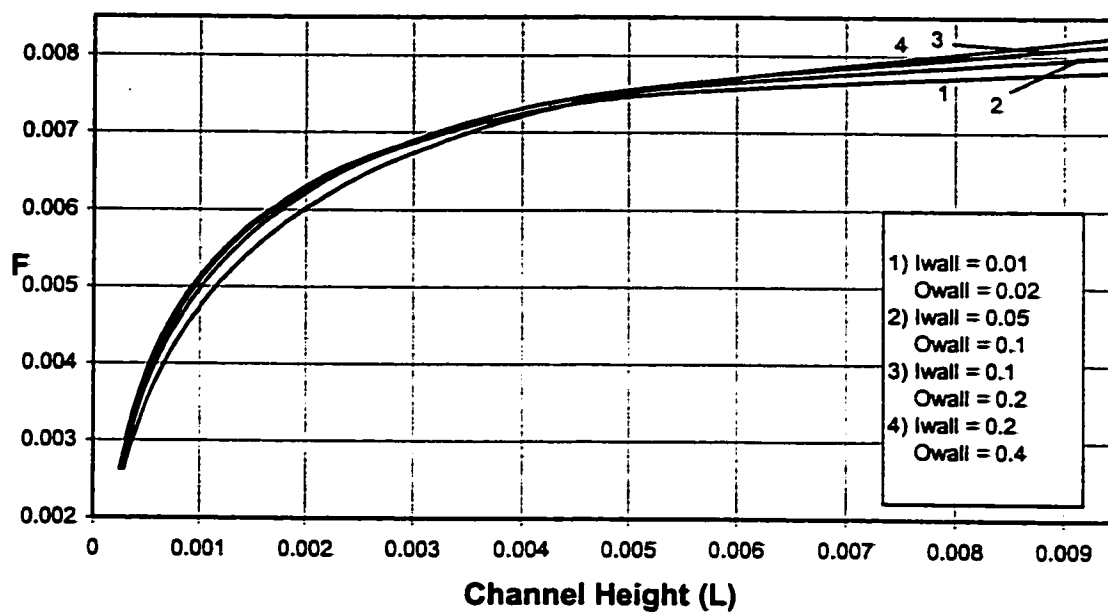
Fig.7.52 .Variation of Flow Rate with Channel Height for Different
Values of Wall Thickness (Case 1.I)
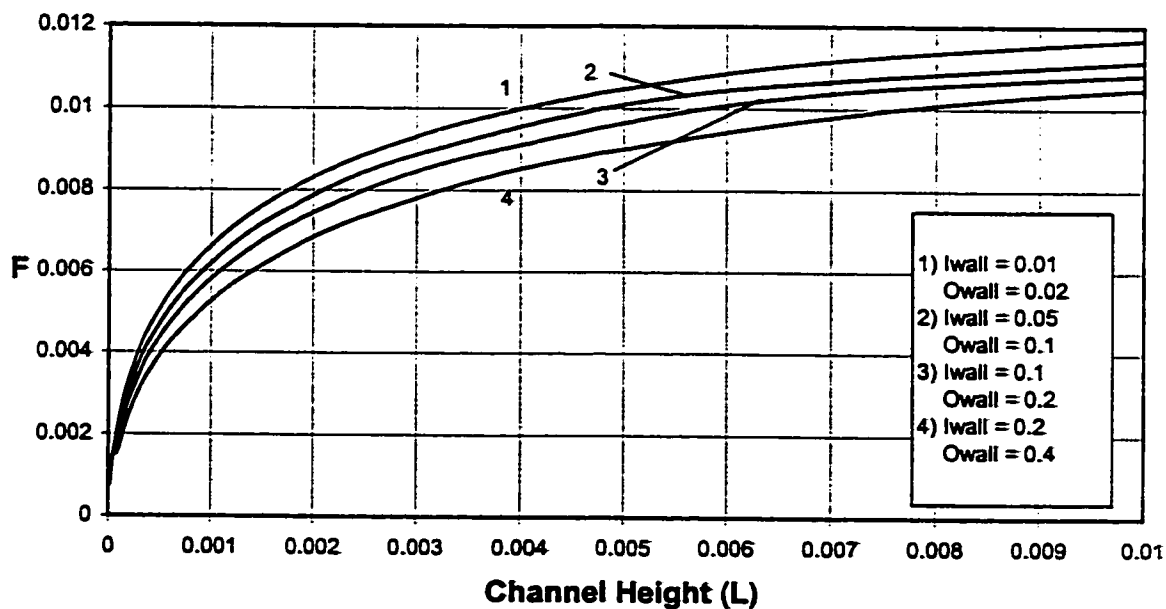
$NR_2 = 0.5$, $KR = 2$, $E = 0.5$

Fig.7.53 .Variation of Flow Rate with Channel Height for Different
Values of Wall Thickness (Case 1.O)
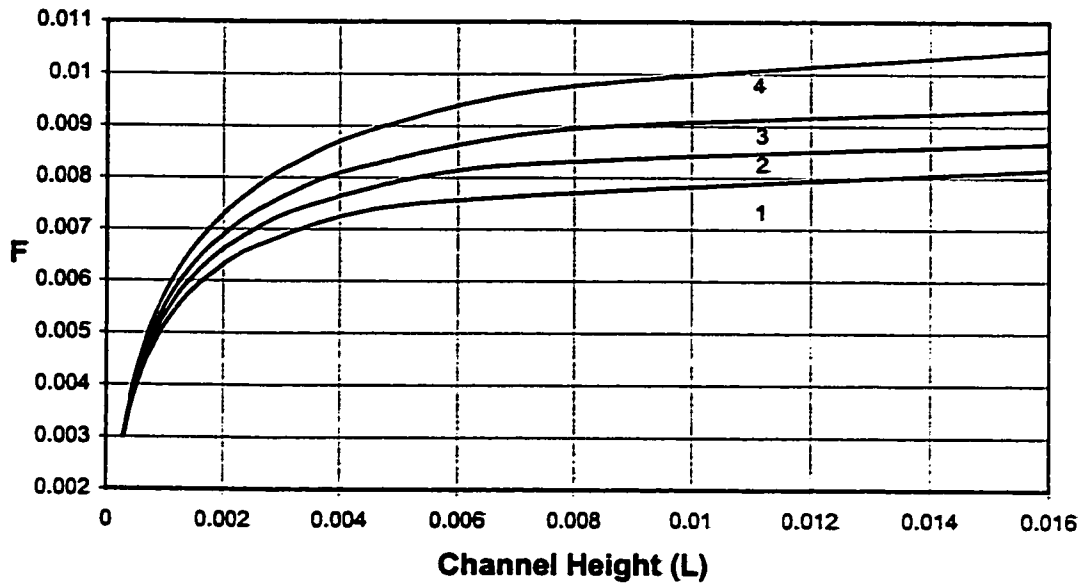
$NR_2 = 0.5$, $KR = 2$, $E = 0.5$

Fig.7.54. Variation of Flow Rate with Channel Height for Different Values of Outer Wall Thickness (Case 1.I)

Inner Wall Thickness = 0.01, Outer Wall Thickness = (1) 0.02, (2) 0.1, (3) 0.2, (4) 0.4, NR_2 = 0.5, KR = 2, E = 0.5
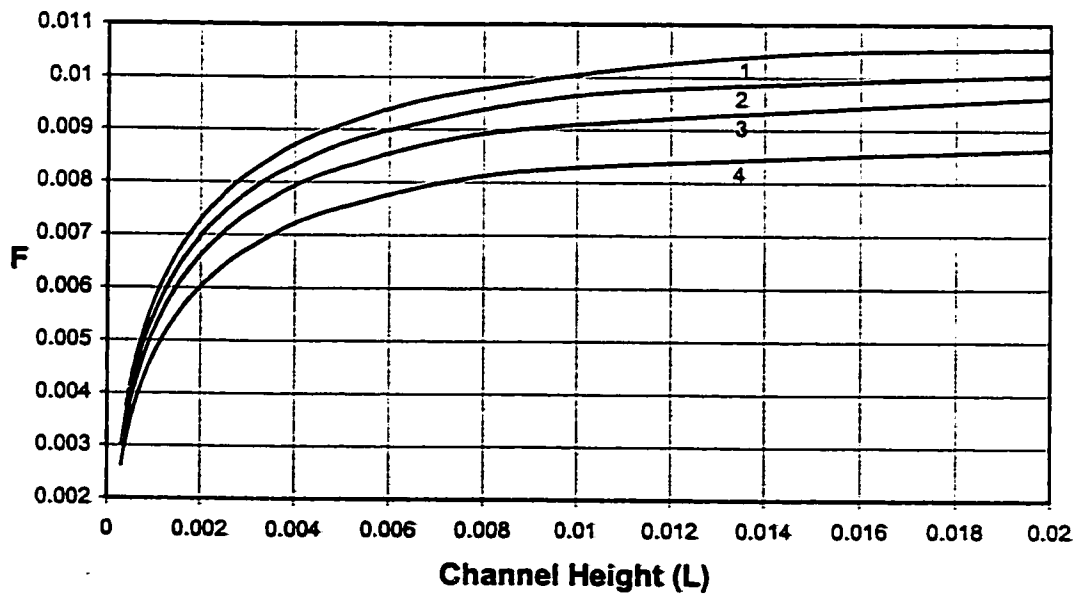
Fig.7.55. Variation of Flow Rate with Channel Height for Different Values of Inner Wall Thickness (Case 1.I)

Outer Wall Thickness = 0.4, Inner Wall Thickness = (1) 0.01, (2) 0.05, (3) 0.1, (4) 0.2, NR_2 = 0.5, KR = 2, E = 0.5

the channel. Secondly, another analysis has been done by keeping the outer wall thickness fixed while increasing the inner heated wall thickness. The thick inner wall resists the heat to enter the fluid annulus, causing the temperature values on the inner solid-fluid interface to decrease. This affects the amount of heat absorbed by the fluid, decreases the mean fluid temperature and consequently the induced flow rate as shown in Fig. (7.55).

Figures (7.56-7.71) explain these phenomena in detail; these figures are for a specific flow rate of 0.00825 for case (1.I) and 0.01125 for case (1.O). All the circumferential analysis is carried out at an axial (vertical) location of $1.58x10^{-2}$ for case (1.I) and $6.86x10^{-3}$ for case (1.O).

7.2.4.2. Local Heat Flux (HF)

Figures (7.56) and (7.57) show the effect of the wall thickness on the circumferential variation of the local heat flux on the inner and outer interfaces respectively for case (1.I). Both the figures (7.56) and (7.57) show a decrease in the value of the heat fluxes with increasing walls thickness. The local heat flux also decreases with the wall thickness for case (1.O) as shown in Figs. (7.58) and (7.59). The reason is that the thick walls resist the heat to flow through it hence, decreasing the local heat flux.

7.2.4.3. Circumferential Temperature (θ)

Circumferential temperature variations on the inner and outer interfaces with increasing walls thickness for case (1.I) are shown in Fig. (7.60) and (7.61) respectively. The resisting effects of the walls, as discussed earlier, decrease the temperature levels on
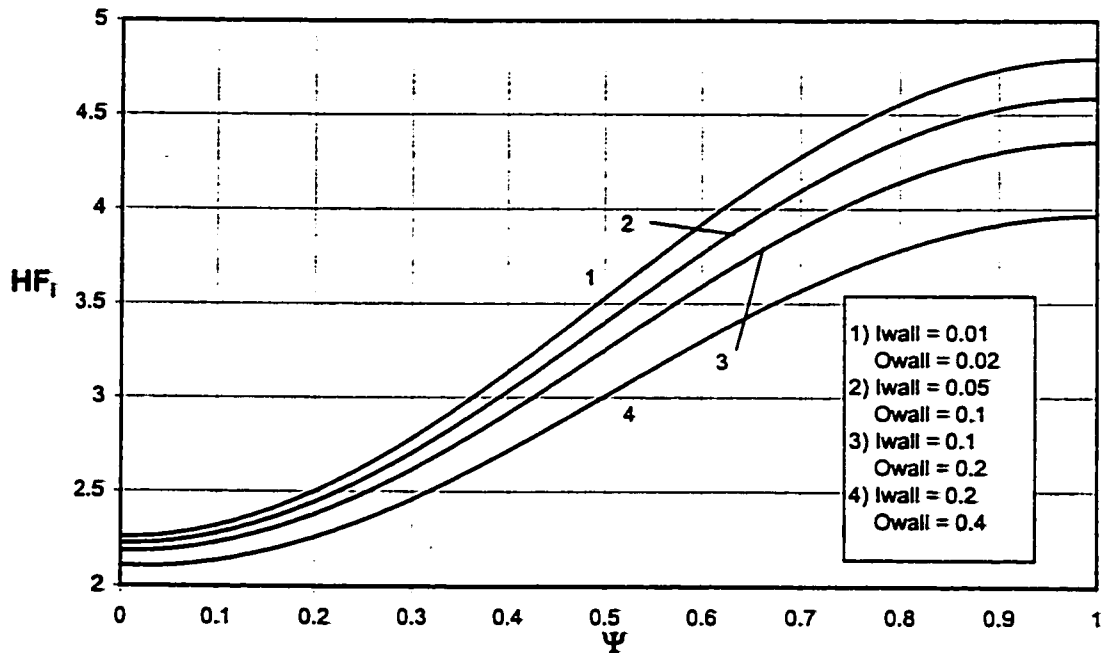
Fig.7.56. Circumferential variation of Local Heat Flux on Inner Interface at an Axial (vertical) Location of 1.59×10^{-2} for Different Values of Wall Thickness (Case 1.I)
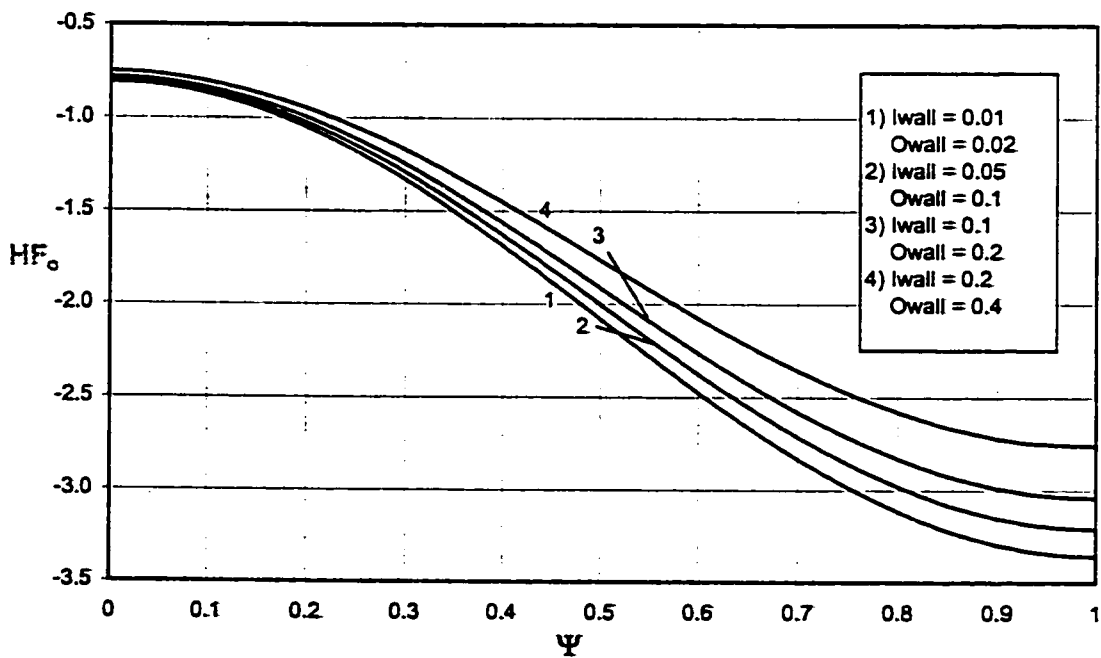
$NR_2 = 0.5$, $KR = 2$, $E = 0.5$

Fig.7.57. Circumferential variation of Local Heat Flux on Outer Interface at an Axial (vertical) Location of 1.59×10^{-2} for Different Values of Wall Thickness (Case 1.I)

$NR_2 = 0.5$, $KR = 2$, $E = 0.5$

Fig.7.58 .Circumferential Variation of Local Heat Flux on Outer Interface at an Axial (vertical) Location of 6.86x10⁻³ for Different Values of Wall Thickness (Case 1.0)

$NR_2 = 0.5$, $KR = 2$, $E = 0.5$

Fig.7.59.Circumferential Variation of Local Heat Flux on Inner Interface at an Axial (vertical) Location of 6.86x10⁻³ for Different Values of Wall Thickness (Case 1.0)

$NR_2 = 0.5$, $KR = 2$, $E = 0.5$
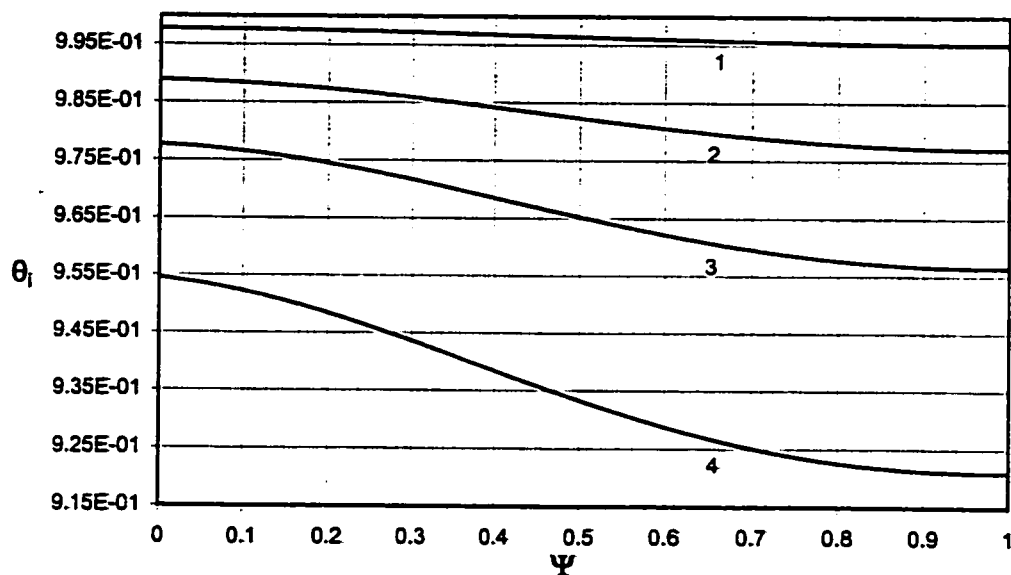
Fig.7.60. Circumferential Variation of Temperature at Inner Interface at an Axial (vertical) Location of 1.59x10^{-2} for Different Value of Wall Thickness (Case 1.I)

(1) Iwall=0.01; Owall=0.02 (2) Iwall=0.05; Owall=0.1 (3) Iwall=0.1; Owall=0.2 (4) Iwall=0.2; Owall=0.4, NR$_2$ = 0.5, KR = 2, E = 0.5
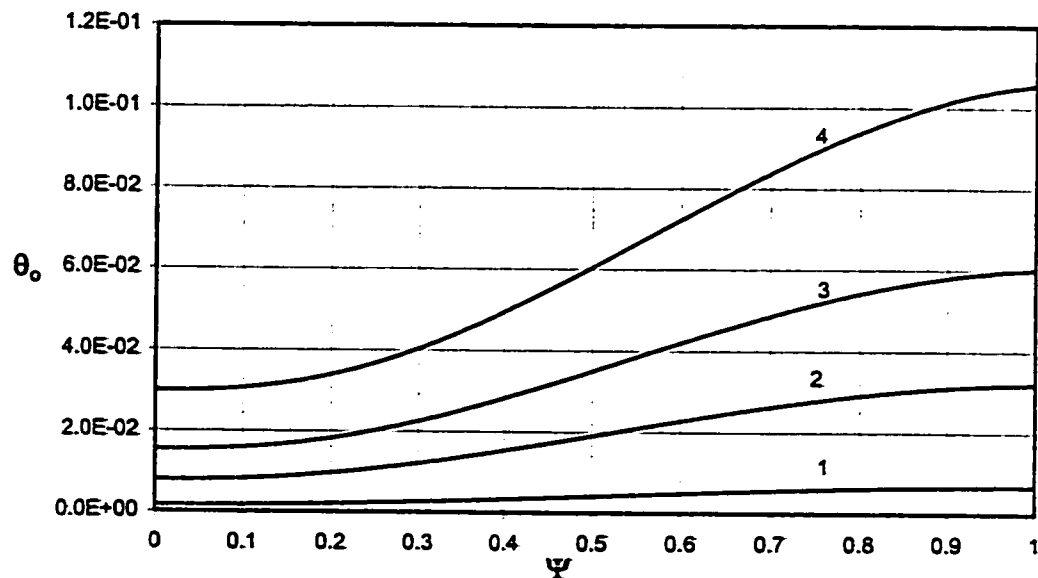
Fig.7.61. Circumferential Variation of Temperature at Outer Interface at an Axial (vertical) Location of 1.59x10^{-2} for Different Value of Wall Thickness (Case 1.I)

(1) Iwall=0.01; Owall=0.02 (2) Iwall=0.05; Owall=0.1 (3) Iwall=0.1; Owall=0.2 (4) Iwall=0.2; Owall=0.4, NR$_2$ = 0.5, KR = 2, E = 0.5

the hot inner interface whereas it increases on the cold outer interface with increasing walls thickness. The outer wall insulating influence with increasing interface temperature values for thick walls enable more flow to be induced in the channel. Figure (7.62) shows decreasing temperature values on the hot outer solid-fluid interface whereas Fig. (7.63) shows increasing temperature values on the cold inner solid-fluid interface, with increasing walls thickness for case (1.O). The temperature values on the outer and inner interfaces have an opposite effect on the flow rate as compared to case (1.I), i.e. increasing the walls thickness reduces the induced flow rate.

7.2.4.4. Temperature Profile

The temperature profiles across the channel along the line of symmetry for thin and thick walls are shown in Figs. (7.64) and (7.65) respectively. These profiles help in explaining the phenomenon. Very thin walls show almost zero temperature gradient as can be seen in Fig. (7.64) whereas the temperature gradient increases in thick walls (Fig. 7.65) leading to a decrease in temperature on the inner interface and an increase in temperature on outer interface. Hence, the heat flow out of the fluid annulus or in other words the cooling effect through the outer wall decreases when walls thickness is increased, leading to an increase in flow rate. Figures (7.66) and (7.67) show the temperature profiles across the channel along the line of symmetry for very thin and very thick walls respectively for case (1.O). The increased temperature gradients lead to reduced temperature values on the outer interface and increased temperature values on the inner interface. The outer wall effect, which is the supporting factor in reducing the flow
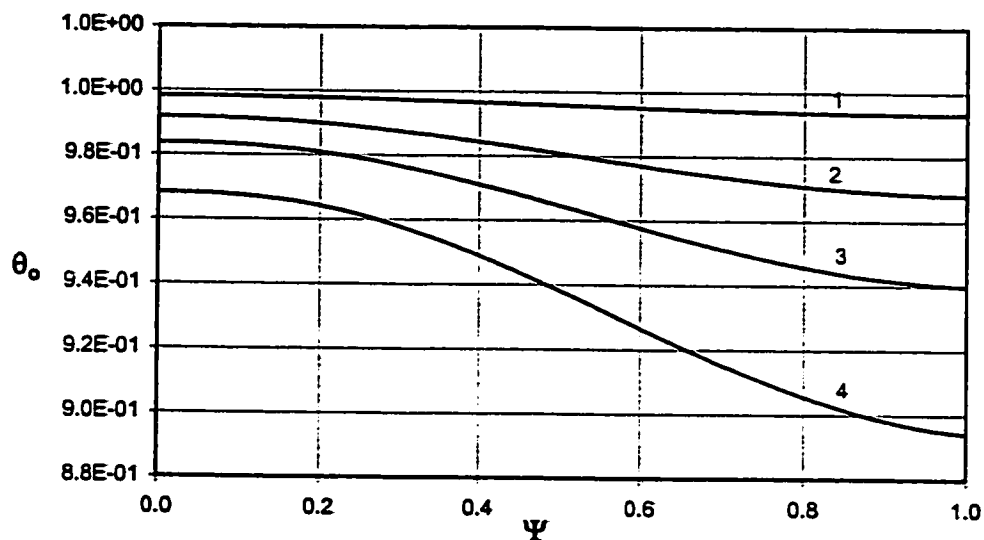
Fig.7.62 .Circumferential Variation of Temperature on Outer Interface at an Axial (vertical) Location of 6.86×10^{-3} for Different Values of Wall Thickness (Case 1.0)

(1) Iwall=0.01; Owall=0.02 (2) Iwall=0.05; Owall=0.1 (3) Iwall=0.1; Owall=0.2 (4) Iwall=0.2; Owall=0.4, $NR_2 = 0.5$, KR = 2, E = 0.5
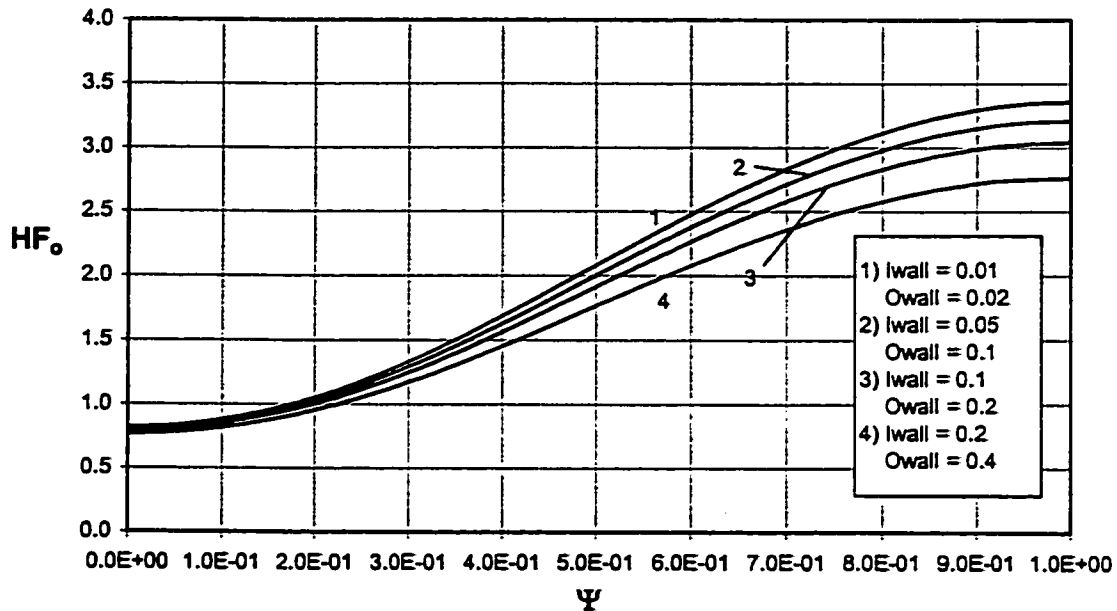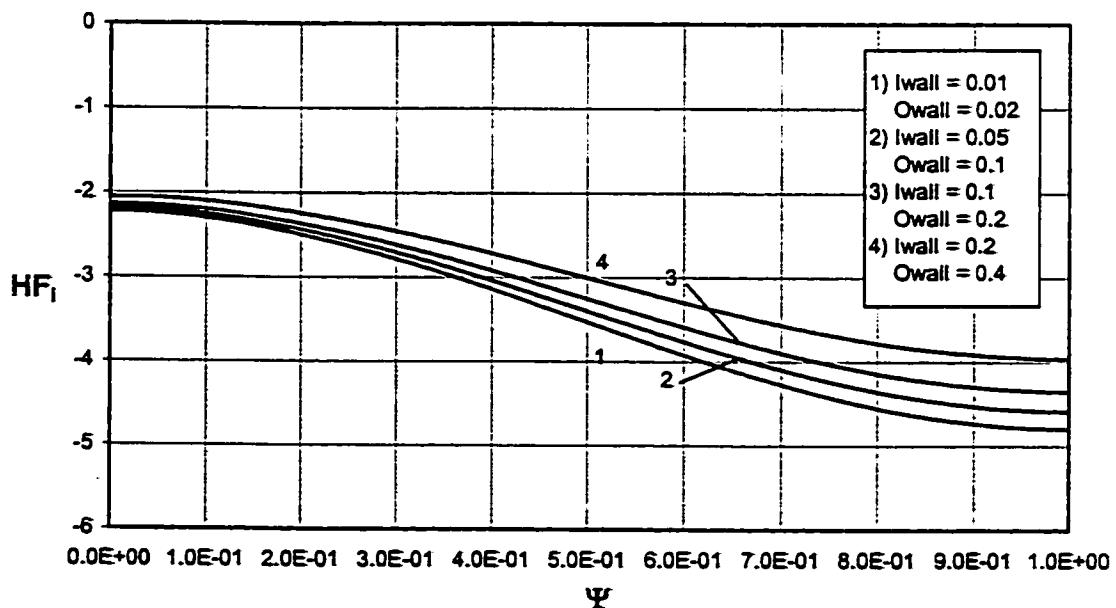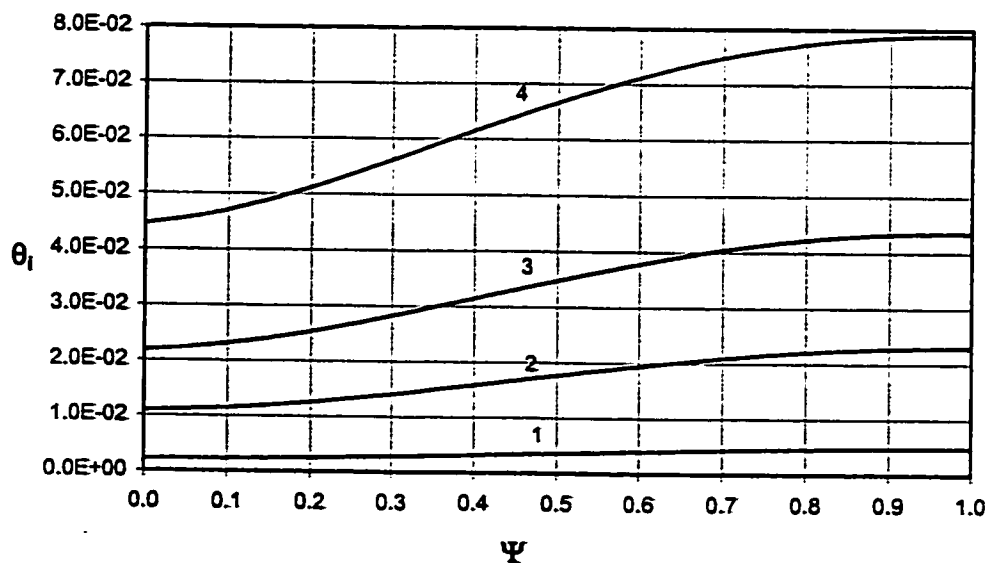

Fig.7.63 .Circumferential Variation of Temperature on Inner Interface at an Axial (vertical) Location of 6.86×10^{-3} for Different Values of Wall Thickness (Case 1.0)

(1) Iwall=0.01; Owall=0.02 (2) Iwall=0.05; Owall=0.1 (3) Iwall=0.1; Owall=0.2 (4) Iwall=0.2; Owall=0.4, $NR_2 = 0.5$, KR = 2, E = 0.5
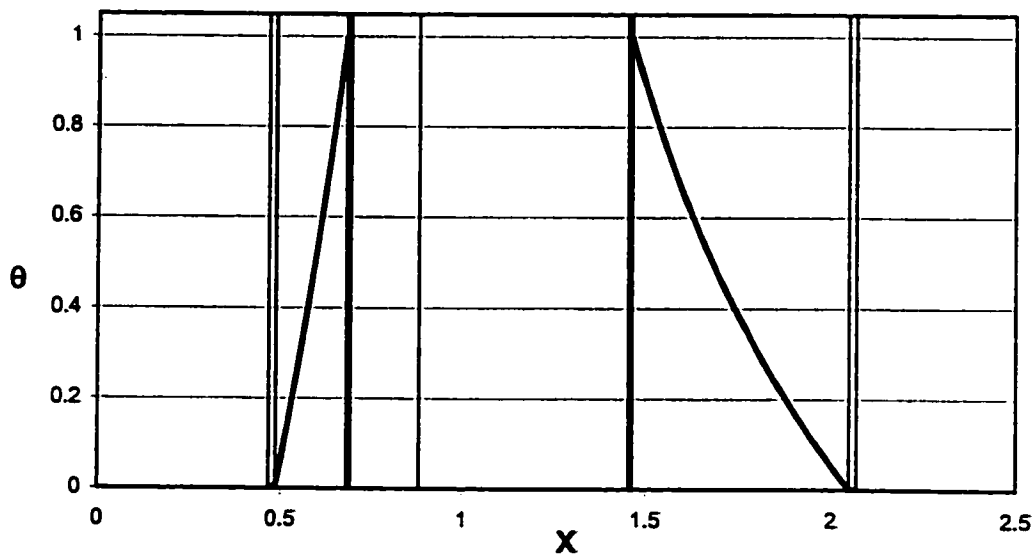
Fig. 7.64. Temperature Profile across the Channel having Inner Wall Thickness=0.01, Outer Wall Thickness=0.02 on the line of symmetry, Axial (Vertical) Location of 1.59×10^{-2} (Case 1.I)
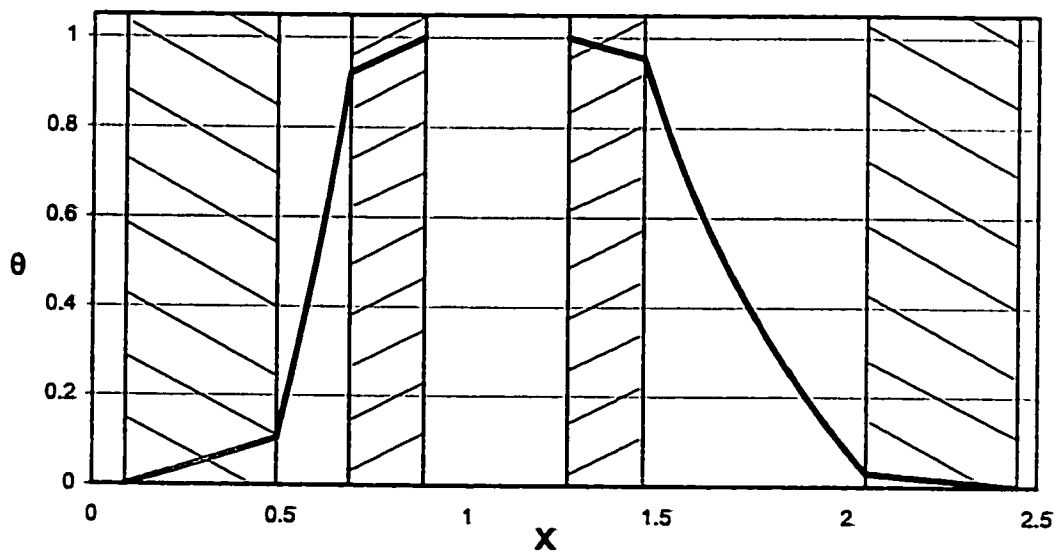
$NR_2 = 0.5$, $KR = 2$, $E = 0.5$

Fig. 7.65. Temperature Profile across the Channel having Inner Wall Thickness=0.2, Outer Wall Thickness=0.4 on the line of symmetry, Axial (Vertical) Location of 1.59×10^{-2} (Case 1.I)
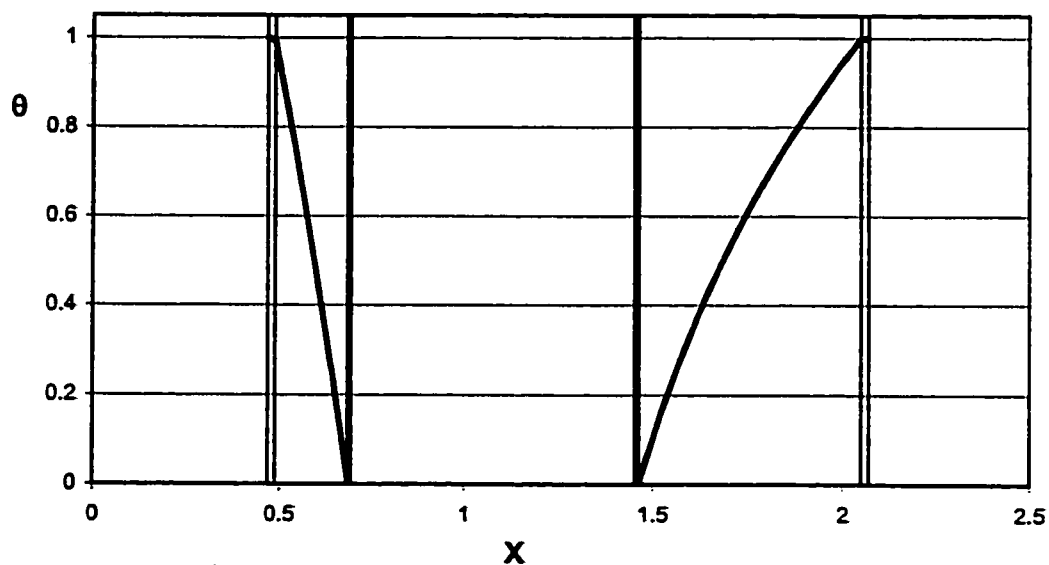
$NR_2 = 0.5$, $KR = 2$, $E = 0.5$

Fig. 7.66. Temperature Profile across the Channel having Inner Wall Thickness=0.01, Outer Wall Thickness=0.02 on the line of symmetry, Axial (vertical) Location of 6.86×10^{-3} (Case 1.0)
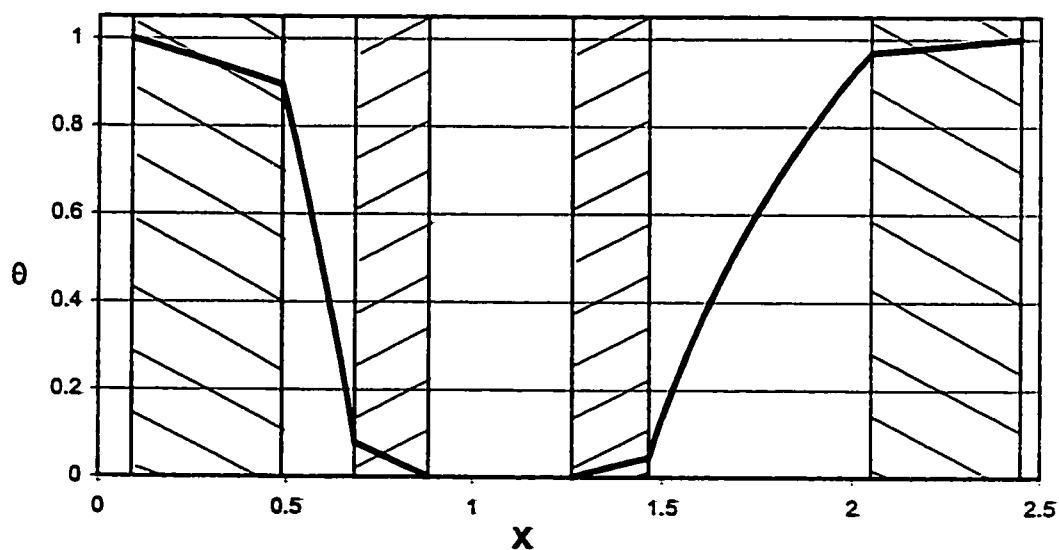
$NR_2 = 0.5$, $KR = 2$, $E = 0.5$

Fig. 7.67. Temperature Profile across the Channel having Inner Wall Thickness=0.01, Outer Wall Thickness=0.02 on the line of symmetry, Axial (vertical) Location of 6.86×10^{-3} (Case 1.0)
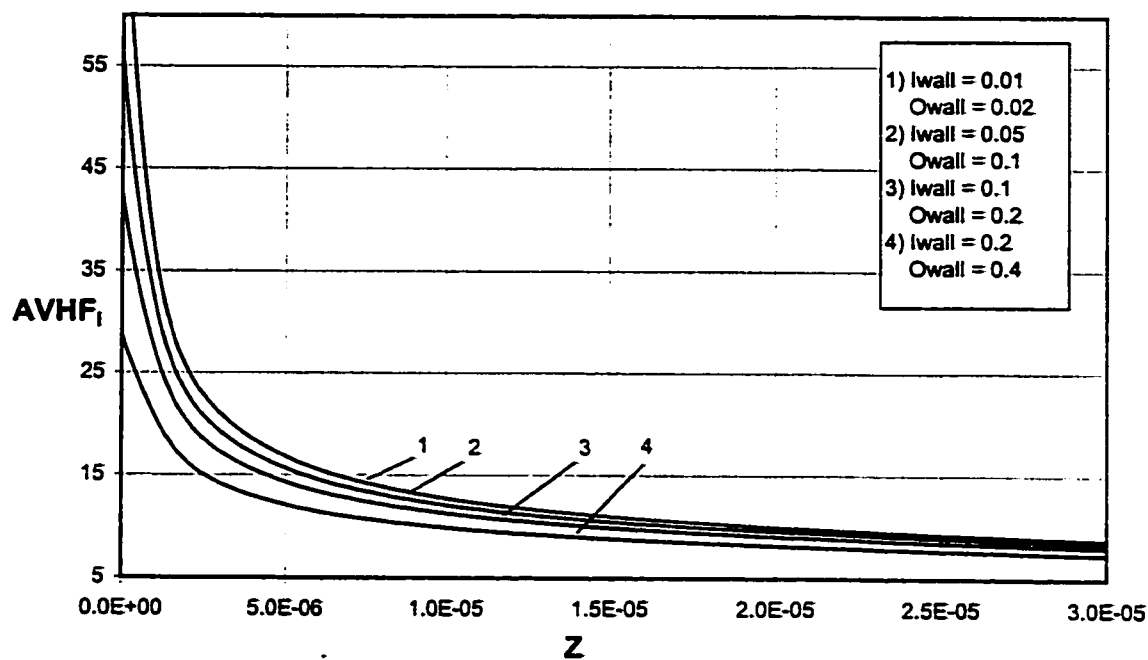
$NR_2 = 0.5$, $KR = 2$, $E = 0.5$

Fig.7.68. Axial Variation of Average Heat Flux at the Inner Interface for Different Value of Wall thickness (Case 1.I)
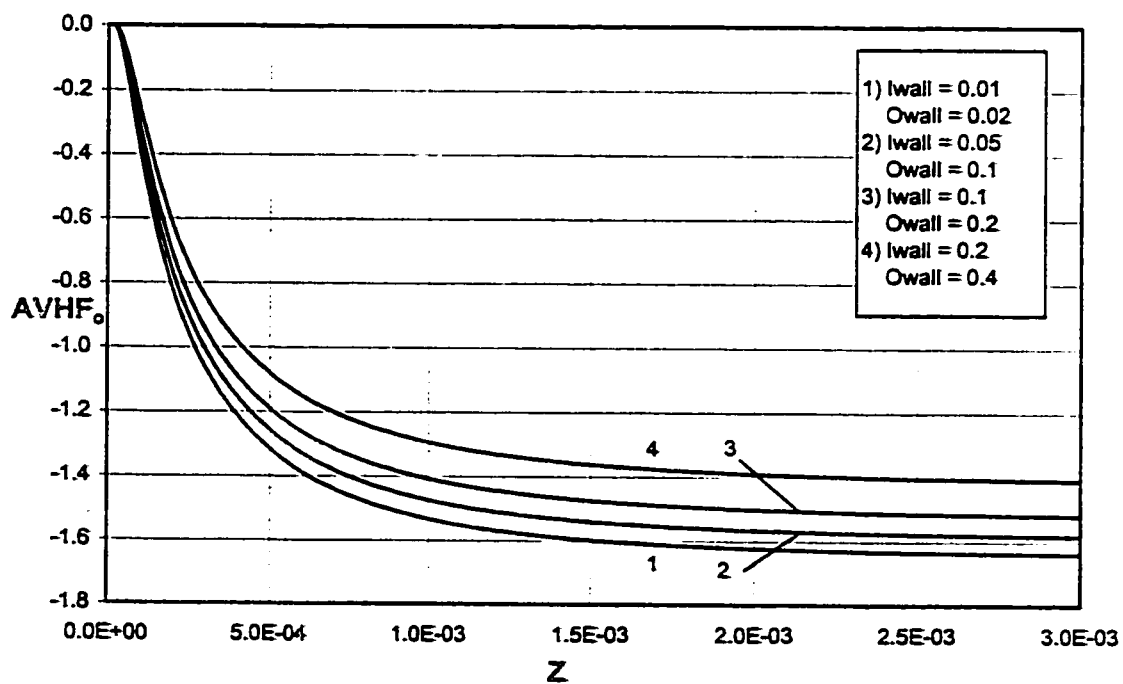
$NR_2 = 0.5$, $KR = 2$, $E = 0.5$

Fig.7.69. Axial Variation of Average Heat Flux at the Outer Interface for Different Value of Wall thickness (Case 1.I)
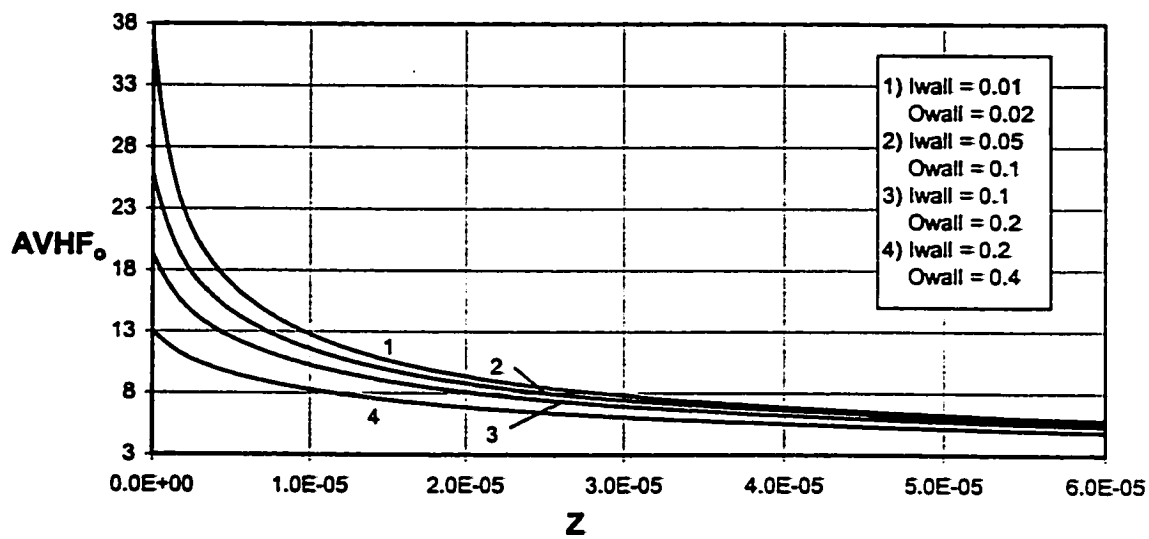
$NR_2 = 0.5$, $KR = 2$, $E = 0.5$

Fig.7.70. Axial Variation of Average Heat Flux at the Outer Interface for Different values of Wall Thickness (Case 1.O)
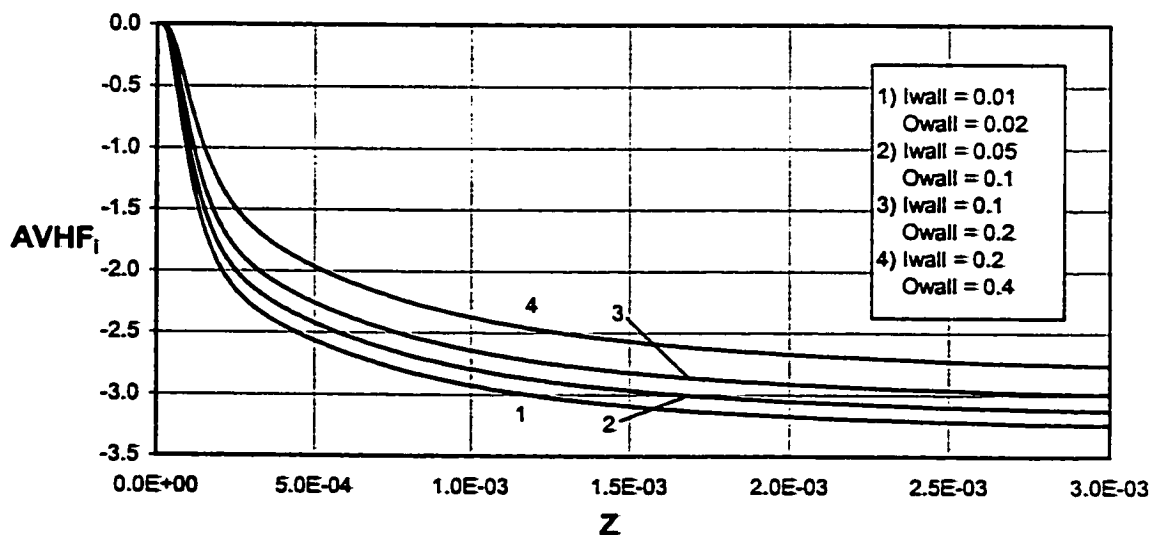
$NR_2 = 0.5$, $KR = 2$, $E = 0.5$

Fig.7.71. Axial Variation of Average Heat Flux at the Inner Interface for Different values of Wall Thickness (Case 1.O)
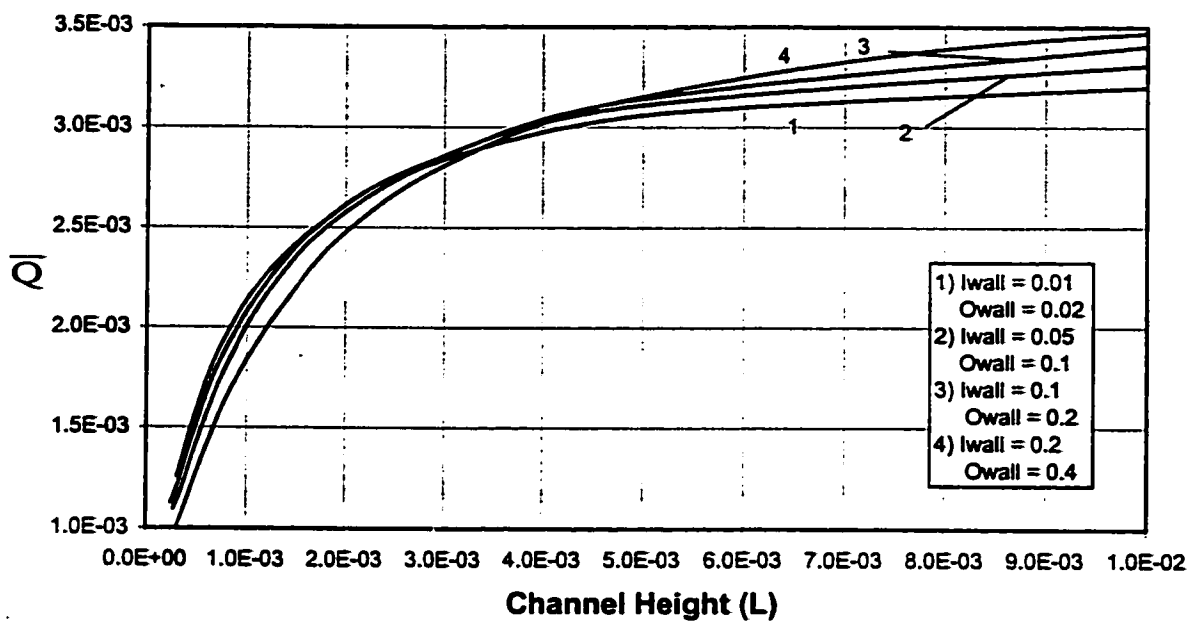
$NR_2 = 0.5$, $KR = 2$, $E = 0.5$

Fig.7.72. Total Heat Absorption versus Channel Height for Different Values of Walls Thickness (Case 1.I)
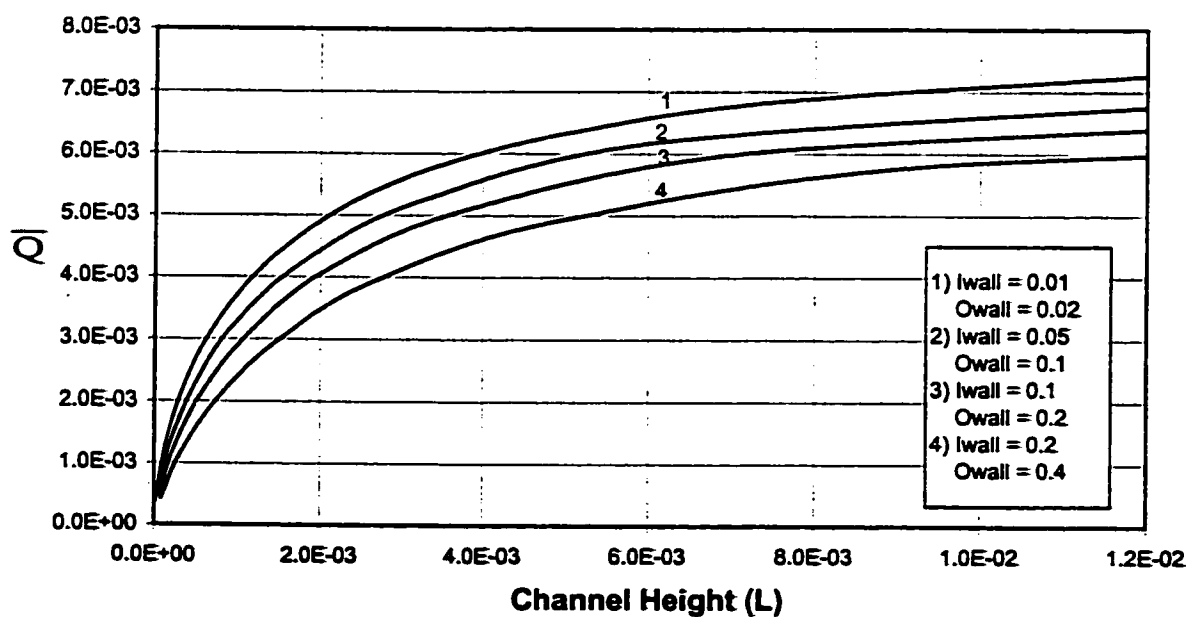
NR$_2$ = 0.5, KR = 2, E = 0.5

Fig.7.73. Total Heat Absorption versus Channel Height for Different Values of Walls Thickness (Case 1.O)

NR$_2$ = 0.5, KR = 2, E = 0.5

Hence it can be concluded that the increase in the temperature level in the fluid and on outer solid-fluid interface by increasing the wall thicknesses causes more flow rate to be induced for high channels for both cases (1.I) and (1.O) whereas for short channels in case (1.O), the reduced heat absorbed along with the lower temperature values on outer solid-fluid interface decreases the induced flow rate and this trend reverses in short channels for case (1.I).

7.3. Critical Conductivity Ratio (KR) with respect to Eccentricity (E)

It is of practical importance to know the values of the conductivity ratio beyond which the conjugate effect can be neglected. Figure (7.74) shows graphically the results of the present work for the variation of the percentage difference in channel height from the conventional case (KR→ ∞) with conductivity ratio for different values of eccentricity for case (1.I). Channel height is the criterion considered to determine the critical values of certain parameters for the conjugate free convection case by comparing it with the conventional case. The percentage difference is based on the conventional values of the channel height. The critical value of the conductivity ratio for given eccentricity and radius ratio, has been arbitrarily defined as that value which causes the channel height to differ by no more than 1% from the conventional solution result for the given eccentricity and radius ratio. According to this definition, the critical values of the conductivity ratio, presented in Fig. (7.74), are also given in Table 7.4. It is obvious from the figure that the higher the values of eccentricity, the higher the critical value of conductivity ratio. It can also be inferred from the figure that conjugate effect increases with eccentricity.

Figure (7.75) shows the graphical representation of the critical values of conductivity ratio for case (1.O). The same parameter (channel height) and criterion (1%) are adopted to determine the critical value of the conductivity ratio beyond which the conjugate effect can be neglected. The results are presented in Table 7.5. It is observed that an increase in eccentricity (E), at a given radius ratio ($NR_2=0.5$), causes the critical value of conductivity ratio (KR) to decrease. Furthermore, the critical values of conductivity ratio at given values of eccentricity and radius ratio for case (1.O) are greater than the corresponding values for case (1.I) indicating that the conjugate effect is more pronounced in case (1.O) than in case (1.I).

7.4. Critical Outer Wall Thickness with respect to Eccentricity (E)

Figure (7.76) shows graphically the obtained results for the variation of the percentage difference in channel height from the corresponding conventional case results with the wall thickness for different values of eccentricity for case (1.I). This percentage is based on the conventional values of channel height and has been arbitrarily defined as the value that causes the channel height to differ by no more than 1% from the conventional solution result for given eccentricity and radius ratio ($NR_2 = 0.5$). According to this definition, the critical values of the outer wall thickness, below which the conjugate effect can be neglected, are given in Table 7.6 and are also presented in Fig. (7.76). The ratio of outer to inner wall thickness is kept fixed at 0.5. It can be seen from the figure that, for a given $NR_2 = 0.5$, the higher the value of eccentricity, the lower the critical wall
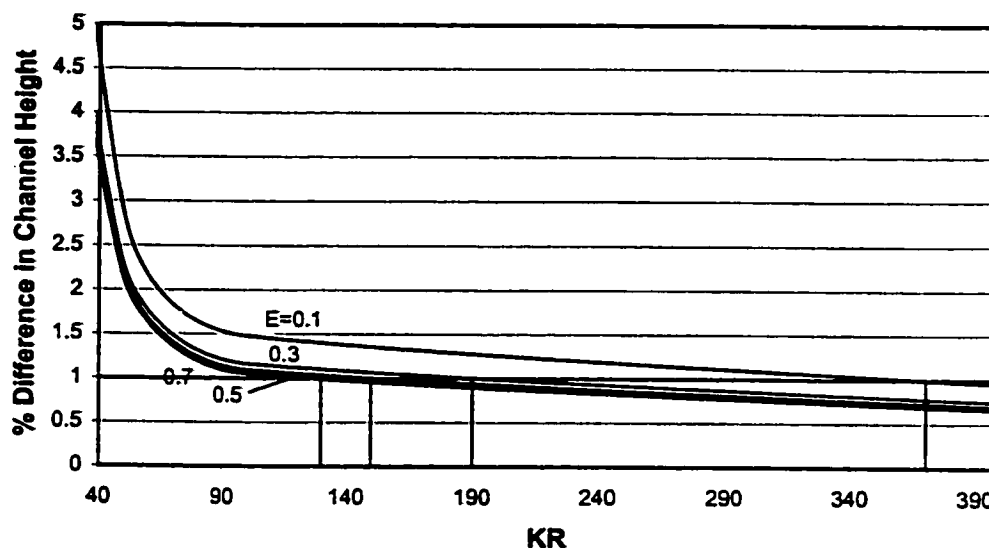
Fig.7.75. Critical Conductivity Ratio for Different
Values of Eccentricity (Case 1.O)
NR$_2$=0.5, Inner Wall Thickness=0.1, Outer Wall Thickness=0.2 Pr=0.7,
F=0.00825

Table. 7.5. Critical Value of Conductivity Ratio for Different Values of
Eccentricity, Case (1.O)

KR	Channel Height	E = 0.1	E = 0.3	E = 0.5	E = 0.7
1	Value	0.00654	0.00476	0.00375	0.00296
	% Difference	160.47060	114.44489	103.38371	98.85896
5	Value	0.00321	0.00271	0.00222	0.00178
	% Difference	27.72369	21.83867	20.66689	19.88858
10	Value	0.00286	0.00247	0.00204	0.00164
	% Difference	13.88091	11.08194	10.52702	10.40245
50	Value	0.00258	0.02271	0.00188	0.00152
	% Difference	2.87438	2.28598	2.17530	2.12058
100	Value	0.00255	0.00225	0.00186	0.00150
	% Difference	1.47983	1.16296	1.09563	1.05087
1000	Value	0.00251	0.00222	0.00185	0.00149
	% Difference	0.19233	0.13342	0.11729	0.10898
Conventional channel height		0.00248	0.00220	0.00183	0.00147
Critical KR		370	190	150	130
Channel Height corresponding to critical KR value		0.00251	0.00222	0.00184	0.00149

Fig.7.76. Critical Wall Thickness for Different Values of Eccentricity (Case 1.I)

$NR_2=0.5$, $KR=2$, $Pr=0.7$, $F=0.006$

Table. 7.6. Critical Value of Wall Thickness for Different Values of Eccentricity, Case (1.I)

Owall	Channel Height	E = 0.1	E = 0.3	E = 0.5	E = 0.7
0.002	Value	0.002684925	0.002057299	0.001664717	0.001488516
	% Difference	0.000994786	0.00479196	0.014927807	0.022204151
0.02	Value	0.00268469	0.002056976	0.001664516	0.001487282
	% Difference	0.009734339	0.020478114	0.026989748	0.105097665
0.1	Value	0.002683342	0.002053543	0.001657797	0.001476362
	% Difference	0.059965049	0.187368226	0.430512296	0.838542907
0.2	Value	0.002667646	0.002035524	0.001637531	0.001453634
	% Difference	0.64454051	1.063174511	1.647755539	2.365100973
0.4	Value	0.002608472	0.001973751	0.001574937	0.001405286
	% Difference	2.848453564	4.065635755	5.40723497	5.612459056
Conventional Channel Height		0.002684952	0.002057398	0.001664965	0.001488847
Critical Wall Thickness		0.236	0.195	0.156	0.112
Channel Height Corresponding to Crtical wall Thickness		0.002658102	0.002036824	0.001648315	0.001473958

thickness. It is also observed in this analysis that the conjugate effect increases with eccentricity.

Figure (7.77) shows the graphical representation of the critical values of outer wall thickness for case (1.O). Same parameter (channel height) and criterion (1%) is adopted to determine the critical value of the wall thickness below which the conjugate effect can be neglected. Same ratio of Outer to inner wall thickness, i.e. 0.5 is also kept fixed for case (1.O). The results, presented in Table 7.7 and Figure (7.77), show that the critical value of outer wall thickness increases with increasing eccentricity (E). Furthermore, the critical values of wall thickness are smaller than the corresponding values for case (1.I) indicating that the conjugate effect is more pronounced for case (1.O).

7.5. Critical Conductivity Ratio (KR) with respect to Radius Ratio (NR$_2$)

This section presents the critical values of thermal conductivity ratio (KR) beyond which the conjugate effect can be neglected for different radius ratios (NR$_2$) for cases (1.I) and (1.O). Figure (7.78) shows graphically the results of the present work for the variation of the percentage difference in channel height from the conventional case with conductivity ratio (KR) for different values of radius ratio (NR$_2$) for case (1.I). The percentage difference is based on the conventional values of the channel height. The critical value of the conductivity ratio (KR) for given radius ratio (NR$_2$) and eccentricity (E), has been chosen as that value which causes the channel height to differ by no more than 1% from the conventional solution result for the given radius ratio and eccentricity. The critical values of the conductivity ratio (KR), presented in Fig. (7.78), are also given
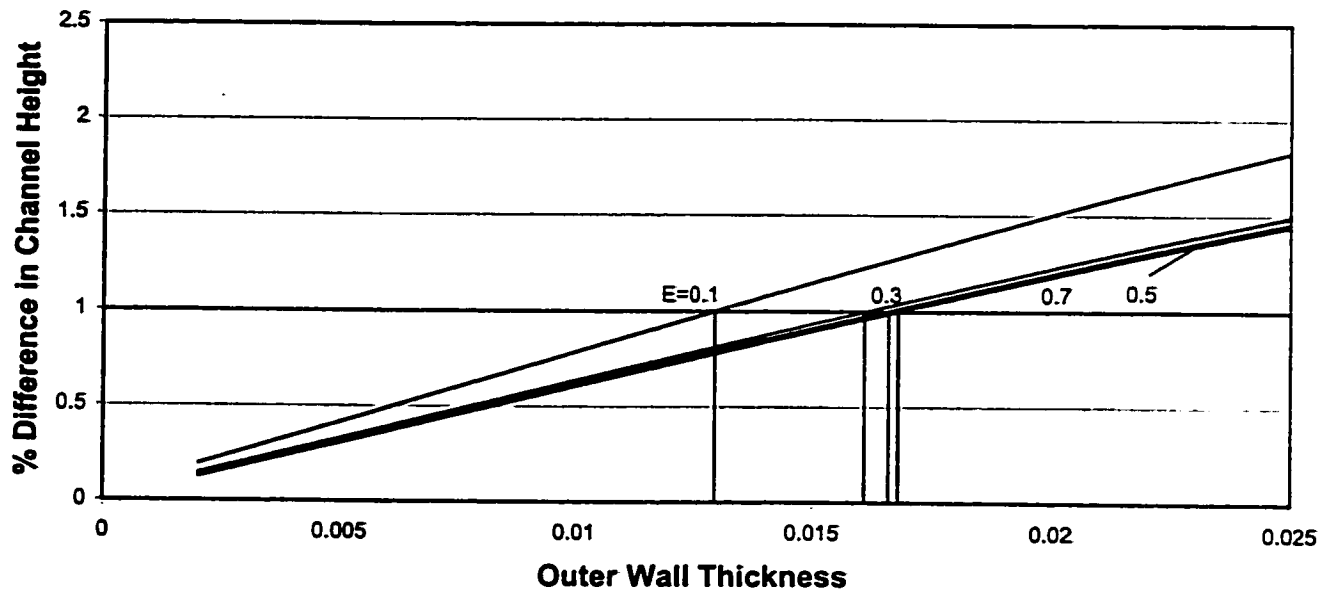
Fig.7.77. Critical Wall Thickness for Different values of Eccentricity (Case 1.O)

NR$_2$=0.5, KR=2, Pr=0.7, F=0.00825

Table.7.7. <u>Critical Values of Wall Thickness for Different Values of Eccentricity. (Case 1.O)</u>

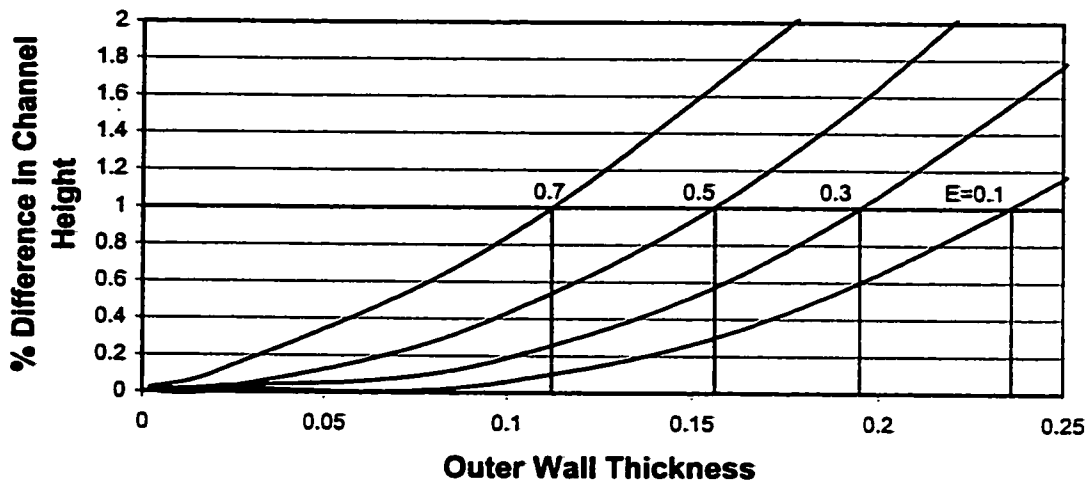| OWALL	Channel Height	E = 0.1	E = 0.3	E = 0.5	E = 0.7
0.002	Value	0.002514254	0.002223385	0.001846115	0.0014881
0.002	% Difference	0.192746213	0.145210691	0.132275791	0.115712441
0.02	Value	0.002547123	0.00224734	0.001865703	0.0015038
0.02	% Difference	1.50257866	1.224186481	1.194766371	1.171969873
0.1	Value	0.002687084	0.002348512	0.001947563	0.00156983
0.1	% Difference	7.080017984	5.78115337	5.634793866	5.614306069
0.2	Value	0.002857747	0.002466198	0.00203776	0.00163587
0.2	% Difference	13.88090549	11.08194466	10.52701905	10.05731504
0.4	Value	0.003191703	0.00267756	0.002191502	0.00174887
0.4	% Difference	27.18903319	20.60207465	18.86589807	17.65967745
Conventional Channel Height		0.002509417	0.002220161	0.001843676	0.00148638
Critical Owall		0.01295	0.0161	0.0166	0.0168
Channel Height Corresponding to Critical Wall Thickness		0.002534511	0.002242363	0.001862113	0.001501244
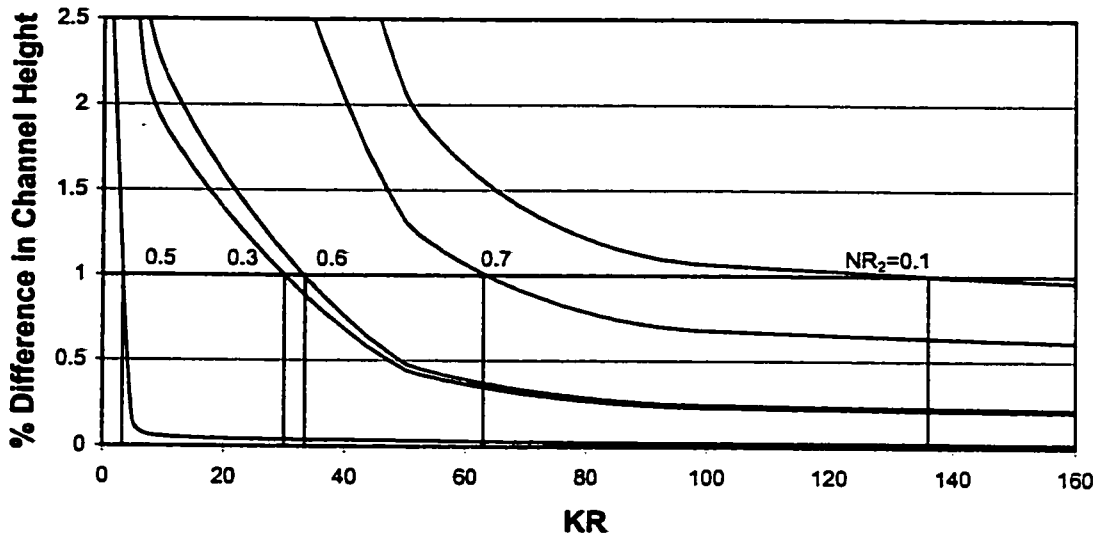
Fig.7.78. Critical Conductivity Ratio For Different Values of
'Radius Ratio (NR$_2$) (Cas 1.I)

E=0.5, Inner Wall Thickness=0.1, Outer Wall Thickness=0.2, Pr=0.7

Table 7.8. Values of Critical Conductivity Ratio for Different Radius
Ratios Case (1.I)

KR	Channel Height	NR$_2$ = 0.1	NR$_2$ = 0.3	NR$_2$ = 0.5	NR$_2$ = 0.6	NR$_2$ = 0.7
1	Value	0.001967175	0.001544043	0.002858583	0.001025	0.006431019
	% Difference	34.95414156	7.986871477	2.849553013	11.64945428	15.27053051
5	Value	0.001695915	0.001474481	0.002775067	0.00111368	0.006861845
	% Difference	16.34485707	3.121882784	0.155266799	4.005620797	9.594346648
10	Value	0.001592169	0.001456778	0.002777826	0.001134559	0.007159751
	% Difference	9.227612458	1.88378705	0.056020008	2.205950772	5.669398445
50	Value	0.001487869	0.001436245	0.002778464	0.00115453	0.007489593
	% Difference	2.07227061	0.447703838	0.03306704	0.484533685	1.323686497
100	Value	0.001473211	0.001433117	0.002778797	0.001157326	0.007538651
	% Difference	1.066700947	0.229002524	0.02109532	0.243516188	0.677347537
1000	Value	0.001459372	0.001430221	0.00277923	0.001159844	0.007584795
	% Difference	0.117284657	0.026422046	0.005511223	0.026511681	0.069391336
Conventioanal Channel Height		0.001457662	0.001429843	0.002779383	0.001160151	0.007590062
Critical KR		136	30	3.3	33.5	63
Channel Height Corresponding to Critical KR value		0.001472239	0.001444141	0.002807177	0.00114855	0.007514161
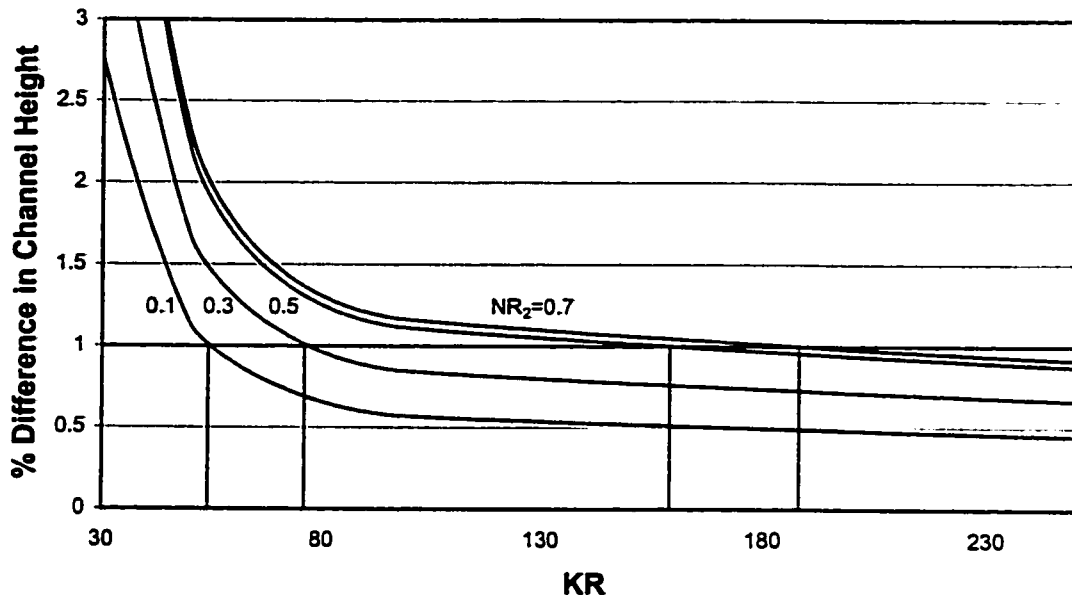
Fig.7.79. Critical Conductivity Ratio For Different Values of Radius Ratio (Cas 1.O)

E =0.5, Inner Wall Thickness=0.1, Outer Wall Thickness=0.2 Pr=0.7

Table 7.9. Values of Critical Conductivity Ratio for Different Radius Ratios Case (1.O)

KR	Channel Height	$NR_2 = 0.1$	$NR_2 = 0.3$	$NR_2 = 0.5$	$NR_2 = 0.7$
1	Value	0.00790041	0.00797402	0.00736902	0.00298963
1	% Difference	58.6794144	89.4171742	116.103715	118.533963
5	Value	0.00553781	0.00490328	0.00414366	0.00166875
5	% Difference	11.2267005	16.4738193	21.5168648	21.9813111
10	Value	0.00525878	0.00455743	0.003779	0.00151679
10	% Difference	5.62235727	8.25861262	10.822729	10.8730172
50	Value	0.00503514	0.00428016	0.00348505	0.00139955
50	% Difference	1.13061992	1.67206362	2.20242604	2.30345053
100	Value	0.00500708	0.00424529	0.0034478	0.00138393
100	% Difference	0.56694626	0.84372979	1.11006548	1.16123709
1000	Value	0.0049822	0.00421347	0.00341393	0.00136966
1000	% Difference	0.06734406	0.08800625	0.11690399	0.118524
Conventioanal Channel height		0.00497885	0.00420977	0.00340995	0.00136804
Critical KR		54	76	159	188
Channel Height Corresponding to Critical KR value		0.00502864	0.00425186	0.00344405	0.00138172

conventional and conjugate cases at a given radius ratio (NR_2). Hence it can be inferred that conjugate effect increases with radius ratio (NR_2) for case (1.O).

7.6. Critical Outer Wall Thickness with Respect to Radius Ratio (NR_2)

Figure (7.80) shows graphically the results of the present investigation for the variation of the percentage difference in channel height from the conventional case with the wall thickness for different values of radius ratio (NR_2) for case (1.I). This percentage is based on the conventional values of channel height and has been chosen as the values that cause the channel height to differ by no more than 1% from the conventional solution results for given radius ratio (NR_2) and eccentricity (E=0.5). The critical values of the wall thickness, below which the conjugate effect can be neglected, are presented in Table 7.10 and are also presented in Fig. (7.80). It is to remind the reader that an increase in the critical value of wall thickness means the conjugate effect is decreasing. It can be seen from the figure that, for a given eccentricity (E=0.5), the critical value of wall thickness increases up to a certain value of radius ratio. After that value of radius ratio, the critical value of wall thickness starts decreasing. This is because with the increase of radius ratio (NR_2), the effect of outer wall increases. Also more heat flows through the fluid annulus causing the percentage difference in channel height between conventional and conjugate cases to decrease resulting in the decrease in the conjugate effect. For large radius ratios (NR_2), such as 0.6 and 0.7, the effect of outer wall dominates causing the channel height to decrease and create higher percentage difference in channel height from the conventional case. It means thinner walls are needed to reach the critical value criterion,
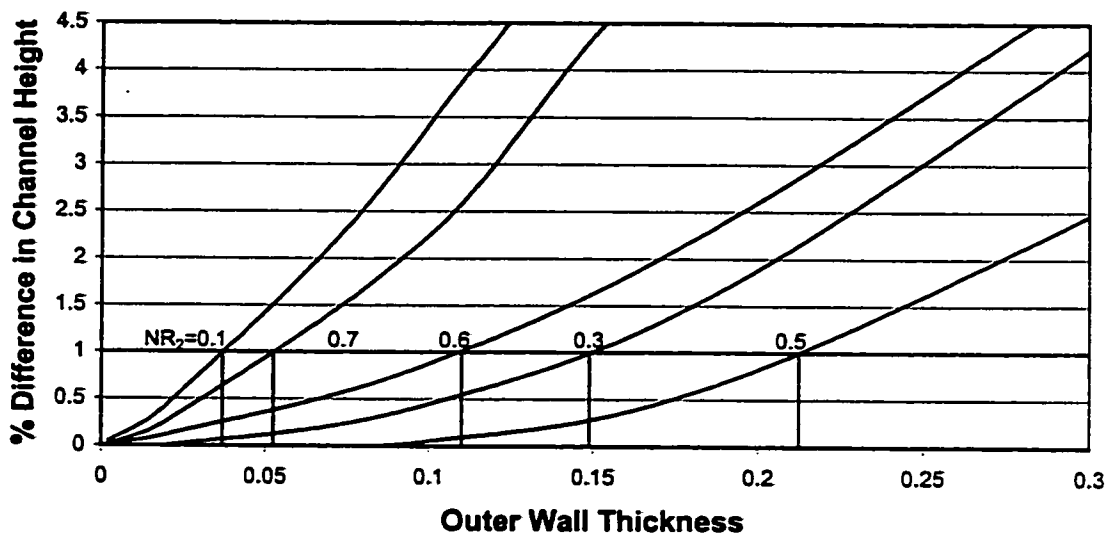
Fig.7.80. Critical Outer Wall Thickness For Different Values of
Radius Ratio (Cas 1.I)

E =0.5, KR=2, Pr=0.7

Table 7.10. Critical Values of Outer Wall Thickness for Different Values of Radius Ratio Case (1.I)

Owall	Channel Height	$NR_2 = 0.1$	$NR_2 = 0.3$	$NR_2 = 0.5$	$NR_2 = 0.6$	$NR_2 = 0.7$
0.002	Value	0.001458319	0.001429858	0.00277936	0.001160014	0.007589
	% Difference	0.045046322	0.001015959	0.000823344	0.011832943	0.013991613
0.02	Value	0.001464109	0.001429881	0.00277934	0.001158765	0.00757
	% Difference	0.442264189	0.002672969	0.001542928	0.11948685	0.26431895
0.1	Value	0.001507423	0.001436187	0.002778	0.001150009	0.00742
	% Difference	3.413723508	0.443660095	0.049755069	0.874224257	2.240587399
0.2	Value	0.001592169	0.001456778	0.0028022	0.00113	0.0071524
	% Difference	9.227612458	1.88378705	0.820941809	2.598910568	5.766250312
0.4	Value	0.001816942	0.001525284	0.00289652	0.001076	0.0070254
	% Difference	24.64767539	6.674902564	4.214500881	7.253475903	7.439490932
Conventioanal Channel Height		0.001457662	0.001429843	0.002779383	0.001160151	0.007590062
Critical KR		0.037	0.149	0.2125	0.11	0.0525
Channel Height Corresponding to Critical KR value		0.001472239	0.001444141	0.002807177	0.00114855	0.007514161

i.e., 1 % channel height difference from the conventional case as can be seen in Fig. (7.80) and Table 7.10. The transition from decreasing to increasing values of conjugate channel height with increasing wall thickness for a radius ratio (NR$_2$ = 0.5) can be observed in Table 7.10.

Figure (7.81) shows the graphical representation of the critical values of wall thickness for case (1.O). Same parameter (channel height) and criterion (1%) is adopted to determine the critical value of the wall thickness below which the conjugate effect can be neglected. The results, presented in Table 7.11 and Figure (7.81), show that, for a given eccentricity (E=0.5), higher the value of radius ratio, the lower the value of critical wall thickness. Hence it is concluded that conjugate effect increases with radius ratio (NR$_2$) for case (1.O).

Chapter 8

RESULTS AND DISCUSSION FOR BOUNDARY

CONDITIONS OF THIRD KIND

8.1. Introduction

This chapter covers the results and discussion of the effect of conductivity ratio, eccentricity, radius ratio and wall thickness on induced flow rate in the vertical eccentric annuli under the boundary conditions of third kind. It is to remind the reader, the boundary conditions of the third kind comprise of one wall heated isothermal (at a prescribed temperature) while the other wall kept adiabatic. Same values of eccentricity (E), radius ratio (NR_2), conductivity ratio (KR) and wall thickness are used in the present analysis as were used for boundary conditions of first kind.

8.2. Results and Discussion

8.2.1. Effect of Conductivity Ratio (KR)

The following results are obtained using geometry of annulus radius ratio 0.5, inner and outer wall thicknesses 0.1 and 0.2, respectively and eccentricity 0.5 imposing boundary conditions of third kind.

8.2.1.1. Induced Flow Rate (F)

Figure (8.1) shows the variation of induced flow rate (F) with channel height (L) for some selected values of conductivity ratio (KR) for case (3.I). Two trends are observed for the flow rate variation for case (3.I). For short channels, when the conductivity ratio increases, the flow rate increases and then it starts decreasing after a certain value of conductivity ratio. For high channels, only one trend of decreasing the flow rate with conductivity ratio is observed. The flow behavior in high channels is attributed to increase in the heat conduction (circumferential and transversal) in the cylinder walls as well as decrease in the amount of heat absorbed in the fluid. The opposite happens for short channels up to a certain value of conductivity ratio because when the conductivity ratio is increased, the amount of heat entering the fluid through the inner wall increases, resulting in increase in the amount of heat absorbed in the fluid and hence the flow rate. After certain value of conductivity ratio (KR) the thermal conductivity of outer wall dominates, resulting in reduced temperature difference between the fluid and outer solid-fluid interface. This causes the induced flow rate in the eccentric channel to reduce. A trend of having increase in the induced flow rate up to a certain value of conductivity ratio (KR) and then decrease in its value is observed for all channel heights in case (3.O) as shown in Fig. (8.2). It means, when the conductivity ratio (KR) is increased up to a certain value, the increased amount of heat causes an increase in the temperature values on the inner solid-fluid interface as well as the heat absorbed in the fluid resulting in increase in the induced flow rate. After that value of conductivity ratio (KR), the temperature difference between the outer solid-fluid interface and the mean fluid temperature decreases (as a

Fig.8.1. Variation of Flow Rate with Channel Height for Different values of Conductivity Ratio (KR) (Case 3.I)

$NR_2 = 0.5$, Inner Wall Thickness = 0.1, Outer Wall Thickness = 0.2, $E = 0.5$
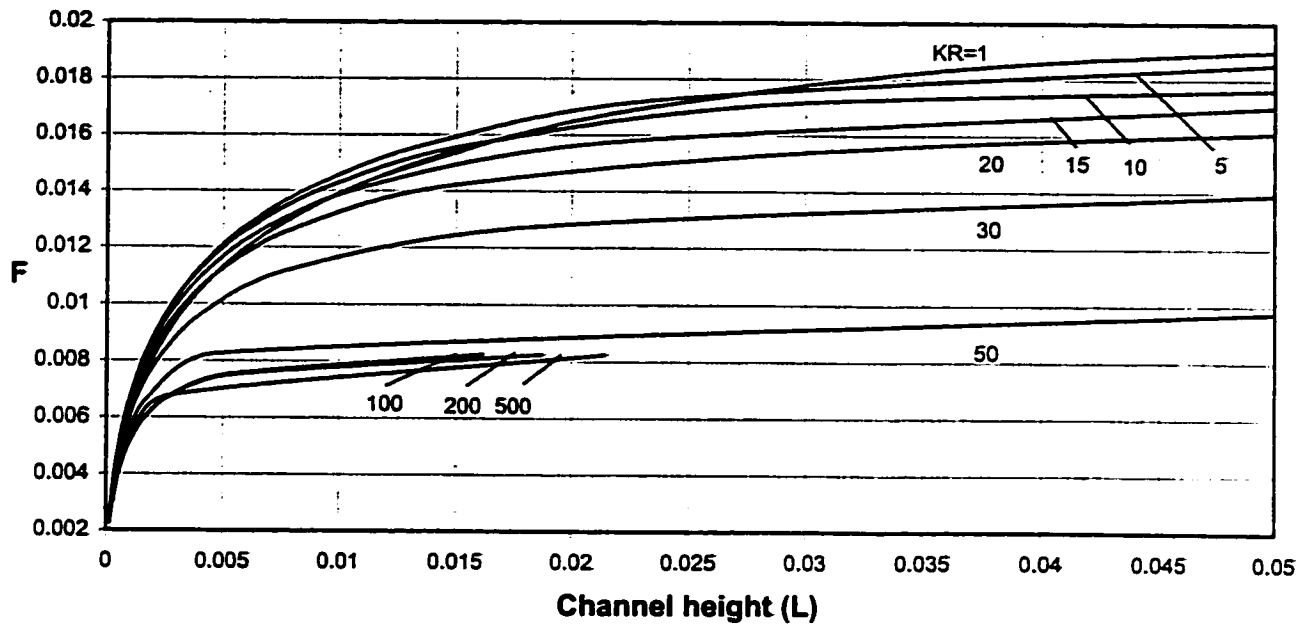

Fig.8.2. Variation of Flow Rate with Channel Height for Different values of Conductivity Ratio (KR) (Case 3.O)

$NR_2 = 0.5$, Inner Wall Thickness = 0.1, Outer Wall Thickness = 0.2, $E = 0.5$
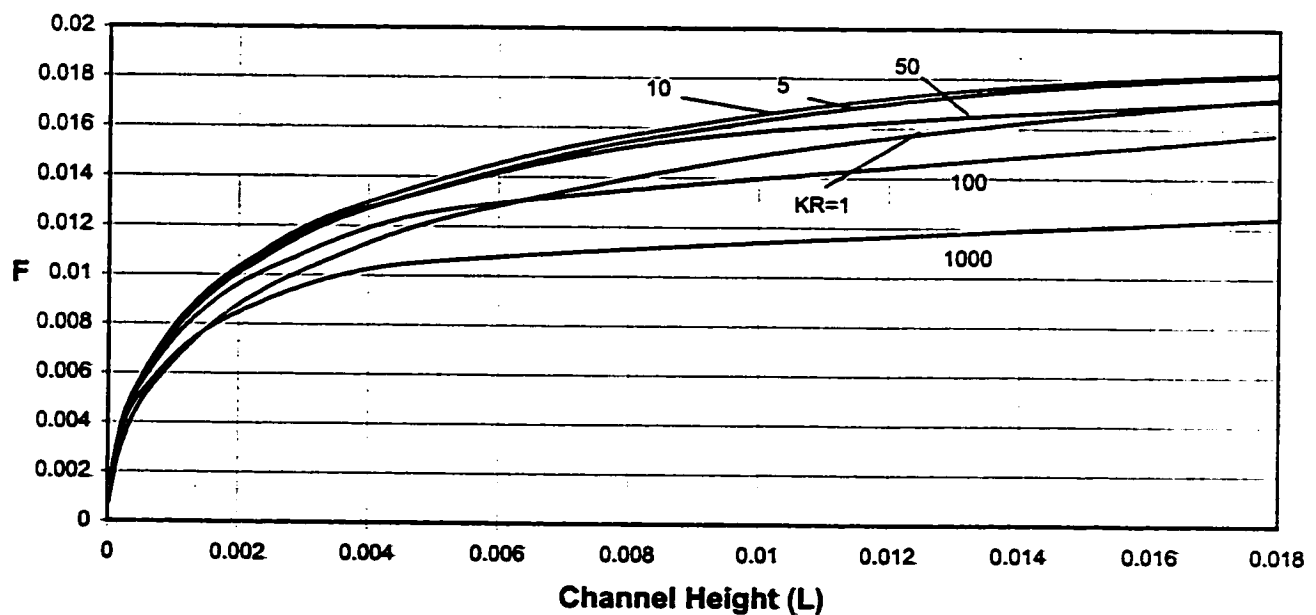
result of insulating the inner wall and high wall conductivity) and hence the heat transfer decreases, causing the reduction in the induced flow rate.

8.2.1.2. Optimum Conductivity Ratio (KR$_{opt}$)

Due to this variation in the trend of induced fluid flow rate, for cases (3.I, short channels) and (3.O), there is need to determine the values of conductivity ratio (KR) at different eccentricities (E) and radius ratios (NR$_2$), at certain specific channel heights, after which the behavior of induced flow rate reverses. We can also say that these values of conductivity ratio (KR) are the optimum values giving maximum induced flow rate at certain specific channel heights abbreviated as (KR$_{opt}$).The channel heights used for analysis are 0.008, 0.01, 0.012 and 0.014. The analysis is carried only for case (3.O) because this induced flow behavior is present in case (3.I) for very small range of channel height, which may be insignificant to analyze.

Figures (8.3 through 8.6) show the graphs of conductivity ratio (KR) plotted against induced flow rate (F) at eccentricities (E) ranging from 0.1 to 0.7, for a given radius ratio (NR$_2$=0.5), at the four specified channel heights. From the figures (8.3 trough 8.6), it is observed that all four channel heights show almost the same values of optimum conductivity ratio (KR$_{opt}$) with the exception for eccentricity 0.3 at channel height of 0.008 as shown in Fig. (8.4). Also for eccentricity 0.7, as can be seen in Fig. (8.6), after an optimum conductivity ratio value of 11.5, there is no significant increase in the induced flow rate. Hence it can be stated that the channel height has no significant effect on the optimum value of conductivity ratio (KR$_{opt}$). This conclusion enables us to take the mean

Fig. 8.3. Optimum Value of Conductivity Ratio (KR_opt) at E = 0.1 for
Case (3.O)

NR₂=0.5. Iwall=0.1, Owall=0.2

Fig. 8.4. Optimum Value of Conductivity Ratio (KR_opt) at E = 0.3 for
Case (3.O)

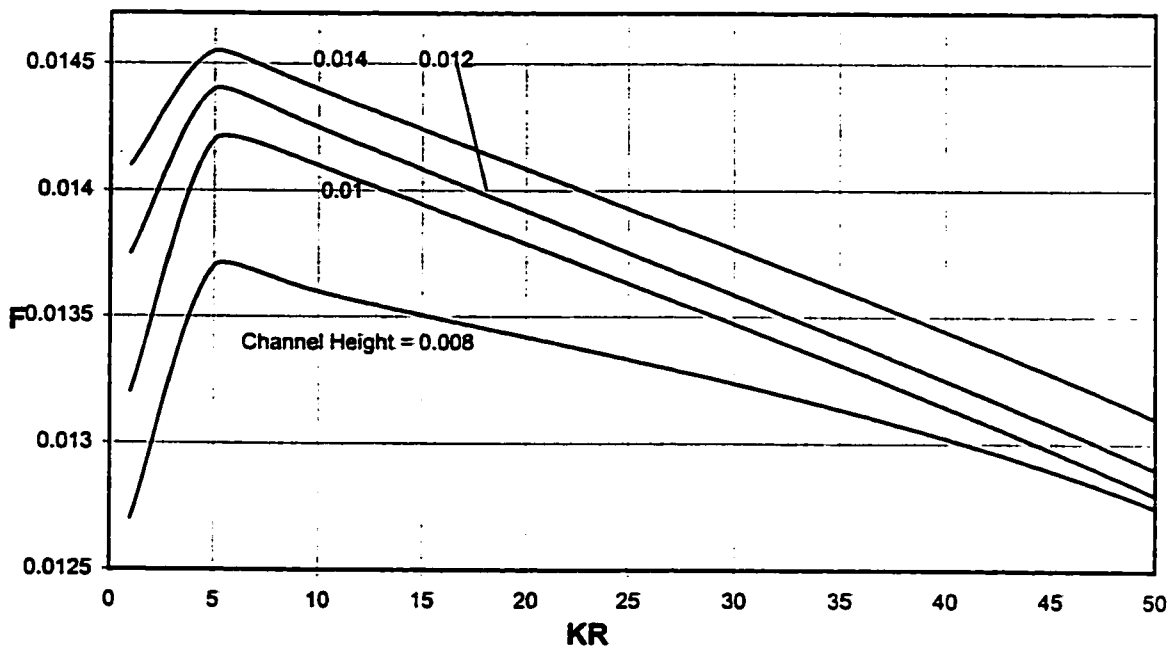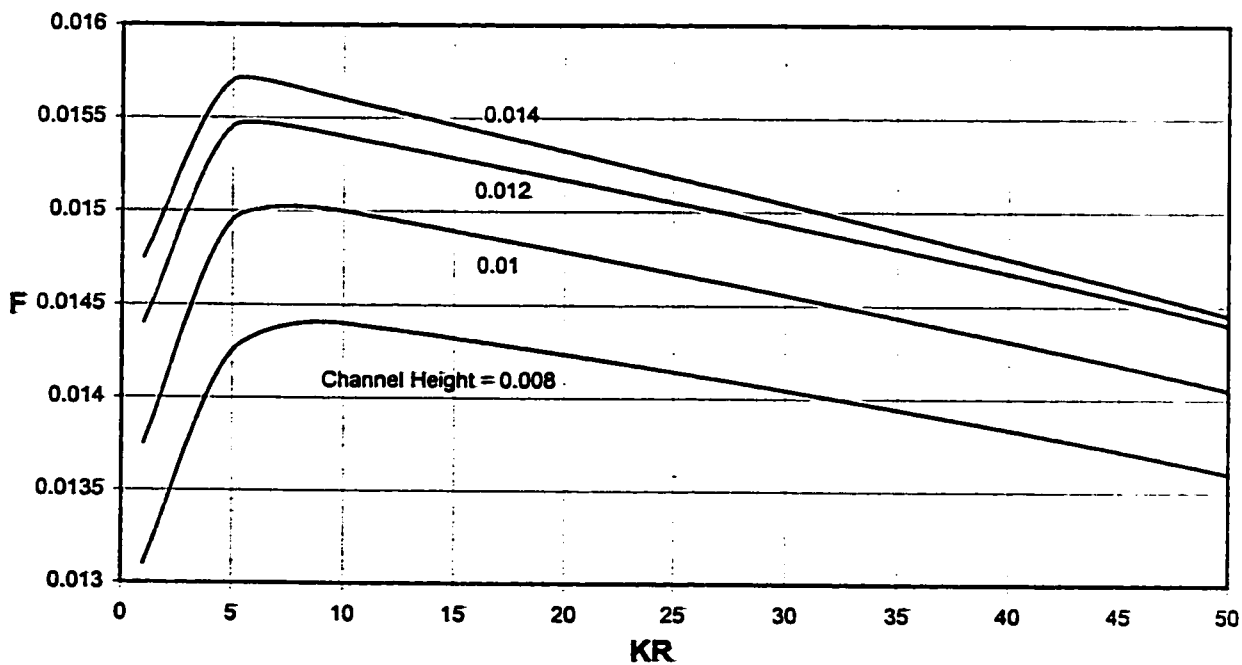NR₂=0.5. Iwall=0.1, Owall=0.2

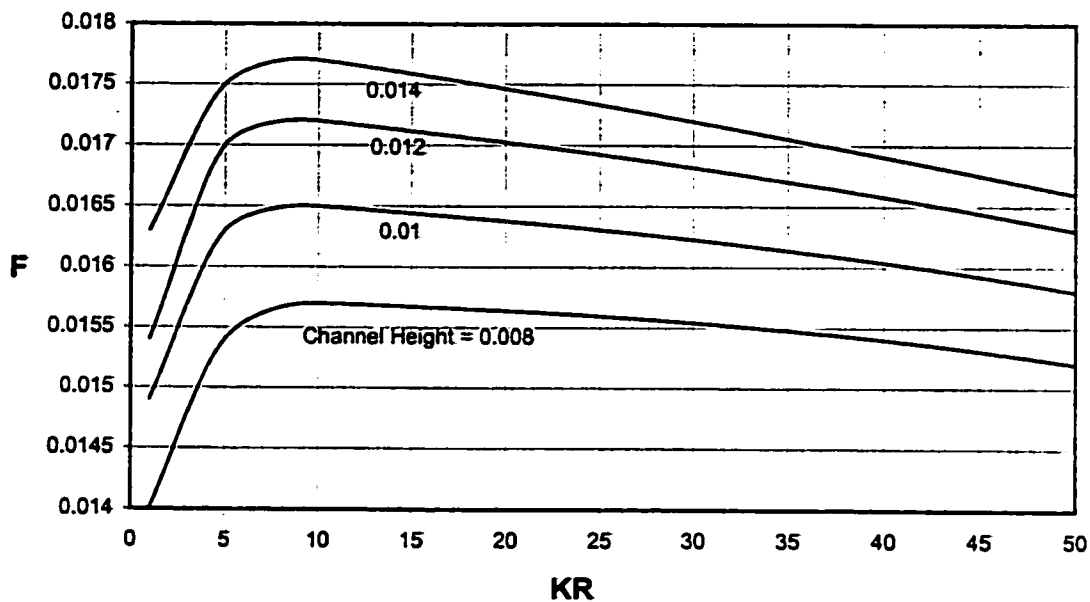**Fig. 8.5.** Optimum Value of Conductivity Ratio (KR_{opt}) at E = 0.5 for Case (3.0)
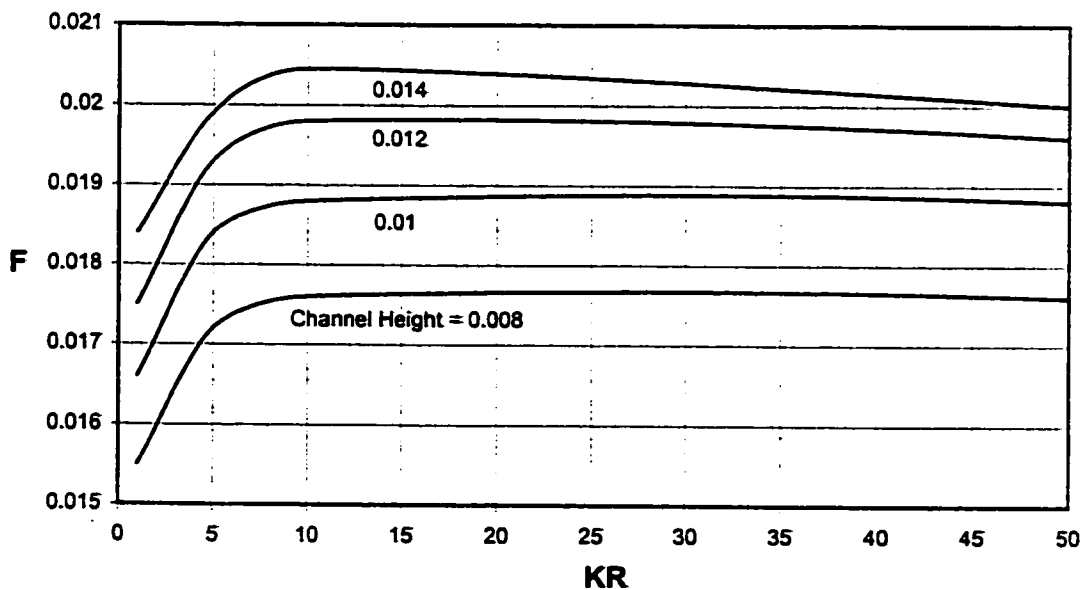
$NR_2=0.5$. Iwall=0.1, Owall=0.2

Fig. 8.6. Optimum Value of Conductivity Ratio (KR_{opt}) at E = 0.7 for Case (3.0)

$NR_2=0.5$. Iwall=0.1, Owall=0.2

of the values of optimum conductivity ratio (KR_{opt}) obtained at the specified channel heights for each eccentricity (E) and plot these values against the eccentricity as shown in Fig. (8.7). The results are also presented in tabular form as shown in Table 8.1. It is obvious from the figure and the table that increasing the eccentricity results in an increase in the optimum value of conductivity ratio (KR_{opt}). The physical interpretation of this phenomenon can be given by considering hydrodynamics that involves the increase in flow rate with increasing eccentricity. At large eccentricity, the increased flow rate enables more heat to carry, which comes from the outer wall and causes the optimum value of conductivity ratio (KR_{opt}) to elevate.

Similar analysis is carried out for different radius ratios at specific channel heights, i.e. 0.008, 0.01, 0.011, 0.012. Figures (8.8 through 8.11) show the graphs of conductivity ratio (KR) plotted against induced flow rate (F), for a given eccentricity (E=0.5), at the specified channel heights. Figure (8.8) for radius ratio ($NR_2=0.1$) shows a shift in the optimum value of conductivity ratio (KR_{opt}) from 5.5 to 1.5 as the channel height increases. Rest of the figures (8.9, 8.10 and 8.11) show almost the same values of optimum conductivity ratio (KR_{opt}) at the specified channel heights indicating no significant effect of channel height on the optimum value of conductivity ratio (KR_{opt}). Taking mean of the values of optimum conductivity ratio (KR_{opt}) at the above mentioned channel heights for each radius ratio (NR_2) and plotting these values against the eccentricity shows an increase in optimum conductivity ratio (KR_{opt}) with radius ratio (NR_2) as shown in Fig. (8.12) and presented in Table 8.2. A possible explanation of the phenomenon can be given by considering the heat absorbed in the fluid, which increases with increasing radius ratio. The increased heat absorbed in the fluid at large radius ratio
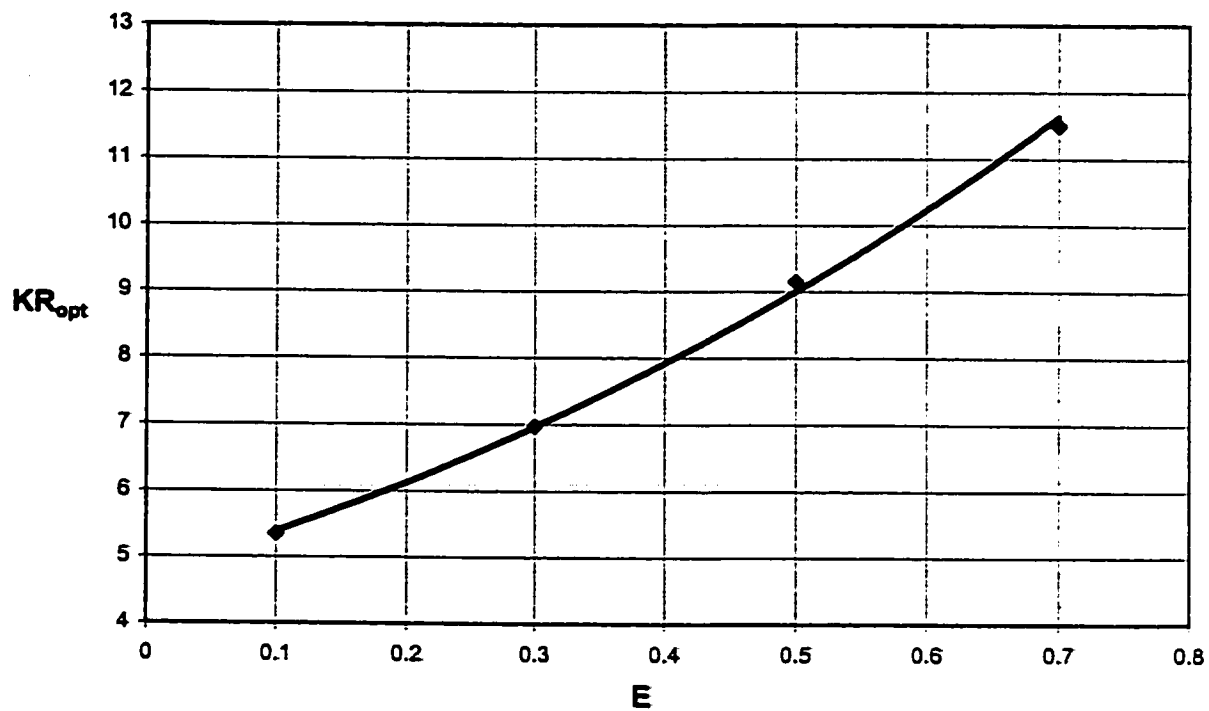
Fig.8.7. Optimum Values of Conductivity Ratio (KR$_{opt}$) Versus Different Values of Eccentricity (E) (Case 3.0)

NR$_2$=0.5, Iwall=0.1, Owall=0.2, Pr=0.7

Table 8.1. Average values of optimum Conductivity Ratios at Different Eccentricities (E)

E	0.1	0.3	0.5	0.7
KR$_{opt}$	5.35	6.975	9.15	11.5
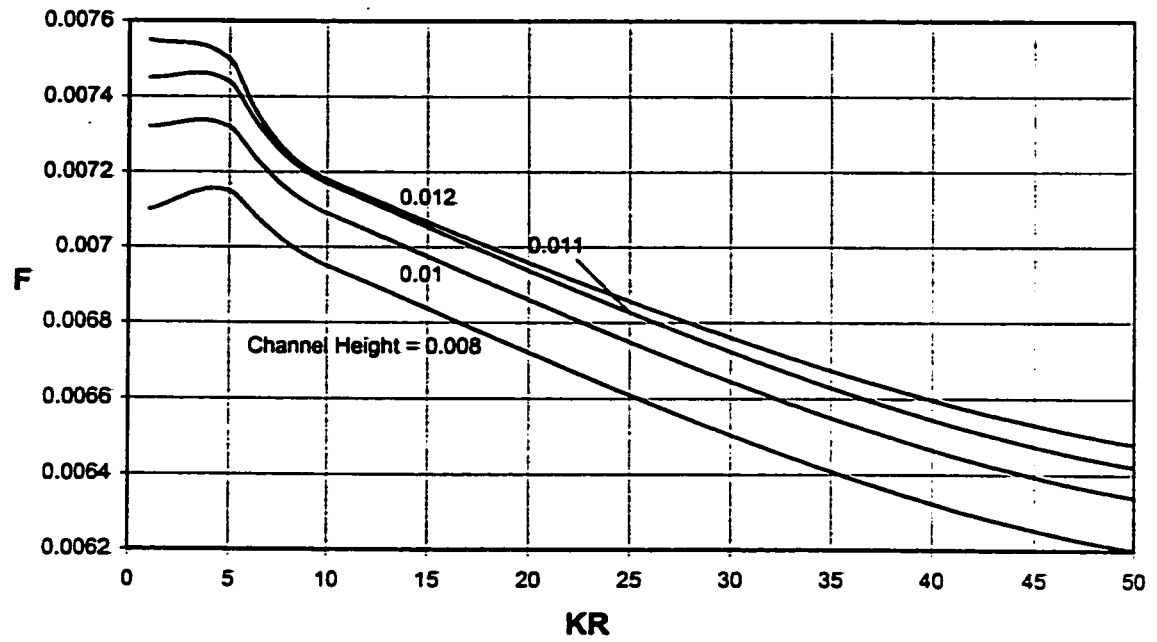
Fig. 8.8. Optimum Value of Conductivity Ratio (KR$_{opt}$) at NR$_2$ = 0.1 for Case (3.O)

E=0.5. Iwall=0.1, Owall=0.2
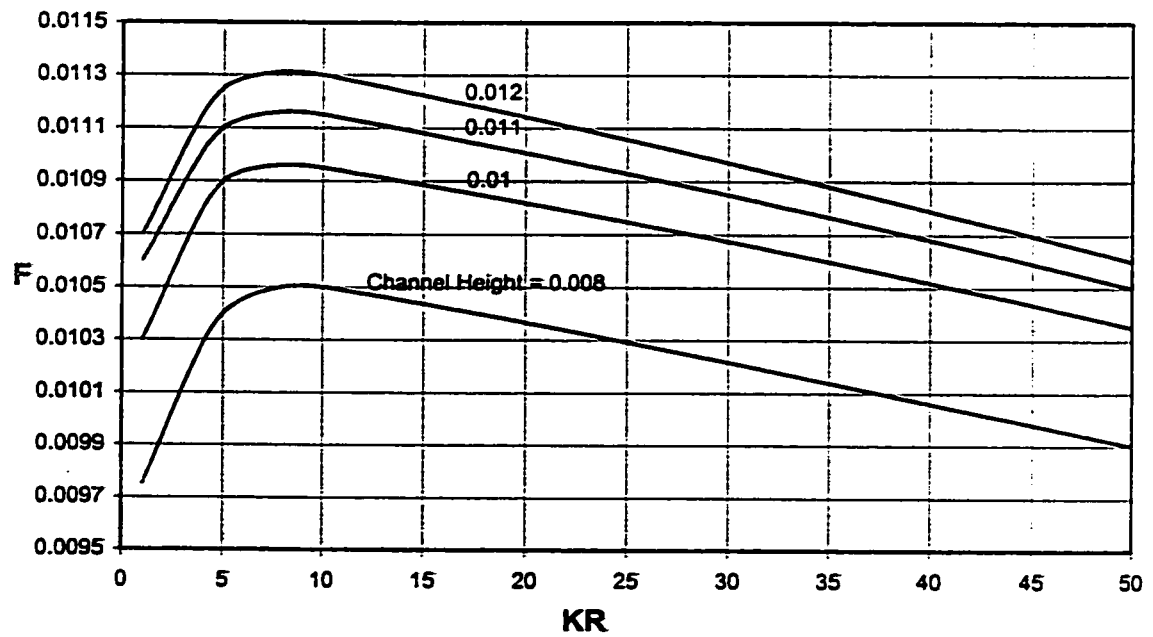
Fig. 8.9. Optimum Value of Conductivity Ratio (KR$_{opt}$) at NR$_2$ = 0.3 for Case (3.O)

E=0.5. Iwall=0.1, Owall=0.2

Fig. 8.10. Optimum Value of Conductivity Ratio (KR_{opt}) at $NR_2 = 0.5$
for Case (3.O)

E=0.5. Iwall=0.1, Owall=0.2

Fig. 8.11. Optimum Value of Conductivity Ratio (KR_{opt}) at $NR_2 = 0.7$
for Case (3.O)

E=0.5. Iwall=0.1, Owall=0.2

in turn increases the buoyancy force and hence the induced flow rate causing the optimum value of conductivity (KR_{opt}) ratio to elevate. The above discussion can be helpful to design the most efficient eccentric channel for having maximum flow rate with known radius ratio, eccentricity and wall thickness.

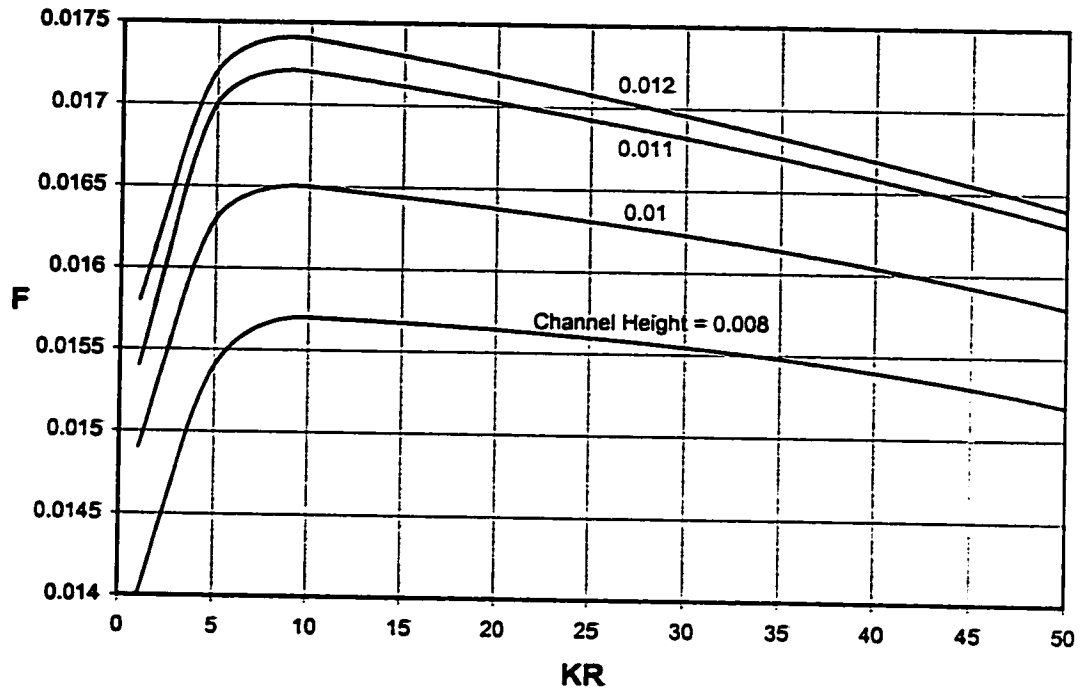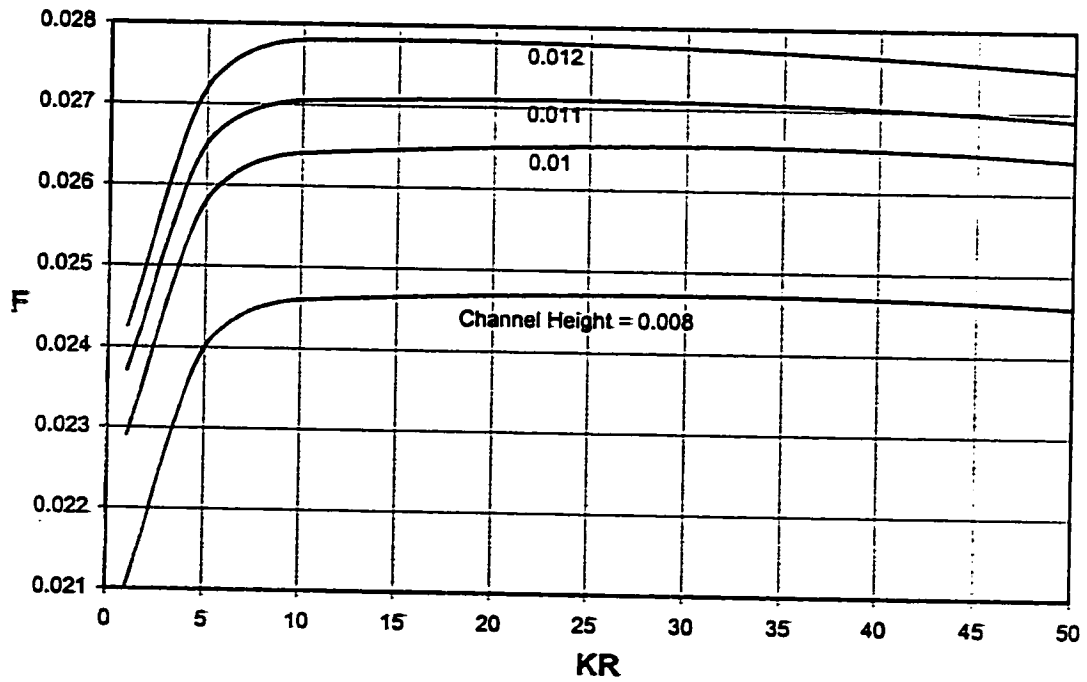Figures (8.13-8.24), obtained for a flow rate of 0.00825 for case (3.I) and 0.01275 for case (3.O), explain the phenomenon. All the circumferential analysis is carried out at an axial (vertical) location of 1.65×10^{-3} for case (3.I) and 3.86×10^{-3} for case (3.O).

8.2.1.3. Local Heat Flux (HF)

Figures (8.13) and (8.14) show the increase in the circumferential values of local heat flux on inner (Case 3.I) and outer (case 3.O) interfaces, respectively. A transition from the circumferential decrease to increase in the heat flux is present for both cases (3.I and 3.O). The figure shows that for conductivity ratio (KR=1 to 10), the values of heat flux decrease circumferentially from widest gap ($\psi = 0$) to narrowest gap ($\psi = 1$). This is because the heat that accumulates on the interface next to insulated wall at the narrowest gap ($\psi = 1$) decreases the temperature difference between the walls. After certain values of the conductivity ratio, as shown in Fig. (8.13) for KR=50 to 100, the circumferential heat conduction in the inner wall from narrowest gap ($\psi = 1$) to widest gap ($\psi = 0$) (clockwise) increases to such an extent to increase the heat flux at the narrowest gap ($\psi = 1$) as compared to the widest gap ($\psi = 0$) on the inner solid-fluid interface for case (3.I). This is also true for case (3.O) as shown in Fig. (8.14). Furthermore, increasing the conductivity ratio (KR) causes the overall circumferential heat flux to increase at the

Fig.8.13. Circumferential Variation of Local Heat Flux on Inner Interface at an Axial (vertical) Location of 1.65×10^{-3} for Different Values of Conductivty Ratio (Case 3.I)

$NR_2 = 0.5$, Inner Wall Thickness $= 0.1$, Outer Wall Thickness $= 0.2$, $E = 0.5$

Fig.8.14. Circumferential Variation of Local Heat Flux on Outer Interface at an Axial (vertical) Location of 3.86×10^{-3} for Different Values of Conductivty Ratio (Case 3.O)

$NR_2 = 0.5$, Inner Wall Thickness $= 0.1$, Outer Wall Thickness $= 0.2$, $E = 0.5$

heated wall interfaces (inner interface for case (3.I) and outer interface for case (3.O)) as shown in Figs. (8.13) and (8.14).

8.2.1.4. Circumferential Temperature (θ)

Figures (8.15-8.18) present the circumferential variation of temperature values on inner and outer solid-fluid interfaces for given values of conductivity ratio (KR) for cases (3.I) and (3.O). Both cases show the same circumferential behavior of temperature with conductivity ratio (KR) on the interfaces next to heated and insulated walls. There is also the change of trends in the circumferential temperature values on inner (case 3.I) and outer (case 3.O) interfaces (Figs. 8.15 and 8.17), which are directly related to the circumferential change of local heat flux as already explained. As can be seen from Figs. (8.16) and (8.18), the widest gap ($\psi = 0$) shows increasing temperature values up to a certain limit of conductivity ratio and then the temperature values start decreasing. The narrowest gap ($\psi = 1$) shows only one trend of decreasing temperature values with increasing KR. This is attributed to the circumferential heat conduction in the outer wall, which remains near the interface for small values of conductivity ratio (KR) and penetrates the wall when conductivity ratio (KR) has large values.

8.2.1.5. Temperature Profile

Figures (8.19-8.22) explain the phenomenon by considering the temperature profiles across the channel at widest ($\psi = 0$) and narrowest gaps ($\psi = 1$) for cases (3.I) and (3.O). These figures are depicting the same results of the temperature values on inner and outer
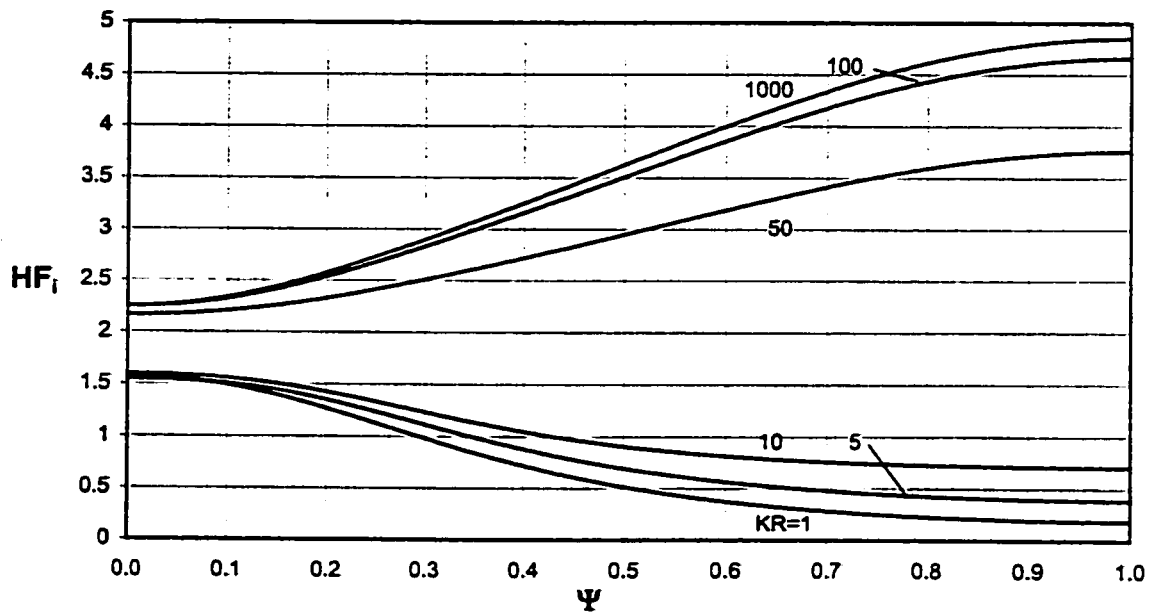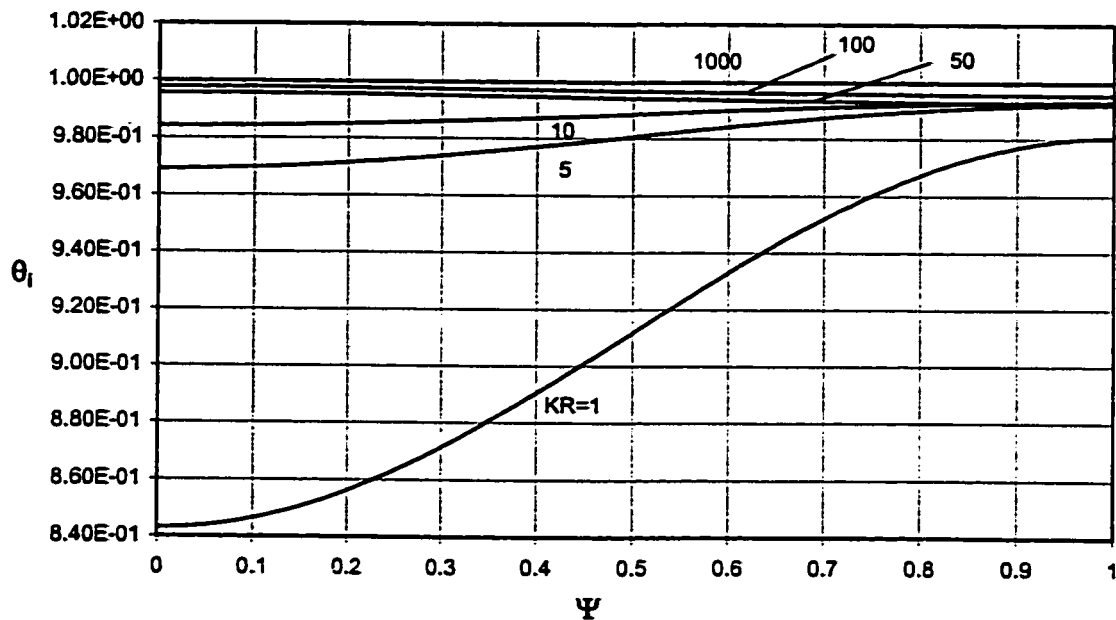
Fig.8.15. Circumferential Variation of Temperature on Inner Interface at an Axial (vertical) Location of 1.65×10^{-3} for Different Values of Conductivty Ratio (Case 3.I)

$NR_2 = 0.5$, Inner Wall Thickness = 0.1, Outer Wall Thickness = 0.2, E = 0.5
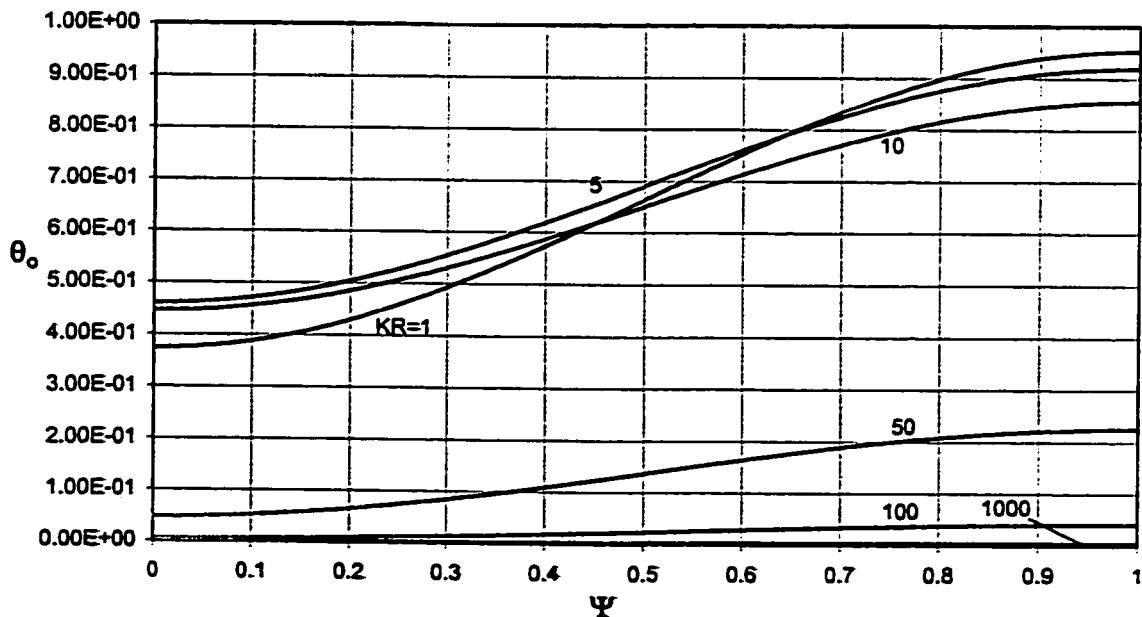
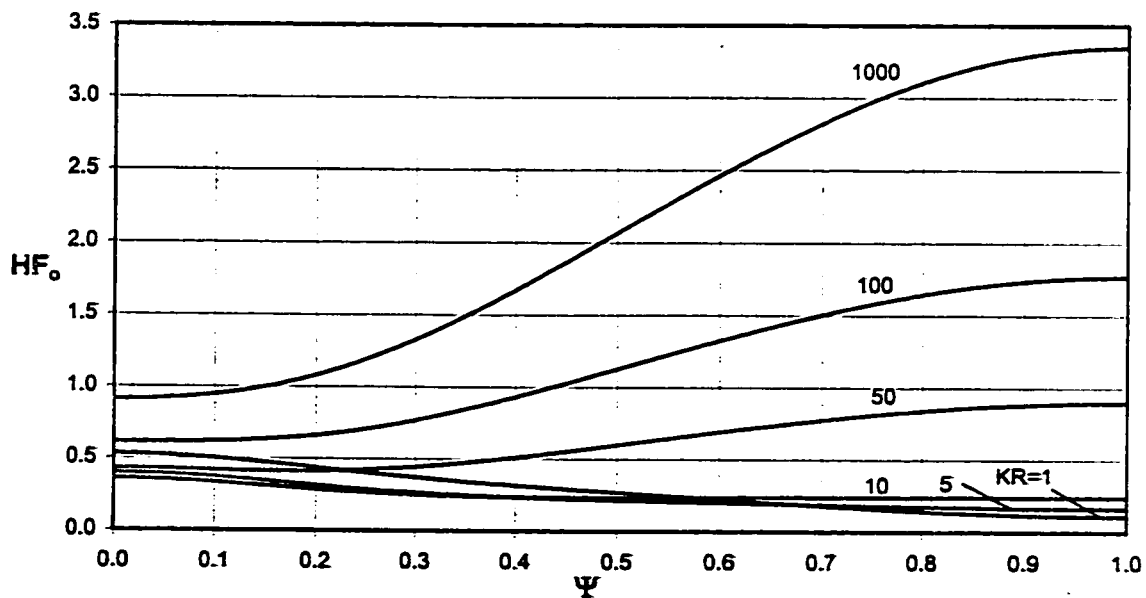**Fig.8.16.** Circumferential Variation of Temperature on Outer Interface at an Axial (vertical) Location of 1.65×10^{-3} for Different Values of Conductivty Ratio (Case 3.I)

$NR_2 = 0.5$, Inner Wall Thickness = 0.1, Outer Wall Thickness = 0.2, E = 0.5
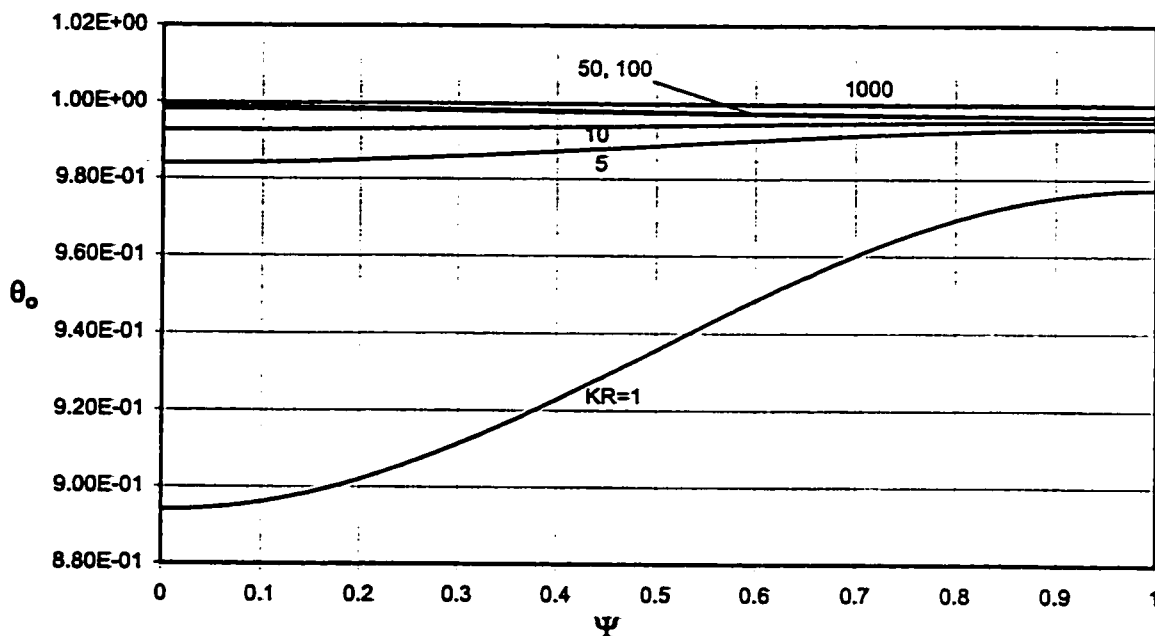
Fig.8.17. Circumferential Variation of Temperature on Outer Interface at a Channel Height of 3.86×10^{-3} for Different Values of Conductivty Ratio (Case 3.O)

$NR_2 = 0.5$, Inner Wall Thickness = 0.1, Outer Wall Thickness = 0.2, E = 0.5
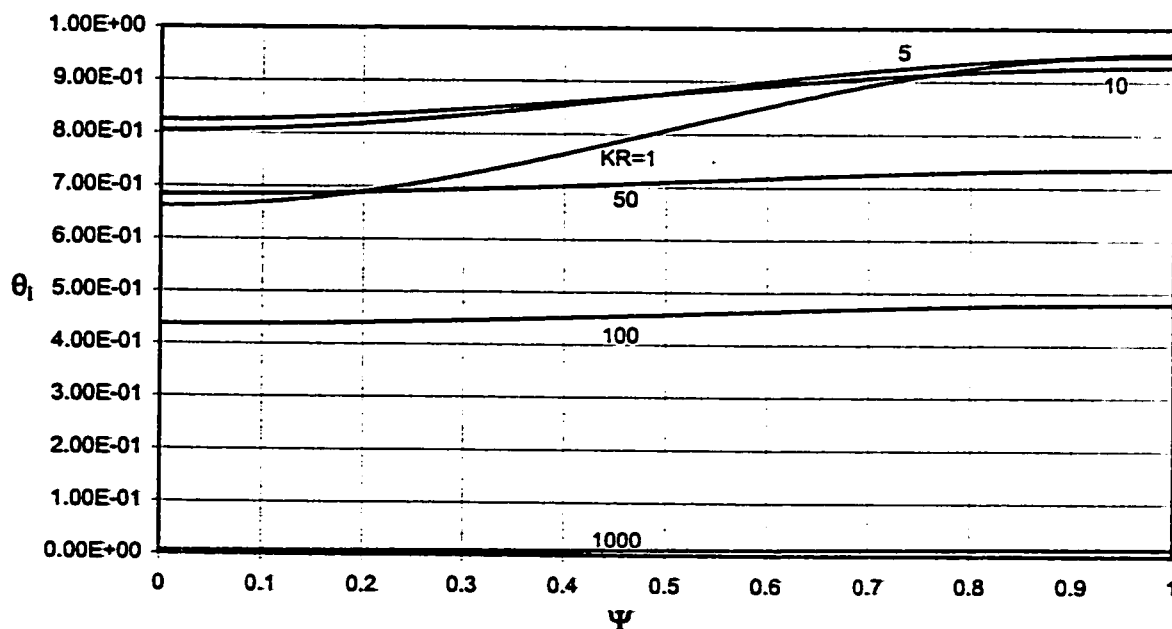
Fig.8.18. Circumferential Variation of Temperature on Inner Interface at a Channel Height of 3.86×10^{-3} for Different Values of Conductivty Ratio (Case 3.O)

$NR_2 = 0.5$, Inner Wall Thickness = 0.1, Outer Wall Thickness = 0.2, E = 0.5

Fig. 8.19. Temperature Profile Across the Channel at the Widest Gap (Ψ=0) at an Axial (vertical) Location of 1.65×10^{-3} for Different Valueso of Conductivity Ratio (KR) (Case 3.I)

$NR_2 = 0.5$, Inner Wall Thickness = 0.1, Outer Wall Thickness = 0.2, E = 0.5

Fig. 8.20. Temperature Profile Across the Channel at the Narrowest Gap (Ψ=1) at an Axial (vertical) Location of 1.65×10^{-3} for Different Valueso f Conductivity Ratio (KR) (Case 3.I)

$NR_2 = 0.5$, Inner Wall Thickness = 0.1, Outer Wall Thickness = 0.2, E = 0.5

Fig. 8.21. Temperature Profile Across the Channel at the Widest Gap (Ψ=0) for Different Valueso of Conductivity Ratio (KR) (Case 3.O)

NR_2 = 0.5, Inner Wall Thickness = 0.1, Outer Wall Thickness = 0.2, E = 0.5

**Fig. 8.22.** Temperature Profile Across the Channel at the Narrowest Gap (Ψ=1) for Different Valueso of Conductivity Ratio (KR) (Case 3.O)

NR_2 = 0.5, Inner Wall Thickness = 0.1, Outer Wall Thickness = 0.2, E = 0.5

solid-fluid interfaces as already explained for circumferential temperature values for these cases. The most important observation is the decrease of temperature gradient in the walls with increasing conductivity ratio (KR).

8.2.1.6. Average Heat Flux (AVHF)

Figures (8.23) and (8.24) show the average value of heat flux on inner (case 3.I) and outer (case 3.O) solid-fluid interfaces, respectively. The increase in the average heat flux is directly linked to the local heat flux. The heat flux increase in turn increases the amount of heat entering the fluid, but due to high thermal conductivity, more heat is conducted in the opposite wall, insulated at one side.

8.2.1.7. Total Heat Absorbed ($\overline{Q}$)

The total heat absorbed ($\overline{Q}$) by the fluid follows the same trend as for the flow rate for cases (3.I) and (3.O) as can be seen in Figs. (8.25) and (8.26) for eccentricity (E = 0.5). When the amount of heat absorbed by the fluid decreases, it also reduces the mean fluid temperature. The axial momentum of the fluid flow decreases and with it decreases the buoyancy force, hence driving less fluid flow in the channel. We have determined the value of conductivity ratio (KR) beyond which the heat absorbed by the fluid decreases for only one case, i.e. E = 0.5, as shown in Fig. (8.27). We can infer from the above discussion that, for the investigated geometry (NR_2=0.5, inner wall thickness=0.1, outer wall thickness=0.2 and E=0.5), we can have shorter channels to induce a specific flow rate of the fluid by taking the material of the cylinders having conductivity ratio (KR) in a

Fig.8.25. Total Heat Absorbed versus Channel Height (L) for Different Values of Conductivity Ratio (KR) (Case 3.I)

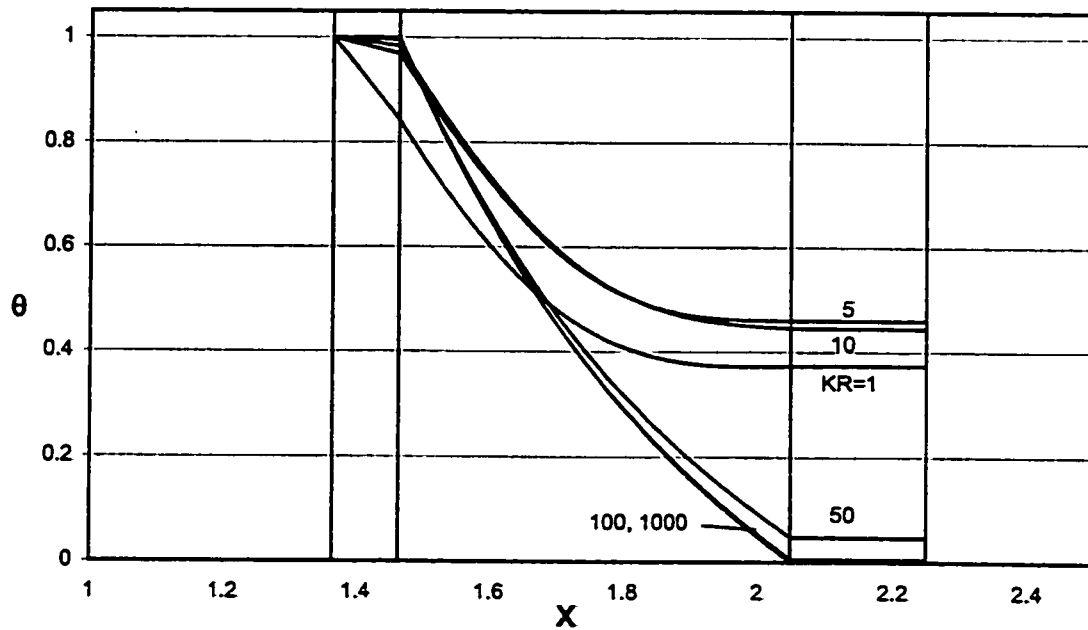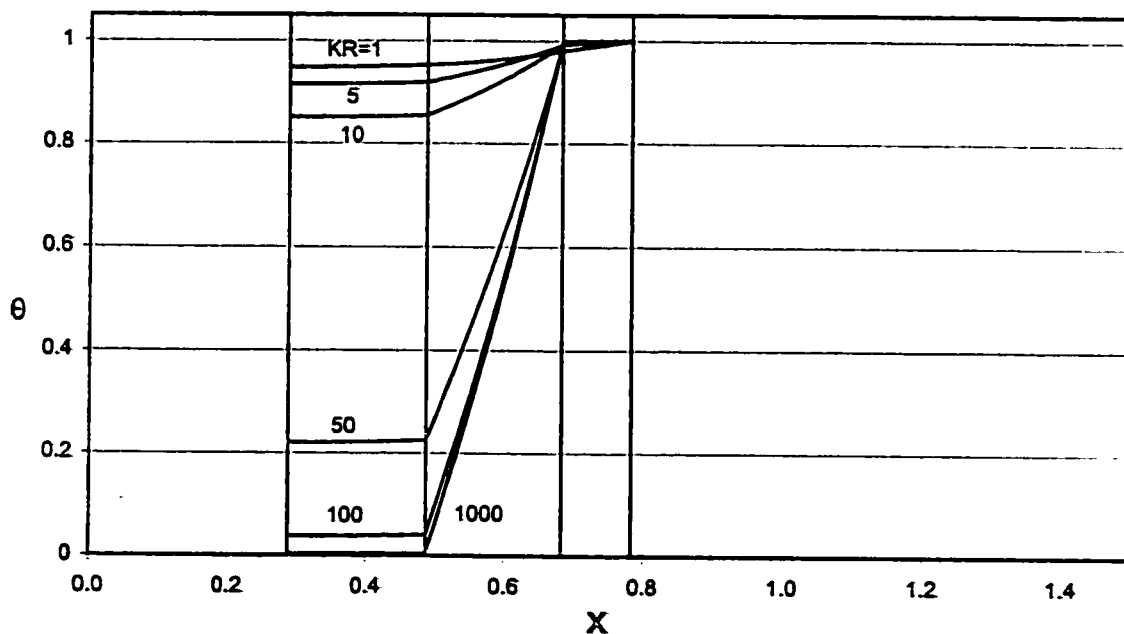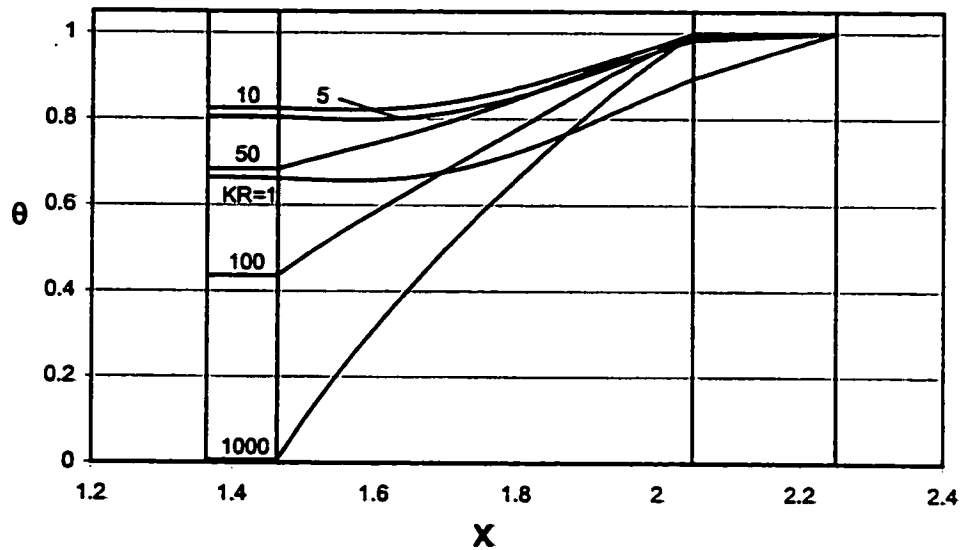$NR_2 = 0.5$, Inner Wall Thickness = 0.1, Outer Wall Thickness = 0.2, E = 0.5

Fig.8.26. Total Heat Absorbed versus Channel Height (L) for Different Values of Conductivity Ratio (KR) (Case 3.O)

$NR_2 = 0.5$, Inner Wall Thickness = 0.1, Outer Wall Thickness = 0.2, E = 0.5

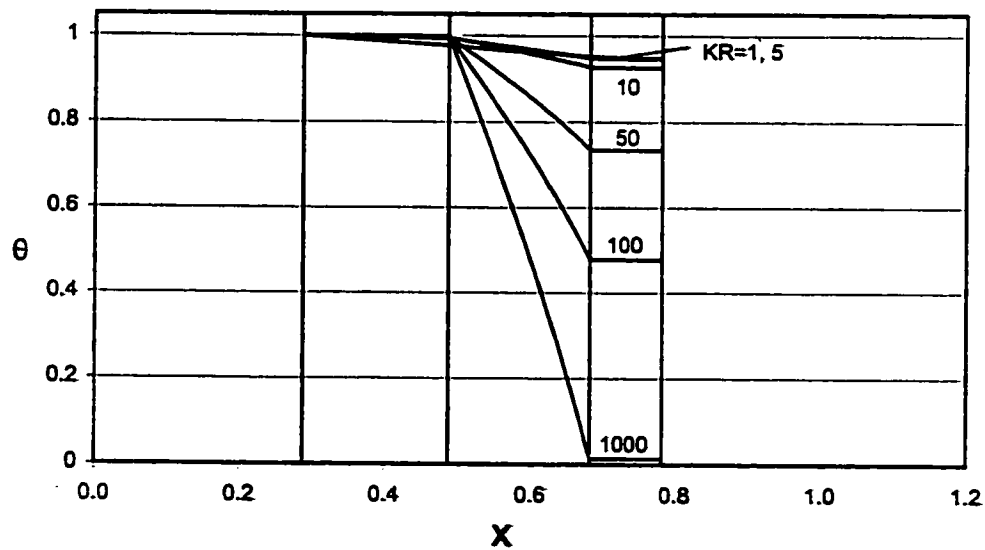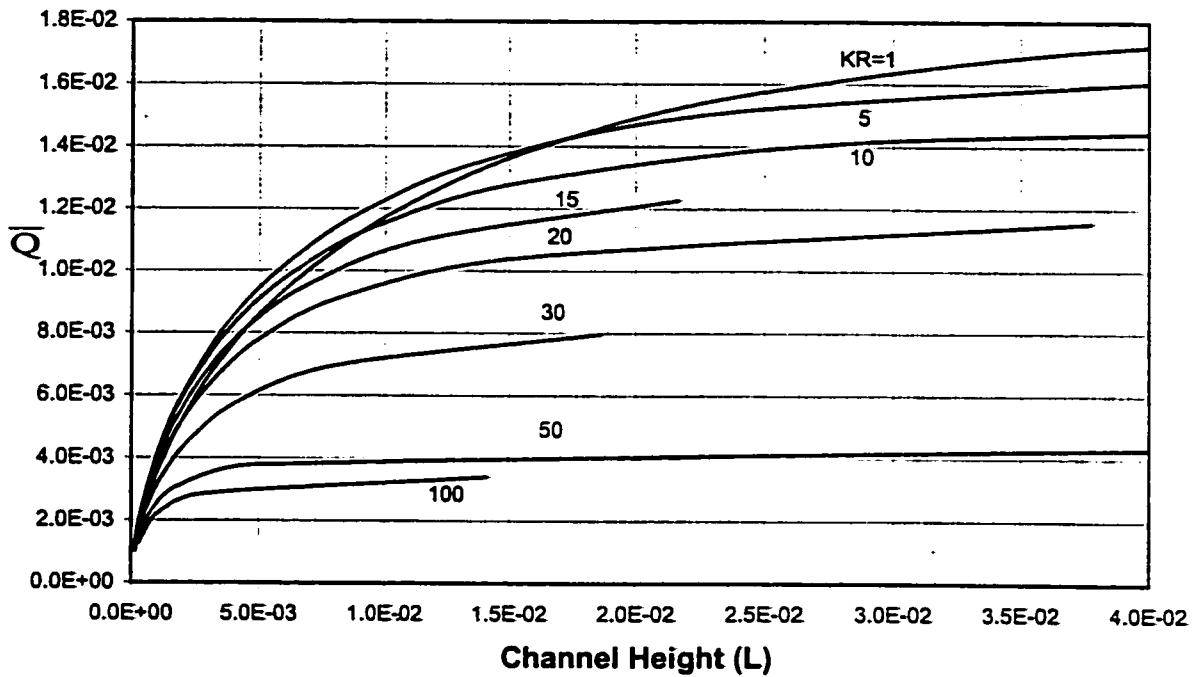**Fig.8.27.** Total Heat Absorbed for Different Values of Conductivity Ratios (KR) at Different Channel Heights (Case 3.O)

$NR_2 = 0.5$, Inner Wall Thickness $= 0.1$, Outer Wall Thickness $= 0.2$, $E = 0.5$

range of 9-10 imposing the boundary conditions of third kind having outer surface isothermally heated wall and inner insulated wall.

8.2.2. Effect of Eccentricity (E)

The results to be presented here are obtained for an annulus radius ratio 0.5, inner and outer wall thicknesses of 0.1 and 0.2, respectively, and conductivity ratio 10.

8.2.2.1. Induced Flow Rate (F)

Figures (8.28) and (8.29) show the variation of the flow rate with the channel height for different values of eccentricity for cases (3.I) and (3.O), respectively. In both cases, increasing the eccentricity, at any given radius ratio and conductivity ratio, results in an increase in the induced flow rate. This is attributed to the reduced resistance to fluid flow at the widest gap ($\Psi = 0$), which enables the fluid to flow with greater velocity at the same gap and hence absorbing more heat. The result is an increase in the mean fluid temperature and hence the induced flow rate. The magnitude of the flow rate, at any specific channel height, is higher for case (3.O) as compared to case (3.I). This indicates that more heat flows through the outer wall to the fluid in case (3.O) due to its larger surface area than that of the inner wall. This imposes a direct impact on the mean fluid temperature and hence the induced flow rate. The switching of the boundary conditions from case (3.I) to case (3.O) results in a change in the behavior of the heat flux and temperature values on the inner and outer solid-fluid interfaces, as discussed hereunder.

Fig. 8.28. Variation of Flow Rate with Channel Height for Different Values of Eccentricity (Case 3.I)

$NR_2 = 0.5$, Inner Wall Thickness = 0.1, Outer Wall Thickness = 0.2, KR = 10

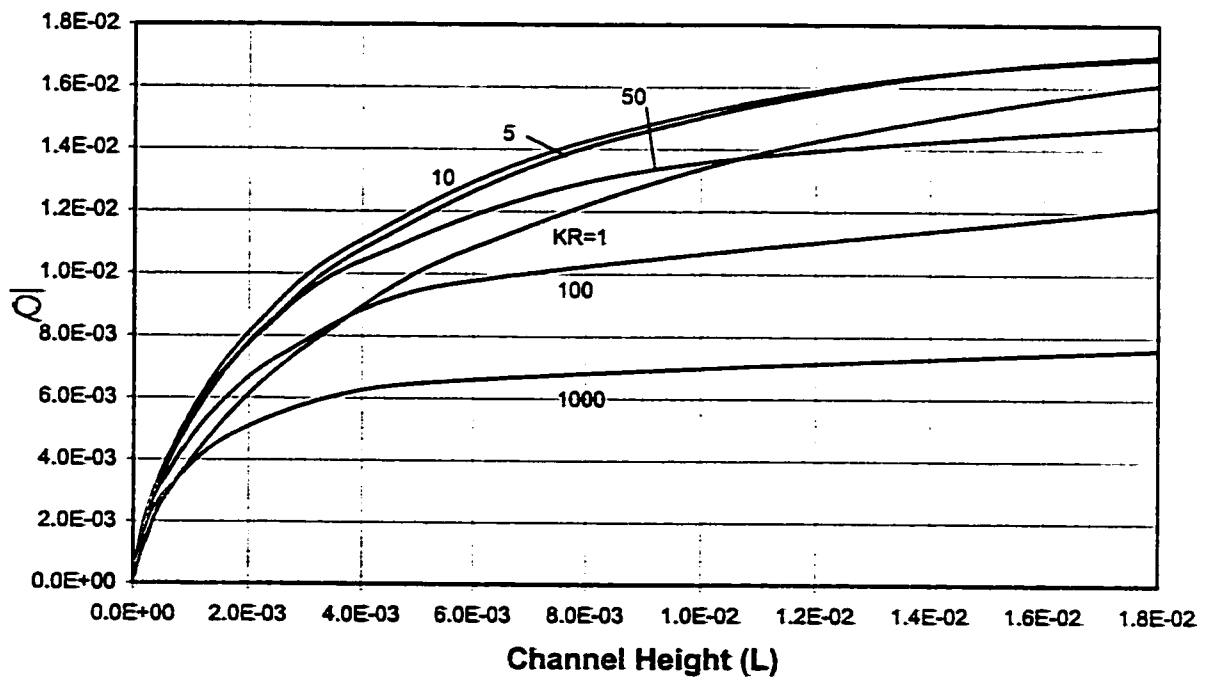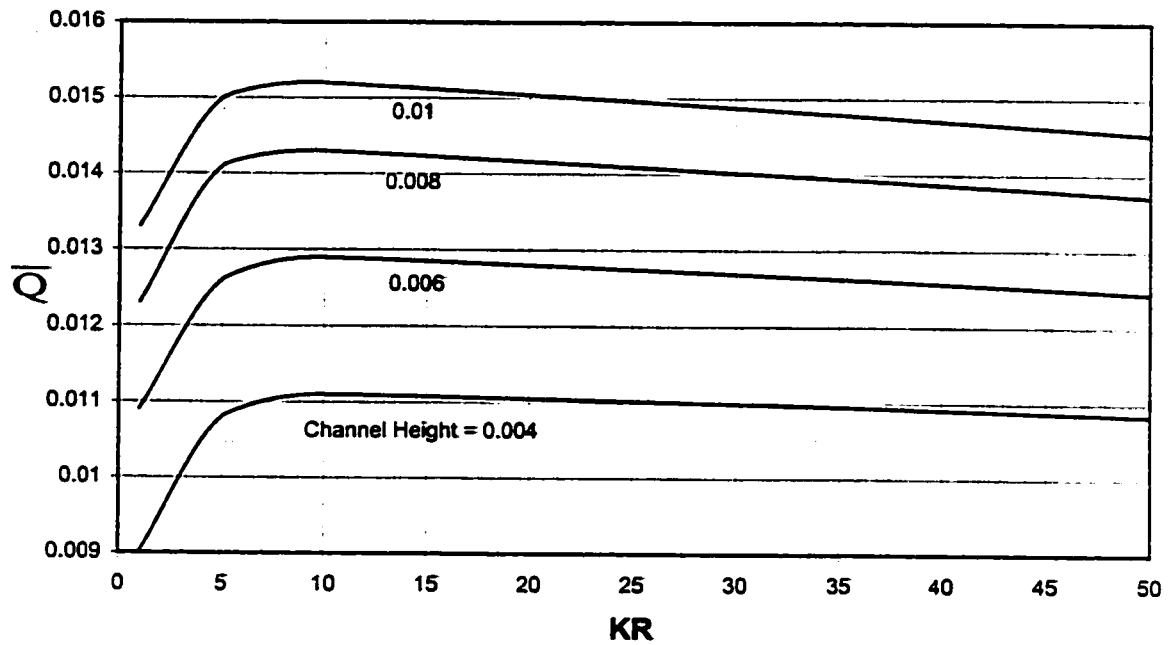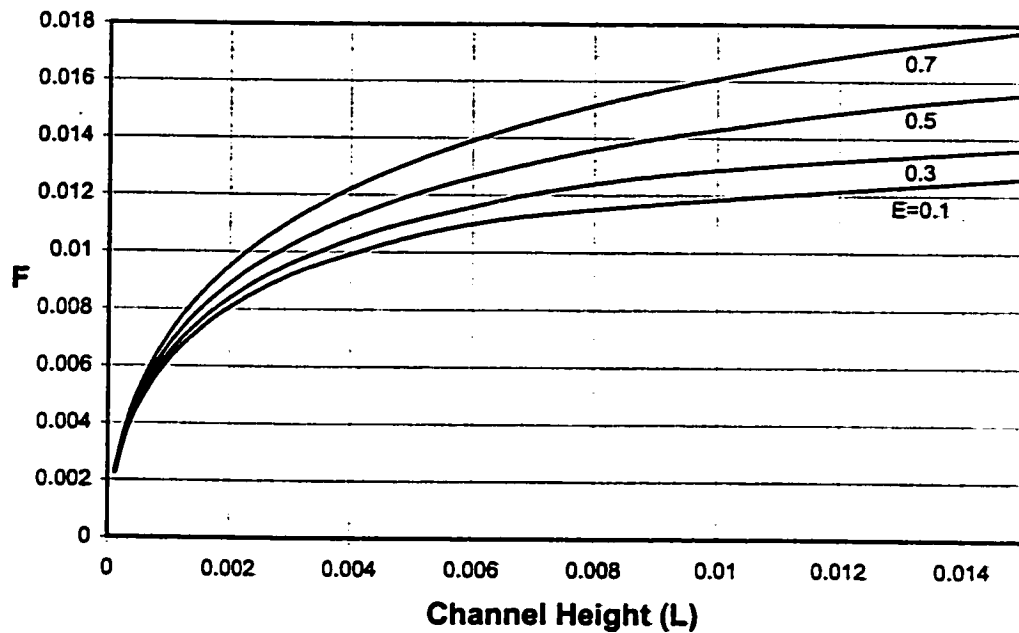**Fig. 8.29.** Variation of Flow Rate with Channel Height for Different Values of Eccentricity (Case 3.O)

$NR_2 = 0.5$, Inner Wall Thickness = 0.1, Outer Wall Thickness = 0.2, KR = 10

Figures (8.30-8.37), obtained for a flow rate of 0.01125 for case (3.I) and 0.015 for case (3.O), explain the phenomenon. All the circumferential analysis is carried out at an axial (vertical) location of 2.86×10^{-3} for case (3.I) and 4.36×10^{-3} for case (3.O).

8.2.2.2. Local Heat Flux (HF)

Figure (8.30) shows circumferential variation of the local heat flux on the inner solid-fluid interface with eccentricity for case (3.I). Here, we can see that, in general, increasing the eccentricity reduces the local heat flux values on inner interface. The reason is that with the increase of eccentricity, the heat flow at the narrowest gap ($\Psi = 1$) increases but the outer insulated wall does not allow the heat to escape, thus, resulting in a rise in the temperature on its outer interface. This reduces the temperature difference between the outer and inner interfaces, hence reducing the incoming heat flux. This decreasing heat flux with increasing eccentricity (E) on the interface next to the heated wall does not occur for case (3.O) as shown in Fig. (8.31). The higher the eccentricity, the higher will be the local heat flux on outer interface. The increased flow of fluid at widest gap absorbs more heat when eccentricity increases and enables more heat to flow through the outer interface indicating an effective contribution of hydrodynamics in the heat transfer. The inner insulated wall has very little effect on the outer wall heat flux. The local heat fluxes on the interfaces next to the adiabatic walls for both cases (3.I and 3.O) have zero values and hence are not presented.
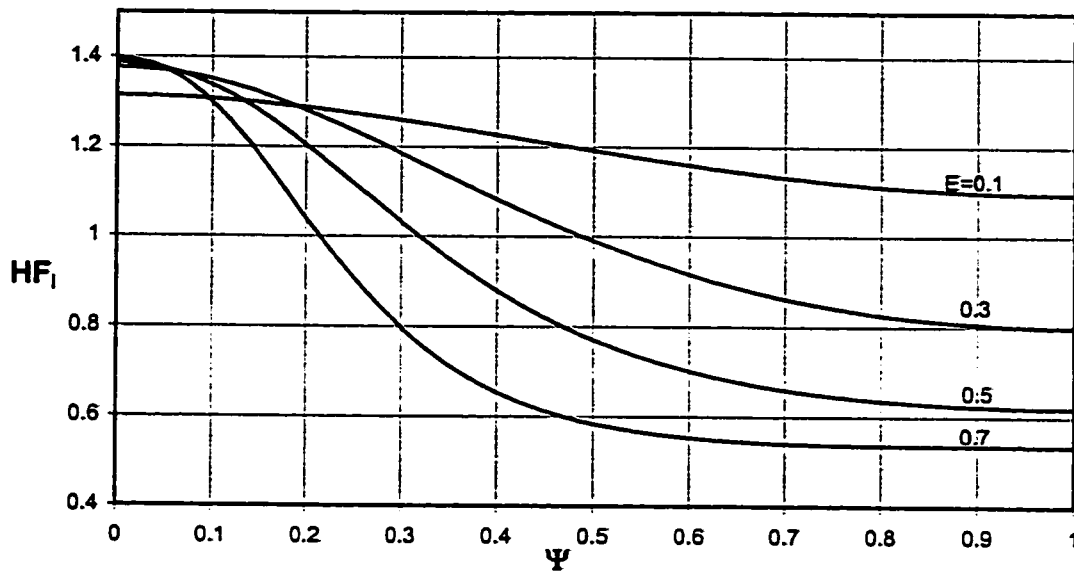
Fig.8.30. Circumferential Heat Flux on Inner Interface at an Axial
(vertical) Location of 2.86×10^{-3} for Different Values of Eccentricity
(Case 3.I)

$NR_2 = 0.5$, Inner Wall Thickness = 0.1, Outer Wall Thickness = 0.2, KR = 10

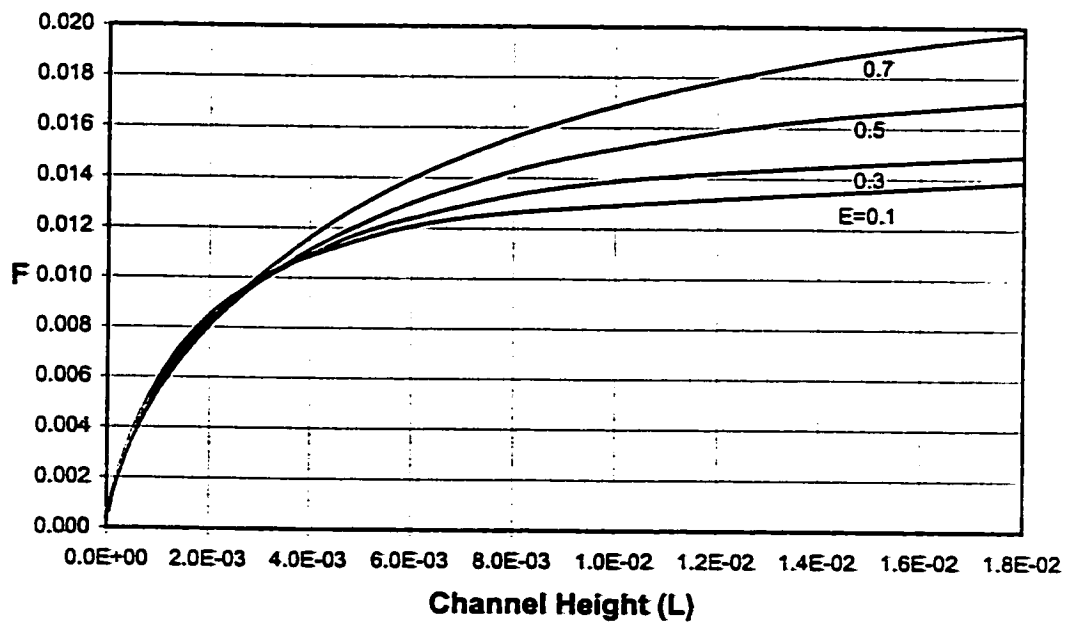**Fig.8.31.** Circumferential Heat Flux on Outer Interface at an Axial
(vertical) Location of 4.36×10^{-3} for Different Values of Eccentricity
(Case 3.O)

$NR_2 = 0.5$, Inner Wall Thickness = 0.1, Outer Wall Thickness = 0.2, KR = 10

Fig.8.32. Circumferential Variation of Temperature on inner Interface at an Axial (vertical) Location of 2.86×10^{-3} for Different Values of Eccentricity (Case 3.I)

$NR_2 = 0.5$, Inner Wall Thickness = 0.1, Outer Wall Thickness = 0.2, KR = 10

Fig.8.33. Circumferential Variation of Temperature on Outer Interface at an Axial (vertical) Location of 2.86×10^{-3} for Different Values of Eccentricity (Case 3.I)

$NR_2 = 0.5$, Inner Wall Thickness = 0.1, Outer Wall Thickness = 0.2, KR = 10

Fig.8.34. Circumferential Temperature Variation on Outer Interface at an Axial (vertical) Location of 4.36×10^{-3} for Different Values of Eccentricity (Case 3.O)

$NR_2 = 0.5$, Inner Wall Thickness = 0.1, Outer Wall Thickness = 0.2, KR = 10

Fig.8.35. Circumferential Temperature Variation on inner Interface at an Axial (vertical) Location of 4.36×10^{-3} for Different Values of Eccentricity (Case 3.O)

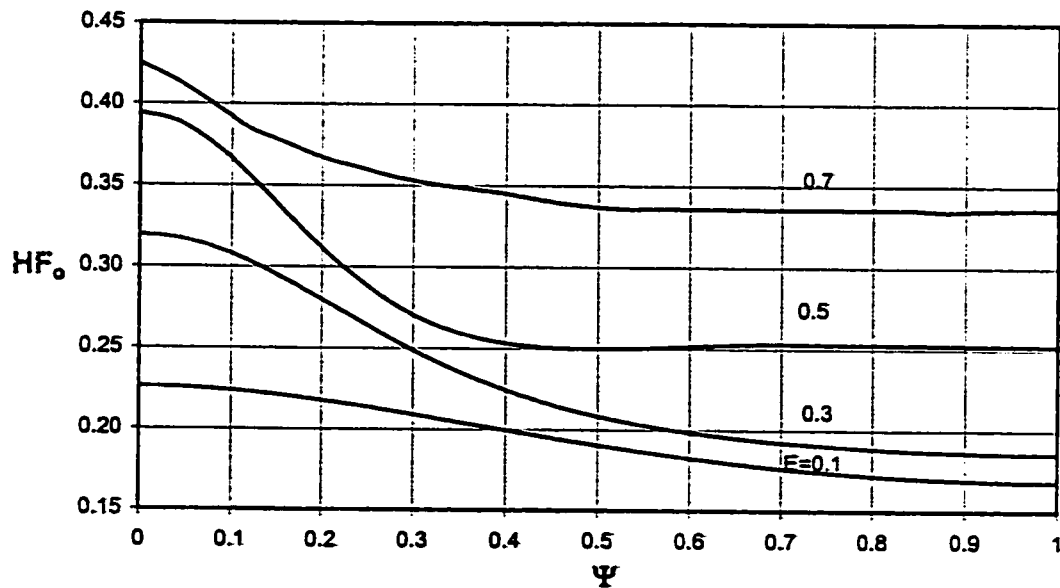$NR_2 = 0.5$, Inner Wall Thickness = 0.1, Outer Wall Thickness = 0.2, KR = 10

8.2.2.5. Total Heat Absorbed ($\overline{Q}$)

Figures (8.38) and (8.39) show the total heat absorbed ($\overline{Q}$) by the fluid varying with eccentricity for case (3.I) and (3.O), respectively. Both cases show same trend of having increased heat absorbed by the fluid with eccentricity. The only difference is the magnitude of heat absorbed which is higher for case (3.O). The reason is the bigger surface area of outer solid-fluid interface than the inner interface allowing more heat to flow through it into the fluid. The graphical comparison is presented in Fig. (8.40). The presence of insulated wall in each case does not allow the heat to flow through this wall. The only way out for the heat is by free convection, which causes the mean bulk temperature and the buoyancy force to increase, thus sucking more fluid in the channel. Hence, for given annulus radius ratio, conductivity ratio and wall thicknesses, the heat transfer in the channel is carried out only by free convection. Furthermore, this analysis can be utilized to determine the heat transfer for a specific channel height with the help of Figs. (8.38) and (8.39) for cases (3.I) and (3.O), respectively, at any particular eccentricity for given conductivity ratio, wall thicknesses and radius ratio.

8.2.3. Effect of Radius Ratio (NR_2)

This analysis is carried out for an annulus of eccentricity 0.5, inner and outer walls thickness of 0.1 and 0.2, respectively, and conductivity ratio 10.

Fig.8.38. Total Heat Absorption versus Channel Height for
Different Values of Eccentricity (Case 3.I)

$NR_2 = 0.5$, Inner Wall Thickness = 0.1, Outer Wall Thickness = 0.2, KR = 10

Fig.8.39. Total Heat Absorption versus Channel Height for
Different Values of Eccentricity (Case 3.O)

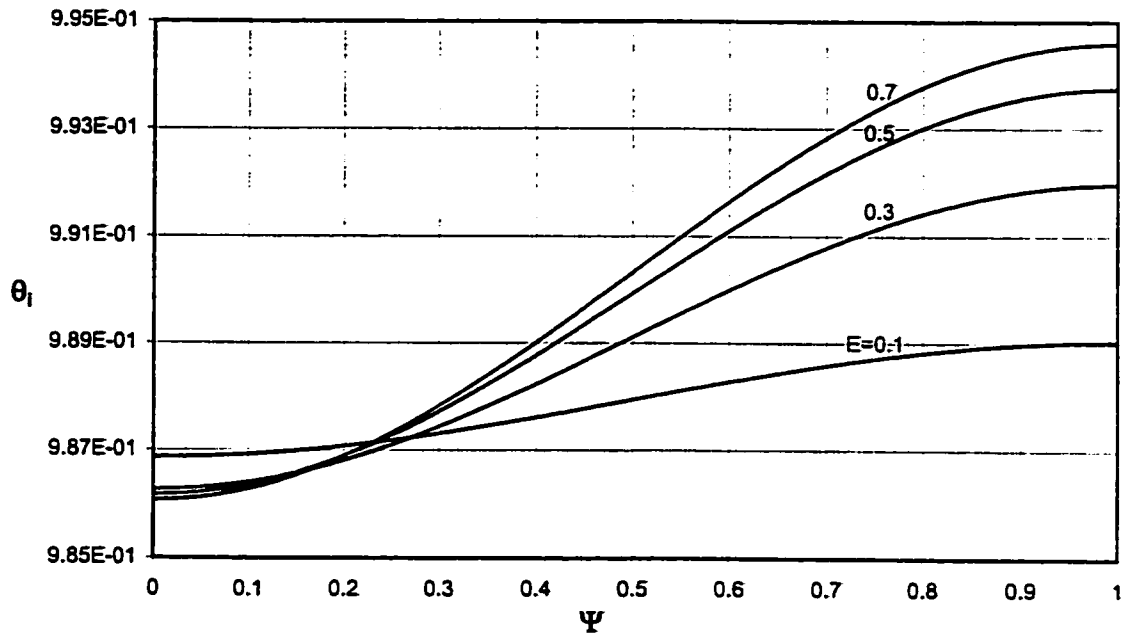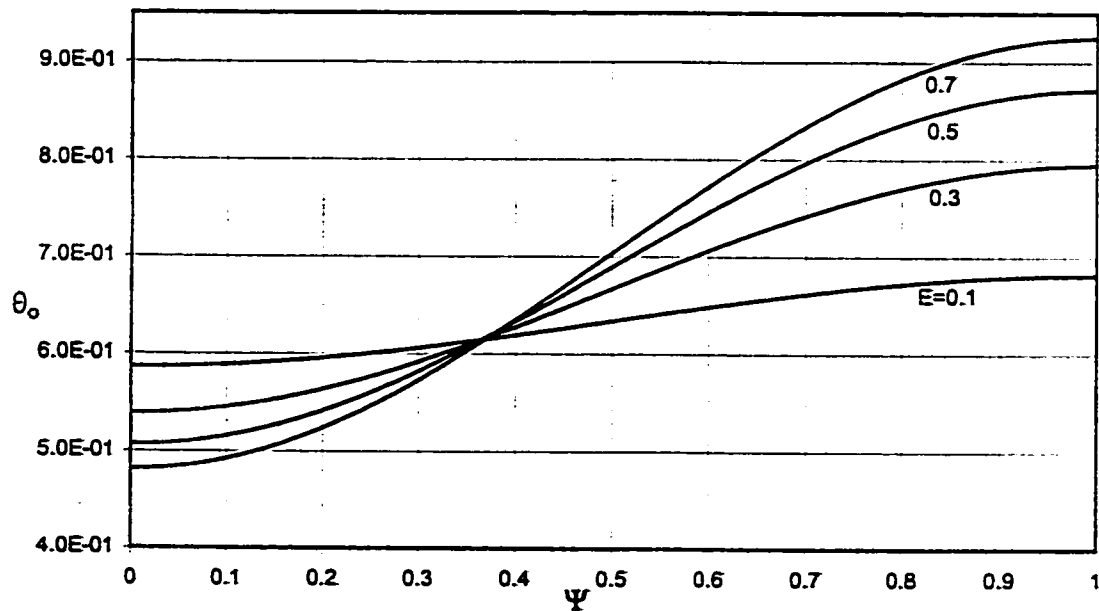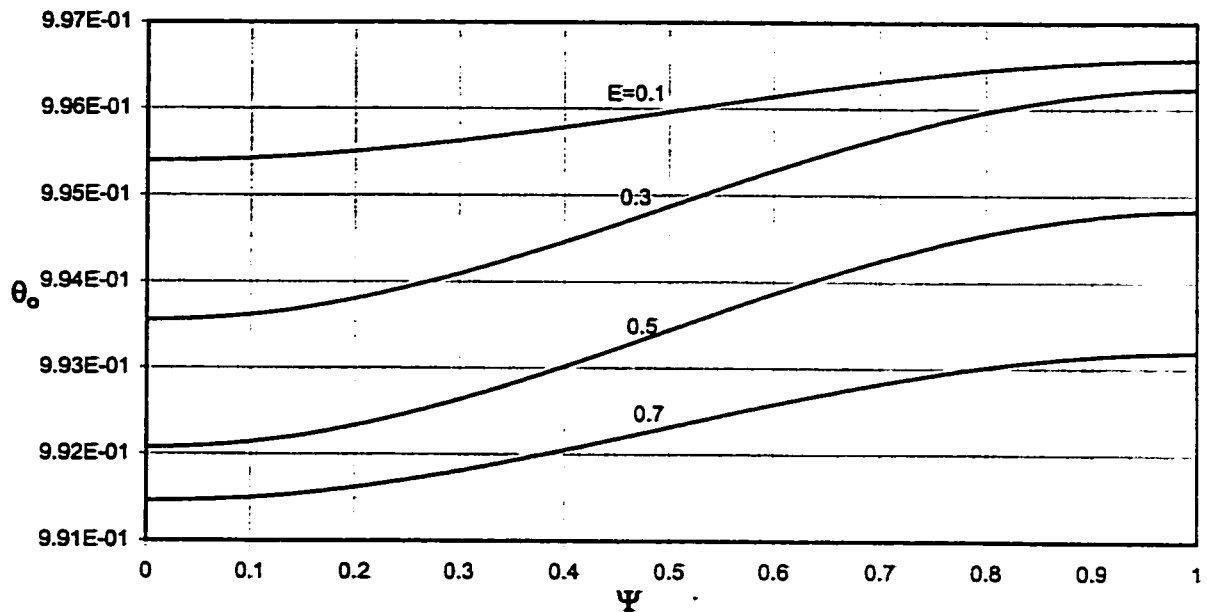$NR_2 = 0.5$, Inner Wall Thickness = 0.1, Outer Wall Thickness = 0.2, KR = 10

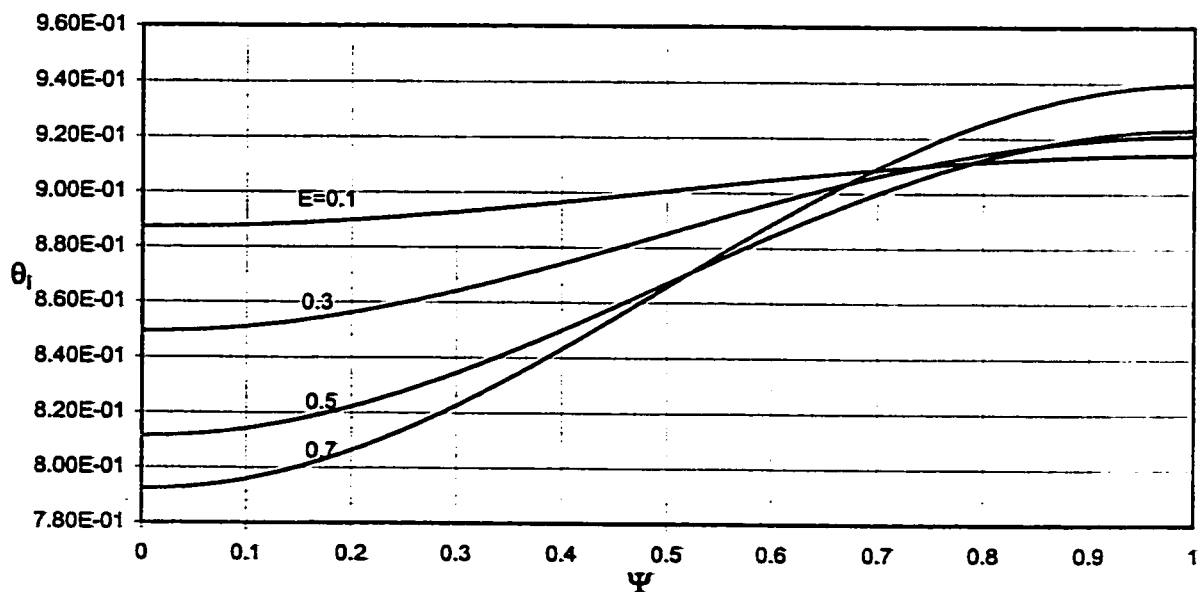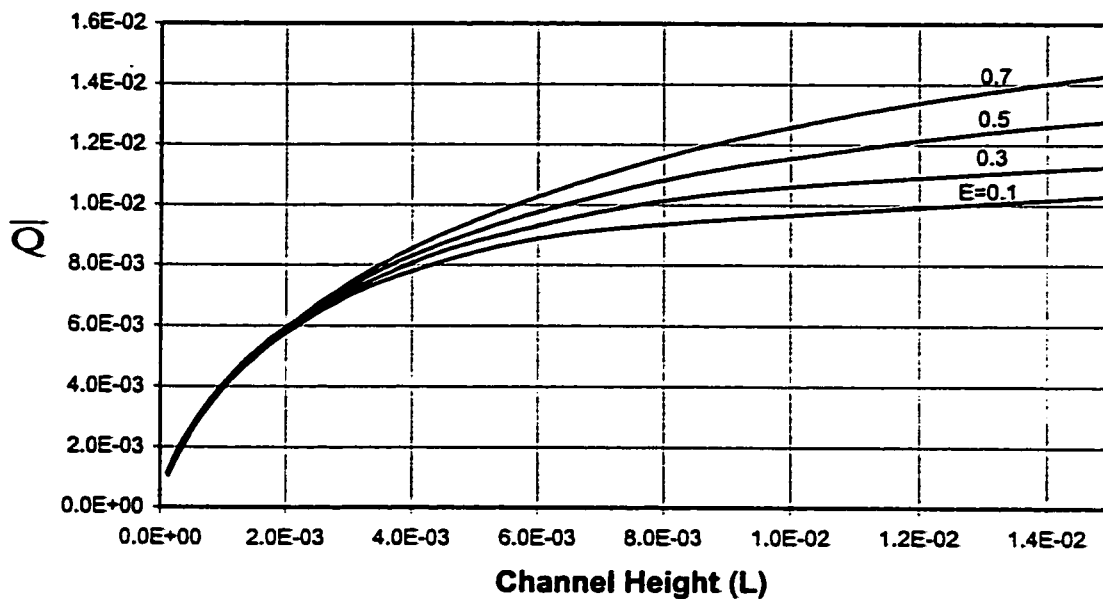**Fig.8.40.** Comparison of Total Heat Absorbed for Different Values of Eccentricity among cases (3.I) and (3.O)

$NR_2 = 0.5$, Inner Wall Thickness = 0.1, Outer Wall Thickness = 0.2, KR = 10

8.2.3.1. Induced Flow rate (F)

Figures (8.41) and (8.42) show the variation of dimensionless flow rate with channel height (L) for different values of annulus radius ratio (NR_2) for case (3.I). For given eccentricity, wall thicknesses and conductivity ratio, increasing the annulus radius ratio increases the dimensionless flow rate. This is also true for case (3.O) as can be seen in Figs. (8.43) and (8.44).

Figures (8.45) and (8.46) are obtained by plotting the values of dimensionless flow rate at a channel height (L) of 0.005 ($F_{0.005}$) and maximum values of the same parameter (F_{max}) against the corresponding annulus radius ratios (NR_2), respectively, for case (3.I). Both figures show increasing trend of the dimensionless flow rate with increasing radius ratio. Similar trend is observed for case (3.O) shown in Figs. (8.47) and (8.48). Fig. (8.47) is obtained at the same channel height (L) as for case (3.I), i.e. 0.005. F_{max} is the maximum flow rate that can be sucked into the channel of a specific radius ratio (NR_2). This can be seen in Figs. (8.41-8.44) showing the curves to become horizontal after a certain channel height indicating the maximum possible induced flow rate in the channel for given eccentricity (E), conductivity ratio (KR), wall thicknesses and radius ratio (NR_2).

In order to explain the flow behavior further, the dimensionless flow rate (F) is converted into its dimensional form (f, m^3/sec) and plotted against the corresponding radius ratios, as shown in Fig. (8.49) for case (3.I). Furthermore, the dimensional flow rate per unit annulus area is calculated and plotted against the corresponding radius ratios (NR_2), shown in Fig. (8.50), due to the reason explained earlier in section 7.2.3. Similar

Fig.8.41. Variation of Flow Rate with Channel Height for Different Values of Radius Ratio (Case 3.I)

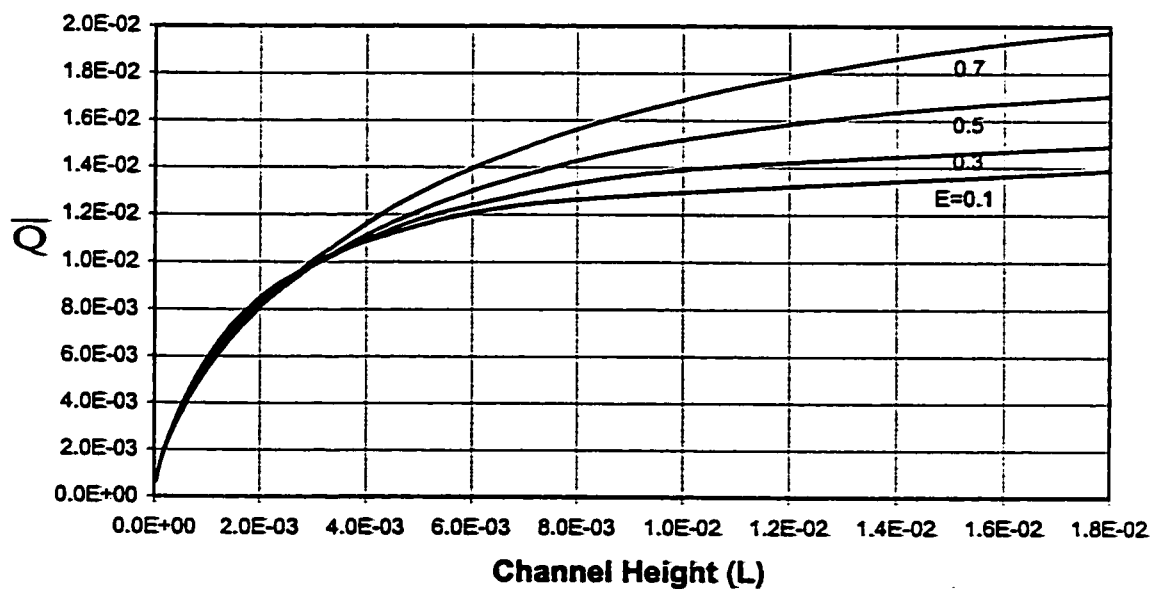KR = 10, Inner Wall Thickness = 0.1, Outer Wall Thickness = 0.2, E = 0.5

Fig.8.42. Variation of Flow Rate with Channel Height for Radius Ratio = 0.7 (Case 3.I)

KR = 10, Inner Wall Thickness = 0.1, Outer Wall Thickness = 0.2, E = 0.5

Fig.8.43. Variation of Flow Rate with Channel Height for Different Values of Radius Ratio (Case 3.0)

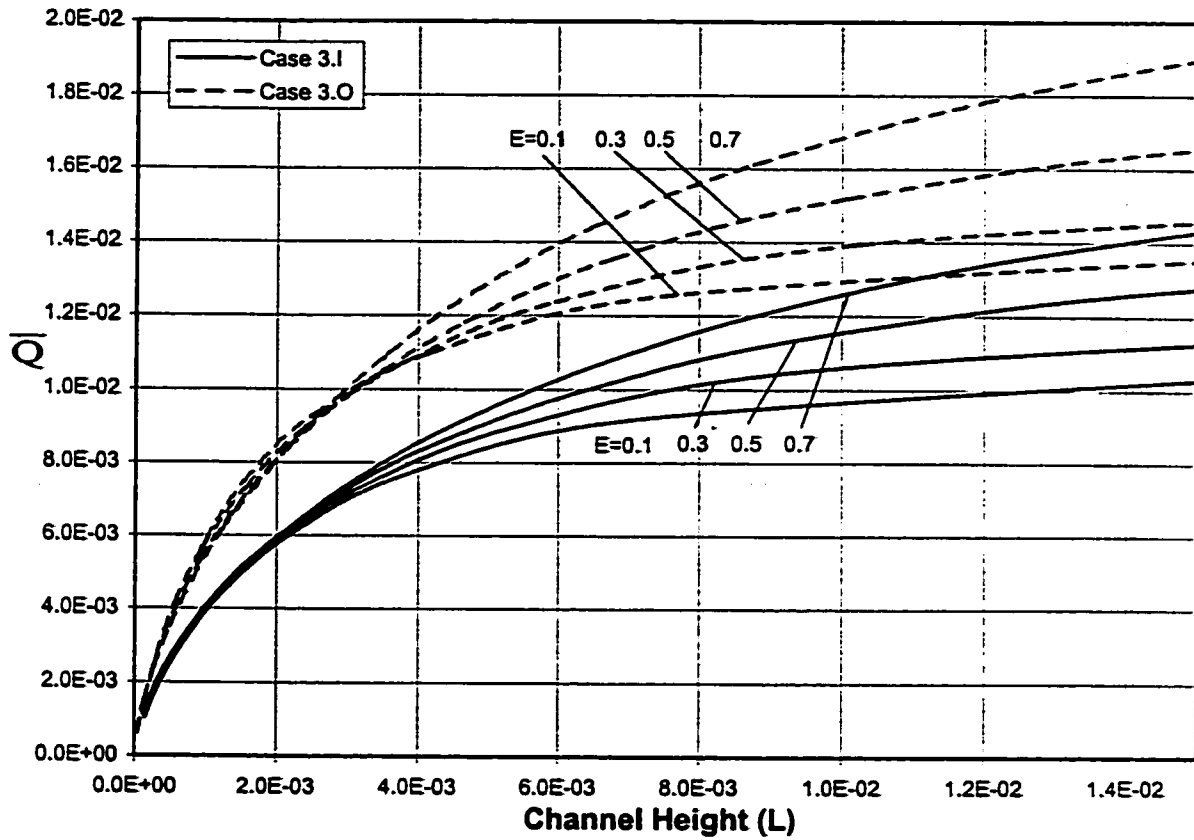KR = 10, Inner Wall Thickness = 0.1, Outer Wall Thickness = 0.2, E = 0.5

Fig.8.44. Variation of Flow Rate with Channel Height for Different Values of Radius Ratio (Case 3.0)

KR = 10, Inner Wall Thickness = 0.1, Outer Wall Thickness = 0.2, E = 0.5
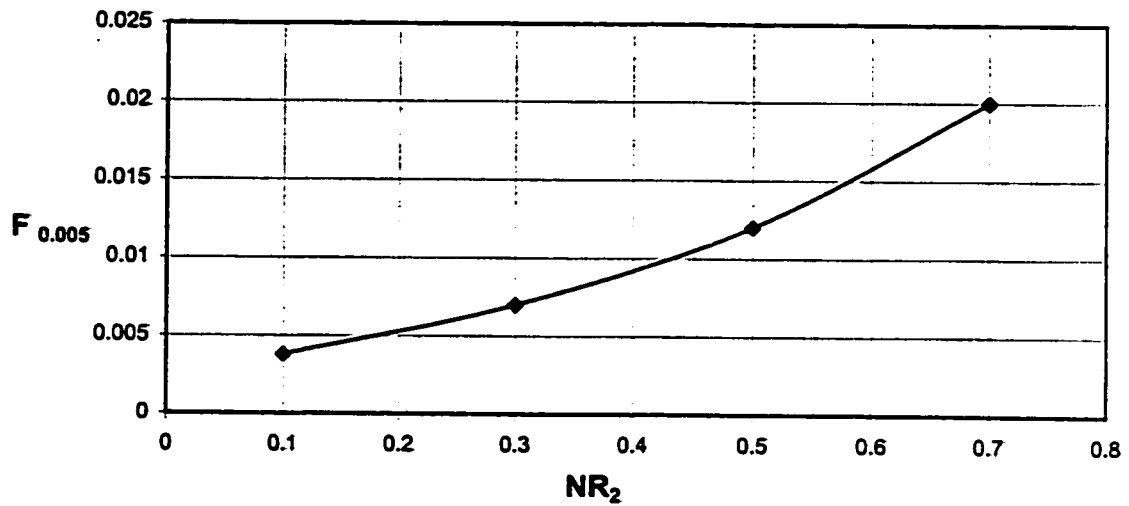
Fig.8.45. Flow Rate Varation with Radius ratio at a Channel
Height of 0.005 (Case 3.I)

KR = 10, Inner Wall Thickness = 0.1, Outer Wall Thickness = 0.2, E = 0.5
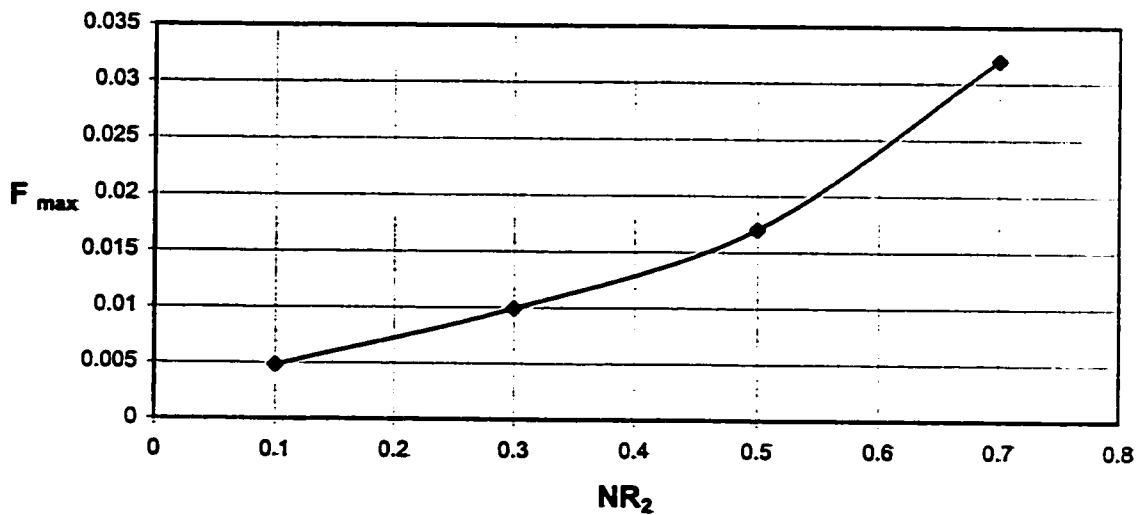
Fig.8.46. Maximum Flow Rate Variation with Radius Ratio
(Case 3.I)

KR = 10, Inner Wall Thickness = 0.1, Outer Wall Thickness = 0.2, E = 0.5

...
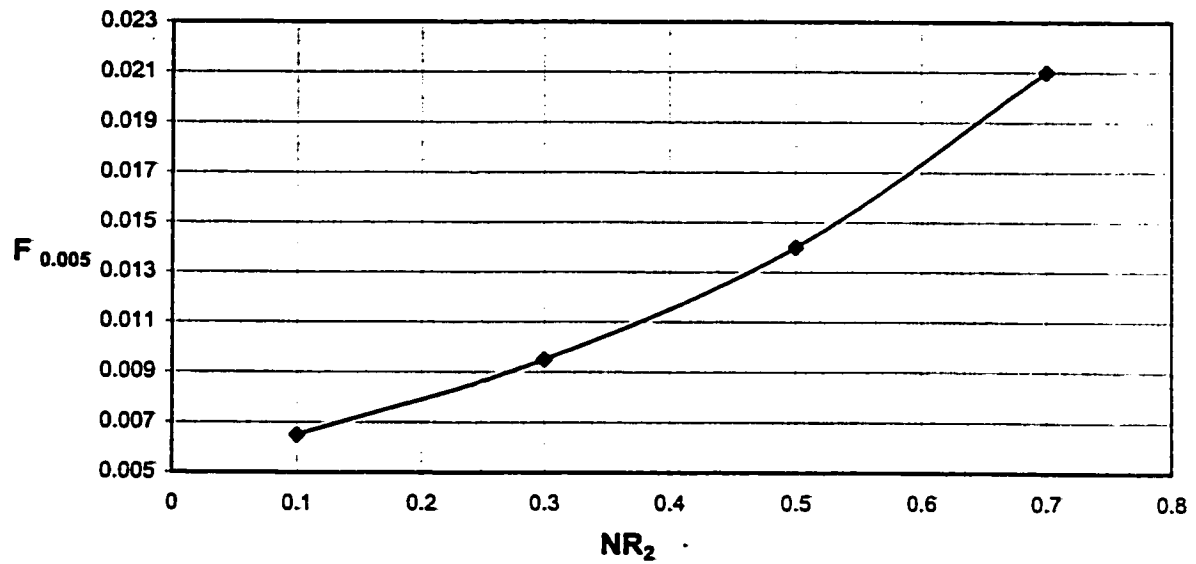
Fig.8.47. Flow Rate Varation with Radius ratio at a Channel
Height of 0.005 (Case 3.O)

KR = 10, Inner Wall Thickness = 0.1, Outer Wall Thickness = 0.2, E = 0.5
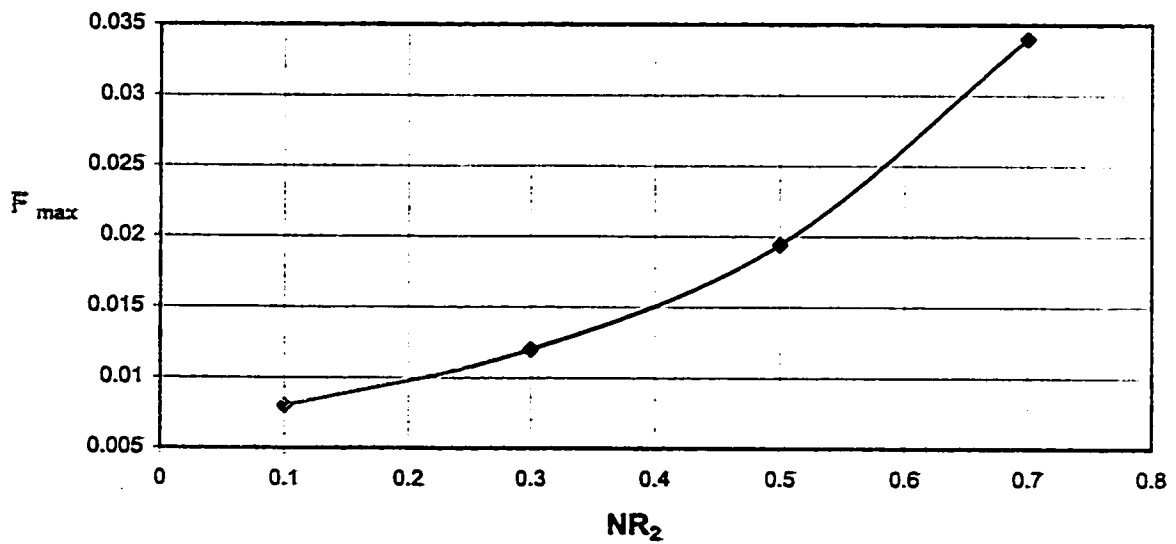
Fig.8.48. Maximum Flow Rate Variation with Radius Ratio
(Case 3.O)

KR = 10, Inner Wall Thickness = 0.1, Outer Wall Thickness = 0.2, E = 0.5

Fig.8.49. Dimensional Flow Rate Variation with
Radius Ratio (NR$_2$) (Case 3.I)

KR = 10, Inner Wall Thickness = 0.1, Outer Wall Thickness = 0.2, E = 0.5

Fig.8.50. Dimensional Flow Rate per Unit Area
Varying with Radius Ratio (NR$_2$) (Case 3.I)

KR = 10, Inner Wall Thickness = 0.1, Outer Wall Thickness = 0.2, E = 0.5

Fig.8.51. Dimensional Flow Rate Variation with
Radius Ratio (NR$_2$) (Case 3.O)

KR = 10, Inner Wall Thickness = 0.1, Outer Wall Thickness = 0.2, E = 0.5

Fig.8.52. Dimensional Flow Rate per Unit Area Varying with
Radius Ratio (NR$_2$) (Case 3.O)

KR = 10, Inner Wall Thickness = 0.1, Outer Wall Thickness = 0.2, E = 0.5

Fig.8.53. Total Heat Absorbed for Different Values of Radius ratio
(Case 3.I)

KR = 10, Inner Wall Thickness = 0.1, Outer Wall Thickness = 0.2, E = 0.5

Fig.8.54. Total Heat Absorbed for Radius ratio 0.5 (Case 3.I)

KR = 10, Inner Wall Thickness = 0.1, Outer Wall Thickness = 0.2, E = 0.5
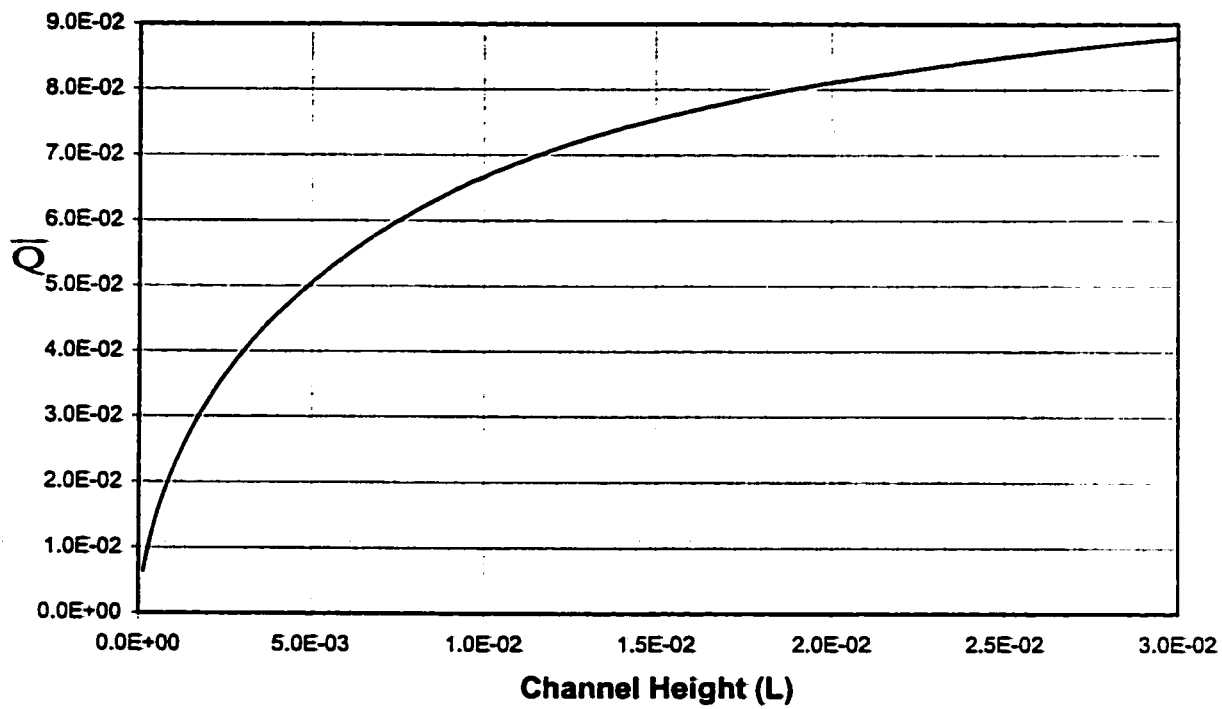
Fig.8.55. Total Heat Absorbed for Radius ratio 0.7 (Case 3.I)

KR = 10, Inner Wall Thickness = 0.1, Outer Wall Thickness = 0.2, E = 0.5
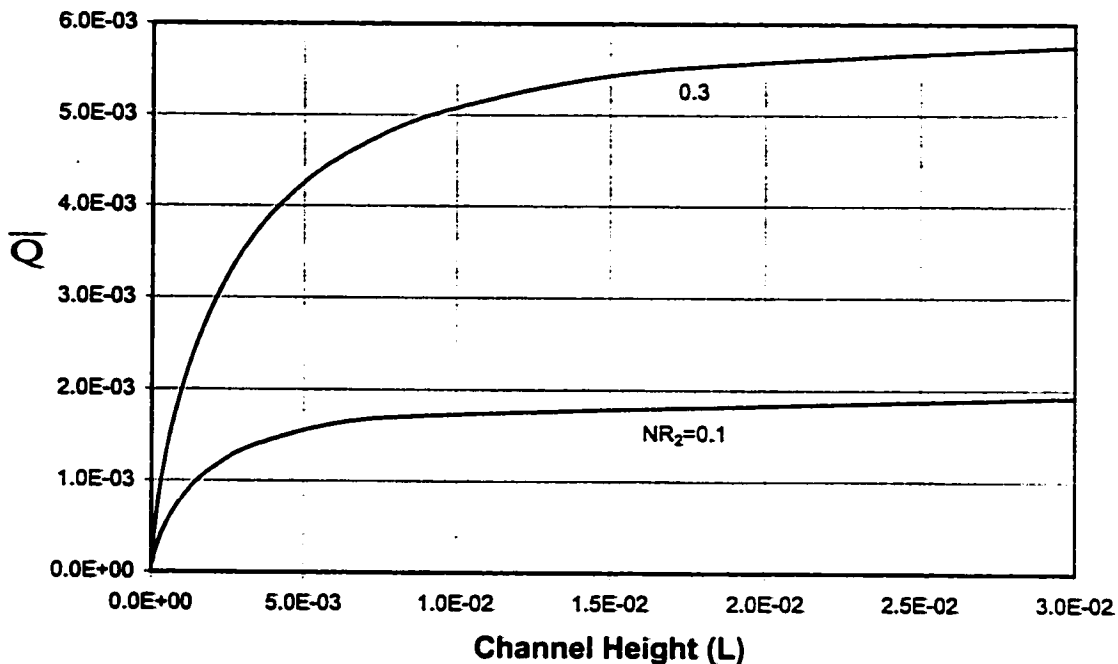
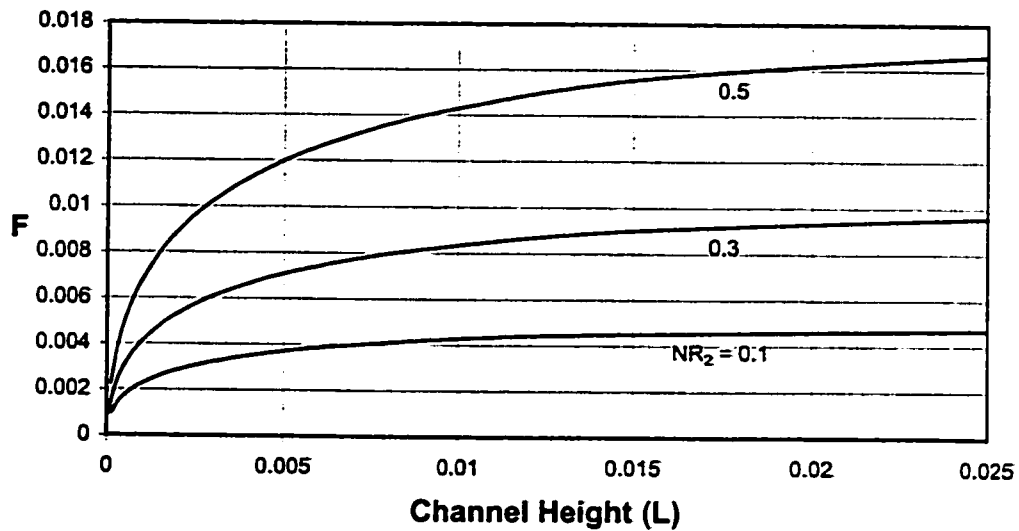**Fig.8.56.** Total Heat Absorption versus Channel Height for Different Values of Radius ratio (Case 3.O)

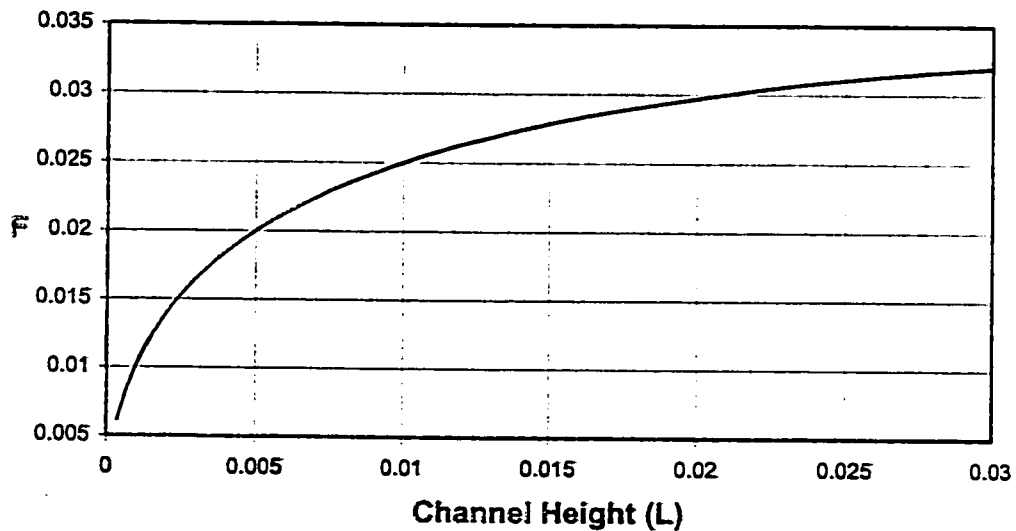KR = 10, Inner Wall Thickness = 0.1, Outer Wall Thickness = 0.2, E = 0.5
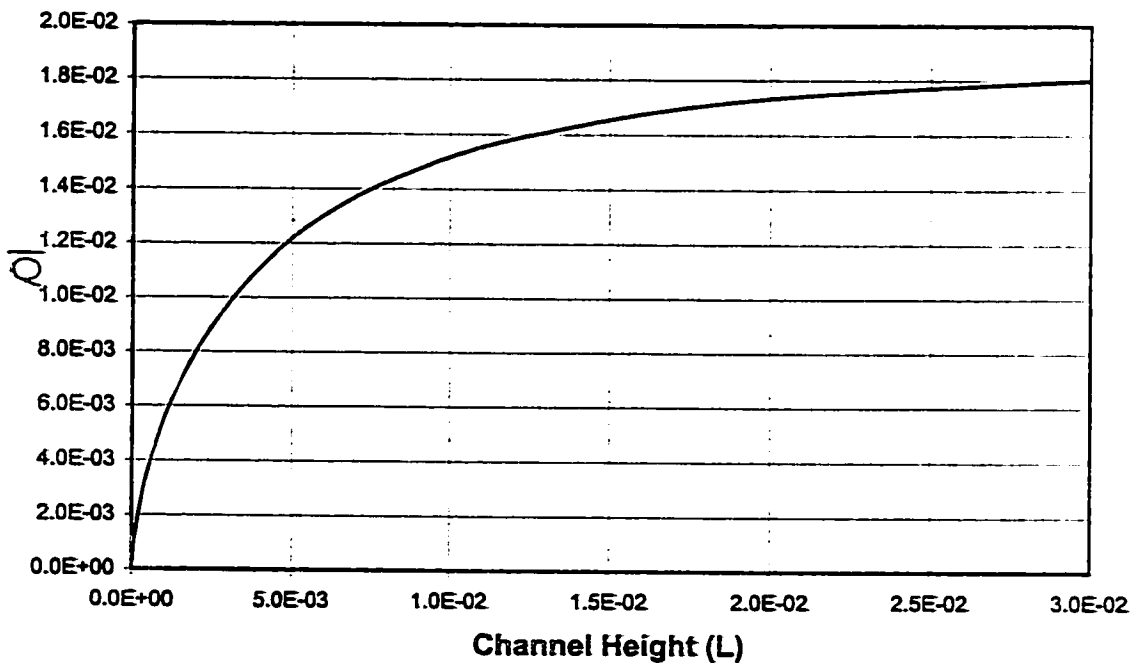
Fig.8.57. Total Heat Absorption versus Channel Height for Radius ratio 0.5 (Case 3.O)

KR = 10, Inner Wall Thickness = 0.1, Outer Wall Thickness = 0.2, E = 0.5
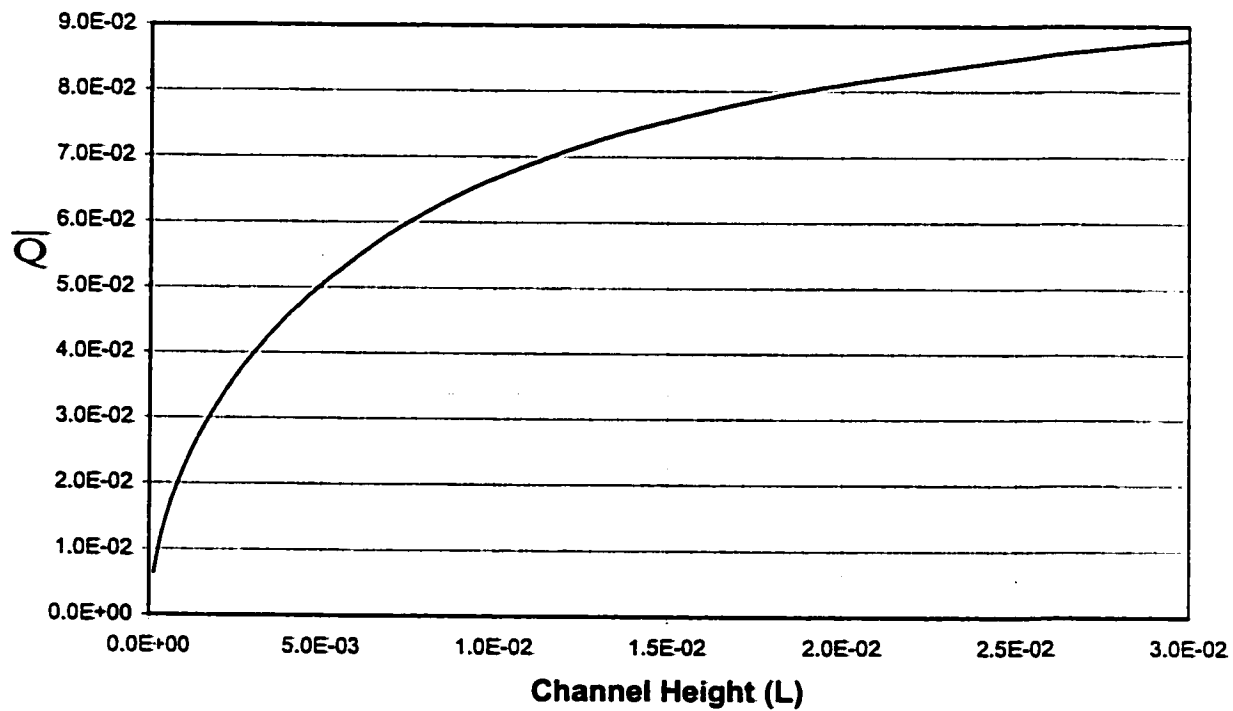
Fig.8.58. Total Heat Absorption versus Channel Height for Radius ratio 0.7 (Case 3.O)

KR = 10, Inner Wall Thickness = 0.1, Outer Wall Thickness = 0.2, E = 0.5

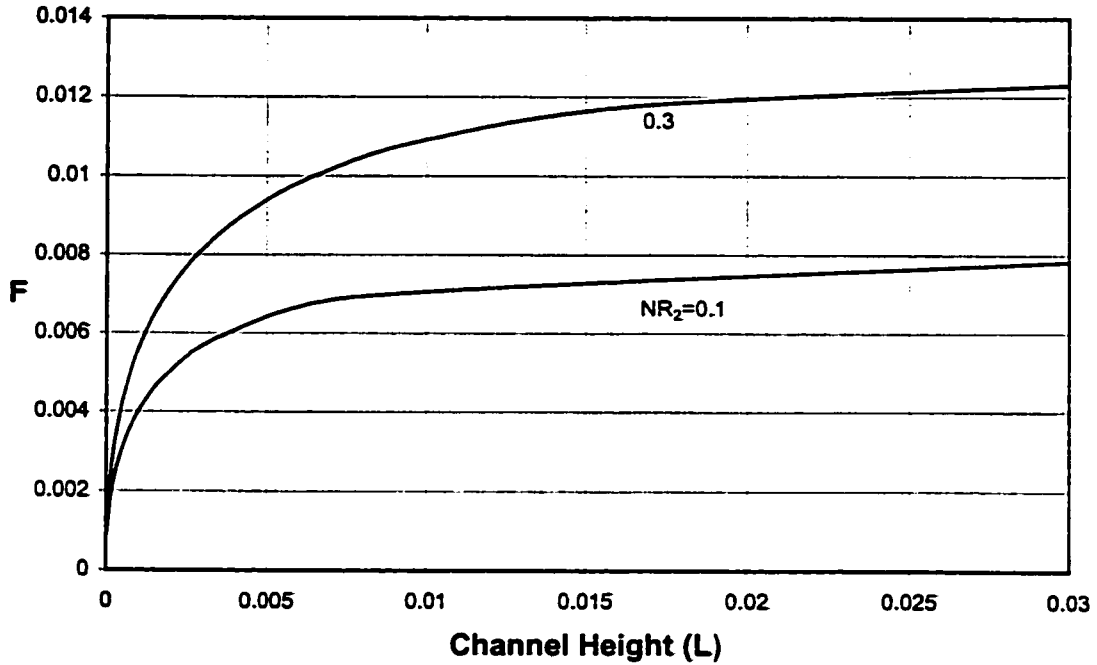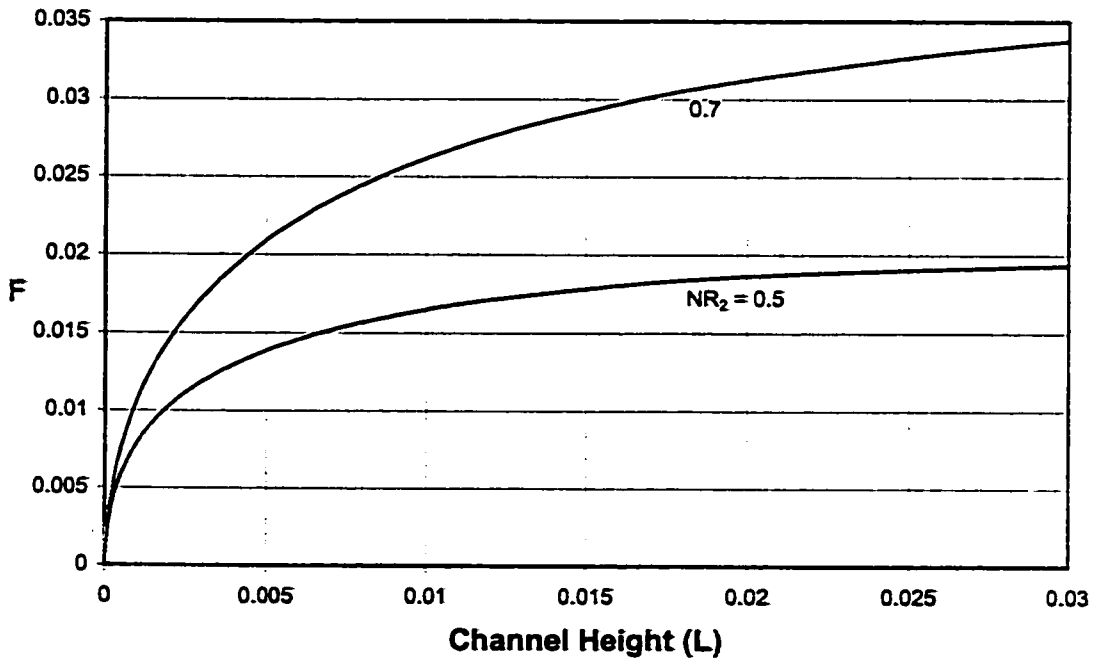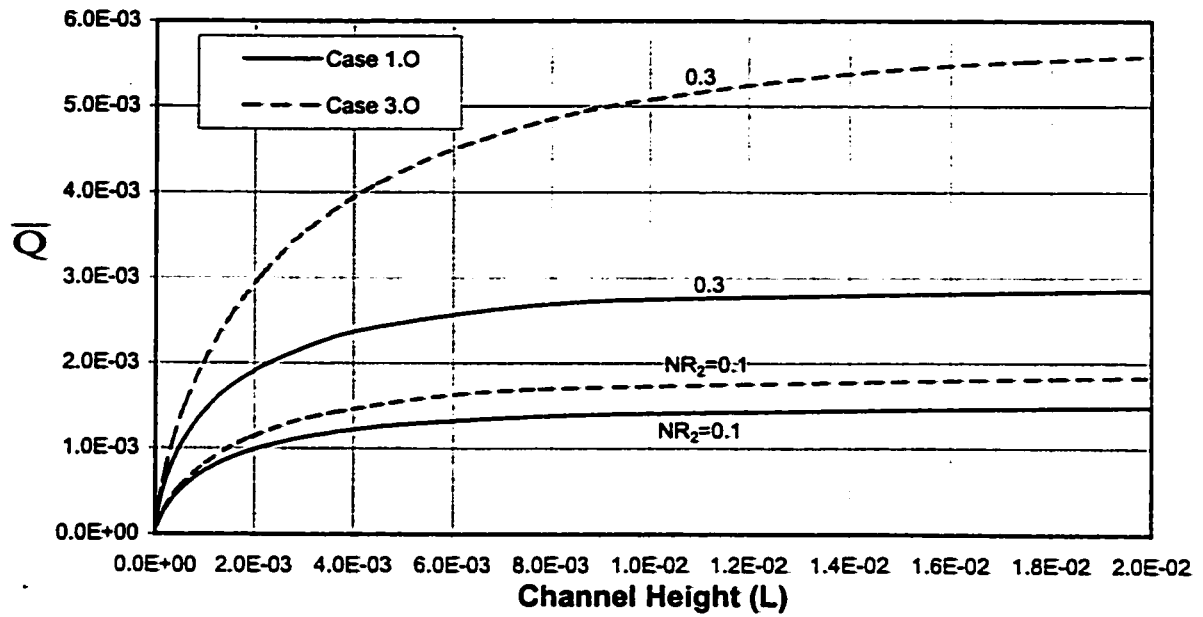**Fig.8.61.** Comparison of Total Heat Absorbed for Different Values of Radius Ratio among cases (1.O) and (3.O)

KR = 10, Inner Wall Thickness = 0.1, Outer Wall Thickness = 0.2, E = 0.5
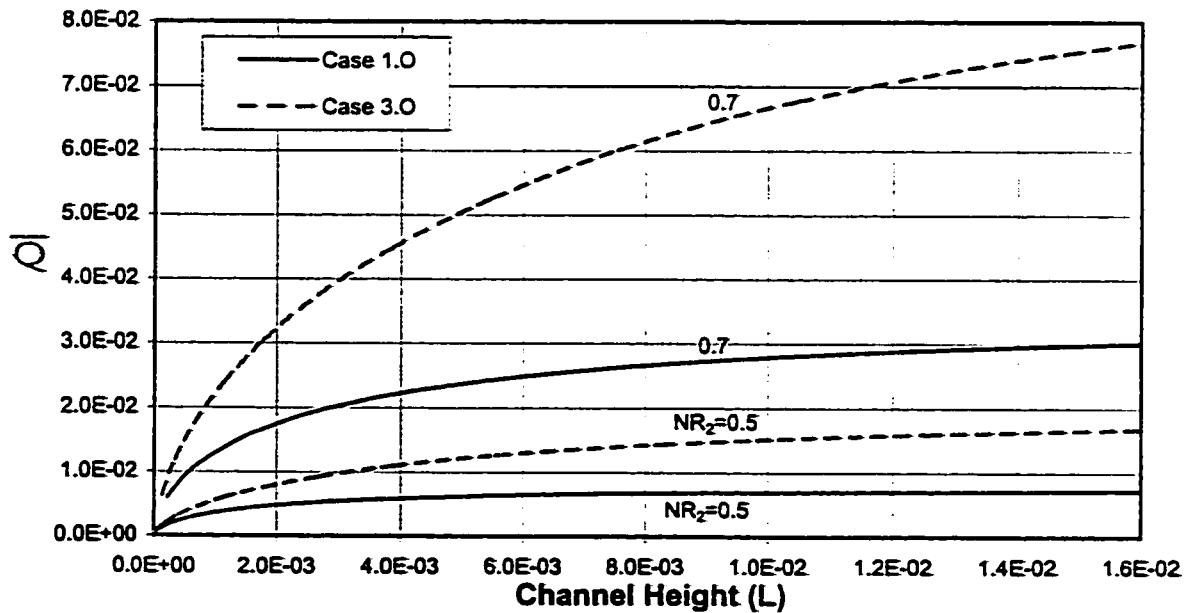
Fig.8.62. Comparison of Total Heat Absorbed for Different Values of Radius Ratio among cases (1.O) and (3.O)

KR = 10, Inner Wall Thickness = 0.1, Outer Wall Thickness = 0.2, E = 0.5
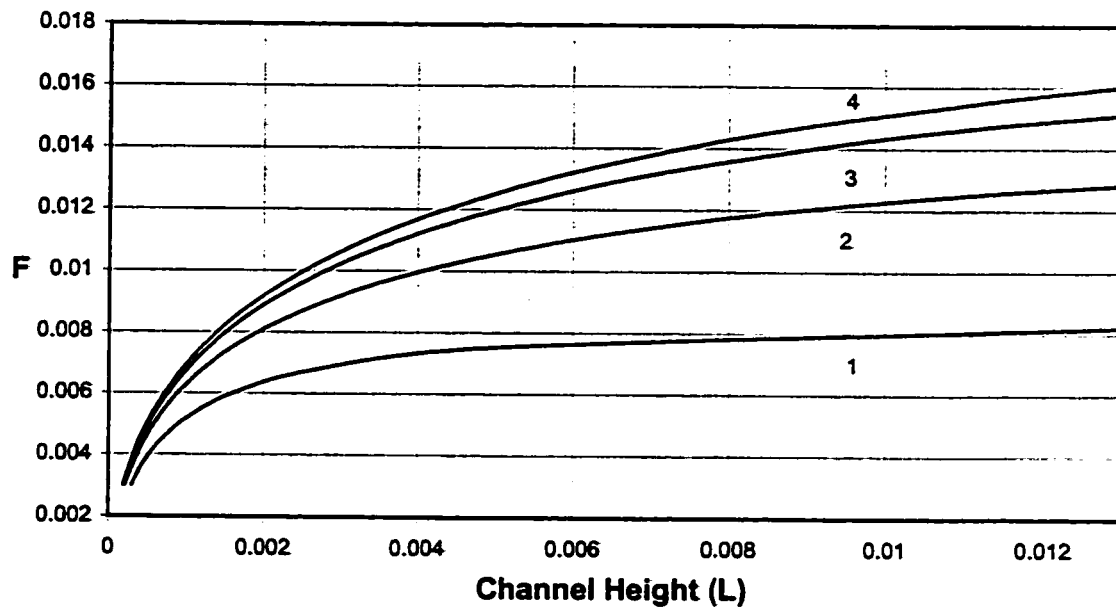
Fig.8.63. Variation of Flow Rate with Channel Height for Different Values of Wall Thickness (Case 3.I)

(1)Iwall=0.01;Owall=0.02 (2)Iwall=0.05;Owall=0.1 (3)Iwall=0.1;Owall=0.2
(4)Iwall=0.2;Owall=0.4, NR_2 = 0.5, KR = 10, E = 0.5
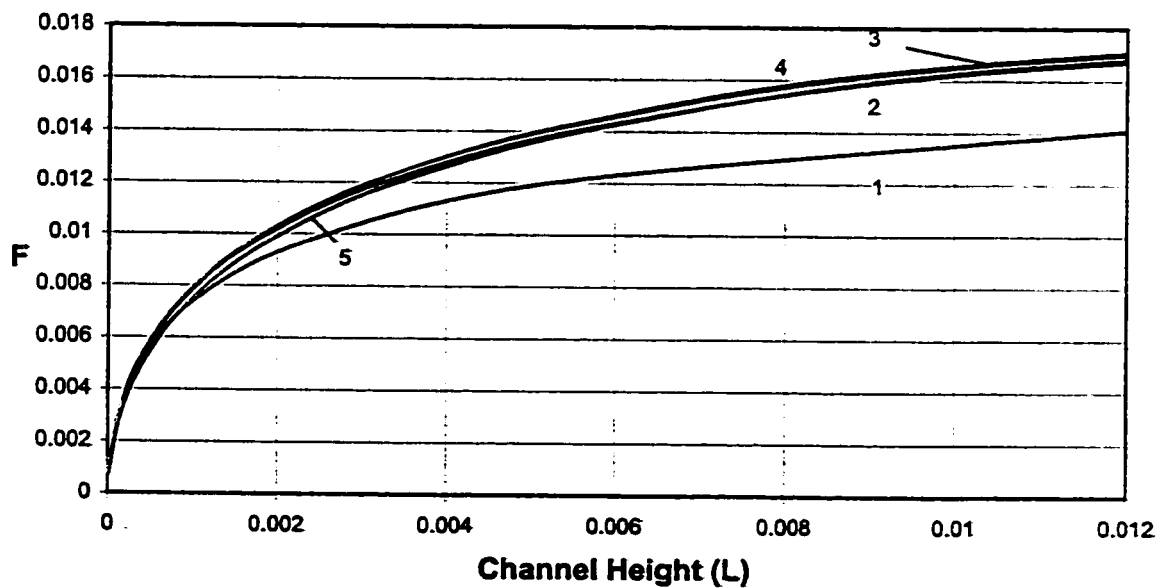
Fig.8.64. Variation of Flow Rate with Channel Height for Different Values of Wall Thickness (Case 3.O)

(1)Iwall=0.01;Owall=0.02 (2)Iwall=0.05;Owall=0.1 (3)Iwall=0.1;Owall=0.2
(4)Iwall=0.2;Owall=0.4 (5)Iwall=0.4; Owall=0.8, NR_2 = 0.5, KR = 10, E = 0.5
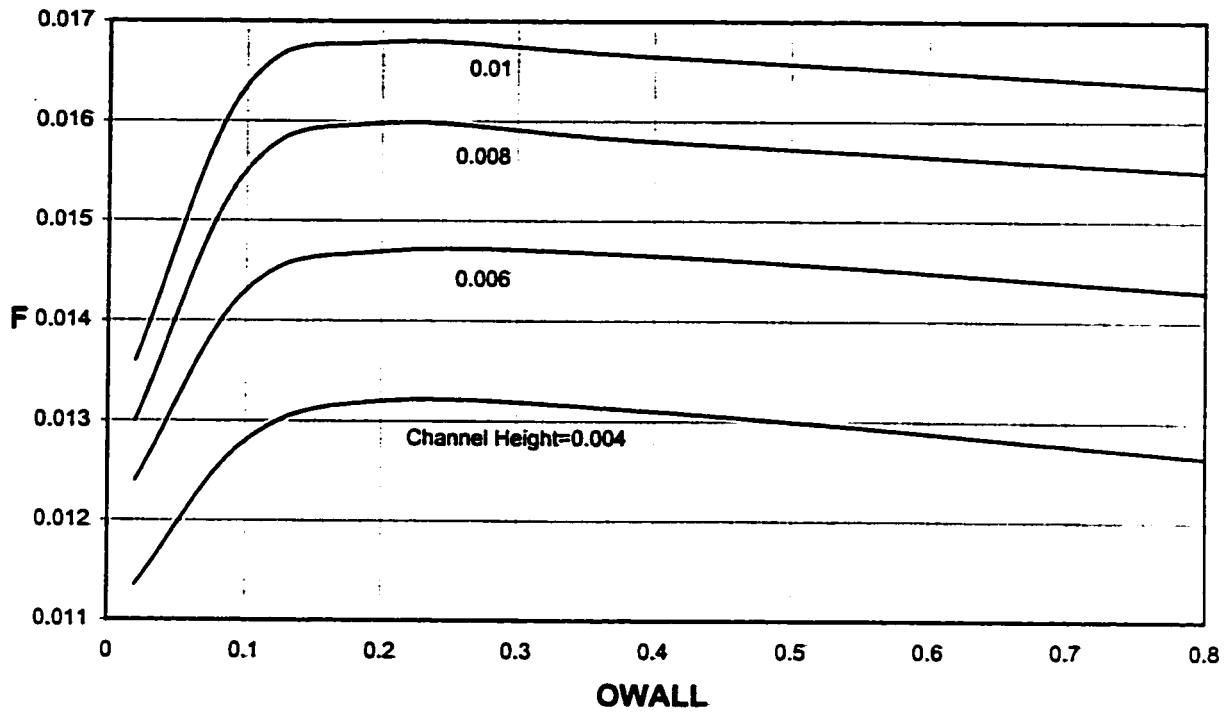
Fig. 8.65. Variation of Flow Rate with Outer Wall Thickness
(Case 3.O)

E=0.5, NR_2=0.5. KR=10

8.2.4.2. Local Heat Flux (HF)

Figure (8.66) shows the circumferential variation of local heat flux on inner solid-fluid interface for given values of walls thicknesses for case (3.I). It is clear from the figure that increasing the wall thickness reduces the local heat flux. This is attributed to the wall thickness, which resists the heat to flow through it. A transition from increasing heat flux values to its decreasing values circumferentially can be observed in the figure. This is because when the thicknesses of the walls are increased, the heat accumulates on the outer interface at the narrowest gap ($\psi = 1$) more than at the widest gap ($\psi = 0$). This reduces the temperature difference and hence the heat fluxes at the narrowest Gap ($\psi = 1$). Similar trend of decreasing circumferential heat flux and transition of circumferential heat flux values with increasing wall thicknesses is observed for Case (3.O) as shown in Fig. (8.67). This can be explained similar to that for case (3.I). The variation of local heat flux at the narrowest gap ($\psi = 1$) is due to some circumferential conduction taking place in the walls. ($\psi = 1$).

8.2.4.3. Circumferential Temperature (θ)

Figures (8.68-8.71) show the circumferential temperature variation for the given values of wall thicknesses for cases (3.I) and (3.O). Figures (8.68) and (8.70) show decreasing circumferential temperature values with increasing wall thicknesses on the solid-fluid interface next to the heated wall (inner wall for case (3.I) and outer wall for case (3.O)) for cases (3.I) and (3.O), respectively. The opposite is observed on the other interfaces in Figs. (8.69) and (8.71) for both cases. The reason, as already explained, is the
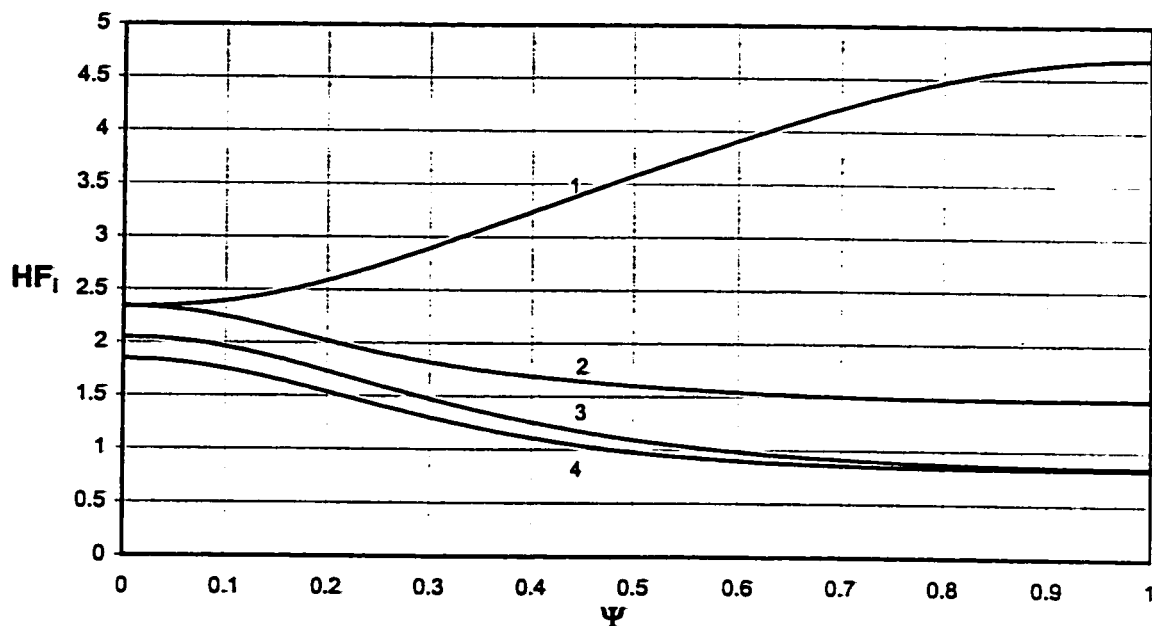
Fig.8.66. Circumferential variation of Local Heat Flux on Inner Interface at an Axial (vertical) Location of 1.13×10^{-3} for Different Values of Wall Thickness (Case 3.I)

(1)Iwall=0.01;Owall=0.02 (2)Iwall=0.05;Owall=0.1 (3)Iwall=0.1;Owall=0.2
(4)Iwall=0.2;Owall=0.4, NR_2 = 0.5, KR = 10, E = 0.5
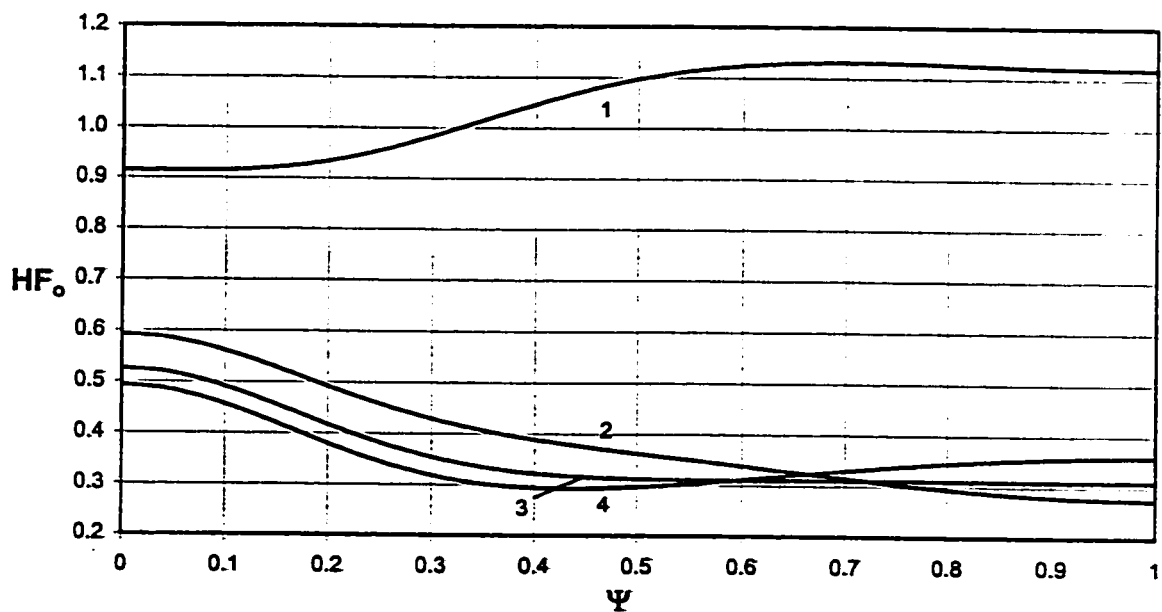
Fig.8.67. Circumferential variation of Local Heat Flux on Outer Interface at an Axial (vertical) Location of 2.86×10^{-3} for Different Values of Wall Thickness (Case 3.O)

(1)Iwall=0.01;Owall=0.02 (2)Iwall=0.05;Owall=0.1 (3)Iwall=0.1;Owall=0.2
(4)Iwall=0.2;Owall=0.4, NR_2 = 0.5, KR = 10, E = 0.5
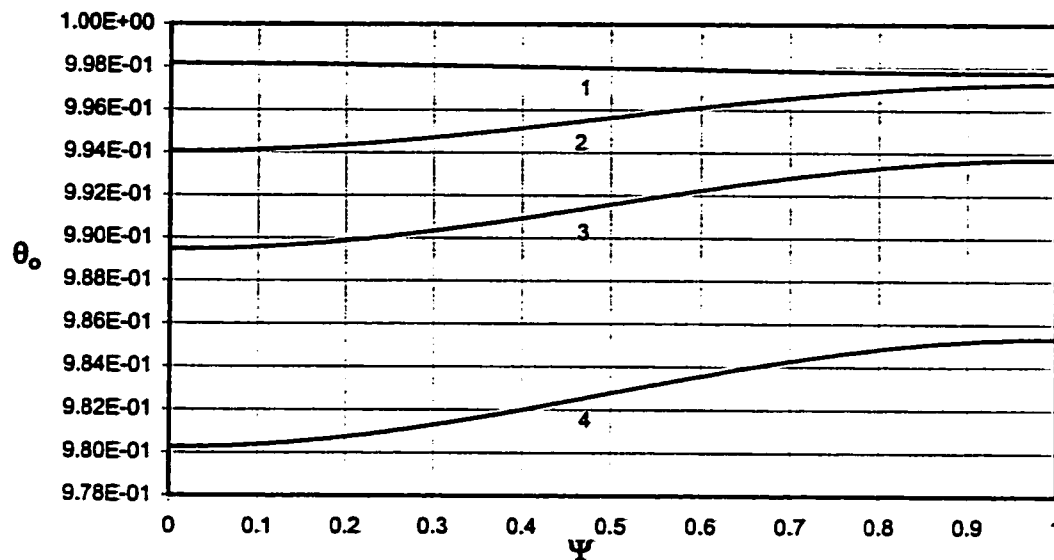
Fig.8.70 .Circumferential Variation of Temperature on Outer Interface at an Axial (vertical) Location of 2.86×10^{-3} for Different Values of Wall Thickness (Case 3.O)

(1)Iwall=0.01;Owall=0.02 (2)Iwall=0.05;Owall=0.1 (3)Iwall=0.1;Owall=0.2
(4)Iwall=0.2;Owall=0.4, NR_2 = 0.5, KR = 10, E = 0.5
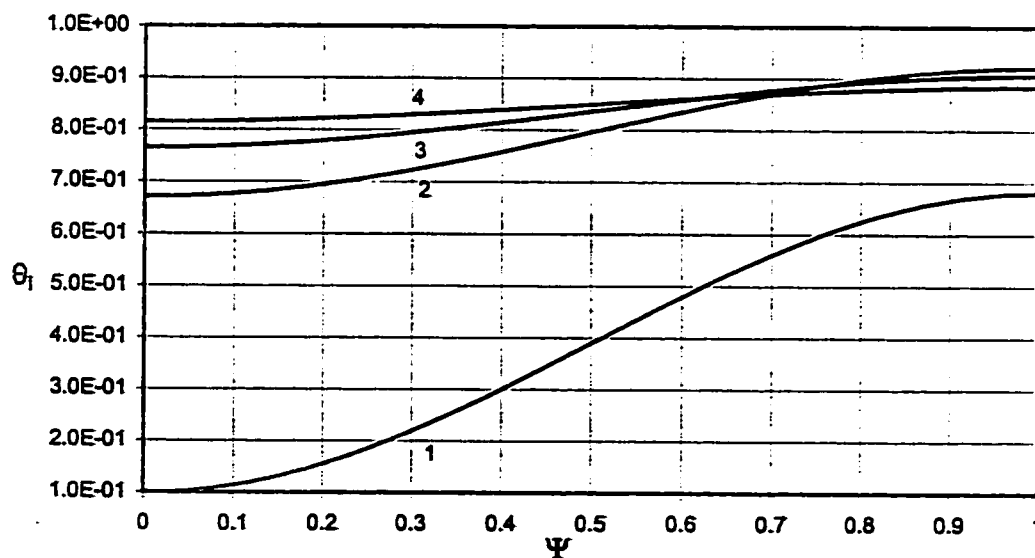
Fig.8.71 .Circumferential Variation of Temperature on Inner Interface at an Axial (vertical) Location of 2.86×10^{-3} for Different Values of Wall Thickness (Case 3.O)

(1)Iwall=0.01;Owall=0.02 (2)Iwall=0.05;Owall=0.1 (3)Iwall=0.1;Owall=0.2
(4)Iwall=0.2;Owall=0.4, NR_2 = 0.5, KR = 10, E = 0.5

wall thickness resisting the heat to enter and leave the annulus, hence contributing to the increased flow rate into the channel. The overlapping of the circumferential temperature values on inner solid-fluid interface for case (3.O) is due to the circumferential conduction in the inner wall.

8.2.4.4. Temperature Profile

The temperature profile across the channel is also helpful in understanding the effect of wall thickness on flow rate into the channel as can be seen in Figs. (8.72-8.75) for cases (3.I) and (3.O). It is clear from the figures that thick walls resist more to heat flow than the thin walls. This effect can be seen by the high temperature values on both the interfaces. The temperature value on the interface next to the insulated wall is more for case (3.O) than for case (3.I). This is due to more heat being conducted through outer wall having larger surface area as compared to the inner wall. Due to increase in the circumferential heat conduction in the insulated thick wall for each case (3.I and 3.O), the temperature in the same wall at the widest gap ($\psi = 0$) increases, hence influencing the temperature in the fluid to raise near that wall at the same gap, shown in Figs. (8.73) and (8.75).

8.2.4.5. Average Heat Flux (AVHF)

The average heat flux also decreases with increasing wall thicknesses as presented in Figs. (8.76) and (8.77) for cases (3.I) and (3.O), respectively.
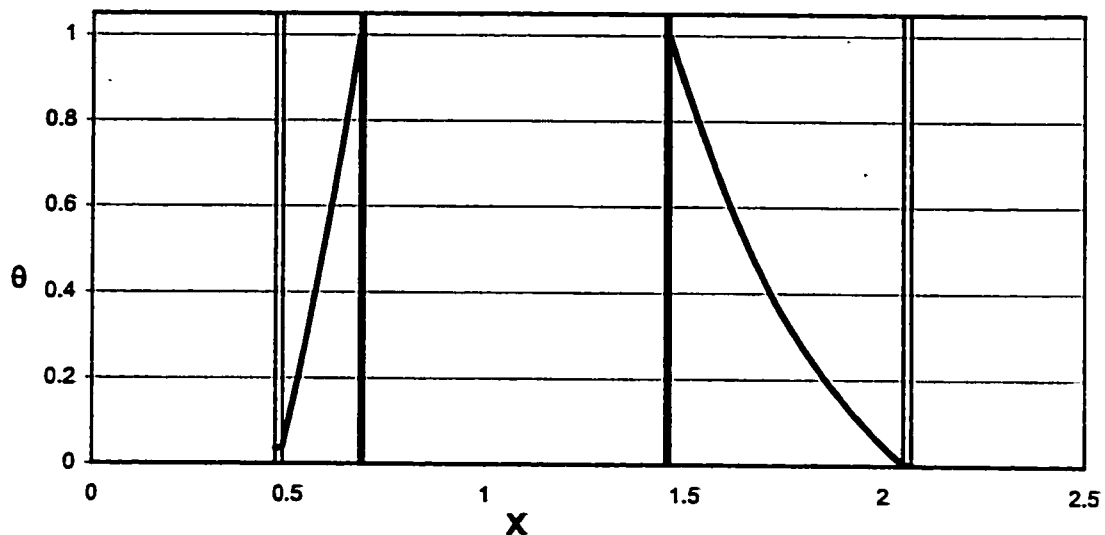
Fig.8.72. Temperature Profile across the Channel having
Iwall=0.01, Owall=0.02 on the line of symmetry at an Axial (vertical)
Location of 1.13×10^{-3} (Case 3.I)
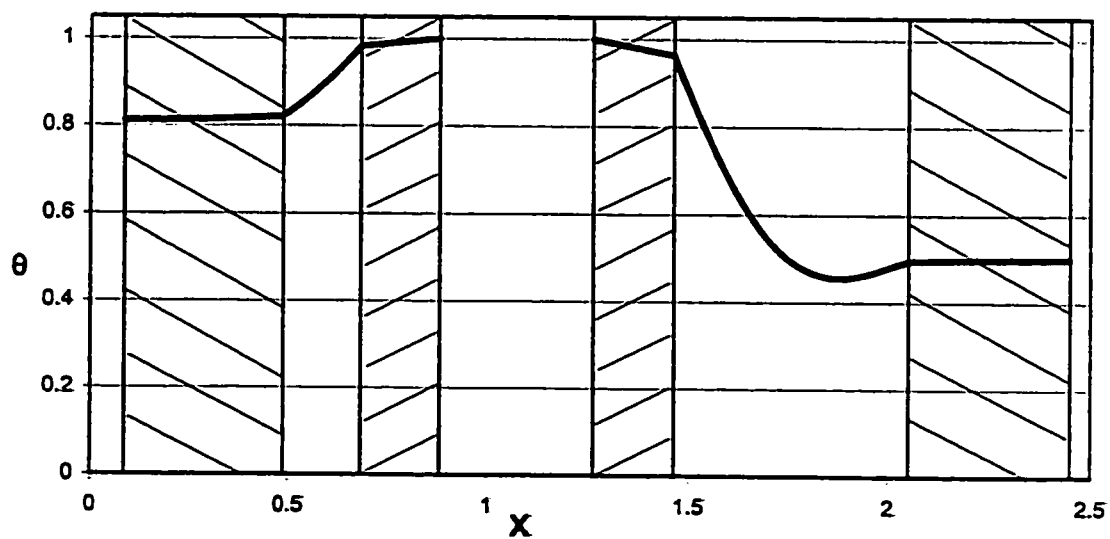
$NR_2 = 0.5$, KR = 10, E = 0.5

Fig.8.73. Temperature Profile across the Channel having Iwall=0.2,
Owall=0.4 on the line of symmetry at an Axial (vertical) Location of
1.13×10^{-3} (Case 3.I)
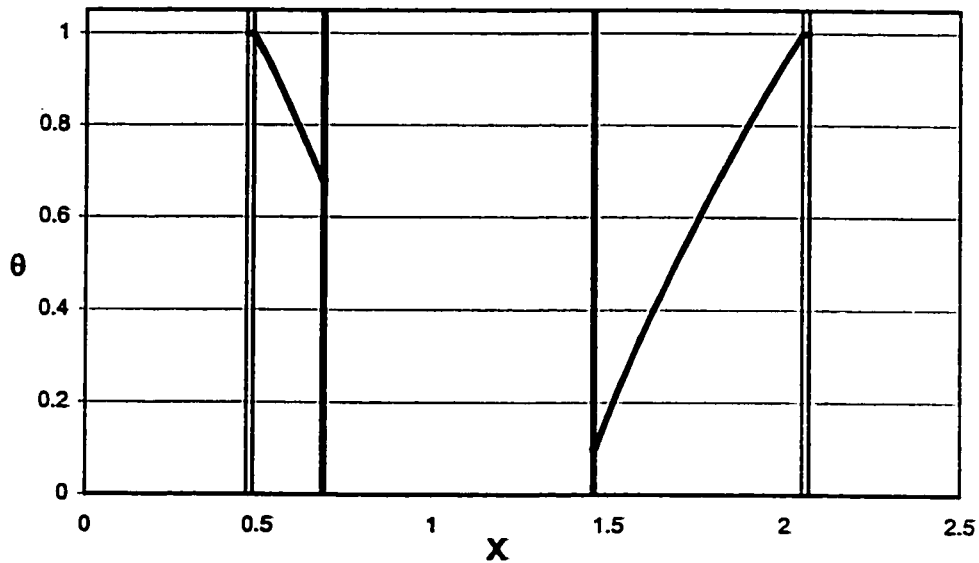
$NR_2 = 0.5$, KR = 10, E = 0.5

Fig.8.74. Temperature Profile across the Channel having Inner Wall Thickness=0.01, Outer Wall Thickness=0.02 on the line of symmetry at an Axial (vertical) Location of 2.86×10^{-3} (Case 3.0)
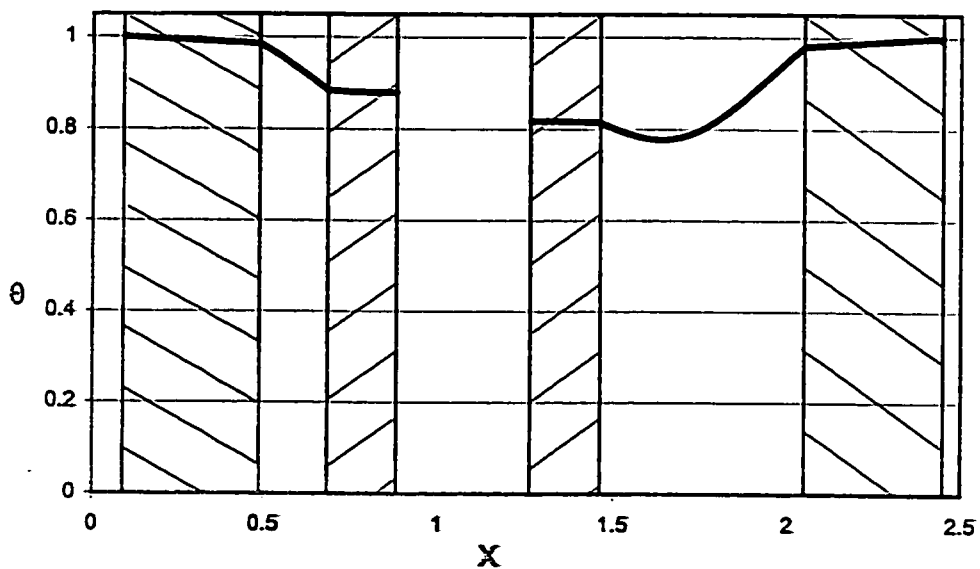
$NR_2 = 0.5$, $KR = 10$, $E = 0.5$

Fig.8.75. Temperature Profile across the Channel having Inner Wall Thickness=0.2, Outer Wall Thickness=0.4 on the line of symmetry at an Axial (vertical) Location of 2.86×10^{-3} (Case 3.0)
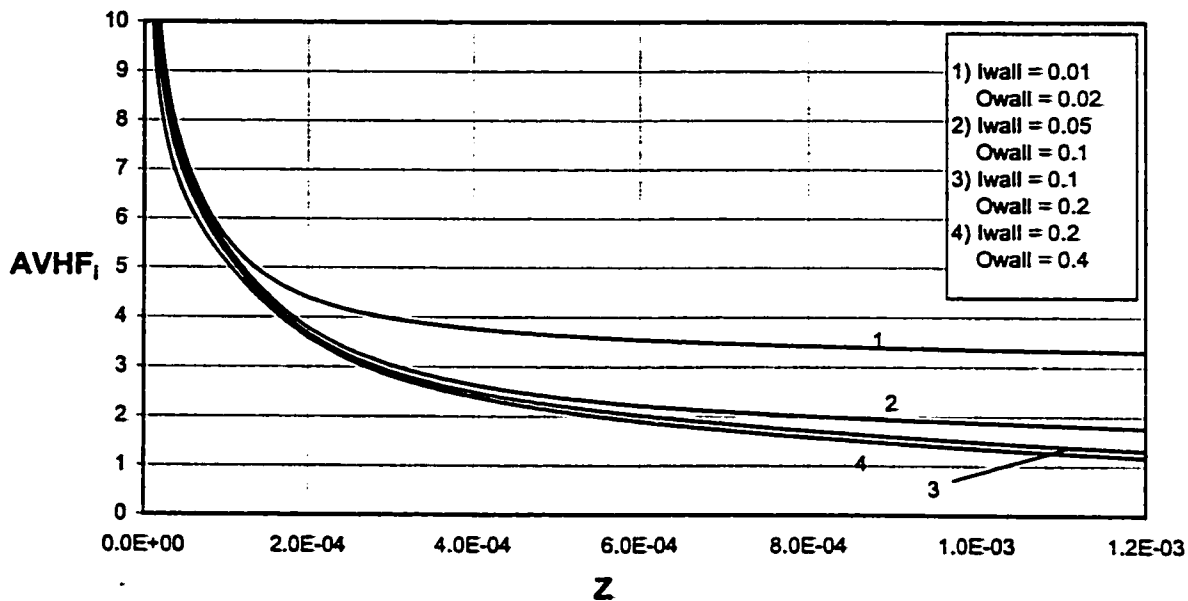
$NR_2 = 0.5$, $KR = 10$, $E = 0.5$

Fig.8.76. Axial Variation of Average Heat Flux at Inner Interface for Different Value of Wall thickness (Case 3.I)

$NR_2 = 0.5$, $KR = 10$, $E = 0.5$
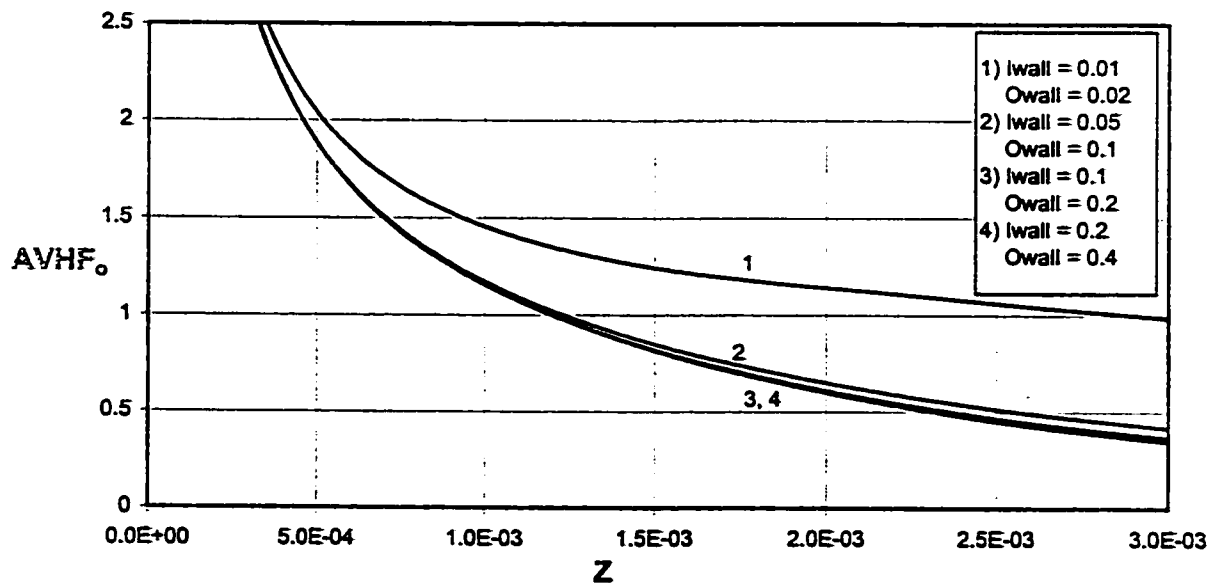
Fig.8.77. Axial Variation of Average Heat Flux at Outer Interface for Different Value of Wall thickness (Case 3.O)

$NR_2 = 0.5$, $KR = 10$, $E = 0.5$

Fig.8.78. Total Heat Absorption versus Channel Height for Different Values of Wall Thickness (Case 3.I)

(1)Iwall=0.01;Owall=0.02 (2)Iwall=0.05;Owall=0.1 (3)Iwall=0.1;Owall=0.2 (4)Iwall=0.2;Owall=0.4, NR_2 = 0.5, KR = 10, E = 0.5

Fig.8.79. Total Heat Absorption versus Channel Height for Different Values of Wall Thickness (Case 3.O)

(1)Iwall=0.01;Owall=0.02 (2)Iwall=0.05;Owall=0.1 (3)Iwall=0.1;Owall=0.2 (4)Iwall=0.2;Owall=0.4 (5)Iwall=0.4; Owall=0.8, NR_2 = 0.5, KR = 10, E = 0.5

Chapter 9

CONCLUSIONS AND RECOMMENDATIONS

The present work has aimed at obtaining a numerical solution for the conjugate laminar free convection heat transfer in vertical eccentric annuli. Two sets of thermal boundary conditions have been applied on the inner and outer surfaces of the two cylinders. One set of boundary conditions comprises of one wall kept isothermally heated while the other wall maintained at the inlet fluid temperature, known as boundary conditions of first kind, represented by cases (1.I) and (1.O). The other set of boundary conditions has one wall adiabatic while the other wall kept isothermally heated, known as boundary conditions of third kind, represented by cases (3.I) and (3.O). A model using bi-polar grids to fit the eccentric fluid annulus and cylindrical grids in the solid walls has been presented. A finite-difference algorithm has been developed to solve the model equations, which comprises the continuity equation, axial and tangential-like momentum equations and the fluid and solid energy equations.

The model has been numerically tested for mesh size and validated with previously reported results. Numerical results have been presented for a fluid of Prandtl number $Pr = 0.7$. In the first part of the study, boundary conditions of first kind were imposed on the cylinder walls to analyze the effect of conductivity ratio (KR), radius ratio (NR_2), eccentricity (E) and walls thicknesses on the induced flow rate.

From the results, it is concluded that induced flow rate is affected by the above-mentioned factors. Furthermore, it is also observed that the conjugate effect in the channel changes with conductivity ratio and wall thicknesses. However, for a given eccentricity, there are some critical values of conductivity ratio above which and walls thicknesses below which, the conjugate effect can be neglected.

In the second part of the work, boundary conditions of third kind were imposed on the cylinder walls to see the effect of the four above-mentioned factors on the induced flow rate. Similarly, the effect of the four above mentioned factors on the induced flow rate and conjugate effect were analyzed for different conductivity ratio (KR) and walls thicknesses at any given eccentricity. Similar trend of having more conjugate effect with decreasing the conductivity ratio and increasing the walls thicknesses is obtained as found for boundary condition of first kind.

9.1. Conclusions

From the obtained results the following conclusions can be deduced:

For a given eccentricity (E), decreasing the value of conductivity ratio (KR), i.e. increasing the thermal resistance of the walls results in the following, at a given axial location (Z):

- For a given channel height (Z = L), increases the induced flow rate for cases (1.I) and (3.I), whereas decreases the induced flow rate for case (1.O). The flow rate first increases and then decreases for case (3.O).

- Makes the conjugate effect more pronounced for cases (1.I and 1.O).

- Lowers the temperature at the inner interface and raise the temperature at the outer interface in all cases, i.e. (1.I and 1.O, respectively) and (3.I and 3.O, respectively).

- Increases the circumferential temperature variation at both interfaces in all cases, i.e. (1.I and 1.O, respectively) and (3.I and 3.O, respectively).

- Reduces the interfacial heat flux at both interfaces for cases (1.I) and (1.O) and at the interface next to the heated wall each for cases (3.I) and (3.O).

- Increases the heat absorbed for cases (1.I) and (3.I), whereas decreases the heat absorbed for case (1.O). The amount of heat absorbed first increases and then decreases for case (3.O).

For a given eccentricity (E), increasing the values of wall thicknesses, i.e. increasing the thermal resistance of the walls results in the following, at a given axial location (Z):

- For a given channel height (Z = L), decreases the induced flow rate for case (1.O), whereas increases the induced flow rate for cases (1.I) and (3.I). The induced flow rate first increases and then decreases after certain wall thickness for case (3.O).

- Make the conjugate effect more pronounced for cases (1.I and 1.O).

o Lowers the temperature at the inner interface and raise the temperature at the outer interface in all cases, i.e. (1.I and 1.O, respectively) and (3.I and 3.O, respectively).

o Increases the circumferential temperature variation at both interfaces for all cases, i.e. (1.I and 1.O, respectively) and (3.I and 3.O, respectively).

- Reduces the interfacial heat flux at both interfaces for cases (1.I) and (1.O) and at the interface next to the heated wall each for cases (3.I) and (3.O).

o Decreases the heat absorbed for case (1.O), whereas increases the amount of heat absorbed for cases (1.I) and (3.I). The heat absorbed first increases and then decreases for case (3.O).

On the other hand, for given conductivity ratio (KR), radius ratio (NR_2) and wall thickness, increasing the eccentricity leads to:

- Increases in the induced flow rate for all cases, i.e. (1.I and 1.O, respectively) and (3.I and 3.O, respectively).

- Makes the conjugate effect more pronounced for cases (1.I and 1.O).

- Decreases and increase the temperatures at the interfaces next to and opposite to the heated walls for cases (1.I) and (1.O), respectively. The increase in the eccentricity increases and decreases the temperature on both interfaces for cases (3.I) and (3.O), respectively.

- Increases the circumferential temperature variation at both interfaces in all cases, i.e. (1.I and 1.O, respectively) and (3.I and 3.O, respectively).

- Increases the interfacial heat flux at both interfaces for cases (1.I) and (1.O) whereas causes reduction/rise in the heat flux value at the interface next to the heated wall for case (3.I)/(3.O).

- Increases the heat absorbed for all cases, i.e. (1.I and 1.O, respectively) and (3.I and 3.O, respectively).

For given eccentricity, conductivity ratio and wall thickness, increasing the radius ratio leads to:

- Increase in the dimensionless induced flow rate for all cases, i.e. (1.I and 1.O, respectively) and (3.I and 3.O, respectively).

- Decrease in the dimensional induced flow rate for all cases, i.e. (1.I and 1.O, respectively) and (3.I and 3.O, respectively).

- Increase in the flow rate per unit area for all cases, i.e. (1.I and 1.O, respectively) and (3.I and 3.O, respectively).

- Increase the heat absorbed for all cases, i.e. (1.I and 1.O, respectively) and (3.I and 3.O, respectively).

The results related to critical conductivity ratio (KR) and wall thickness show that:

- For a given radius ratio (NR_2=0.5), The conjugate effect for case (1.O) is more pronounced than that of case (1.I) with eccentricity variation. This can be judged by the higher critical values of KR and lower wall thickness values for case (1.O) than case (1.I).

- For a given eccentricity (E=0.5), increasing the radius ratio (NR_2) decreases/increases the critical value of thermal conductivity ratio (KR) for case (1.I)/(1.O) with an exception of an increase in the critical value at large radius ratios (NR_2) for case (1.I). The critical value of outer wall thickness increases/decreases for case (1.I)/(1.O) with increasing radius ratio (NR_2) with an exception of decrease in the critical value at large radius ratios (NR_2) for case (1.I).

9.2. Recommendations

Due to the wide scope of the present research work, the following suggestions for the future research in the same area can be given.

- Experimental work can be suggested to validate the presently obtained results for the cases investigated.

- Conjugate free convection heat transfer analysis can be carried out in vertical eccentric annuli with rotating boundaries.

- Transient case for conjugate free convection heat transfer in vertical eccentric annuli can be investigated.

- Conjugate mixed convection heat transfer in vertical eccentric annuli can be investigated.

- The effect of conductivity ratio, eccentricity, radius ratio and wall thickness on the induced flow rate along with the critical values of conductivity ratio and wall thickness can also be investigated by employing boundary conditions of 2nd and 4th kind.

APPENDIX A

NORMALIZATION OF GOVERNING EQUATIONS

The governing equations in bipolar coordinate system and cylindrical coordinate system can be written in dimensionless form in order to make it applicable for any value of the parameter and for any similar problem. The dimensionless parameters are given in the nomenclature. The procedure to normalize momentum equation in η-direction is shown hereinafter.

The momentum equation in η-direction for steady state condition in bipolar coordinate system can be written as:

$$\rho\left[\frac{w}{h^2}\frac{\partial(hv)}{\partial\xi}+\frac{v}{h}\frac{\partial v}{\partial\eta}+u\frac{\partial v}{\partial z}-\frac{w^2}{h^2}\frac{\partial h}{\partial\eta}\right]=F_\eta-\frac{1}{h}\frac{\partial p}{\partial\eta}+\frac{\mu}{h}\left[\begin{array}{l}\frac{\partial^2(hv)}{\partial z^2}+\frac{1}{h^2}\frac{\partial^2(hv)}{\partial\eta^2}+\frac{1}{h^2}\frac{\partial^2(hv)}{\partial\xi^2}-\\[2mm]\frac{2}{h^3}\left\{\frac{\partial(hv)}{\partial\xi}-\frac{\partial(hw)}{\partial\eta}\right\}\frac{\partial h}{\partial\xi}+\frac{2}{h^2}\frac{\partial h}{\partial\eta}\frac{\partial(hu)}{\partial z}\end{array}\right]$$

Neglecting the body force in η - direction.

$$\frac{w}{h^2}\frac{\partial(hv)}{\partial\xi}+\frac{v}{h}\frac{\partial v}{\partial\eta}+u\frac{\partial v}{\partial z}-\frac{w^2}{h^2}\frac{\partial h}{\partial\eta}=-\frac{1}{\rho h}\frac{\partial p}{\partial\eta}+\frac{\mu}{\rho h}\left[\begin{array}{l}\frac{\partial^2(hv)}{\partial z^2}+\frac{1}{h^2}\frac{\partial^2(hv)}{\partial\eta^2}+\frac{1}{h^2}\frac{\partial^2(hv)}{\partial\xi^2}-\\[2mm]\frac{2}{h^3}\left\{\frac{\partial(hv)}{\partial\xi}-\frac{\partial(hw)}{\partial\eta}\right\}\frac{\partial h}{\partial\xi}+\frac{2}{h^2}\frac{\partial h}{\partial\eta}\frac{\partial(hu)}{\partial z}\end{array}\right]$$

$$(1)$$

Take L.H.S.

$$= \frac{w}{h^2}\frac{\partial(hv)}{\partial\xi} + \frac{v}{h}\frac{\partial v}{\partial\eta} + u\frac{\partial v}{\partial z} - \frac{w^2}{h^2}\frac{\partial h}{\partial\eta}$$

Putting the dimensionless values:

$$= \frac{\gamma W}{D_h^{3}H^2}\frac{\partial}{\partial\xi}\left(D_h H.\frac{\gamma V}{D_h}\right) + \frac{\gamma V}{D_h^{2}}\frac{\partial}{\partial\eta}\left(\frac{\gamma V}{D_h}\right) + \frac{Ul\gamma Gr^{\bullet}}{r_o^{2}}\frac{\partial}{\partial z}\left(\frac{\gamma V}{D_h l Gr^{\bullet}}\right) - \frac{\gamma^2 W^2}{D_h^{4}H^2}\frac{\partial(HD_h)}{\partial\eta}$$

Multiply the equation by $\dfrac{D_h^{3}}{\gamma^2}$ and simplify to get:

$$\boxed{= \frac{W}{H^2}\frac{\partial(HV)}{\partial\xi} + \frac{V}{H}\frac{\partial V}{\partial\eta} + 4(1-NR_2)^2 U\frac{\partial V}{\partial Z} - \frac{W^2}{H^2}\frac{\partial H}{\partial\eta}}$$

Now R.H.S.

$$= \frac{D_h^{3}}{\gamma^2}\left\{-\frac{1}{\rho h}\frac{\partial p}{\partial\eta} + \frac{\gamma}{h}\left[\frac{\partial^2(hv)}{\partial z^2} + \frac{1}{h^2}\frac{\partial^2(hv)}{\partial\eta^2} + \frac{1}{h^2}\frac{\partial^2(hv)}{\partial\xi^2} - \frac{2}{h^3}\left\{\frac{\partial(hv)}{\partial\xi} - \frac{\partial(hw)}{\partial\eta}\right\}\frac{\partial h}{\partial\xi} + \frac{2}{h^2}\frac{\partial h}{\partial\eta}\frac{\partial(hu)}{\partial z}\right]\right\}$$

$$= -\frac{D_h^{3}}{\gamma^2\rho h}\frac{\partial p}{\partial\eta} + \frac{D_h^{3}}{\gamma h}\left[\frac{\partial^2(hv)}{\partial z^2} + \frac{1}{h^2}\frac{\partial^2(hv)}{\partial\eta^2} + \frac{1}{h^2}\frac{\partial^2(hv)}{\partial\xi^2} - \frac{2}{h^3}\left\{\frac{\partial(hv)}{\partial\xi} - \frac{\partial(hw)}{\partial\eta}\right\}\frac{\partial h}{\partial\xi} + \frac{2}{h^2}\frac{\partial h}{\partial\eta}\frac{\partial(hu)}{\partial z}\right]$$

Take,

$$P = \frac{P'D_h^{4}}{\rho l^2\gamma^2 Gr^{\bullet 2}}$$

$$P = \frac{(p-p_s)D_h^{4}}{\rho l^2\gamma^2 Gr^{\bullet 2}}$$

$$P = \frac{pD_h^{4} - p_s D_h^{4}}{\rho l^2\gamma^2 Gr^{\bullet 2}}$$

where,

$$p_s = \rho g z$$

$$Gr^\bullet = \frac{GrD_h}{l}$$

Putting the value of $Gr^\bullet$ and simplifying gives:

$$P = \frac{pD_h^2}{\rho\gamma^2 Gr^2} - \frac{gzlGr^\bullet D_h^4}{l^2\gamma^2 Gr^{\bullet 2}}$$

$$P = \frac{pD_h^2}{\rho\gamma^2 Gr^2} - \frac{gD_h^3 Z}{\gamma^2 Gr}$$

Differentiate w.r.t η:

$$\frac{\partial P}{\partial \eta} = \frac{\partial}{\partial \eta}\left(\frac{pD_h^2}{\rho\gamma^2 Gr^2}\right) - \frac{\partial}{\partial \eta}\left(\frac{gD_h^3 Z}{\gamma^2 Gr}\right)$$

Second term on R.H.S. will be zero as it is not a function of η.

$$\frac{1}{\rho}\frac{\partial p}{\partial \eta} = \frac{\gamma^2 Gr^2}{D_h^2}\frac{\partial P}{\partial \eta}$$

Multiply the above relation by $\dfrac{D_h^3}{\gamma^2}$ to get:

$$\frac{D_h^3}{\gamma^2 \rho h}\frac{\partial p}{\partial \eta} = \frac{Gr^2}{H}\frac{\partial P}{\partial \eta}$$

Now, the remaining terms can be normalized as:

$$= \frac{D_h^3}{\gamma h}\left[\frac{\partial^2(hv)}{\partial z^2} + \frac{1}{h^2}\frac{\partial^2(hv)}{\partial \eta^2} + \frac{1}{h^2}\frac{\partial^2(hv)}{\partial \xi^2} + \frac{2}{h^3}\left\{\frac{\partial(hv)}{\partial \xi} - \frac{\partial(hw)}{\partial \eta}\right\}\frac{\partial h}{\partial \xi} + \frac{2}{h^2}\frac{\partial h}{\partial \eta}\frac{\partial(hu)}{\partial z}\right]$$

$$= \frac{D_h^3}{\gamma D_h H}\left[\begin{array}{l} \dfrac{\partial^2}{\partial Z^2}\left(\dfrac{D_h H \cdot \frac{\gamma V}{D_h}}{l^2 Gr^{\bullet 2}}\right) + \dfrac{1}{H^2 D_h^2}\dfrac{\partial^2}{\partial \eta^2}\left(HD_h \cdot \dfrac{\gamma V}{D_h}\right) + \dfrac{1}{H^2 D_h^2}\dfrac{\partial^2}{\partial \xi^2}\left(HD_h \cdot \dfrac{\gamma V}{D_h}\right) - \dfrac{2}{H^3 D_h^3} \\[2em] \left\{\dfrac{\partial}{\partial \xi}\left(HD_h \cdot \dfrac{\gamma V}{D_h}\right) - \dfrac{\partial}{\partial \eta}\left(HD_h \cdot \dfrac{\gamma W}{D_h}\right)\right\}\dfrac{\partial(HD_h)}{\partial \xi} + \dfrac{2}{H^2 D_h^2}\dfrac{\partial H}{\partial \eta}D_h\dfrac{\partial}{\partial Z}\left(\dfrac{HD_h Ul\gamma Gr^\bullet}{r_o^2 lGr^\bullet}\right) \end{array}\right]$$

Finally, we get after simplification and rearrangement of terms.

$$
= -\frac{Gr^2}{H}\frac{\partial P}{\partial \eta} + \frac{1}{HGr^2}\frac{\partial^2(HV)}{\partial Z^2} + \frac{1}{H^3}\frac{\partial(HV)}{\partial \eta^2} + \frac{1}{H^3}\frac{\partial^2(HV)}{\partial \xi^2} - \frac{2}{H^4}\left\{\frac{\partial(HV)}{\partial \xi} - \frac{\partial(HW)}{\partial \eta}\right\}\frac{\partial H}{\partial \xi} +
$$

$$
\frac{8(1 - NR_2)^2}{H^2}\frac{\partial H}{\partial \eta}\frac{\partial U}{\partial Z}
$$

The momentum equation in η-direction becomes:

$$
\frac{V}{H}\frac{\partial V}{\partial \eta} + \frac{W}{H^2}\frac{\partial(HV)}{\partial \xi} + 4(1 - NR_2)^2 U\frac{\partial V}{\partial Z} - \frac{W^2}{H^2}\frac{\partial H}{\partial \eta} = -\frac{Gr^2}{H}\frac{\partial P}{\partial \eta} + \frac{1}{H^3}\left\{\frac{\partial^2(HV)}{\partial \eta^2} + \frac{\partial^2(HV)}{\partial \xi^2}\right\} +
$$

$$
\frac{1}{HGr^2}\frac{\partial^2(HV)}{\partial Z^2} + \frac{2}{H^4}\left\{\frac{\partial(HW)}{\partial \eta} - \frac{\partial(HV)}{\partial \xi}\right\}\frac{\partial H}{\partial \xi} + \frac{8(1 - NR_2)^2}{H^2}\frac{\partial H}{\partial \eta}\frac{\partial U}{\partial Z}
$$

Similar Steps can be followed to obtain the following non-dimensional equations.

Momentum equation along ξ-direction

$$
\frac{W}{H}\frac{\partial W}{\partial \xi} + \frac{V}{H^2}\frac{\partial(HW)}{\partial \eta} + 4(1 - NR_2)^2 U\frac{\partial W}{\partial Z} - \frac{V^2}{H^2}\frac{\partial H}{\partial \xi} = -\frac{Gr^2}{H}\frac{\partial P}{\partial \xi} + \frac{1}{H^2}\left\{\frac{\partial^2(HW)}{\partial \eta^2} + \frac{\partial^2(HW)}{\partial \xi^2}\right\} +
$$

$$
\frac{1}{HGr^2}\frac{\partial^2(HW)}{\partial Z^2} - \frac{2}{H^4}\left\{\frac{\partial(HW)}{\partial \eta} - \frac{\partial(HV)}{\partial \xi}\right\}\frac{\partial H}{\partial \eta} + \frac{8(1 - NR_2)^2}{H^2}\frac{\partial H}{\partial \xi}\frac{\partial U}{\partial Z}
$$

Momentum equation along Z-direction

$$
\frac{W}{H}\frac{\partial U}{\partial \xi} + \frac{V}{H}\frac{\partial U}{\partial \eta} + 4(1 - NR_2)^2 U\frac{\partial U}{\partial Z} = \frac{\theta}{4(1 - NR_2)^2} - \frac{1}{4(1 - NR_2)^2}\frac{\partial P}{\partial Z} + \frac{1}{H^2}\left(\begin{array}{c}\frac{\partial^2 U}{\partial \xi^2} + \frac{\partial^2 U}{\partial \eta^2} + \\ \frac{H^2}{Gr^2}\frac{\partial U}{\partial Z^2}\end{array}\right)
$$

APPENDIX B

PRINCIPLE OF CONTINUITY OF HEAT FLUX

The present study is focused on the analysis of conjugate free convection heat transfer in vertical eccentric annuli. The geometry of the problem consists of two solid cylinders, one within the other having eccentricity. The annulus between the inner surface of outer cylinder and outer surface of inner cylinder provides space for fluid flow. There is heat transfer between the cylinders. Two solid fluid interfaces exist in the geometry. One is at the outer surface of inner cylinder and the other is at the inner surface of outer cylinder. The amount of heat flowing at any point from the interface of heated wall is equal to the amount of heat flowing in the annulus. In other words, continuity of heat flow is present at the interfaces. Derivation of this principle of continuity of heat flux is going to be presented here.

The expression of heat flux in any curvilinear coordinate system can be written as [56]:

$$q = -k\nabla T = -k\sum_{i=1}^{3} u_i \frac{1}{a_i} \frac{\partial T}{\partial u_i}$$

And the three components of the heat flux vector along the u_1, u_2 & u_3 coordinates are given by:

$$q_i = -k\frac{1}{a_i}\frac{\partial T}{\partial u_i}$$

where,

i = 1, 2, 3

Here, in cylindrical coordinate system,

$u_1 = r$

$u_2 = \phi$

$u_3 = z$

a_i can be defined as:

$$a_i = \left(\frac{\partial x}{\partial u_i}\right)^2 + \left(\frac{\partial y}{\partial u_i}\right)^2 + \left(\frac{\partial z}{\partial u_i}\right)^2$$

where,

i = 1, 2, 3

The coefficients a_1, a_2, a_3 are called the scalar factors which may be constant or functions of the coordinates. The conversion factors for the axes in cylindrical and bipolar coordinates are:

Cylindrical coordinate system:

$x = r\cos\phi$
$y = r\sin\phi$
$z = z$

Bipolar coordinate system [57]:

$$x = \frac{a \sinh \eta}{\cosh \eta - \cos \xi}$$

$$y = \frac{a \sin \xi}{\cosh \eta - \cos \xi}$$

$$z = z$$

No heat is flowing in z-direction. It means there is no heat flux in z-direction, therefore, the z-direction term will vanish. First of all heat flux relation in solid walls will be derived. The generalized form of heat flux relation in radial direction is given by:

$$q_1 = -k \frac{1}{a_1} \frac{\partial T}{\partial u_1} \tag{1}$$

$$a_1^2 = \left(\frac{\partial x}{\partial r}\right)^2 + \left(\frac{\partial y}{\partial r}\right)^2 \tag{2}$$

$$x = r \cos \phi$$

$$\frac{\partial x}{\partial r} = \cos \phi$$

$$y = r \sin \phi$$

$$\frac{\partial y}{\partial r} = \sin \phi$$

Therefore, Eq. (2) becomes:

$$a_1^2 = \sin^2 \phi + \cos^2 \phi$$

$$a_1 = 1$$

Eq. (1) then becomes:

$$q_1 = -k \frac{\partial T}{\partial r}$$

Flux in ϕ-direction is given by:

$$q_2 = -k \frac{1}{a_2} \frac{\partial T}{\partial \phi} \tag{3}$$

$$a_2{}^2 = \left(\frac{\partial x}{\partial \phi}\right)^2 + \left(\frac{\partial y}{\partial \phi}\right)^2 \tag{4}$$

$$x = r \cos \phi$$

$$\frac{\partial x}{\partial \phi} = -r \sin \phi$$

$$y = r \sin \phi$$

$$\frac{\partial y}{\partial \phi} = r \cos \phi$$

Therefore, Eq. (4) becomes:

$$a_2 = r$$

Substituting in Eq. (3), results in

$$q_2 = -k\frac{1}{r}\frac{\partial T}{\partial \phi}$$

Combining fluxes in both directions, we get:

$$\boxed{q_{solid} = -k_s\left(\frac{\partial T}{\partial r} + \frac{1}{r}\frac{\partial T}{\partial \phi}\right)} \tag{A}$$

Now to derive the relation in bipolar coordinate system. Here we have:

$$u_1 = \eta$$

$$u_2 = \xi$$

$$u_3 = z$$

Flux in η-direction is given by:

$$q = -k\frac{1}{a_1}\frac{\partial T}{\partial \eta} \tag{5}$$

$$a_1{}^2 = \left(\frac{\partial x}{\partial \eta}\right)^2 + \left(\frac{\partial y}{\partial \eta}\right)^2 \tag{6}$$

$$q_2 = -k \frac{1}{a_2} \frac{\partial T}{\partial \xi} \tag{7}$$

$$a_2{}^2 = \left(\frac{\partial x}{\partial \xi}\right)^2 + \left(\frac{\partial y}{\partial \xi}\right)^2 \tag{8}$$

$$x = \frac{a \sinh \eta}{\cosh \eta - \cos \xi}$$

$$\frac{\partial x}{\partial \xi} = -\frac{a \sinh \eta \sin \xi}{(\cosh \eta - \cos \xi)^2}$$

$$y = a \frac{\sin \xi}{\cosh \eta - \cos \xi}$$

$$\frac{\partial y}{\partial \xi} = a \frac{\cos \xi \cosh \eta - 1}{(\cosh \eta - \cos \xi)^2}$$

Therefore, Eq. (8) becomes:

$$a_2{}^2 = \frac{a^2 \sinh^2 \eta \sin^2 \xi}{(\cosh \eta - \cos \xi)^4} + a^2 \frac{\cos^2 \xi \cosh^2 \eta + 1 - 2 \cos \xi \cosh \eta}{(\cosh \eta - \cos \xi)^4}$$

$$a_2 = \frac{a}{\cosh \eta - \cos \xi}$$

$$a_2 = h$$

Therefore, Eq. (7) can be written as:

$$q_2 = -k \frac{1}{h} \frac{\partial T}{\partial \xi}$$

The total heat flux in the fluid is:

$$\boxed{q_{fluid} = -k_f \left(\frac{1}{h} \frac{\partial T}{\partial \eta} + \frac{1}{h} \frac{\partial T}{\partial \xi} \right)} \tag{B}$$

Applying continuity of heat flux at the solid-fluid interface:

$$q_{solid} = q_{fluid}$$

$$-k_s\left(\frac{\partial T}{\partial r} + \frac{1}{r}\frac{\partial T}{\partial \phi}\right) = -k_f\left(\frac{1}{h}\frac{\partial T}{\partial \eta} + \frac{1}{h}\frac{\partial T}{\partial \xi}\right)$$

$$\frac{k_s}{k_f}\left(\frac{\partial T}{\partial r} + \frac{1}{r}\frac{\partial T}{\partial \phi}\right) = \frac{1}{h}\left(\frac{\partial T}{\partial \eta} + \frac{\partial T}{\partial \xi}\right)$$

$$\boxed{KR\, h\left(\frac{\partial T}{\partial r} + \frac{1}{r}\frac{\partial T}{\partial \phi}\right) = \left(\frac{\partial T}{\partial \eta} + \frac{\partial T}{\partial \xi}\right)} \tag{C}$$

Hence, this relation can be used at all interface mesh points but first we have to normalize it. From nomenclature,

$$h = \frac{a}{\cosh \eta - \cos \xi}$$

$$R = \frac{r}{r_{io}} \implies r = R\, r_{io}$$

$$\theta = \frac{T - T_o}{T_w - T_o} \implies T = T_o + \theta\left(T_w - T_o\right)$$

Taking Eq. (C) and applying the normalized relations:

$$KR\frac{a}{(\cosh \eta - \cos \xi)}\left[\frac{\partial\{T_o + \theta(T_w - T_o)\}}{\partial r_{io}R} + \frac{1}{r_{io}R}\frac{\partial\{T_o + \theta(T_w - T_o)\}}{\partial \phi}\right] = \left[\begin{array}{c}\dfrac{\partial\{T_o + \theta(T_w - T_o)\}}{\partial \eta} + \\[2mm] \dfrac{\partial\{T_o + \theta(T_w - T_o)\}}{\partial \xi}\end{array}\right]$$

$$\frac{KR}{r_{io}}\frac{r_{io}\sinh \eta_o}{(\cosh \eta - \cos \xi)}\left(\frac{\partial \theta}{\partial R} + \frac{1}{R}\frac{\partial \theta}{\partial \phi}\right) = \left(\frac{\partial \theta}{\partial \eta} + \frac{\partial \theta}{\partial \xi}\right)$$

$$\boxed{KR.H(J)\left(\frac{\partial \theta}{\partial R} + \frac{1}{R}\frac{\partial \theta}{\partial \phi}\right) = \left(\frac{\partial \theta}{\partial \eta} + \frac{\partial \theta}{\partial \xi}\right)} \tag{D}$$

where,

$$H(J) = \frac{\sinh \eta_o}{(\cosh \eta - \cos \xi)}$$

Equation (D) is the dimensionless form of the continuity of heat flux.

The finite difference form of equation (D) for outer interface can be written as:

$$\theta_{so}(NSO+1,j) = \frac{\Delta R_o.\Delta \eta}{\Delta \eta.KR.HO(j)+\Delta R_o} \left[KR.HO(j) \left\{ \frac{\theta_{so}(NSO,j)}{\Delta R_o} + \frac{\theta_{so}(NSO+1,j-1)-}{2\Delta \phi.NR_3} \right\} + \frac{T_f(2,j)}{\Delta \eta} + \frac{\theta_{so}(NSO+1,j+1)-\theta_{so}(NSO+1,j-1)}{2\Delta \xi} \right]$$

where,

$$HO(j) = \frac{\sinh \eta_o}{\cosh \eta_o - \cos \Delta \xi}$$

$T_f(2,j)$ is unknown as can be seen in Fig. (B.1). The following interpolation relation is used to determine the unknown values of $T_f(2,j)$.

$$T_f(2,j) = \theta_f(2,jj) + [\theta_f(2,jj+1)-\theta_f(2,jj)] \left[\frac{X_{io}(2,j)-X_f(2,jj)}{X_f(2,jj+1)-X_f(2,jj)} \right]$$

The unknown $X_{io}(2,j)$, which is the x-coordinate of $T_f(2,j)$, is calculated using the following interpolation relation:

$$X_{io}(2,j) = X_f(2,jj) + [X_f(2,jj+1)-X_f(2,jj)] \left[\frac{X_{so}(1,j)-X_f(1,jj)}{X_f(1,jj+1)-X_f(1,jj)} \right]$$

Equation (D) for inner wall in finite difference form can be written as:
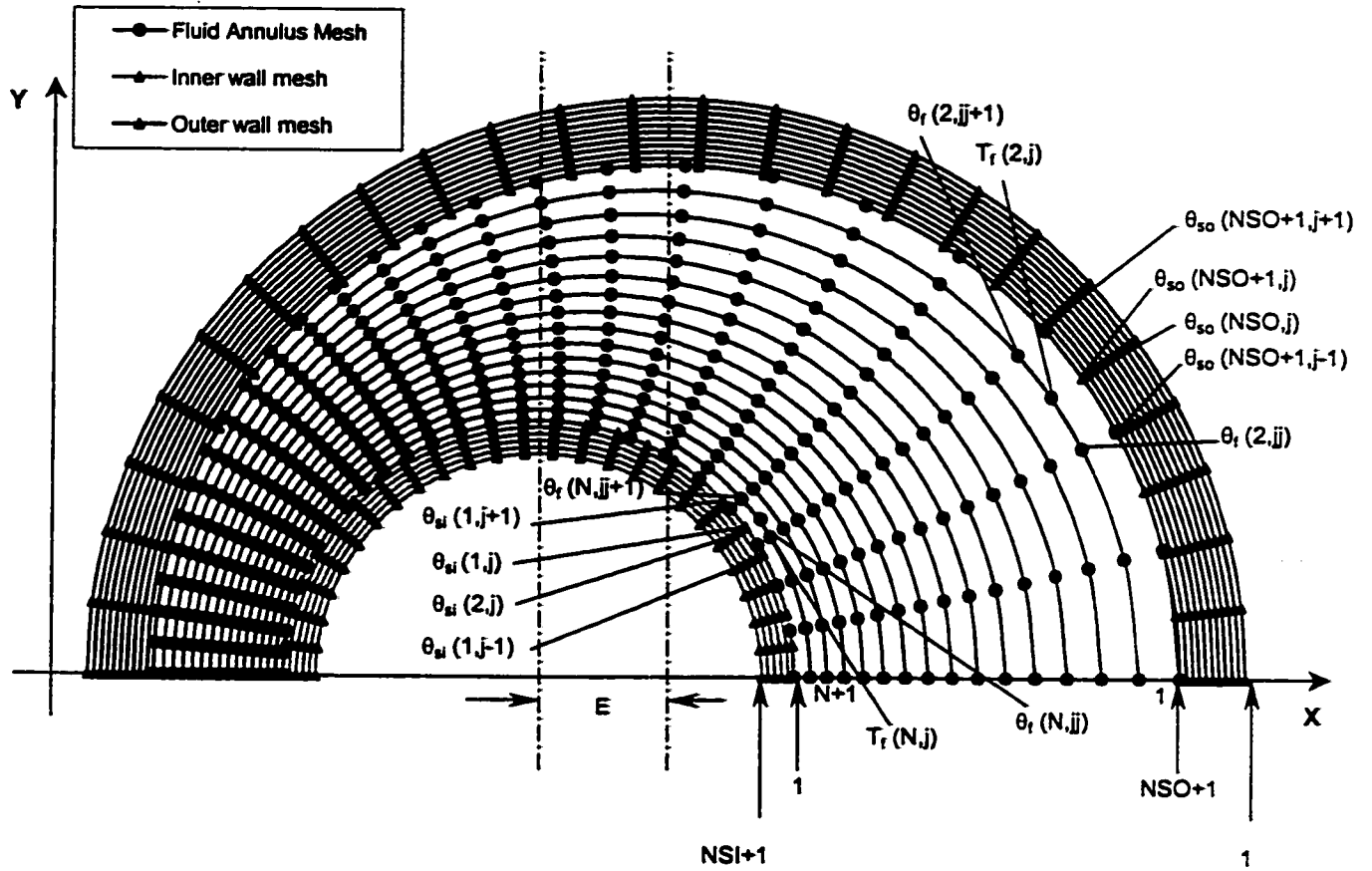
Fig. B.1. Two-Dimensional Half Symmetric Mesh of Eccentric Annuli

NSO=10, NSI=5, N=15, M=25, E=0.5, NR$_2$=0.5, Inner wall thickness=0.05, Outer wall thickness=0.1

$$\theta_{si}(1,j) = \frac{\Delta R_i.\Delta \eta}{\Delta \eta.KR.HI(j) + \Delta R_i} \left[\begin{array}{l} KR.HI(j)\left\{ \dfrac{\theta_{si}(2,j)}{\Delta R_i} + \dfrac{\theta_{si}(1,j+1) - \theta_{si}(1,j-1)}{2\Delta \phi.NR_2} \right\} \\[3mm] + \dfrac{T_f(N,j)}{\Delta \eta} + \dfrac{\theta_{si}(1,j-1) - \theta_{si}(1,j+1)}{2\Delta \xi} \end{array} \right]$$

where,

$$HI(j) = \frac{\sinh \eta_o}{\cosh \eta_i - \cos \Delta \xi}$$

$T_f(N,j)$ is calculated using the following interpolation relation:

$$T_f(N,j) = \theta_f(N,jj) + [\theta_f(N,jj+1) - \theta_f(N,jj)]\left[\frac{X_{io}(N,j) - X_f(N,jj)}{X_f(N,jj+1) - X_f(N,jj)} \right]$$

$X_{io}(N,j)$ is the x-coordinate of $T_f(N,j)$ and is calculated from the following equation:

$$X_{io}(N,j) = X_f(N,jj) + [X_f(N,jj+1) - X_f(N,jj)]\left[\frac{X_{si}(1,j) - X_f(N+1,jj)}{X_f(N+1,jj+1) - X_f(N+1,jj)} \right]$$

APPENDIX C

INTERPOLATION FORMULATION

The continuity of temperature and continuity of heat flux are used to determine the temperature values for cylindrical coordinate mesh points at the two solid-fluid interfaces. The temperature values at bipolar coordinate mesh points at the interfaces can easily be calculated using the cylindrical coordinate temperature values at the respective interfaces by interpolation. Lets take one case. Consider a point at outer interface where the temperature value $\theta_f(1,j)$ is unknown as shown in Fig. (5.1). The two neighboring points θ_{so} (NSO+1, jj) and θ_{so} (NSO+1, jj+1) have already been calculated using principle of continuity of temperature and continuity of heat flux. The coordinates of all the three points are known. All these known and unknown values are tabulated in Table C.1. Now two types of interpolation can be performed.

1. Logarithmic interpolation.

2. Linear interpolation.

1. Logarithmic Interpolation

The logarithmic interpolation formula consists of logarithmic functions. The constraint in this interpolation is that there should not be any zero (0) or negative Value

Table C.1. Temperature and coordinate values on the two interfaces

Interface		Temperature	X-Coordinate
	Outer Interface	$\theta_{so}(NSO+1, jj)$	$X_{so}(NSO+1, jj)$
		$\theta_{f}(1,j)$	$X_{f}(1,j)$
		$\theta_{so}(NSO+1, jj+1)$	$X_{so}(NSO+1, jj+1)$
	Inner Interface	$\theta_{si}(1, jj)$	$X_{so}(1, jj)$
		$\theta_{f}(N+1,j)$	$X_{f}(N+1,j)$
		$\theta_{si}(1, jj+1)$	$X_{so}(1, jj+1)$

REFERENCES

1. Lowry, W.E., Davis, B.W. and Cheung, H. , "The effect of annular air gaps surroundings an emplaced nuclear waste canister in deep geological storage", In Heat Transfer in Nuclear Waste Disposal (Edited by Kulaki, F.A. and Lyezkowski, R.W.), ASME Winter annual meeting HTD, Vol. 11, pp. 69-76 (1980).

2. Shah, R.K. and London, A.L. , *Laminar flow forced convection in ducts*, Academic Press, New York, 1978.

3. Faghri, M. and Sparrow, E.M. , "Simultaneous wall and fluid axial conduction in laminar pipe flow heat transfer", Journal of heat transfer, Vol. 102, pp. 58-63 (1980).

4. Pagliarini, G. , "Conjugate heat transfer for simultaneously developing laminar flow in a circular tube", Journal of heat transfer, Vol. 113, pp. 763-766 (1991).

5. Wen, M.Y. and Jang, K.J. , "Forced convection heat transfer at an inclined and yawed round tube", International journal of heat and mass transfer, Vol. 45, pp. 2031-2042 (2002).

6. Kirshan, B. , "On conjugated heat transfer in fully developed flow", International journal of heat and mass transfer, Vol. 25, pp. 288-289 (1982).

7. Olek, S., Ellias, E., Wacholder, E. and Kaizerman, S. , "Unsteady conjugated heat transfer in laminar pipe flow", International journal of heat and mass transfer, Vol. 34, pp. 1443-1450 (1991).

8. Higuera, F.J and Ryazantsev, Y.S. , "Natural convection flow due to a heat source in a vertical channel", International journal of heat and mass transfer, Vol. 45, pp. 2207-2212 (2002).

9. Bilir, S. , "Transient conjugated heat transfer in pipes involving two-dimensional wall and axial fluid conduction", International journal of heat and mass transfer, Vol. 45, pp. 1781-1788 (2002).

10. Floryan, J.M. and Novak, M. , "Free convection heat transfer in multiple vertical channels", International journal of heat and fluid flow, Vol. 16, pp. 244-253 (1995).

11. Al-Nimr, M.A., El-Shaarawi, M.A.I. , "Analytical solutions for transient conjugated heat transfer in parallel plate and circular ducts", International communications in Heat and mass transfer, Vol. 19, pp. 869-878 (1992).

12. Sucec, J. , "Unsteady forced convection with sinusoidal duct wall generation: the conjugate heat transfer problem", International journal of heat and mass transfer, Vol. 45, pp. 1631-1642 (2002).

13. Medina, M., Luna, E. and Trevino, C. , "Numerical solution of the conjugate heat transfer between forced counter flowing streams", Heat and mass transfer, Vol. 30, pp. 297-302 (1995)

14. Mosaad, M. , "Laminar forced convection conjugate heat transfer over a flat plate", Heat and mass transfer, Vol. 35, pp. 371-375 (1999).

15. Shu, J.J. and Pop, I. , "Thermal interaction between free convection and forced convection along a vertical conducting wall", Heat and mass transfer, Vol. 35, pp. 33-38 (1999).

16. Stein, C.F., Johansson, P., Bergh, J., Lofdahl, L., Sen, M. and Gad-el-Hak, M. , "An analytical asymptotic solution to a conjugate heat transfer problem", International journal of heat and mass transfer, Vol. 45, pp. 2485-2500 (2002).

17. Moukalled, F. and Acharya, S. , "Natural convection in the annulus between concentric horizontal circular and square cylinders", Journal of thermo physics and heat transfer, Vol. 10, No. 3, pp. 524-531 (1996).

18. Adjlout, L., Imine, O., Azzi, A. and Belkadi, M. , "Laminar natural convection in an inclined cavity with a wavy wall", International journal of heat and mass transfer, Vol. 45, pp. 2141-2152 (2002).

19. Reynolds, W.C., Lundberg, R.E. and McCuen, P.A. , "Heat transfer in annular passages. General formulation of the problem for arbitrary prescribed wall temperatures or heat fluxes", International journal of heat and mass transfer, Vol. 5, pp. 483-493 (1963).

20. Heaton, H.S., Reynolds, W.C. and Kays, W.M. , "Heat transfer in annular passages. Simultaneous development of velocity and temperature fields in laminar flow", International journal of heat and mass flow, Vol. 5, pp. 763-781 (1964).

21. Coney, J.E.R. and El-Shaarawi, M.A.I. , "Finite difference analysis for laminar flow heat transfer in concentric annuli with simultaneously developing hydrodynamic and thermal boundary layers", International journal of numerical methods in Engineering, Vol. 9, pp. 17-38 (1975).

22. El-Shaarawi, M.A.I. and Alkam, M.K. , "Transient forced convection in the entrance region of concentric annuli", International journal of heat and mass transfer, Vol. 35, No. 12, pp. 3335-3344 (1992).

23. El-Shaarawi, M.A.I. and Al-Nimr, M.A. , "Fully developed laminar natural convection in open ended vertical concentric annuli", International journal of heat and mass transfer, Vol. 33, No. 9, pp. 1873-1883 (1990).

24. El-Shaarawi, M.A.I. and Al-Attas, M.A. , " Unsteady natural convection in open ended vertical concentric annuli", International journal of numerical methods in heat and fluid flow, Vol. 2, pp. 503-516 (1992).

25. Cadiou, P., Desrayaud, G. and Lauriat, G. , "Natural convection in a narrow horizontal annulus: The effects of thermal and Hydrodynamic instabilities:, Journal of heat transfer, Transactions ASME, Vol. 120, No. 4, pp. 1019-1025 (1998).

26. Hadjadj, A., Maamir, S. and Zeghmati, B. , "A new study of laminar natural convection in two concentric vertical cylinders", Heat and mass transfer, Vol. 35, No. 2, pp. 113-121 (1999)

27. Leppinen, D.M. , "Natural convection in a shallow cylindrical annuli", International journal of heat and mass transfer, Vol. 45, pp. 2967-2981 (2002).

28. El-Shaarawi, M.A.I. and Sarhan, A. , "Developing laminar free convection in an open ended vertical annulus with a rotating inner cylinder", Journal of heat transfer, Transactions of the ASME, Vol. 103, pp. 52-558 (1981).

29. El-Shaarawi, M.A.I. and Sarhan, A. , "Developing laminar free convection in a heated vertical open ended annulus", Ind. Eng. Chem, Fundam., Vol. 20, pp. 388-394 (1981).

30. Lor, W.B. and Chu, H.S. , " Forced and mixed convection in finite vertical concentric cylindrical annuli", American Society of Mechanical Engineers, Heat Transfer Division, Vol. 357-2, pp. 77-84 (1998)

31. Sakakibara, M., Mori, S. and Tanimoto, A. , "Conjugate heat transfer laminar flow in an annulus", The Canadian journal of chemical engineering, Vol. 65, pp. 541-549 (1987).

32. MacGrath, D., Yang, G. and Ebadian, M.A. , "Conjugated heat transfer in a concentric annular pipe", Heat Transfer Division, Numerical modeling of basic heat transfer phenomena in nuclear systems, Vol. 165, pp. 53-61 (1991).

33. El-Shaarawi, M.A.I., Al-Nimr, M.A. and Hader, M.A. , "Transient conjugated heat transfer in concentric annuli", International journal of numerical methods in heat and fluid flow, Vol. 5, pp. 459-473 (1995).

34. El-Shaarawi, M.A.I. and Negm, A.A.A. , "Transient combined natural convection-conduction in open-ended vertical concentric annuli", Heat and mass transfer, Vol. 35, pp. 133-141 (1999)

35. El-Shaarawi, M.A.I. and Negm, A.A.A. , "Conjugate natural convection heat transfer in an open ended vertical concentric annulus", Numerical heat transfer, Part A: Applications, Vol. 36, pp. 639-655 (1999)

36. Redberger, P.J. and Charles, M.E. , "Axial laminar flow in a circular pipe containing a fixed eccentric core", The Canadian journal of Chemical Engineering, Vol. 40, pp. 148-151 (1962).

37. Snyder, W.T. and Goldstein, G.A. , "An analysis of a fully developed laminar flow in an eccentric annulus", A. I. Ch. E. Journal, Vol. 11, No. 3, pp. 462-469 (1965).

38. Cheng, K.C. and Hwang, G.J. , "Laminar forced convection in eccentric annuli", A. I. Ch. E. Journal, Vol. 14, No. 3, pp. 510-512 (1968).

39. Trombetta, M.L., "Laminar forced convection in eccentric annuli", International Journal of Heat and Mass Transfer, Vol. 14, pp. 1161-1172 (1972).

40. Feldman, E.E., Hornbeck, R.W. and Osterle, J.F. , "A numerical solution of laminar developing flow in eccentric annular ducts", International journal of heat and mass transfer, Vol. 25, No. 2, pp. 231-241 (1982).

41. Feldman, E.E., Hornbeck, R.W. and Osterle, J.F. , "A numerical solution of temperature for laminar developing flow in eccentric annular ducts", International journal of heat and mass transfer, Vol. 25, No. 2, pp. 243-253 (1982).

42. Suzuki, K., Szmyd, J.S. and Ohtsuka, H. , "Laminar forced convection heat transfer in eccentric annuli", Originally published in Trans. JSME, Vol. 56, pp. 3445-3450 (1990).

43. Manglik, R.M. and Fang, P.P. , "Effect of eccentricity and thermal boundary conditions on laminar fully developed flow in annular ducts", International journal of heat and fluid flow, Vol. 16, pp. 298-306 (1995).

52. Moukalled, F. and Darwish, M. , "New bounded skew central difference scheme, Part II: Application to natural convection in an eccentric annulus", Numerical heat transfer, Part B, Vol. 31, pp. 111-133 (1997).

53. El-Shaarawi, M.A.I. and Haider, S.A. , "Critical conductivity ratio for conjugate heat transfer in eccentric annuli", International journal of numerical methods for heat and fluid flow, Vol. 11, No. 2, pp. 255-277 (2001).

54. Mokheimer, E.M.A. , "Heat transfer in eccentric annuli", PhD dissertation, Mechanical engineering department, King Fahd University of Petroleum and Minerals (KFUPM), Dhahran, Saudi Arabia, 1996.

55. Haider, S.A. , "Conjugate forced convection heat transfer in eccentric annuli", M.S. Thesis, Mechanical Engineering department, King Fahd University of Petroleum and Minerals(KFUPM), Dhahran, Saudi Arabia, 1999.

56. Özisik, M.N., Heat Conduction, John Wiley and Sons, Inc. New York, pp. 9-11, 1993.

57. Hughes, W.F. and Gaylord, E.W., Basic equations of Engineering Science, Schaum Outline series, pp. 150-151, 1964.

VITAE

- Ahmad Jamal

- Born in Jeddah, Saudi Arabia in 1974

- Received Bachelor of Engineering (BE) in Mechanical Engineering from University of Engineering and Technology, Lahore, Pakistan in 1998

- Served as Mechanical Engineer at Tetra Pak Pakistan, Lahore, Pakistan from 1999 to 2000

- Received Master of Science (MS) in Mechanical Engineering from King Fahd University of Petroleum and Minerals, Dhahran, Saudi Arabia in 2002